CREEP DEFORMATION STUDY OF AZ91-BASED MAGNESIUM ALLOYS

Ph.D. THESIS

By

HITESH DEVIDAS PATIL

DEPARTMENT OF METALLURGICAL ENGINEERING AND MATERIALS SCIENCE

INDIAN INSTITUTE OF TECHNOLOGY INDORE

NOVEMBER 2024

CREEP DEFORMATION STUDY OF AZ91-BASED MAGNESIUM ALLOYS

A THESIS

Submitted in partial fulfillment of the
requirements for the award of the degree
of
DOCTOR OF PHILOSOPHY

by
HITESH DEVIDAS PATIL

DEPARTMENT OF METALLURGICAL ENGINEERING AND MATERIALS SCIENCE
INDIAN INSTITUTE OF TECHNOLOGY INDORE
NOVEMBER 2024

INDIAN INSTITUTE OF TECHNOLOGY INDORE

I hereby certify that the work which is being presented in the thesis entitled **“CREEP DEFORMATION STUDY OF AZ91-BASED MAGNESIUM ALLOYS”** in the partial fulfillment of the requirements for the award of the degree of **DOCTOR OF PHILOSOPHY** and submitted in the **DEPARTMENT OF METALLURGICAL ENGINEERING AND MATERIALS SCIENCE, Indian Institute of Technology Indore**, is an authentic record of my own work carried out during the time period from **July 2019** to **July 2024** under the supervision of Dr. Hemant Borkar, Assistant Professor, Department of Metallurgical Engineering and Materials Science, IIT Indore and Dr. Abhijit Ghosh, Assistant Professor, Department of Metallurgical Engineering and Materials Science, IIT Indore.

The matter presented in this thesis has not been submitted by me for the award of any other degree of this or any other institute.

(Hitesh Devidas Patil)

This is to certify that the above statement made by the candidate is correct to the best of our knowledge.

07/05/2025

Signature of Thesis Supervisor #1 with date

(Dr. Hemant Borkar)

Abhijit Ghosh

07/05/25

Signature of Thesis Supervisor #2 with date

(Dr. Abhijit Ghosh)

HITESH DEVIDAS PATIL has successfully given his Ph.D. Oral Examination held on **05/05/2025**

07/05/2025

Signature of Thesis Supervisor #1 with date

(Dr. Hemant Borkar)

Abhijit Ghosh

07/05/25

Signature of Thesis Supervisor #2 with date

(Dr. Abhijit Ghosh)

ACKNOWLEDGEMENTS

First and foremost, I would like to express my sincere gratitude to my supervisors, Dr. Hemant Borkar and Dr. Abhijit Ghosh, for their invaluable guidance, encouragement, and insight throughout this research. I thank them for giving me an opportunity to work under their supervision and undertaking my PhD degree at IIT Indore. Their expertise, patience, and helpful nature have been instrumental in the successful completion of this work.

I am also deeply grateful to my Ph.D. Student's Progress Committee (PSPC) members Dr. Shailesh Kundalwal and Dr. Jayaprakash Murugesan for their constructive feedback and suggestions that have greatly enhanced the quality of my research. I also take this opportunity to thank Dr. Ajay Kumar Kushwaha, HOD of the Department of Metallurgical Engineering and Materials Science (MEMS), for his support in conducting my research experiments.

I am grateful to the Advanced Mechanical and Physical Metallurgy Lab, Foundry Engineering Lab, Microstructure and Texture Engineering Lab, Welding Engineering Lab, Non-equilibrium Advanced Materials Engineering Lab, Metal Forming and Surface Engineering Lab, and Central Workshop at IIT Indore for providing research facilities. I also thank all staff members of the Dept. of MEMS, IIT Indore, for assisting in the research facility.

I acknowledge MHRD, Govt. of India for Teaching Assistantship (TA).

I genuinely express my special thanks to my lab mates, Dr. Ankush Marodkar, Dr. Piyush Kumar, and Mr. Akshay Jain, for having a cheerful and friendly working environment with them. I wish to acknowledge my beloved friends Dr. Gyanesh Patnaik, Dr. Mukul Saxena, Dr. Venkatesh Verma, Mr. Avinash Bharadwaj, Ms. Shital Wankhede, Ms. Astha Sharma, Ms. Ritu Nain, and Ms. Aparna Gangwar for making my stay at IIT Indore enjoyable.

I would like to extend my deepest gratitude to Ms. Vandana Govindani, whose unwavering support and friendship have been a cornerstone of my PhD journey. Thanks for being my confidant and my source of motivation throughout this process. I am incredibly fortunate to have you by my side.

Above all, I am forever indebted to my parents, Mr. Devidas Patil and Mrs. Pushpa Patil, and other family members and friends for their heartfelt love, endless patience, and extreme support during this venture.

Dedicated to

My Family

and

All Well-Wishers

TABLE OF CONTENTS

ABSTRACT

In order to improve vehicle fuel efficiency and reduce carbon emissions in the environment, the demand for lightweight materials has increased day by day in the transportation industry. Magnesium (Mg) and alloys serve as the exceptionally lightest structural materials available compared to Aluminium, Titanium, and Steel. Amongst the available, AZ91 (Mg-Al-Zn) alloy is the most widely used Mg alloy in the automotive industry owing to its excellent die-castability and adequate mechanical properties at room temperature. However, the poor creep resistance limits its service temperatures above 120 °C, making it incompetent for major powertrain applications. The α-Mg (Mg-Al solid solution) and β-$Mg_{17}Al_{12}$ are the main phases observed in the microstructure of AZ91 alloy. The latter appears to be thermally unstable and starts partially dissolving above the temperature of 120-125 °C. Also, the die casting of the alloy involves porosity and blow holes, which further affects the creep performance of the alloys adversely. So, it is desirable to adopt a potential strategy to enhance the creep performance of AZ91 alloy without sacrificing other properties. Therefore, addressing this challenge involves incorporating suitable alloying elements such as rare earth (RE), calcium (Ca), antimony (Sb), strontium (Sr), silicon (Si), bismuth (Bi), and others into the AZ91 alloy. Although these efforts can strengthen the material for the creep performance, they involve higher production costs and a longer cycle time. Therefore, an attempt has been made to introduce a suitable heat treatment process for the AZ91 alloy and investigate its effect on its creep performance. In addition, the squeeze casting technique has been adopted for AZ91 alloy fabrication in order to overcome the problems associated with die-casting.

The thesis comprises comprehensive work aimed at strengthening the AZ91 alloy against creep deformation at elevated temperatures (min. 150 °C to max. 250 °C) using the suitable alloying addition and heat treatment. The investigation involves the addition of low-cost alkaline earth metals like Ca and Sr into the AZ91 alloy and their effect on the microstructure evolution and creep properties of the alloy. Further, the investigated AZ91 alloys were subjected to heat treatment and compared their creep properties with the same alloys in as-cast conditions. Analytical techniques utilized in this work include optical microscopy, X-ray diffractometry (XRD), field emission scanning electron microscopy (FESEM), electron backscattered diffraction (EBSD), macro hardness testing, and tensile creep testing.

The investigated AZ91-based alloys containing individual and combined Ca/Sr are prepared using a squeeze casting technique. The prepared alloys are subjected to tensile creep tests at temperatures between 150 °C-250 °C under 50-80 MPa stress. The microstructure of AZ91 alloy was observed to be unstable as a result of the thermally unstable β-$Mg_{17}Al_{12}$ phase. The addition of Ca and Sr into the AZ91 alloy incorporated thermally stable Al_2Ca and Al_4Sr phases at the expense of the β-$Mg_{17}Al_{12}$ phase into the alloy, which are confirmed using Scanning Electron Microscopy and X-ray Diffraction studies. Further, thermodynamic and thermal analysis carried out using the Thermo-Calc® database and Differential Scanning Calorimetry reveals that the dissolution temperature associated with the Al_2Ca and Al_4Sr phases is much higher compared to the β-$Mg_{17}Al_{12}$ phase. As a result, the AZ91 alloy with the individual addition of Ca and Sr demonstrates an improved creep performance compared to the AZ91 base alloy, while the combined addition of Ca and Sr to AZ91 alloy demonstrates a superior creep performance compared to individual Ca or Sr-modified AZ91 alloys. In all the investigated alloys, further analysis of the creep data indicates that the creep mechanism based on stress exponent (n) and activation energy (Q) values is a dislocation climb controlled by lattice diffusion. Microstructural investigation on the post-creep samples of the alloys indicates the dissolution of the thermally unstable β-$Mg_{17}Al_{12}$ phase, while the specimens containing Ca and/Sr demonstrate thermally stable Al_2Ca and Al_4Sr phases, which are observed to be unaffected, leading to the stable microstructure during the creep deformation. However, the needle-shape morphology of the Al_4Sr acts as a crack/cavity initiator, while a skeleton shape interconnected network consisting of Al_2Ca and/or Al_4Sr precipitates is effective in retarding crack propagation. In summary, the higher thermal stability of Al_2Ca and Al_4Sr phases, along with the grain size refinement with the individual and combined addition of Ca and Sr, are found to be the major factors contributing to improved creep performance in Sr-Ca modified AZ91 alloys.

Moreover, the application of heat treatment to the as-cast AZ91-Ca/Sr alloys further improves its creep performance by countering grain growth. This improvement is primarily attributed to the dissolution of the β-$Mg_{17}Al_{12}$ phase leading to solid solution strengthening within the Mg matrix, while the undissolved Al_2Ca and Al_4Sr phases continue to contribute to precipitation strengthening. Additionally, the change in needle shaped morphology of the Al_4Sr phase on heat treatment is also observed to be beneficial for the alloy's creep performance. Conversely, in AZ91 alloy with combined addition of Ca and Sr, the suppression of the β-$Mg_{17}Al_{12}$ phase during solidification does not incorporate the solid solution

strengthening on heat treatment. Consequently, the undissolved Al_2Ca and Al_4Sr precipitate alone in the alloy was insufficient to counteract the effect of grain growth, leading to reduced creep performance.

To summarize, this study demonstrates enhanced creep performance in the AZ91 Mg-based alloy, attributed to the incorporation of thermally stable Al-Ca and Al-Sr intermetallic phases within the alloy's microstructure. Additionally, the grain refinement induced by these stable phases, along with the use of squeeze casting, further contributed to the improved creep resistance in AZ91 Mg alloys. Among the investigated alloys, the AZ91 alloy with combined Ca and Sr additions exhibited the highest creep resistance. Moreover, solutionizing heat treatment led to a further improvement in creep performance for the AZ91 and AZ91-1Sr alloys; however, in the case of the AZ91-1Ca-0.6Sr alloy, this heat treatment resulted in reduced creep performance.

Keywords: AZ91 Mg alloy, Ca/Sr Addition, Squeeze Casting, Creep Properties, Creep Mechanism, Heat Treatment

LIST OF PUBLICATIONS

Journal articles

1. **Hitesh Patil**, Akshay Jain, Ankush Marodkar, Piyush Kumar, Abhijit Ghosh, Hemant Borkar, "*Creep deformation study of squeeze cast AZ91 magnesium alloy*", Materials Science and Technology (United Kingdom) (2023), vol. 39, no. 15, pp. 1926–1938. (DOI: 10.1080/02670836.2023.2186055)

2. **Hitesh Patil**, Ankush Marodkar, Abhijit Ghosh, Hemant Borkar, "*Study on the investigation of creep behavior in squeeze cast Ca-modified AZ91 magnesium alloy*", Philosophical Magazine (2024). (DOI: 10.1080/14786435.2024.2415300)

3. **Hitesh Patil**, Abhijit Ghosh, Hemant Borkar, "*Role of intermetallics in creep behaviour of squeezed cast Ca and Sr modified AZ91 Magnesium Alloy*", submitted to the Journal, Advanced Engineering Materials (2024). (DOI: 10.1002/adem.202402249

4. **Hitesh Patil**, Ankush Marodkar, Abhijit Ghosh, Hemant Borkar, "*Effect of heat treatment on the microstructure evolution and creep performance of squeezed cast AZ91-based alloys*", The Journal of The Minerals, Metals & Materials Society (Under Revision).

Conference articles

1. **Hitesh Patil**, Ankush Marodkar, Abhijit Ghosh and Hemant Borkar, "*Effect of Ca addition on the microstructure and creep behaviour of AZ91 Mg alloy*", Materials Today: Proceedings (2023). (DOI: 10.1016/j.matpr.2023.03.056)

2. **Hitesh Patil**, Abhijit Ghosh, Hemant Borkar, "*Effect of Individual Alloying Addition on the Microstructure and Creep Behavior of Squeeze Cast AZ91 Magnesium alloy*", Key Engineering Materials (2023) Vol. 973, pp. 45-50. (DOI: 10.4028/p-iX5ZlE)

LIST OF FIGURES

LIST OF TABLES

ACRONYMS

AGS	Average Grain Size
BCC	Body Centred Cubic
HCP	Hexagonal Closed Packed
FCC	Face-Centred Cubic
Ca	Calcium
Sr	Strontium
Mg	Magnesium
REs	Rare earth Elements
DC	Die Casting
SC	Squeeze Casting
CRSS	Critical Resolved Shear Stress
OM	Optical Microscopy
FE-SEM	Field Emission Scanning Electron Microscopy
EDS	Energy Dispersive Spectroscopy
EBSD	Electron Back Scattered Diffraction
XRD	X-Ray Diffraction
GBs	Grain Boundaries
ICSD	Inorganic Crystal Structure Database
IPFs	Inverse Pole Figures
RT	Room Temperature
HT	High Temperature
SFE	Stacking Fault Energy

STS	Star Testing System
TYS	Tensile Yield Stress
UTS	Ultimate Tensile Stress
EDM	Electro Discharge Machining
ASTM	American Society for Testing Materials

Chapter 1

Introduction

1.1 General background

In the automotive industry, the demand for lightweight materials stems from a variety of critical factors aimed at enhancing vehicle efficiency, sustainability, and performance. A primary motivation is to improve fuel efficiency, which directly reduces emissions. Lighter vehicles require less energy to accelerate, resulting in lower fuel consumption and, consequently, reduced CO_2 emissions, an essential factor for meeting environmental regulations and minimizing the vehicle's carbon footprint. From a safety perspective, lightweight materials like high-strength steel and Aluminum can absorb energy more effectively in collisions, providing enhanced protection for passengers. However, maintaining structural integrity remains crucial, so these materials must be engineered to offer necessary strength while reducing weight. Additionally, the growing popularity of electric vehicles (EVs) heightens the need for lightweight materials to offset the weight of heavy batteries, thereby improving EV efficiency. Although lightweight materials can be costlier, long-term savings on fuel and extended vehicle lifespan often justify the initial investment. With consumers increasingly seeking vehicles with better fuel economy and lower emissions, automakers are adopting lightweight materials as a key strategy in vehicle manufacturing.

The common lightweight materials in automobiles include:

- **Aluminum:** Mostly used in engine components and body panels attributed to its superior strength-to-weight ratio and recyclability.
- **High-strength Steel (HSS):** Being lighter than conventional steel, it provides improved strength and durability.
- **Magnesium alloys:** The ultra-lightweight material generally used in gearboxes, steering wheels, doors, steering rods, and transmission cases.
- **Titanium:** Enforced in high-performance vehicles for manufacturing of exhaust systems requiring excellent strength and low weight.
- **Composites:** The carbon fiber-reinforced polymers (CFRP) employed in high-performance vehicles for chassis components and structural elements. In addition, advanced composites such as glass fiber-reinforced plastics (GFRP) are used in various

sophisticated non-structural and structural applications where cost is not a factor, like in aerospace industries. In automobiles, the cost-effective metal matrix composites at the expense of the above CFRP and GFRP are widely accepted in incorporating required specific strength for automotive components at both room temperature and elevated temperatures.

Among the materials discussed, Magnesium has gained the attention of automakers focused on reducing vehicle weight due to its lightweight nature, abundance, and superior castability compared to Aluminum, Steel, and Titanium. Magnesium has a density of about 1.78 g/cm^3, significantly 33% lower than Aluminum (2.79 g/cm3), 75% lower than Steel (7.85 g/cm3), and 60% lower than Titanium (4.51 g/cm3), making it one of the lightest structural metals available. Magnesium is the eighth most abundant element in the Earth's crust and the third most abundant in seawater, making it relatively accessible. Also, its excellent castability allows for complex shapes, which are beneficial for producing intricate automotive parts. Pure Magnesium is not as strong as some other metals, but alloying Magnesium with other elements can significantly enhance its mechanical properties. Despite of being lightweight, Magnesium alloys exhibit high relative strength and stiffness, damping capacity, and good machinability, making them suitable for structural applications involving both strength and weight savings. In-depth automotive applications of the Mg alloys at room temperature include car doors, front-end carriers, panel roofs, hoods, trunk lids, chassis systems, seat frames, cross-car beams, subframes, bracket mounts, etc [1].

The composition of Magnesium alloys involves the addition of various elements to the Mg, such as Al, Zn, Mn, Ca, Si, Sr, Sb, RE (Rare earth), Bi, etc [2-7]. Aluminum (Al) has been identified as an ideal additive to Magnesium to enhance both its strength and castability. In the early 1900s, alloys based on the Mg-Al-Zn system (*known as the AZ series*) were developed and widely commercialized in Germany. Subsequent research revealed that adding manganese improved the corrosion resistance of Mg-Al alloys [8]. As a result, the Mg-Al-Zn/Mn alloy system has become the foundation for many commercially available Magnesium alloys. These alloys are valued for their balanced mechanical properties, adequate corrosion resistance, affordability, and high castability, especially when compared with other Magnesium alloy systems like WE43 and ZK60, etc. This makes it an attractive choice for large-scale production in the automotive industry. Typical commercial alloys include the AZ91 (Mg-9Al-1Zn), AZ61 (Mg-6Al-1Zn), AZ31 (Mg-3Al-1Zn), AM50 (Mg-5Al-0.4Mn), and AM60 (Mg-6Al-0.4Mn) [9]. The cost-effective commercial die-cast AZ91 (Mg-Al-Zn) alloy is most widely used in automotive components in both cast and wrought conditions because of its lower cost, excellent die-castability, and adequate room-temperature mechanical properties. This alloy is mainly served in automatic components driven at room temperature only because of severe loss of strength or creep resistance at working temperatures above 120 °C. The poor creep resistance of the AZ91 alloy above 120 °C restricts its powertrain applications involving automatic transmission housing, engine blocks, engine pistons, oil pan, engine cylinder head cover, intake manifolds, etc, that operate above 175 °C [10].

The microstructure of AZ91 Mg alloy comprises the matrix α-Mg phase and a continuous network of secondary intermetallic β-$Mg_{17}Al_{12}$ phases uniformly distributed along the grain boundaries. The β-$Mg_{17}Al_{12}$ phase in the alloy appears to be thermally unstable and starts dissolving above 120 °C [111]. In addition, the interface shared by the β-$Mg_{17}Al_{12}$ (cubic lattice) phase and α-Mg matrix (hcp lattice) is incoherent, causing severe cracking and cavity formation at the interface [4]. So, it is well known that the poor creep performance of the AZ91 alloy is attributed to the low thermal stability of the secondary intermetallic β-$Mg_{17}Al_{12}$ phase. The β-$Mg_{17}Al_{12}$ phase is associated with a lower dissolution temperature. Hence, it can be softened and/or coarsened at elevated temperatures, leading to grain boundary sliding and migration during the creep process. The coarsened β-$Mg_{17}Al_{12}$ phase, in addition, also provides less obstruction to dislocation motion. No evidence suggests that Magnesium itself has low creep resistance; rather, this property depends on other alloying elements, such as aluminum. Thus, high-temperature creep resistance in Magnesium alloys can be improved through careful selection of solutes. In terms of applications and manufacturing, there are two primary strategies to enhance creep resistance in Magnesium alloys [9]. One approach involves modifying the AZ91 alloy by adding small amounts of other elements to improve component creep performance. The other approach focuses on developing new, age-hardenable alloys that can be further used as cast or wrought alloys. In many applications, the AZ91 (Mg-Al) alloy system is irreplaceable due to its good castability and low cost. In such cases, it is preferable to modify the AZ91 alloy in order to enhance its creep resistance. The modification in AZ91 alloy will be taken care of by the addition of suitable alloying elements whose effect on the creep performance has been investigated. The alloying elements considered for the addition to the AZ91 alloy are Si [4], Bi [12], Ca [3], [13], Sr [14], [15], Ce [16], RE (Rare-earths) [9], [17], etc, and their combined effect [12], [18], [19]. The addition of these alloying elements to AZ91 alloy causes the precipitation of thermally stable intermetallic phases and substitutes the β-$Mg_{17}Al_{12}$ phase [9], [20]. The increased creep resistance of the AZ91 alloy post-alloying addition is attributed to these thermally stable grain boundary intermetallic phases restricting the migration of the grains at elevated temperatures or the pinning effect by thermally stable intermetallic particles to the dislocation motion. The strengthening of the Mg matrix by solid solution and/or precipitation hardening can also be experienced. As a result, several commercialized creep-resistant Mg- Al-based alloys, such as AS (Al-Si), AE (Al-RE), AX (Al-Ca), and AJ (Al-Sr) series, were developed over recent decades [9]. Although the addition of RE (rare earth) elements in AZ91 alloy promotes precipitation with higher thermal stability, their commercialization in automobile industries is limited because they are too expensive [6], [7]. The addition of low-cost Si to the Mg alloy results in the precipitation of Mg_2Si intermetallic having coarse 'Chinese-script' morphology, leading to the stress concentration during deformation [9], [21], [22]. On the other hand, cost-effective alkaline earth metals, such as Sr and Ca, are alternatively used as suitable additives in AZ91 alloy. The formation of the thermally stable Al-Sr and Al-Ca compounds in those AZ91-modified alloys is expected to be beneficial for improving elevated temperature properties [7][23], [24]. *Amberger et al.* [25] and *Qudong et al.* [26] reported the precipitation of thermally stable Al_2Ca phase post-Ca addition, and a simultaneous decrease in phase fraction of the β-$Mg_{17}Al_{12}$ phase, thus contributing to the improved creep performance of the AZ91 Mg alloy. However, poor die castability is an important drawback of the Ca-modified AZ91 alloys, which limits commercialization [10], [17], [27]. The die-cast Mg-Al alloys containing Ca are observed to be prone to hot cracking and die sticking. The small casting cracks resulting from stress concentration during solidification shrinkage are also observed post-Ca addition [28], [29], [30]. The authors, *Nakaura et al.* [19] and *Hirai et al.* [18], reported the emergence of casting cracks during solidification in the die-casted AZX911 Mg alloy. Applying the squeeze casting technique to fabricate the Mg alloy containing Ca may overcome the problem associated with die casting. Moreover, the addition of Sr along with Ca in the AZ91 alloy may also help in reducing the hot cracking during die casting [18], [31]. Nowadays, squeeze casting is becoming popular due to its high productivity, high precision, good machinability, and high melt fluidity [10], [27]. In squeeze casting, the melt solidifies under applied pressure, leading to minimal porosity and substantial grain refinement in squeeze-cast components [32], [33]. The refined microstructure and reduced defect in squeeze-casted products are expected to improve the creep performance of the alloy. Therefore, due to the availability of limited literature, it is interesting to investigate the tensile creep performance of the AZ91 Mg alloy having the individual and combined addition of Ca and Sr fabricated using the squeeze-casting technique. As these routes of alloying addition and employing different processing techniques involve higher production costs and a longer cycle time, the researchers are trying to incorporate the heat treatment processes to further achieve the desired creep performance of the Mg-Al alloys. On solutionizing heat treatment, the β-$Mg_{17}Al_{12}$ phase responsible for the poor creep performance of the AZ91 alloy is expected to dissolve homogeneously into the α-Mg matrix, which is perhaps expected to enhance the mechanical properties of the alloy at both ambient and elevated temperatures, also expected to improve the creep performance of the investigated alloy [34-40]. In the majority of studies conducted over the past decade, numerous researchers have concentrated on investigating the impact of various heat treatment processes, such as solutionizing and aging, on the mechanical properties of Mg-Al alloys [34], [39], [41-43]**.** However, there has been a scarcity of studies examining the effect of different heat treatment processes on the creep performance of the Mg-Al alloys. Yeoh et al. [44] reported an improvement in the ultimate tensile strength, yield strength, and elongation of the AZ80 Mg alloy on solution treatment and age hardening treatment. A similar observation is made by Wang et al. [45] and Kang et al. [21] on the mechanical properties in the case of Mg-3Al-1Si-0.3Mn-xSr and Al-Si-Mg alloy, respectively. Pu et al. [20] reported the improved comprehensive mechanical properties and corrosion resistance of the AZ91 Mg alloy attributed to the decomposition of the eutectic structure following solution treatment. In addition, Ming-bo et al. [46] experienced both improved mechanical and creep properties in the Mg-3Sn-1Mn alloy as a result of aging treatment. To the best of the author's knowledge, investigations on the tensile creep performance of squeeze-casted AZ91 (Mg-Al-Zn) alloy having the addition of Sr and Ca followed by heat treatment are not available.

Moreover, a detailed understanding of the creep mechanism of the Mg-Al creep system subjected to creep deformation is crucial for developing new creep-resistant materials. Although various advantages of Mg-Al alloys are due to the Al addition to Mg, the poor creep resistance of these commercial alloys is also associated with Al, which can be confirmed through investigation of the creep mechanism of alloys. The presence of Al in AZ91 alloy results in the precipitation of thermally unstable β-$Mg_{17}Al_{12}$ phase, which generally starts dissolving above the creep temperature of 110-120 °C, thus making the AZ91 alloy unsuitable for most automotive powertrain applications. Generally, the dominant creep mechanism of the alloy is identified on the basis of stress exponent (n) and activation energy (Q) estimated under applied stress and temperature range of interest. These values of n and Q are estimated from the empirical equation associated with the steady-state creep rate of the alloy as a function of applied stress and temperature [8]. The equation is expressed as

$$\dot{\varepsilon} = A\,(\sigma)^{n} \exp\left(-\frac{Q}{RT}\right) \qquad (1.1)$$

Where A is a material-related constant, σ the applied stress, T is the creep temperature, R is the gas constant, Q is the apparent activation energy for creep, and n is the stress exponent. Following Eq. 1, the activation energy (Q) is obtained from the Arrhenius plot between log ($\dot{\varepsilon}$) vs. (1/T) at specific stress under a temperature range of interest, and stress exponent (n) can be estimated from the slope of the plot between log ($\dot{\varepsilon}$) vs log (σ) at a specific temperature in the stress range of interest. In general, when n=1 and the activation energy Qc is around 92–135 kJ/mol, the mechanism is indicative of diffusional creep. An n value of 2 is associated with grain-boundary sliding, while dislocation creep corresponds to n values ranging from 3 to 8. Specifically, n=3 suggests solute drag creep, and values between 5 and 8 indicate that dislocation climb and gliding are the dominant mechanisms. Research has shown that dislocation climb and grain boundary sliding are the primary mechanisms responsible for the creep deformation in Mg-Al alloys, which largely determines their creep behavior [8],[17] [25], [47], etc. So, in order to retard the movement of dislocation climb or grain boundary sliding in the Mg-Al alloys during the elevated temperature creep deformation, the incorporation of strong thermally stable phases along the grain boundary inside the matrix becomes necessary by the addition of suitable alloying elements to the Mg-Al alloys. On the other hand, among the few studies discussing the creep mechanisms of the die-cast AZ91 (Mg-Al) alloys, there is non-uniformity observed in specifying the creep mechanisms at different stresses and temperatures, as listed in **Table 2.2**. Also, there is no study has been found investigating the creep mechanism of the base AZ91 alloy fabricated using the squeeze casting technique. In addition, the study investigating the creep mechanism of the AZ91 alloy subjected to tensile creep deformation having the addition of individual Ca/Sr and combined Ca-Sr, fabricated via squeeze casting route, has not been found as listed in **Tables 2.3 and 2.4**.

Based on a thorough review of current literature on the need for lightweight materials in automotive components, Magnesium (Mg) and its alloys stand out as exceptional choices. AZ91 (Mg-Al-Zn) is the most widely used Magnesium alloy in the automotive industry for room-temperature applications due to its excellent castability and strength at room temperature. However, it has been concluded that the AZ91 alloy lacks sufficient creep resistance at elevated temperatures and stresses because of its unstable microstructure. Therefore, it is important to modify the AZ91 alloy by adding suitable, cost-effective alloying additions such as Ca and Sr without altering its beneficial properties like good castability and room temperature strength. Further, in order to improve the casting quality of the alloy by reducing the casting defects that arise from Ca addition to die-cast AZ91 alloy during solidification, the squeeze casting technique instead of die-casting can be employed. The additional grain refinement in the alloy as a result of squeeze casting may further help in increasing the creep strength of the squeeze-casted alloys. Moreover, the application of heat treatment to the AZ91 alloys is expected to bring a considerable improvement in the creep performance of the investigated alloys. The investigation of the creep mechanism of the AZ91 alloy subjected to creep deformation is crucial in order to develop new alloys that are more creep resistant. There is a non-uniformity observed in the creep mechanism of the base AZ91 alloy under a specific range of stress and temperature. In addition, there has been no study investigating the creep mechanism of the AZ91 alloy fabricated using the squeeze casting technique. Further, the scarcity of investigation on the creep mechanism of the squeeze-cast AZ91 alloy subjected to tensile creep deformation with the individual addition of Ca and Sr is also very limited, whereas no study on the creep mechanism found in the case of combined addition of Ca& Sr to the squeeze cast AZ91 alloy.

In the current thesis work, the most widely used commercial AZ91 (Mg-Al-Zn) alloy has been considered in order to investigate its microstructure and tensile creep properties. To enhance its creep performance, it is further alloyed with suitable, cost-effective Ca and Sr elements using Mg-Ca and Mg-Sr master alloys. The alloying elements addition initially takes place individually, like 1 wt% Ca and then 1 wt% Sr. Finally, in order to investigate the combined effect of alloying addition, the 1 wt% Ca and (0.3& 0.6 wt% Sr) are added together with the AZ91 alloy. The investigated alloy preparation is carried out using a squeeze-casting technique. The kind of secondary phases and their thermostability in AZ91 alloy on alloying addition are examined through thermodynamic analysis carried out using Thermo-Calc® software DSC analysis. Furthermore, the alloys under consideration are subjected to heat treatment to investigate their effect on microstructure evolution and creep performance. An attempt has also been made to investigate the underlying creep mechanism of the AZ91 alloy considered for the creep deformation under specific stress and temperature ranges of interest.

Based on the underlying creep mechanism associated with the creep deformation of base AZ91 alloy, the further compositions of the AZ91 alloys with Ca and Sr are prepared to counteract the deformation mechanism. Further, the creep mechanism associated with the prepared AZ91 alloys with Ca and Sr is also studied.

1.2 Objectives

Based on the literature review and research gap discussed above, the primary objectives of the present thesis are as follows:

1. To study the microstructure and tensile creep properties of the base AZ91 (Mg-Al-Zn) alloy fabricated through the squeeze casting route.

2. To study the microstructural modification and tensile creep properties of the squeeze-cast AZ91 alloy modified with 1wt% Ca addition.

3. To develop the squeeze-cast AZ91 alloy modified by the individual addition of 1 wt% Sr and the combined addition of 1 wt% Ca with (0.3& 0.6) wt% Sr and to investigate their respective microstructure and creep properties.

4. To investigate the effect of heat treatment on the microstructure evolution and creep performance of the squeeze cast AZ91, AZ91+1%Sr, and AZ91+1%Ca+0.6%Sr Mg alloys analyzed in the present study.

1.3 Thesis structure

The thesis outlines to fulfill the above-mentioned primary objectives as per the structure summarized in the following sections:

Chapter 1 is the introductory chapter, which describes the background, motivation, and goals of the current work.

Chapter 2 presents a comprehensive literature review on the needs and application of lightweight Mg alloys in automotive industries. Literature focuses on the microstructure and creep deformation studies of the widely utilized commercial AZ91 alloy, its modification using different alloying additions, and the governing creep mechanisms under different stresses and temperatures. Finally, the literature on the role of heat treatments on the mechanical and creep performance of the different Mg alloys has also been presented.

Chapter 3 summarizes in detail the experimental methodology implemented in the present thesis.

Chapter 4 describes the creep deformation study of squeeze-cast base AZ91 Mg alloy. The study includes the microstructural investigation, tensile creep deformation curves of the specimens, post-creep microstructure of the deformed specimens. Most importantly, the governing creep mechanism of the squeeze cast AZ91 alloy under specific stress and temperature has been studied. Further, an attempt has been made to estimate the dislocation density in the deformed specimens and estimate the threshold stress for the creep deformation at the selected stresses and temperatures.

Chapter 5 describes the effect of Ca addition on the creep properties of the squeeze-cast AZ91 Mg alloy. The study includes the microstructural investigation, tensile creep deformation curves of the specimens, post-creep microstructure of the creep-deformed specimens, and the governing creep deformation mechanism of the alloy *AZ91-Ca* at specific stress and temperature. Further, the thermal stability of the intermetallic phases appearing in the microstructure of the alloy has been examined using thermodynamic analysis. On the other hand, an attempt has been made to investigate the impact of solutionizing heat treatment on the microstructure and creep performance of the *AZ91-Ca* alloy.

Chapter 6 investigates the creep properties of the squeeze cast AZ91 Mg alloy containing individual Sr and combined Sr/Ca addition. The study includes an in-depth microstructural investigation, tensile minimum creep rate estimation, and post-creep microstructure of the creep-deformed specimens. The governing creep deformation mechanism of the investigated AZ91-Sr/Ca alloys at specific stress and temperature has also been investigated and compared with the alloys investigated previously in Chapters 4 and 5. Further, the thermal stability of the intermetallic phases appearing in the microstructure of the alloys has been examined using thermodynamic analysis.

Chapter 7 describes the effect of heat treatment on the microstructure evolution and creep performance of the squeeze-cast AZ91 alloys having individual Sr and combined Sr/Ca addition. The study includes the microstructural investigation, tensile minimum creep rate estimation using the tensile curves of the specimens, and post-creep microstructure of the creep-deformed specimens. Further, the activation energy of the creep deformation has been estimated for the investigated heat-treated alloys within the range of temperatures and compared with the same alloys in as-cast conditions.

Chapter 8 contains the overall conclusions of the present thesis and the scope for future work.

Chapter 9 discusses the contribution of the thesis work to original knowledge.

Chapter 2

Literature Review

2.1 Magnesium

Magnesium was first identified as a distinct element in 1755 in the region of Magnesia in eastern Thessaly, Greece. In 1808, Humphry Davy, a chemist from England, succeeded in isolating Magnesium in its metallic form [1]. This element ranks as the eighth most prevalent in the Earth's crust and occurs in significant quantities in minerals like magnesite, dolomite, and carnallite. Additionally, seawater provides a substantial source of Magnesium, which can be extracted using electrolysis. In the periodic table, Magnesium, with atomic number 12 and space group P6_3/mmc (no. 194), belongs to the alkaline earth metal group and is situated in period 3. Characterized by a silvery-white appearance, Magnesium is one of the lightest structural metals, with a density of around 1.7 g/cm^3, lower than that of Aluminum, Steel, or Titanium [45], [48-50]. It has a melting point of 650 °C. Due to its abundance and high strength-to-weight ratio, Magnesium plays a crucial role in industries such as transportation, where demand for lighter materials aligns with goals to reduce fuel consumption and CO_2 emissions [50].

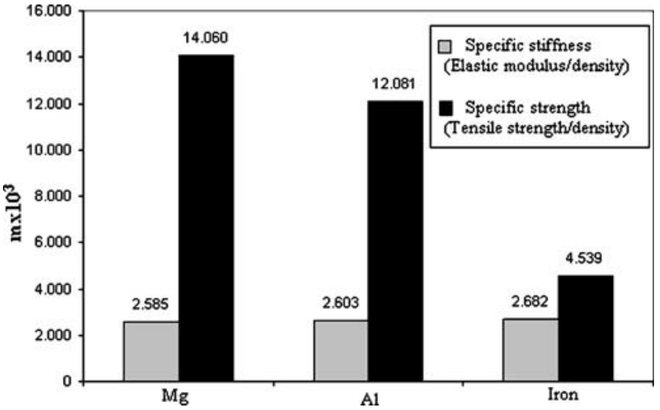

Fig. 2.1: Comparison of basic structural properties of Magnesium with Al and iron [50].

Mg has a hexagonal closed-packed (HCP) crystal structure with a c/a ratio of 1.624. The primitive unit cell associated with the HCP crystal structure of Mg, illustrated in **Fig. 2.2a**, indicates that a unit cell is comprised of two axes (a=b≠c). An interaxial angle of 120° separates the axes a and b. Mg HCP crystal structure has six comparable atoms stacked in the *ABABAB* pattern, as shown in **Fig. 2.2b**.

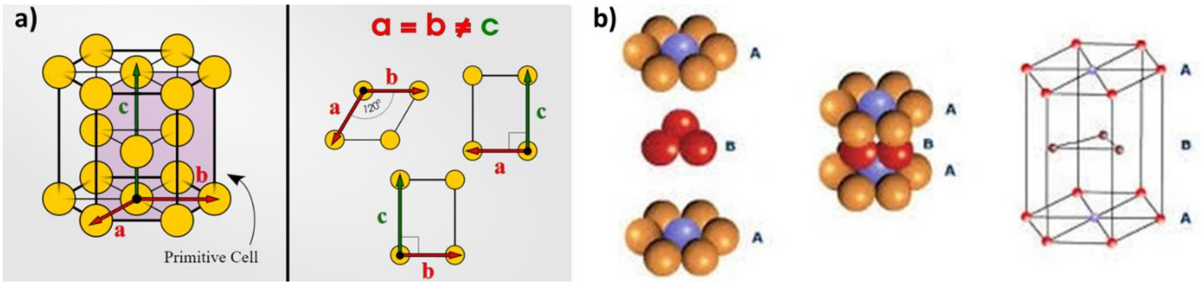

Fig. 2.2: a) Hexagonal closed-pack crystal structure of Magnesium and b) stacking sequence (*ABABAB*) of HCP crystal structure [51], [52].

Mg exhibits low ductility and low formability at ambient temperature due to the limited number of slip systems available [52]. The von Mises criterion states that five independent slip systems are needed for uniform plastic deformation [53]. Mg has only two independent slip systems at room temperature, thus limiting its formability. The additional slip systems must be activated in order to improve its formability. At ambient temperature, the deformation of Mg takes place by slip, which is actually a glide of dislocations along the definite crystallographic planes known as slip planes. In Mg, the principal slip system is on the basal plane, and prismatic and pyramidal slip systems are known to be activated at elevated temperatures, depending on the alloy compositions [51], as shown in **Fig. 2.3**. Since the hexagonal close-packed (HCP) structure of Mg results in strong anisotropy, deformation along the c-axis is particularly challenging due to the lack of sufficient slip systems. To accommodate strain along the c-axis, <c+a> pyramidal slip becomes active, enabling dislocation motion along non-basal planes and thereby contributing to plasticity. In addition to pyramidal slip, twinning also plays a crucial role in accommodating deformation. Extension twinning ($\{10\bar{1}2\}\ \langle 10\bar{1}1\rangle$) is commonly activated under tensile loading along the c-axis, allowing for rapid reorientation of the crystal lattice to enhance deformability. Conversely, contraction twinning ($\{10\bar{1}1\}\ \langle 10\bar{1}2\rangle$) operates under compressive stress along the c-axis, further facilitating plastic deformation. The combined activation of these mechanisms is essential for overcoming the limited slip behavior inherent to Mg, improving its overall ductility and formability.

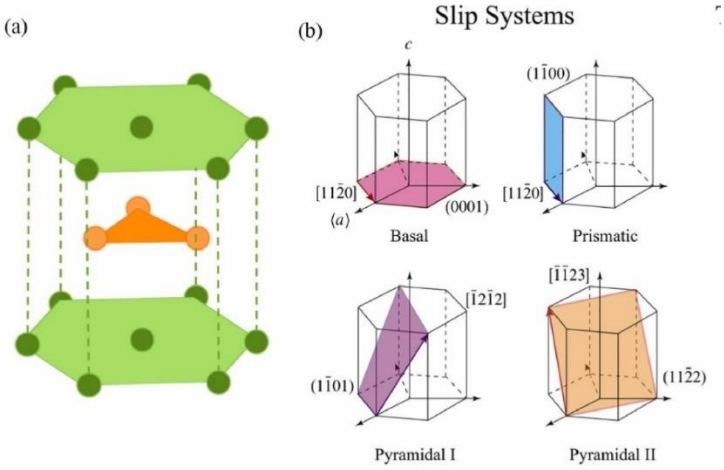

Fig. 2.3: Slip systems in HCP Magnesium [51].

2.2 Magnesium alloys

Magnesium alloys can be categorized into two main types: cast alloys and wrought alloys, based on how they are fabricated. Wrought alloys are first cast into ingots, which are then shaped through mechanical processes like hot or cold working to achieve the desired form. In contrast, cast alloys are directly molded into their final shape through methods such as sand casting, die casting, or pressure die casting, making them ideal for complex geometries.

Pure Magnesium has limited strength for industrial use, so it is typically combined with other elements to enhance its mechanical properties and resistance to corrosion. Key alloying elements for Magnesium include Aluminum (Al), zinc (Zn), beryllium (Be), silicon (Si), rare earth elements (RE), and calcium (Ca). Common commercial Magnesium alloys are grouped into several series: AZ (Mg-Al-Zn), AM (Mg-Al-Mn), AE (Mg-Al-RE), EZ (Mg-RE-Zn), ZK (Mg-Zn-Zr), and WE (Mg-RE-Zr) [54]. The improvement in the mechanical properties of the alloy post-alloying addition is explained with the help of different strengthening mechanisms of the Mg alloys that arise due to the various alloying additions. The strengthening mechanisms observed in Mg alloys are explained in the section below.

2.2.1 Strengthening mechanisms

The addition of alloying elements to Mg leads to the formation of secondary phases, which are assumed to play a key part in the strengthening of the alloys at both room temperature and elevated temperatures. To provide insights into underlying strengthening mechanisms, the following strengthening mechanisms are expected to be active in the Mg alloys, having individual and combined addition of suitable alloying elements: grain refinement strengthening, dislocation strengthening, load-bearing strengthening, and particle strengthening [104].

A) Grain size strengthening

Grain boundaries are obstructions to the dislocation motion. The well-known Hall-Petch relation is used to express the effect of average grain size (D) on the yield strength (σ_y) and hardness (*H*) of metallic polycrystalline materials.

$$\sigma_y = \sigma_0 + \frac{K_y}{\sqrt{D}} \tag{2.1}$$

Where σ_0 is the intrinsic lattice resistance to the basal slip (yield strength of a single crystal in the absence of any strengthening mechanisms except solid solution effect), and K_y is the Hall-Petch slope representing the magnitude by which crystal boundaries in a polycrystalline material resist slip. Significant efforts have been made to refine the grain structure of AZ91 by incorporating elements like Mn, Ca, Sr, RE, and Zr. The inclusion of these alloying elements leads to a reduction in grain size compared to the base alloy processed under identical conditions, resulting in enhanced yield strength due to the grain refinement, $\Delta\sigma_{GR}$ can be expressed as [105],

$$\Delta\sigma_{GR} = K_y \left(\frac{1}{\sqrt{D}} - \frac{1}{\sqrt{D_o}}\right) \tag{2.2}$$

Where D and D_0 are the average grain size of the designed alloy and base alloy, respectively.

B) Dislocation strengthening

Dislocation strengthening refers to the creation of dislocations when an alloy undergoes loading, such as tension or compression [105]. To adjust for differences in modulus between the matrix and reinforcing particles or phases, dislocations develop during plastic deformation [105]. As these dislocations interact and obstruct one another's movement, a higher dislocation density leads to an increase in yield strength [106]. The enhancement in strength due to modulus mismatch can be estimated by [105-107],

$$\Delta\sigma_D = \sqrt{3}\beta G_m b\sqrt{\rho}_{modulus}, \tag{2.3}$$

$$\sqrt{\rho}_{modulus} = \frac{6Vp\varepsilon}{bdp} \tag{2.3a}$$

Where β is a material-specific coefficient, G_m is a matrix shear modulus, b is a burger vector, $\rho_{modulus}$ is the dislocation density caused by the modulus mismatch, and ε is the microstrain.

C) Load-bearing strengthening

Load-bearing strengthening provides direct strengthening through the presence of precipitate phases. This phenomenon is generally observed in the case of metal matrix composites. Based on shear-lag theory, load transfer happens at the phase/matrix interface through shear stresses, which can be expressed as,

$$\sigma_{Load} = \sigma_m \left[\frac{V_p(S+2)}{2} + V_m\right], \tag{2.4}$$

where Vp and Vm are the volume fraction of phase and matrix, respectively, and S is the aspect ratio. For equiaxed particles, S is close to 1, and for plate-like precipitates, S is close to 5.

D) Particle strengthening

Particles and dislocations interact through two primary mechanisms: (i) dislocations shearing particles, or (ii) dislocations looping around particles that cannot be penetrated. When particles are sheared by dislocations, the resulting strengthening effect arises from one or a combination of the following mechanisms [108-110]: (a) coherency strengthening, (b) modulus strengthening, and (c) order strengthening. Typically, only very small and relatively soft particles can be sheared by dislocations. In contrast, when dislocations loop around particles, this behavior aligns with the Orowan model and is commonly referred to as Orowan strengthening.

Orowan strengthening:

In Orowan strengthening, the strength is provided by the resistance of closely spaced hard particles to the passing of dislocations [110]. The dislocation movement bypasses the particles by bowing, leaving behind loops surrounding the particles [111], [112]. To propagate a dislocation loop around the precipitates, further stress is needed to bow it before gliding in the solid solution. This latter stress corresponds to the elastic limit of the precipitate or phase. The strength improvement related to Orowan strengthening is given as follows [112], [113],

$$\Delta\sigma_{\text{Orowan}} = \frac{0.13 G_m b}{\lambda} \ln \frac{d_p}{2b} \tag{2.5}$$

Where λ is the interparticle spacing, which can be expressed as,

$$\lambda = d_p \left[\left(\frac{1}{2V_p}\right)^{1/3} - 1\right]. \tag{2.5a}$$

In summary, the strengthening mechanisms discussed above are expected to play an active role in the improvement of the mechanical properties of the Mg alloyed with suitable alloying addition.

E) Solid solution strengthening

Solid solution strengthening enhances matrix strength by incorporating soluble elements into the matrix (or solvent). This addition distorts the atomic lattice due to mismatches in atomic radii, which in turn hinders dislocation movement. The effectiveness of solid solution hardening generally increases with differences in atomic sizes, reaching an optimum when the difference exceeds about 10%. Moreover, solid solution strengthening can reduce the stacking fault energy (SFE) of the crystal lattice, impeding dislocation cross-slip—a primary deformation mode in imperfect crystals at higher temperatures. Another contributing mechanism of solid solution is the formation of atomic clusters or short-range ordering, which further strengthens the material. In single-crystal superalloys, for instance, rhenium atoms are observed to gather in regions under tensile stress near the γ/γ' interfacial dislocation cores. This clustering forms a “Cottrell atmosphere,” which effectively blocks dislocation motion and crack propagation [114]. Research by Caceres and Rovera [115] on polycrystalline Mg-Al alloys with varying Aluminum content demonstrates that hardness and flow strength consistently increase with higher Aluminum content. In this context, AZ91 alloy shows greater strength than Mg-8%Al, benefiting from additional strengthening from zinc. Alloys with higher solute concentrations also tend to exhibit more strain hardening. Similarly, Akthar and Teghtsoonian [116] reported an increase in dislocation density on the basal plane due to the strain field with higher Aluminum concentration in their alloys, with forest hardening effects being amplified by the presence of solute atoms.

The solid solution strengthening is expressed by the following equation,

$$\sigma_{ss} = CX^{2/3} \tag{2.6}$$

where X is the atomic fraction of the solute.

2.3 Major alloying elements of Magnesium

Aluminum (Al) is considered one of the most effective solutes to enhance the strength and castability of Magnesium alloys. At 437 °C, it forms a eutectic system that improves the castability, strength, and hardness of Magnesium alloys [62]. Magnesium-Aluminum-zinc (Mg-Al-Zn) alloys, specifically the AZ series, were first developed and widely used in Germany in the early 20th century [9]. The addition of zinc (Zn) to these alloys boosts both strength and castability. Zinc reduces the solubility of Aluminum in Magnesium while contributing to a moderate increase in strength [63]. Later, the incorporation of manganese (Mn) was found to enhance the corrosion resistance of Mg-Al-based alloys. As a result, the Mg-Al-Zn/Mn system has become the foundation for most commercial Magnesium alloys today. These alloys offer a balance of good mechanical properties, reasonable corrosion resistance, affordability, and high castability compared to other Magnesium alloy systems. Common commercial alloys include AZ91 (Mg-9Al-0.7Zn), AZ61 (Mg-6Al-0.7Zn), AM50 (Mg-5Al-0.4Mn), and AM60 (Mg-6Al-0.4Mn) [9], [45], [48-50], [55], [64-66]. These alloys are primarily used in automotive parts, computer housings, instrument panel beams, steering components, car doors, and wheels [67]. However, their use is typically limited to room temperature applications due to a significant decrease in strength and creep resistance at temperatures exceeding 120 °C.

2.3.1 Designation of Mg alloys

Magnesium alloys are categorized by their alloying elements and named according to the conventions defined by the American Society for Testing and Materials (ASTM). This naming system uses a three-part letter-number-letter format. For example, an alloy designation is shown in **Fig. 2.4**.

1. The first part consists of letters representing the two principal alloying elements, listed in order of decreasing content, as shown in **Table 2.1**.
2. The second part is the weight percentages of these elements, rounded to the nearest whole number and listed in the same order as the code letters.
3. The third part is an assigned letter starting with "A" to distinguish between alloys with the same nominal designation.
4. Sometimes, a letter and a digit follow to indicate the alloy's temper designation.

Table 2.1: Code letters for the designation system of Magnesium alloys [68].

Aluminum	A
Copper	C
Rare Earth Metals	E
Zirconia	K
Lithium	L
Manganese	M
Calcium	X
Strontium	J
Silicon	S
Yttrium	W
Zinc	Z
Antimony	Y
Bismuth	B

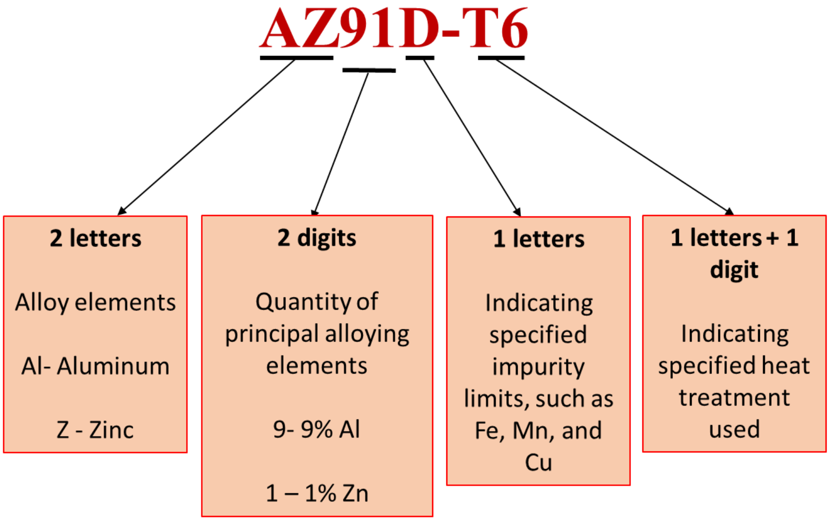

Fig. 2.4: An example of Magnesium alloy designation.

2.3.2 AZ91 (Mg-Al-Zn) alloy

Mg alloys are categorized into two groups based on the quantity of Aluminum contained [69].

1. Mg-Al-Zn-Mn and Mg-Al-Mn alloys include 2-10 wt.% Al and minor quantities of Zn and Mn. These alloys are distinguished by their low manufacturing costs, excellent corrosion resistance, and restricted mechanical characteristics at high temperatures.
2. Mg-Zr-Zn, Mg-RE-Zr, Mg-Ag-RE-Zr, and Mg-Y-RE-Zr alloys substitute Aluminum with elements such as REs, Zr, Ag, and Si. These alloys stand out for their high manufacturing costs and resilience at high temperatures.

A Magnesium-Aluminum alloy with a high Aluminum concentration (3-9 wt.%) has excellent castability, mechanical characteristics, and corrosion resistance at room temperature. The AZ91 alloy (Mg-9wt.%Al-1wt.%Zn-0.3wt.%Mn) is a widely used alloy of the Mg-Al-Zn family. This alloy exhibits the following characteristics [70]:

- Cast alloys have high Aluminum content, making them easier to produce and machine
- Good strength-to-weight ratio
- Good corrosion resistance owing to low amounts of impurities (Fe, Cu, and Ni)

The microstructure of AZ91 alloy is mostly comprised of the α-Mg matrix phase (solid solution of Mg-Al) and intermetallic β–$Mg_{17}Al_{12}$ phase. Al has a maximum solid solubility of 12.7 wt.% in Mg at 437 °C, which is reduced to 2 wt.% at 100 °C, as shown in the Mg-Al phase diagram in **Fig. 2.5** [71]. The intermetallic compound known as the β–$Mg_{17}Al_{12}$ phase contains a significant amount of Al (43 wt.%) and is produced as a result of the elevated reactivity of Mg [63]. At room temperature, the β–-phase exists near the grain boundaries, which is strong enough to restrict the movement of dislocation during deformation [72]. In addition, its higher hardness compared to the matrix may contribute to the overall strengthening of the alloy [73].

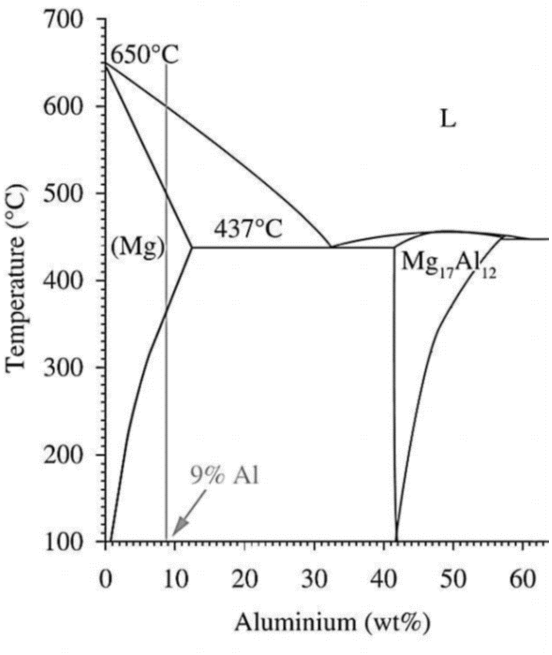

Fig. 2.5: A part of the Mg-Al phase diagram [71].

The AZ91 alloy exhibits poor creep resistance due to the β–$Mg_{17}Al_{12}$ phase, which begins to partially dissolve at temperatures above 120-130 °C. This limits its suitability for high-temperature applications in powertrain components, which operate at temperatures around 175 °C-300 °C [9], [20], [70]. The β–$Mg_{17}Al_{12}$ phase has a relatively low melting point of 458 °C, and its eutectic structure, with a eutectic temperature of 437 °C, also contributes to its vulnerability. At elevated temperatures above 120 °C, the intermetallic compound softens and coarsens, promoting grain boundary sliding and migration during creep. As the β–$Mg_{17}Al_{12}$ precipitates grow larger, they offer less resistance to dislocation climb. Furthermore, the segregation of Al solutes at grain boundaries can raise the local homologous temperature, softening the grain boundaries and further encouraging their sliding, which leads to poor creep performance [10], [63], [72]. Further, the existence of incoherency at the interface between the Mg matrix and the β-$Mg_{17}Al_{12}$ phase causes severe cracking and cavity formation during creep deformation. All this together results in poor creep resistance in AZ91 Mg alloy [10]. So, addressing the creep resistance at elevated service temperatures is necessary to extend the scope of AZ91 Mg alloy in automotive powertrain components. Also, it is desirable to adopt a potential strategy to enhance the creep performance of AZ91 alloy without sacrificing other properties.

2.4 Creep

Creep refers to the time-dependent plastic deformation of a material that occurs with long-term exposure to stress, which is below the yield strength of the material. This phenomenon typically occurs in metals at operating temperatures exceeding 30-50% of their absolute melting temperature (Tm). Creep testing is conducted under constant stress or load conditions, which may involve tension, compression, or torsion. During the test, the temperature is held constant, and the resulting elongation of the material is continuously recorded. A typical creep curve shown in **Fig. 2.6** exhibits three stages of creep: primary creep, secondary creep, and tertiary creep.

Primary stage: This occurs after instantaneous deformation. Here, strain hardening increases the creep resistance. Therefore, the creep rate decreases with time, and slow plastic deformation occurs.

Secondary creep: The constant creep rate observed in this region due to the balance between thermal recovery and strain hardening.

Tertiary creep: As thermal recovery dominates the strain hardening and due to the formation of cracks and voids in this region, the accelerated creep rate is observed till rupture.

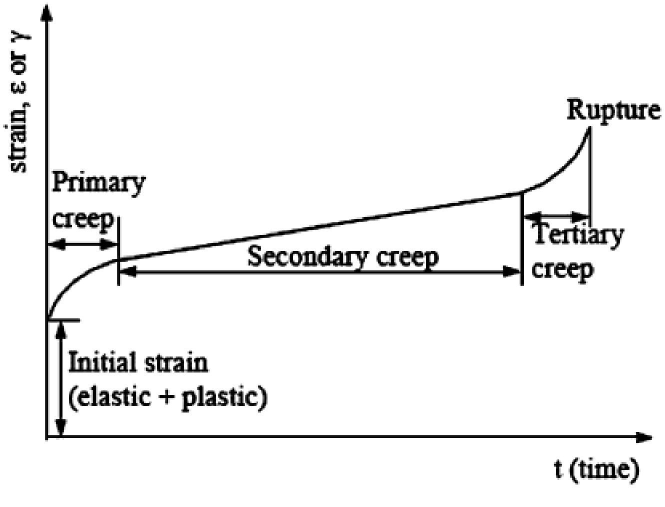

Fig. 2.6: Typical creep curve of metal or alloy [61].

During creep deformation, two opposing processes influence the material's behavior. The first is softening, which involves mechanisms such as cavitation, cross-slip, and recovery through low-energy sub-structures. The second is hardening, which can result from mechanisms like solid solution and precipitation hardening. When hardening effects dominate, the creep rate declines, whereas an increase in softening shifts the creep rate higher. The minimum creep rate occurs when these two processes reach equilibrium [61]. This minimum, observed at a given load and temperature, is referred to as the steady-state creep rate. The steady-state creep rate as a function of stress (σ) and temperature (T) is described by a power law equation **2.7** [61].

$$\dot{\varepsilon} = A\sigma^{n} \exp\left(\frac{-Q}{RT}\right) \tag{2.7}$$

Where $\dot{\varepsilon}$ is the steady state creep rate, A is a dimensionless material constant, Q is the activation energy for creep deformation, and R is the gas constant. The slope of the log $\dot{\varepsilon}$ versus ln σ at a given temperature results in the stress exponent (n), while the slope of the Arrhenius plot (log $\dot{\varepsilon}$ vs., 1/T) multiplied by R (8.314 kJ/mol) at specific stress gives the creep apparent activation energy (Q). The estimated values of the stress exponent (n) and apparent activation energy (Q) determine the governing creep mechanism of the material subjected to creep deformation under the stress and temperature range of interest. At a low-stress regime, the n value of 1 for diffusion creep includes three different mechanisms, such as Nabarro-Herring creep, Coble creep, and Harper-Dorn creep, with respect to the lattice self-diffusion activation energy (Q) of the material. At n=2, the grain-boundary sliding is an operative mechanism. Further, at the intermediate stress regime, where the stress exponent (n) varies from 3 to 8, and activation energy (Q) equals the activation energy for the lattice self-diffusion in the material, the creep deformation occurs due to the dislocation creep, with n = 5–8 representing the creep controlled by dislocation climb. Otherwise, it is dislocation glide for n=3-4 [12]. In fact, the deformation in the material during the creep process occurs due to a sequence of glide and thermally assisted climb, but since a slower mechanism is a glide, climbs control the creep [61]. In a high-stress regime, where the power law is replaced with an exponential dependence of strain rate on stress, the power law breakdown occurs due to the existence of a very high strain rate, which is not important in creep. The table illustrated below (**Table 2.2**) lists the dominant creep deformation mechanisms for Magnesium alloys on the basis of n and Q values estimated within the stress and temperature range of interest.

Table 2.2. Stress exponent (n) and activation energy (Q) for the different dominant creep mechanisms of the Magnesium alloys.

Creep mechanisms	*n*	*Q (kJ/mol)*
Nabarro-Herring creep	1	135
Coble creep	1	92
Grain boundary sliding	2	92
Harper Dorn creep	1	135
Solute drag creep (dislocation glide)	3-4	138
Dislocation Climb-controlled creep	5-8	135

2.4.1 Creep mechanisms in Mg alloys

Creep is a plastic deformation that happens due to the motion of dislocations. But, during a deformation beyond a certain point, a material hardens due to the stain hardening, such that deformation should stop. So, at a given stress, the deformation is finite. In order to get further plastic deformation, stress has to be increased. However, in creep, we have seen that constant stress itself results in the continued plastic deformation of the material. So, there may be mechanisms in creep that are different from normal plastic deformation. The current section summarizes the various creep mechanisms that are prevailing in Magnesium alloys under different stresses and temperatures.

1) Dislocation creep

Dislocation creep occurs when dislocations move through a crystal lattice, separating sections along a glide plane. This movement involves breaking and reforming atomic bonds with minimal energy input, allowing the dislocation to propagate. As it progresses, a linear lattice defect forms, termed a dislocation, which can travel through the crystal until it encounters a grain boundary, where it disappears, resulting in the shearing of the entire crystal structure. The velocity of this movement varies depending on factors like material anisotropy, as dislocations may travel at different velocities along different planes. Additionally, interactions with other lattice defects, such as other dislocations or point defects, can impede or halt this movement. Creep from dislocation motion generally occurs at moderate temperatures. The flow stress is composed of a thermal (τ_t) and an athermal component (τ_{at}), as shown in Equation **2.8** [20], [22].

$$\tau = \tau_t + \tau_{at} \tag{2.8}$$

The thermal component originates from atomic vibrations, which assist the stress in enabling dislocations to bypass obstacles with localized stress fields. In contrast, the athermal component involves motion through stress fields whose cores are around 300 atomic distances apart and are associated with work hardening. The long-range component has movements of long segments of parallel dislocations, while the thermal component has only movement of small sections of a dislocation (e.g., dislocation jogs, dislocation cutting by another). This causes slow and permanent deformation. Atoms vibrate anywhere above absolute zero, and the thermal component exists at very low temperatures; hence, creep is possible even at very low temperatures, given sufficient time [20], [22], [117], [118]. Thermally aided dislocation creep mechanisms can be classified as follows:

a) Dislocation climb

Dislocation climb refers to the movement of dislocations out of their original slip plane, often occurring near obstacles like precipitates or vacancies. This climb process can happen under conditions of elevated vacancy concentration or compressive stress perpendicular to the extra half-plane of atoms. A dislocation step that alters its slip plane is termed a jog, where vacancies accumulate, allowing the jog to migrate along the dislocation line, thus producing a climb. This mechanism enables a dislocation halted by an obstacle to bypass it, provided vacancies can diffuse within the crystal lattice. When vacancies reach the stopped dislocation, they facilitate the climb by moving it out of the glide plane. The rate of dislocation climb is influenced by vacancy diffusion velocity and temperature; at higher temperatures, dislocations move more readily around obstacles, which explains the reduced strength of hardened materials under these conditions. The activation energy required for dislocation climb aligns with that for self-diffusion.

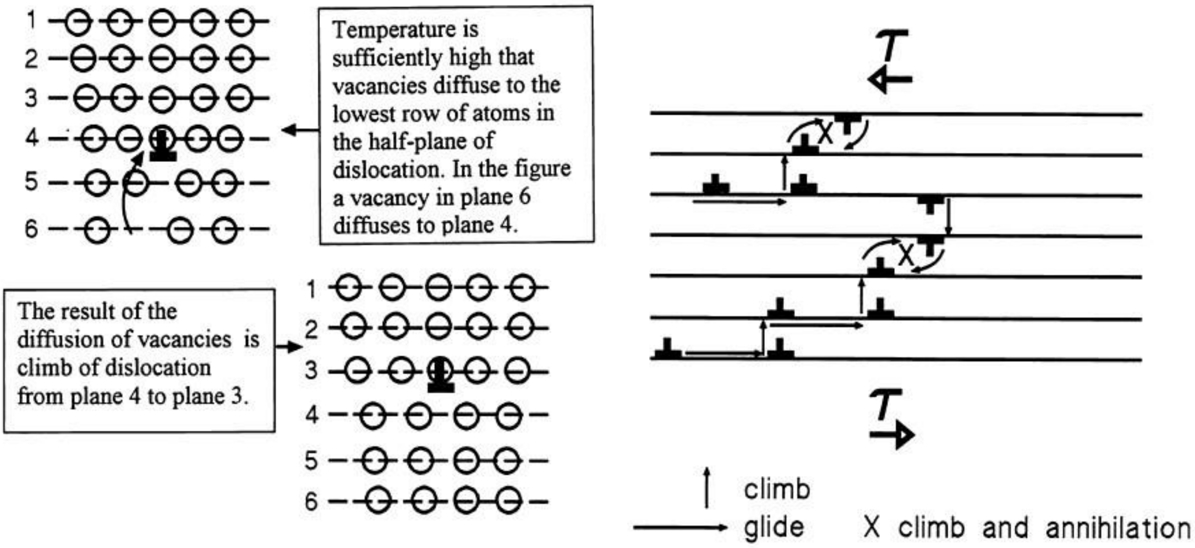

Temperature is sufficiently high that vacancies diffuse to the lowest row of atoms in the half-plane of dislocation. In the figure a vacancy in plane 6 diffuses to plane 4.

The result of the diffusion of vacancies is climb of dislocation from plane 4 to plane 3.

Fig. 2.7: Dislocation climb controlled creep mechanism [22].

b) Dislocation glide

Edge dislocations move along specific crystallographic directions through a process called slip or glide. For glide to happen, a local shear stress must be applied in the appropriate direction to the dislocation. This dislocation glide allows plastic deformation to occur at significantly lower stress levels compared to the stress needed to shift an entire plane of atoms [61].

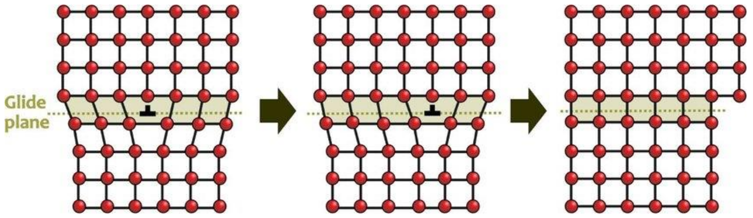

Fig. 2.8: Schematic demonstration of the edge dislocation glide [119].

c) Activated Cross-slip

In cross-slip, a change in the direction of a screw dislocation from one slip plane to another slip plane due to interaction with obstacles (precipitate or reinforcement) occurs. Here, screw dislocation dissociates into a pair of partial dislocations with a stacking fault connecting layer, or it is the thermal activation to unite partial dislocations, which are further broken down into partials on different slip systems. Stacking fault energy (SFE) is the activation energy. Since cross-slip is related to SFE, the solutes that can decrease SFE and thus increase the creep resistance by decreasing the cross-slip are preferred. Further, understanding the role of precipitates and their modification to prevent cross-slip will be an important step in creep resistance.

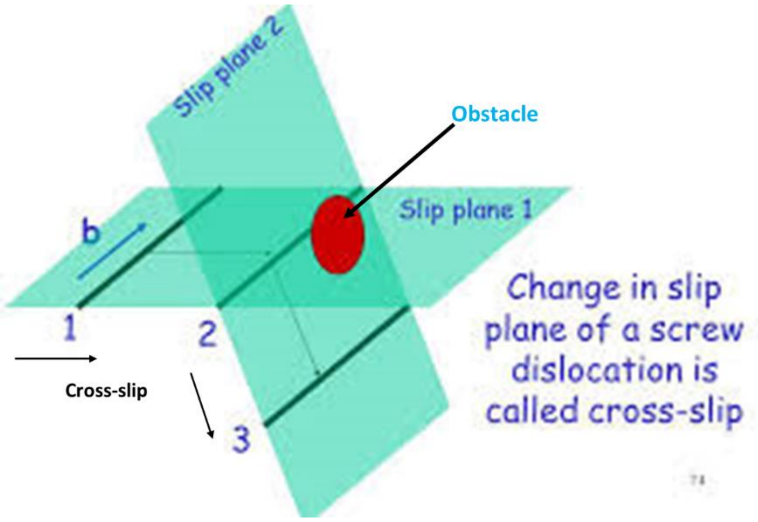

Fig. 2.9: Schematic demonstration of the cross slip [120].

d) Movement of dislocation atmospheres

Solute atmospheres increase the shear stress, thereby hindering the dislocation movement. At higher temperatures, creep deformation increases due to the dislodging of the dislocation atmosphere. In the presence of the atmosphere, the rate of dislocation movement and the creep strain rate are expected to correspond to the diffusion rate of solute atoms. At higher temperatures, the solutes in the dislocation atmosphere become mobile and dissociate from the dislocations. Therefore, to improve the creep resistance, solutes with high melting points and low diffusivity are preferable.

2) Diffusional Creep

At low temperatures, the elongation and contraction of grain shown in **Fig. 2.10a** can be obtained by dislocation motion, but at higher temperatures, since diffusivities are higher and atomic jumps are easier, the elongation along the tensile axis and contraction parallel to the tensile axis of grains occurs due to vacancy diffusion. Diffusion creep refers to the deformation of crystalline solids that occurs through the movement of vacancies within the crystal lattice, resulting in plastic deformation. This process is highly temperature-dependent and involves the migration of crystalline defects, driven by vacancies. These vacancies facilitate a net transport of atoms, effectively leading to a mass movement in the opposite direction to the vacancy flow. Grain boundaries act as a source and sink for vacancies. The atoms that are on grain boundaries parallel to the applied stress axis can move to grain boundaries perpendicular to the stress axis, as shown in **Fig. 2.10b**. Migration of grain boundary atoms from a parallel position to the stress axis to a perpendicular position, the change in dimension of the grain observed. This type of migration is possible at higher temperatures only because of higher atomic mobility and higher diffusion rate [117], [118]. This diffusion is governed by applied stress. So, this is called stress-assisted diffusion. Also, these atoms are those that make up the crystal; these are not interstitial atoms. So, these atoms can only be diffused by the substitutional diffusion mechanism. So, when diffusion is still substitutional, we need vacancy. Therefore, this is vacancy-assisted diffusion. Vacancies are migrating just the opposite way to atomic migrations. Also, we know that vacancy concentrations are higher at higher temperatures, so this kind of diffusion is more actively occurring at higher temperatures.

In the creep deformation, if the atomic migration occurs through the crystal lattice, it is called Nabarro-Herring creep, where high stresses and strain rates cause the grain to move within the specimen and grains to get elongated in the direction of applied strain; if it is through grain boundaries it is called Coble creep which occurs at low-stress levels, and if it is through dislocation cores it is called pipe diffusion [117], [121].

If the grains are of bigger (coarser) size, then this type of grain boundary atom migration will require a longer time or more temperature, which results in increasing creep resistance of the material, thus increasing creep life.

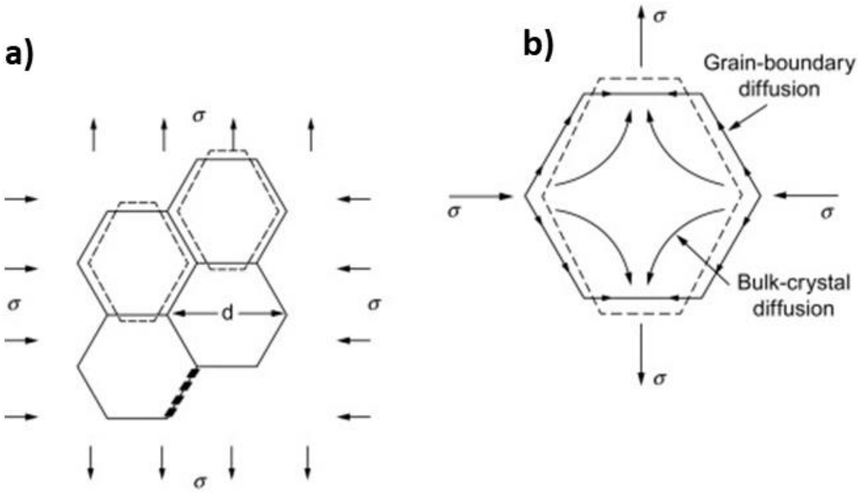

Fig. 2.10: Schematic representation of diffusion creep [121].

3) Grain boundary sliding

Grain Boundary Sliding (GBS) refers to the movement of grains relative to each other, which occurs primarily at low strain rates and elevated temperatures. This process allows the grains to shift without altering their individual shapes, resulting in a deformed material with grain structure and texture that closely resemble those of the original material, as shown in **Fig. 2.11a**. On application of stress and high temperature, the grain boundaries become weaker than the grains. The random arrangements of atoms at grain boundary have weak bonding between them. So, they act like somewhat viscous liquids along the grain boundary, so it is easier for the grains to slide on these grain boundaries at higher temperatures under the influence of stress. The slide of one grain past another may occur by dislocation or diffusive mechanisms. The grain boundary sliding shows a close relation to the grain boundary energy, i.e., high-energy grain boundaries tend to increase the grain boundary sliding. Two predominant mechanisms such as Nabarro-Herring Creep and Coble Creep are also usually involved in deformation at or close to the grain boundaries in conjunction with grain boundary sliding [61]. GBS has been observed in different metals mostly by line scratched on polished surface and showing a step at the grain boundaries after creep, **Fig. 2.11b**. The improvement in the creep performance against grain boundary sliding can be achieved by the presence of big, coarser grains (which delay grain boundary sliding), the presence of zig-zag grain boundaries, and the presence of thermally stable precipitates at the triple points. Further, the rate of diffusional creep should decrease with an increase in grain boundary viscosity. Fine precipitates are usually dispersed in polycrystalline material to increase the sliding resistance of high-temperature alloys [122-124]. In contrast, the sliding-resistant particles cause an increase in grain boundary stresses and accelerate the grain boundary cavitation, which adversely affects the mechanical properties.

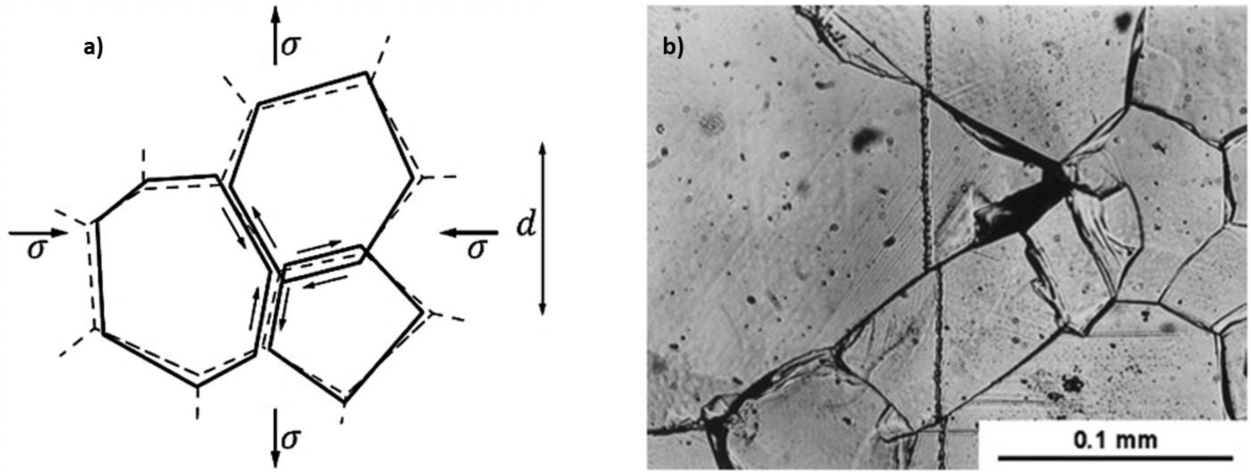

Fig. 2.11: The figure indicates a) a schematic illustration of the grain boundary sliding [125] and b) explains the grain boundary sliding through the use of a transverse marker line across grain boundaries for a Mg-0.78Al (wt%) alloy creep [124].

2.5 Creep Studies of Magnesium alloys

In order to make the Mg alloy useful at elevated temperatures, some research has been carried out to improve its creep resistance [55]. The present thesis work primarily deals with the creep performance of the Mg alloy. Therefore, further literature will focus on the context of Mg alloys designed for elevated-temperature automotive applications. Strategies to improve the creep resistance of Mg alloys include: (i) incorporating fine dispersions of thermally stable precipitates, (ii) introducing secondary phases at grain boundaries to restrict grain boundary sliding (GBS), and (iii) preventing the formation of thermally unstable phases. Techniques such as solid solution strengthening and dispersion strengthening are effective methods to enhance the creep resistance of these alloys.

Baghani et al. [56] and Hort et al. [57] reported the proportionality between the creep resistance of the Magnesium alloy and the thermal stability of precipitated intermetallic phases at grain boundaries. These thermally stable intermetallic phases are effective in restricting the grain boundary sliding, leading to improvement in the creep properties of the alloy. On the basis of current observation, the formation of high melting point intermetallic phases post alloying addition becomes the most interesting way to develop new creep-resistant Mg alloys. In this reference work, the creep performance of the Mg-Sn alloys has been studied alone and with the addition of Ca up to 4 wt.%. The addition of Sn into the Mg alloy resulted in the formation of a thermally stable Mg_2Sn intermetallic phase, as shown in **Fig. 2.12a &e**. Based on the creep performance of the Mg-Sn alloy, it is found that the intermetallic phase Mg_2Sn is not effective enough to retard the creep deformation, as shown in the creep curve **Fig. 2.16a**. It is observed that the addition of Ca more than 2 wt.% suppresses the less stable Mg_2Sn phase and instead forms more thermally stable phases of Mg-Sn-Ca and Mg_2Ca at the grain boundaries, as shown in **Fig. 2.12 (b-d) &(f-h) and Fig. 2.13**& **2.14** which improve the creep resistance of Mg-4Sn alloys, as shown in **Fig. 2.16(a-d)**. The thermal stability of the Mg-Sn-Ca phase was further confirmed using a Thermo-Calc® plot shown in **Fig. 2.15**. The compositions of the alloys prepared here are Mg-4Sn, Mg-4Sn-2Ca, Mg-4Sn-3Ca, and Mg-4Sn-4Ca. In the microstructures, the rod shape morphology is **(Fig. 2.12b &f)** associated with the Mg-Sn-Ca phase, where the other Mg_2Ca **(Fig. 2.12d &h)** phase is demonstrated as a continuous phase at grain boundaries.

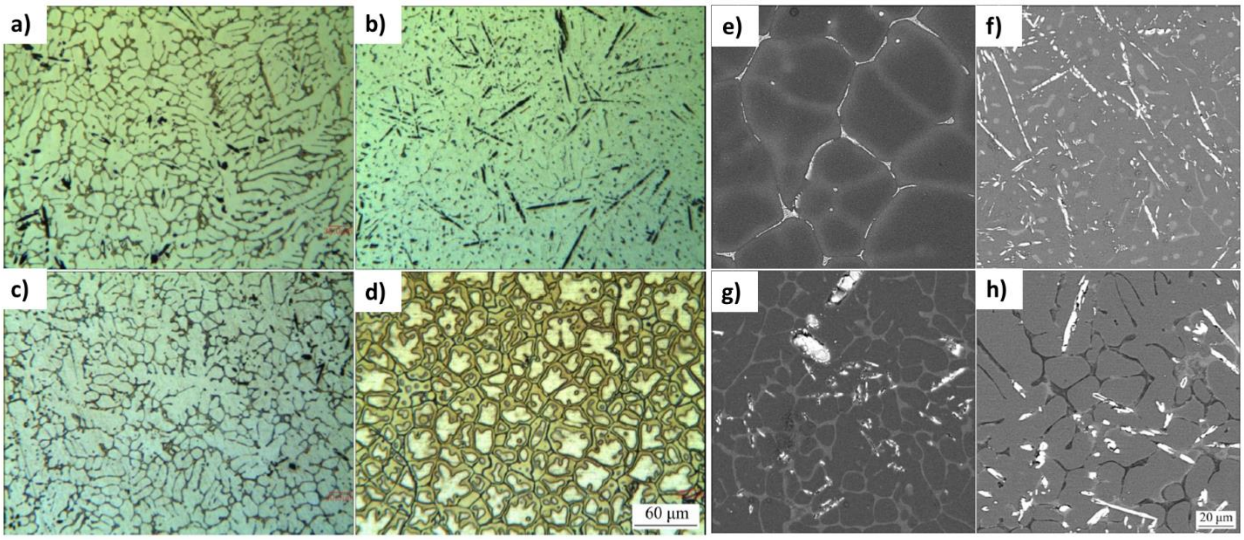

Fig. 2.12: a-d) Optical and e-h) Scanning electron micrograph of the Mg-4Sn alloy with the addition of different amounts (2-4wt.%) of Ca [56].

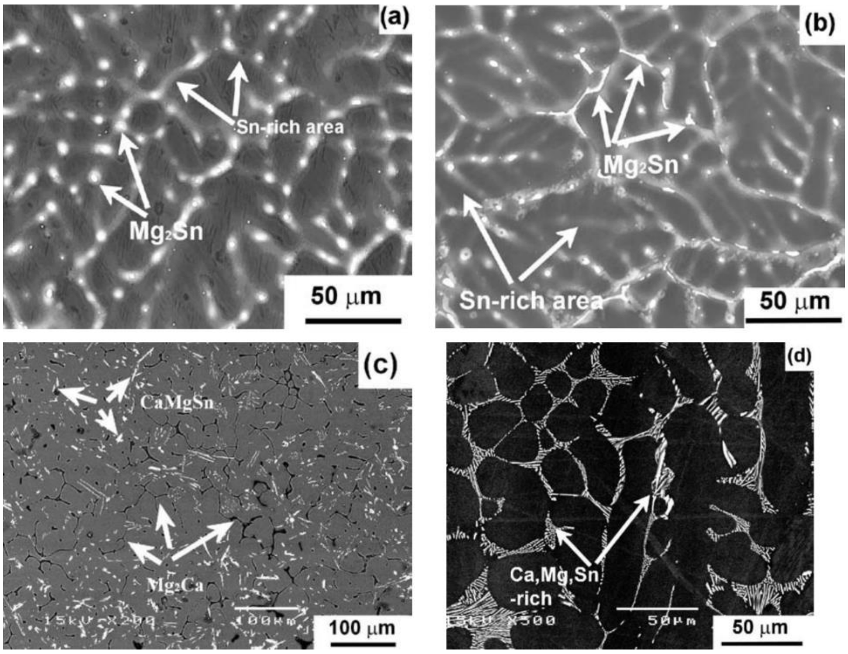

Fig. 2.13: SEM micrographs taken from as-cast samples of (a) Mg-3Sn, (b) Mg-5Sn, (c) Mg-3Sn-2Ca, and (d) Mg-5Sn-2Ca alloys [56].

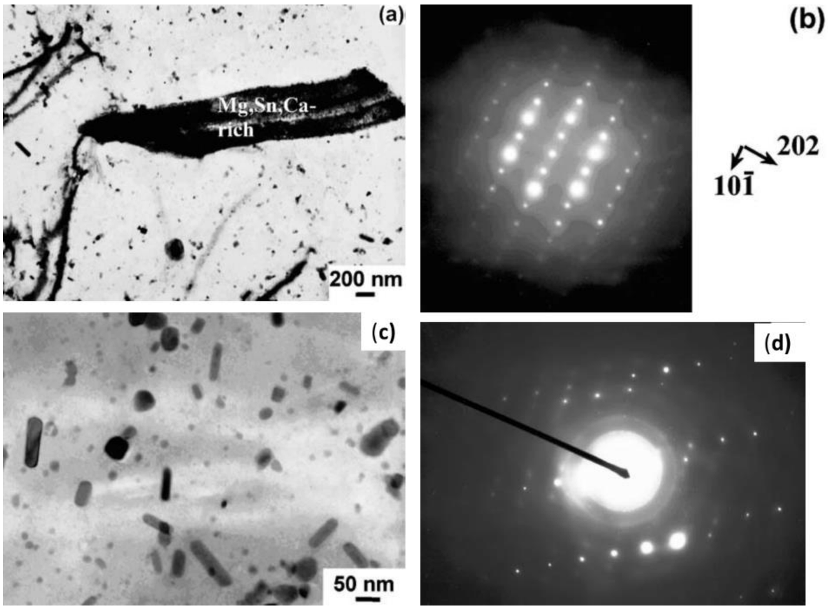

Fig. 2.14: Observation of the large particle in the as-cast Mg-5Sn-1Ca Magnesium alloy: (a) morphology of the particle by TEM investigation and (b) diffraction pattern, the zone axis is [040]. It is identified as the phase CaMgSn. Observation of the fine particles in the as-cast Mg-5Sn-1Ca Magnesium alloy: (c) morphology of the particles and (d) diffraction rings from this area. The phases are identified as the Mg_2Sn phases [56].

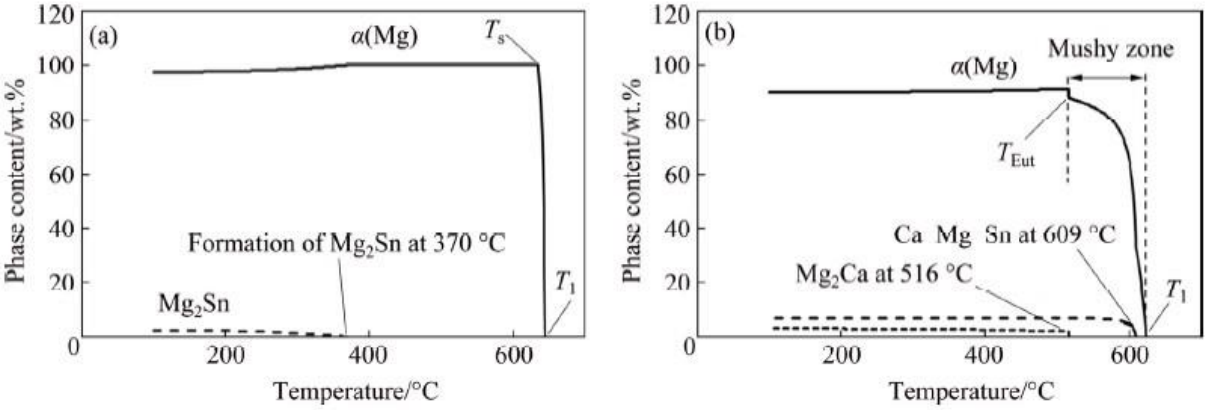

Fig. 2.15: Formation of different phases during and after solidification: a) Mg-4Sn and b) Mg-4Sn-4Ca [56].

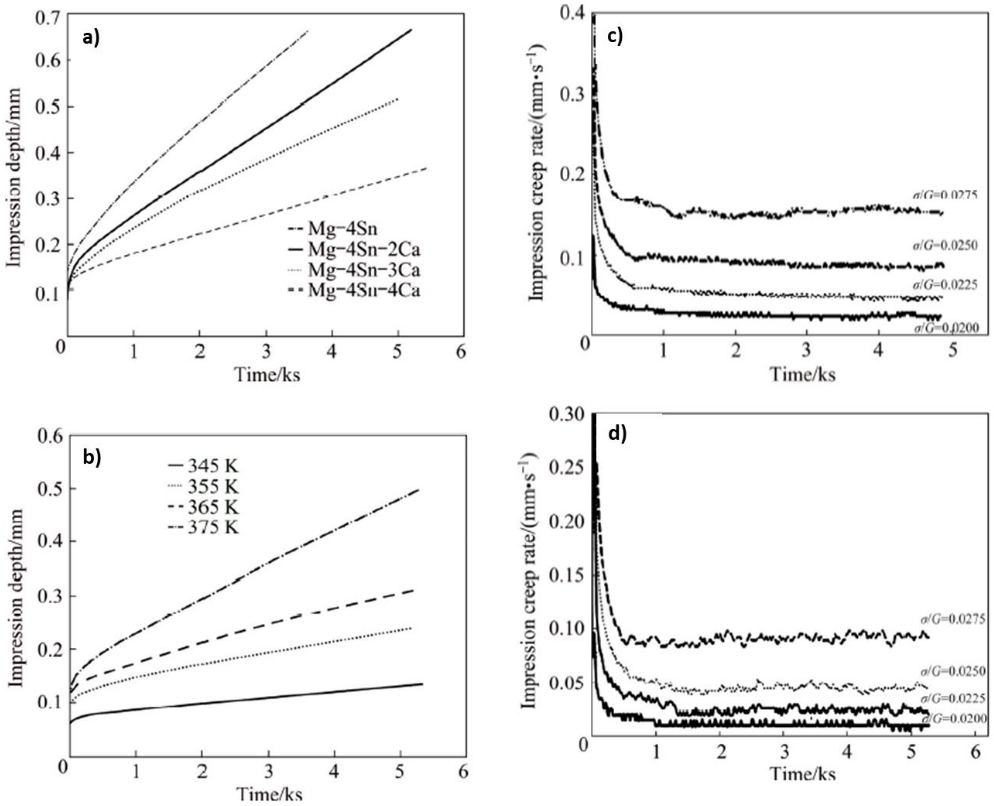

Fig. 2.16: a) Variation of impression depth with time at 455 K and normalized stress of 0.0300 for four alloys, b) Variation of impression depth with time for Mg-4Sn-3Ca at normalized stress of 0.0250 and different temperatures, c &d) Variation of impression creep rate with time for different contents of Ca at a constant temperature of 475 K and different normalized stresses: (a) Mg−4Sn−2Ca; (b) Mg−4Sn−4Ca [56].

Similarly, Haun et al. [58] have also reported poor creep performance in the case of the Mg-Sn alloy attributed to the segregation of Sn at dendritic and grain boundaries, as shown in **Fig. 2.17a**. Diffusive bright bands in **Fig. 2.17a** are associated with the distribution of Sn. Sn segregation in certain regions reduces the local solidus temperature compared to the interior of the grains. As a result, these areas experience a higher homologous temperature. Additionally, grain misorientation and differences in thermal expansion between precipitates and the matrix cause elevated local stresses in these regions. Consequently, creep deformation tends to initiate at these sites. In the post-creep microstructure of the Mg-Sn alloy shown in **Fig. 2.17b and 2.17c**, voids are visible along dendritic boundaries **(Fig. 2.17b)**. The propagation of cracks along these boundaries suggests deformation through phase boundary sliding.

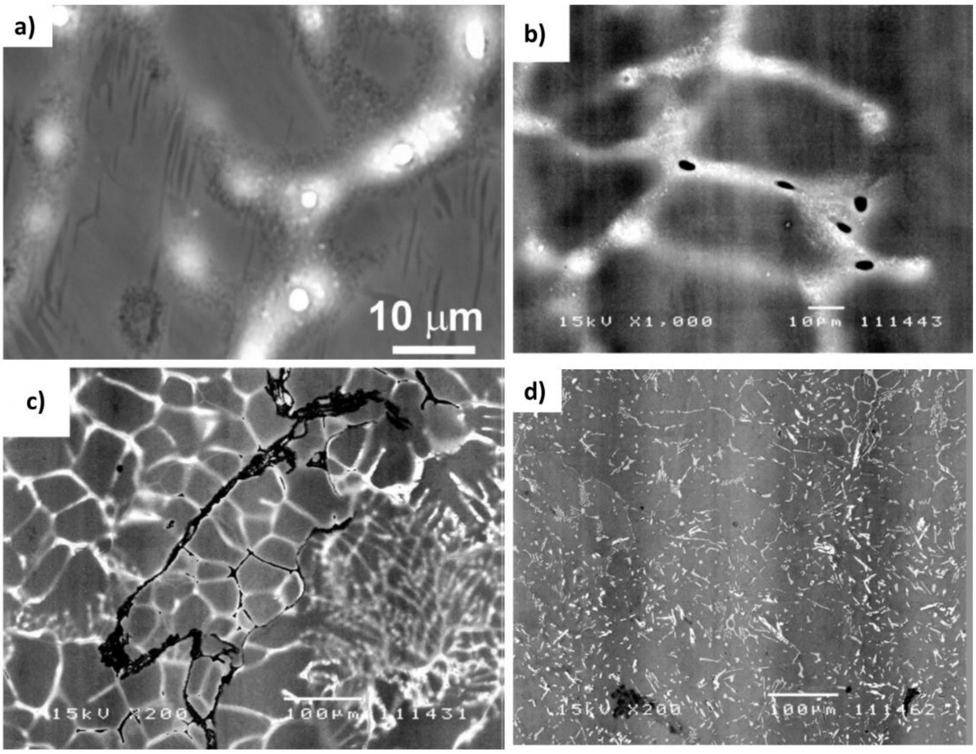

Fig. 2.17: Scanning electron micrograph indicating a) Microstructure of Mg-Sn alloy, b&c) Mg-Sn alloy post creep microstructure, and d) post creep microstructure of the Mg-Sn alloy post-Ca addition (Mg-3Sn-2Ca) [58].

To improve the creep resistance of Mg alloys, reducing the segregation of elements is essential. Various factors influence solute atom segregation at dendritic and grain boundaries, including [59]:

- Solidification rate: Higher solidification rates tend to increase segregation due to less favorable diffusion conditions for solute atoms. As a result, AZ91D alloy produced by ingot casting, which has a lower solidification rate, exhibits superior creep resistance compared to die-cast AZ91D alloy [60]
- Diffusivity of solute atoms within solid phases
- Alloying elements used in the composition
- Temperature range between solidus and liquidus: A wider gap between these temperatures tends to intensify segregation

In addition to alleviating the segregation of the solute atoms, the creep resistance of the alloy can also be improved by suppressing the sliding of the grain boundary. The contributions of alloying to the improvement of creep properties include two aspects: solid solution strengthening and particle strengthening (obstruction to the movement of dislocations and to the sliding of grain boundaries). Alloying also modifies the microstructural morphologies and then indirectly affects the creep response. In the present referred study on the creep performance of the Mg-Sn alloy [58], after the alloying element Ca was added, the band of Sn segregation disappeared due to the formation of the CaMgSn phase, as shown in **Fig. 2.9d**. Creep resistance significantly increases after Mg-Sn alloy is modified with Ca addition. The improved creep resistance of the alloy is not only attributed to the formation of thermally stable phases but also due to the suppression of segregation of primary alloying elements in these alloys.

Moreover, the work presented by Majhi et al. [12] has reported an improvement in the creep performance of the AZ91 alloy post-alloying addition of the optimum quantity of Bi and Sr. The addition of Bi and Sr to the AZ91 alloy results in a precipitation of the thermally stable Sr_2Bi and Al_4Sr intermetallic phases over the thermally unstable β-$Mg_{17}Al_{12}$ phase along the grain boundaries of the alloy. The X-ray diffraction analysis and SEM backscattered electron (BSE) images with EDS analysis shown in **Fig. 2.18** and **2.19**, respectively, confirm the precipitation of these phases. These phases successfully obstruct the motion of dislocations during the creep deformation. The TEM bright field micrograph shown in **Fig. 2.20** indicates the pile-up dislocations at the interface of these stable phases, which in relation results in an improved creep performance of the AZ91 alloy with the alloying addition of Bi and Sr, as shown in the creep curve indicated in **Fig. 2.21**.

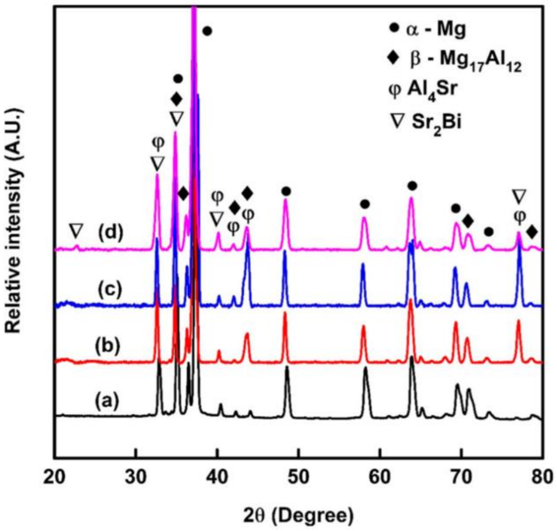

Fig. 2.18: X-ray diffraction pattern obtained from the a) AZ91, b) AZ91+0.5Bi+0.25Sr, c) AZ91+0.5Bi+0.5Sr, and d) AZ91+1Bi+0.5Sr alloys [12].

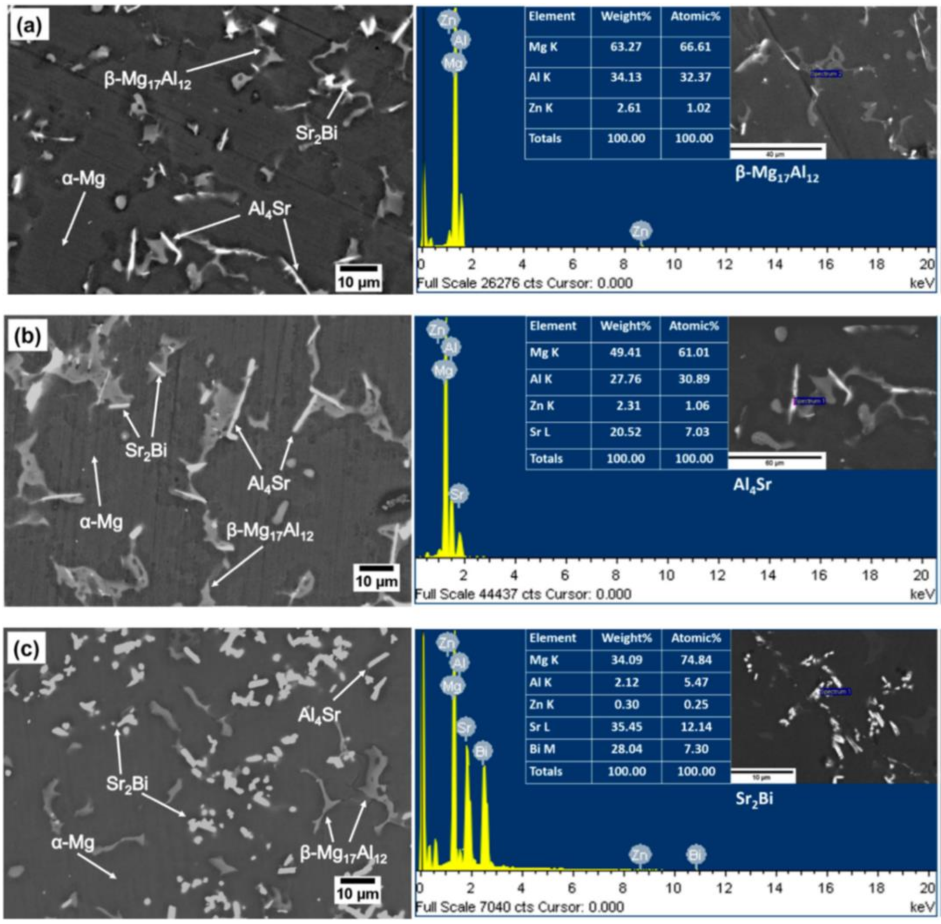

Element	Weight%	Atomic%
Mg K	63.27	66.61
Al K	34.13	32.37
Zn K	2.61	1.02
Totals	100.00	100.00

Element	Weight%	Atomic%
Mg K	49.41	61.01
Al K	27.76	30.89
Zn K	2.31	1.06
Sr L	20.52	7.03
Totals	100.00	100.00

Element	Weight%	Atomic%
Mg K	34.09	74.84
Al K	2.12	5.47
Zn K	0.30	0.25
Sr L	35.45	12.14
Bi M	28.04	7.30
Totals	100.00	100.00

Fig. 2.19: Typical SEM micrographs in backscattered electron (BSE) mode of the squeeze cast (a) AZ91+0.5Bi+0.25Sr, (b) AZ91+0.5Bi+0.5Sr and (c) AZ91+1.0Bi+0.5Sr alloys with EDS results showing the presence of β-$Mg_{17}Al_{12}$, Al_4Sr, and Sr_2Bi phases [12].

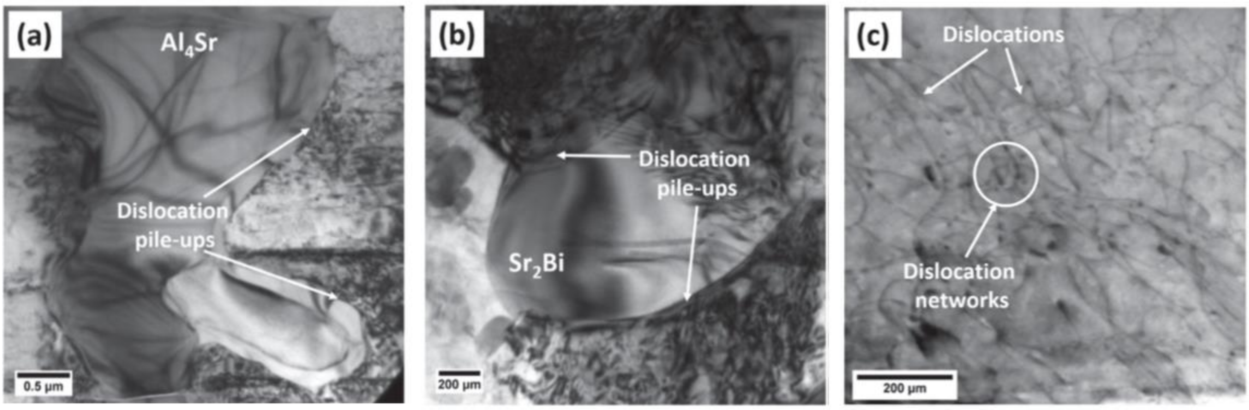

Fig. 2.20: TEM bright field micrograph of the AZ91+1Bi+0.5Sr alloy following creep tested at T=473K and σ/G= 0.029 showing the a) dislocations pile-ups around the Al_4Sr phase, b) dislocations pile-ups around the Sr_2Bi phase, and c) dislocation with their networks [12].

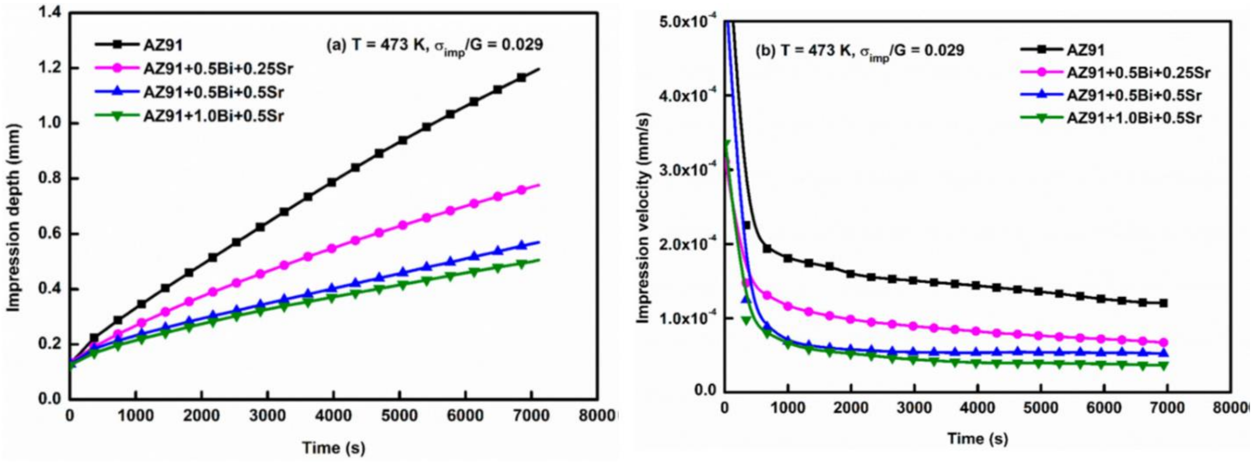

Fig. 2.21: Typical impression creep curves demonstrating the a) impression depth vs. time and b) impression velocity vs. time for all alloys [12].

There are several studies available discussing the alloying of Mg alloys in order to improve their creep performance using microstructural modifications [2], [20], [27], [61], etc. On the other hand, the implication of solid solution strengthening in order to improve the creep performance of the Mg alloy may be experienced as one of the most effective techniques. A detailed explanation of solid solution strengthening is available in **section 2.2.1E**.

Till now, most of the studies performed are based on the investigation of the mechanical properties of Mg alloys which exhibited solid solution strengthening [34-40]. Solid solution strengthening in the Mg alloys can be a result of alloying addition or solutionizing (T4) heat treatment, which is influenced by the presence of interstitial and substitutional atoms of the alloying element. There is a scarcity of studies on the creep performance of Mg alloys experiencing solid solution strengthening. Therefore, there is a wide scope to explore it. Yeoh et al. [44] investigated the effect of solutionizing (T4) and aging (T6) on the microstructure and mechanical properties of the cast AZ80 Mg alloy. Compared to the as-cast condition, a significant increase in the tensile properties of the AZ80 alloy was obtained post-heat treatment since the T6-treated Mg alloy exhibited the most superior mechanical properties. As demonstrated in **Fig. 2.22a-d**, the microstructure of AZ80 Mg alloy comprises the α-Mg matrix phase and β-$Mg_{17}Al_{12}$ phase. Further, in **Fig. 2.22e**, the successful dissolution of the β-$Mg_{17}Al_{12}$ phase can be observed with different solution treatment duration.

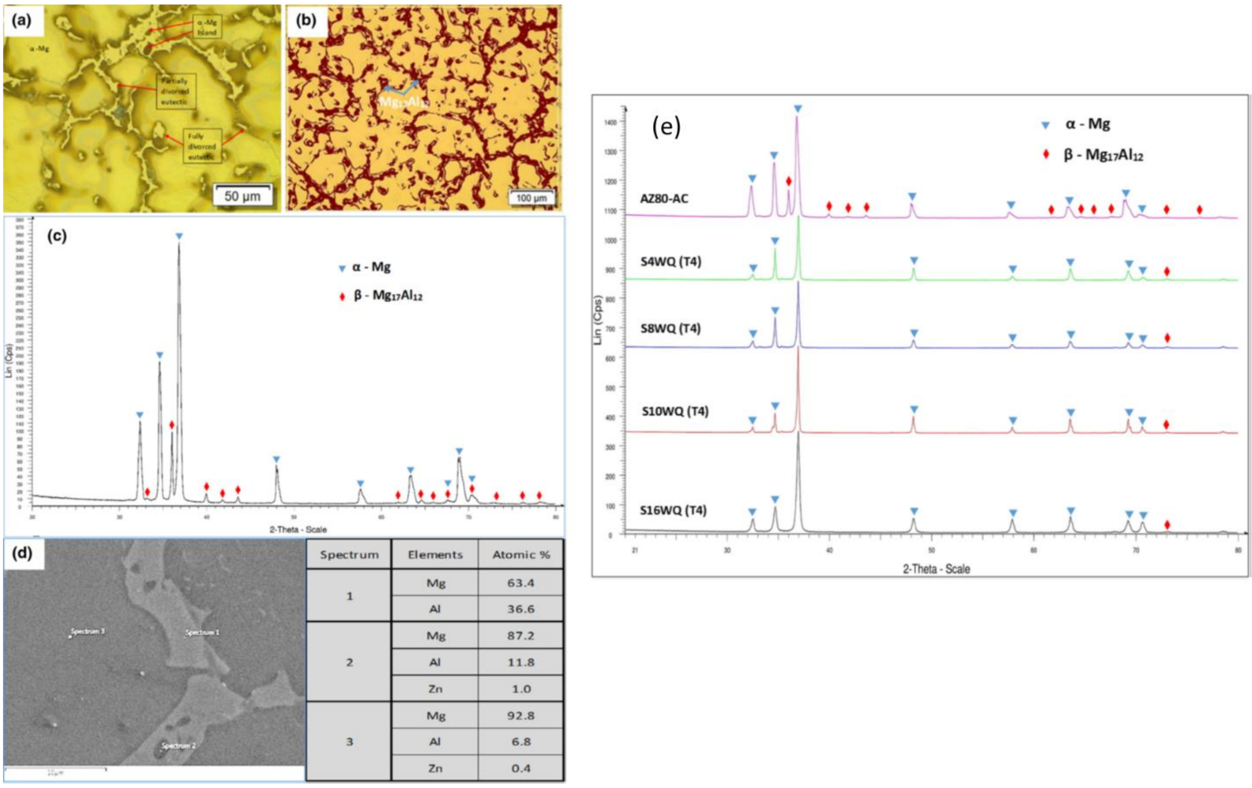

Spectrum	Elements	Atomic %
1	Mg	63.4
	Al	36.6
2	Mg	87.2
	Al	11.8
	Zn	1.0
3	Mg	92.8
	Al	6.8
	Zn	0.4

Fig. 2.22: As-cast condition of AZ80 Mg alloy with (a) OM, (b) phase determination on β-$Mg_{17}Al_{12}$ phase with image analyzer, (c) XRD pattern, (d) SEM image and EDS analysis results, and e) XRD patterns of AZ80 Mg alloy subjected to various solution treatment durations and dissolution of β-$Mg_{17}Al_{12}$ phase occurred during solution treatment [44].

Solution treatment enhances the homogenization of the microstructure by promoting a more uniform distribution of alloying elements, such as Aluminum, within the matrix. Achieving a homogeneous microstructure typically requires longer soak times due to the slow diffusion rate of Aluminum in the Magnesium matrix. By selecting the optimal temperature and soaking duration, a supersaturated solution can be formed. Upon cooling to room temperature after soaking, discontinuous precipitates with lamellar and tree-like structures form within the grains, as shown in **Fig. 2.23**. When compared to the as-cast AZ80 Mg alloy, the solution-treated (T4) material exhibits notable improvements in ultimate tensile strength (UTS) and ductility **(Fig. 2.24)**. These enhancements can be attributed to: (a) the dissolution of the brittle β-$Mg_{17}Al_{12}$ phase into the Magnesium matrix, (b) the formation of lamellar discontinuous precipitates that contribute to secondary phase strengthening, and (c) a reduction in the volume fraction of the β-$Mg_{17}Al_{12}$ phase. The decrease in yield strength (YS) is primarily due to grain growth and an increase in the spacing between precipitates.

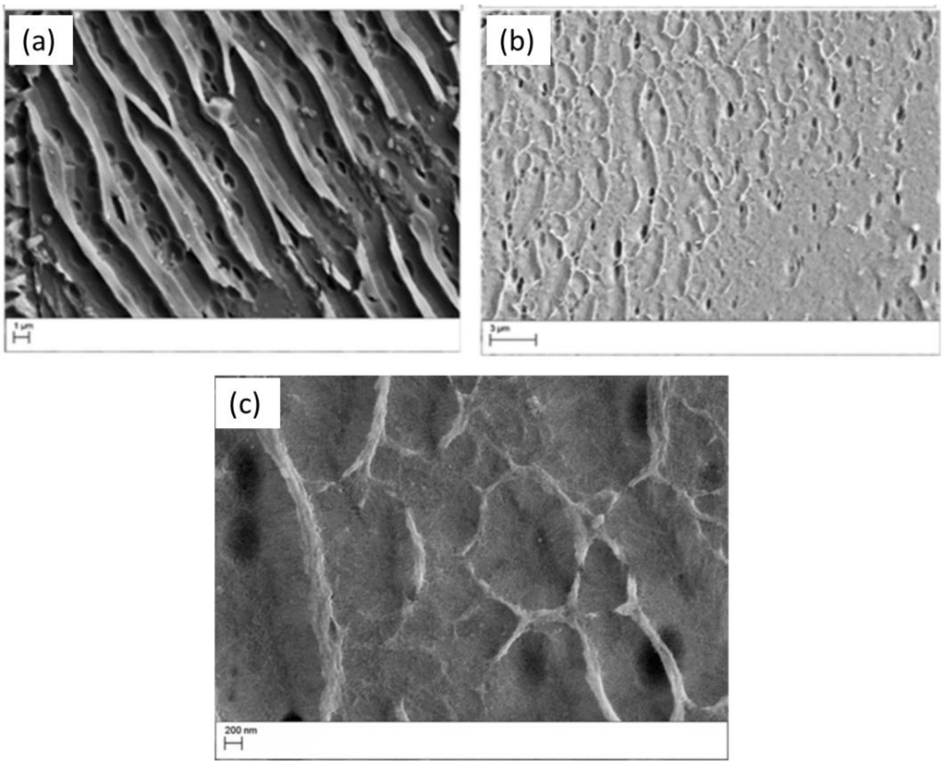

Fig. 2.23: SEM image showing precipitation morphology of solutionized AZ80 alloy with different solution treatment duration of a) 10 h, b) 16 h, and c) SEM image showing tree-like precipitates morphology in 16 h specimen [44].

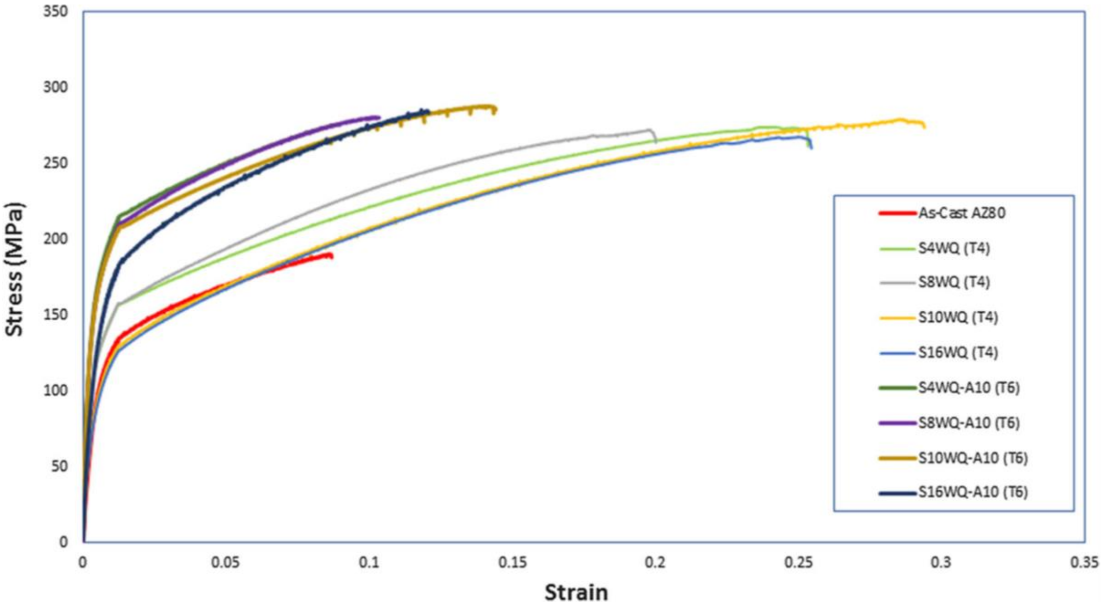

Fig. 2.24: The tensile stress-strain curves of various heat treatment conditions on as-cast AZ80 Mg alloy [44].

In a similar way, Bo et al. [46] investigated the effects of heat treatment on the microstructure, mechanical, and creep properties of Mg−3Sn−1Mn alloy. The microstructure of the alloy, as demonstrated in **Fig. 2.25**, indicates precipitation of the Mg_2Sn phase in addition to the α-Mg phase. This is further confirmed using an X-ray diffraction analysis shown in **Fig. 2.25e**. On heat treatment (T4) at an optimal temperature of 420^oC for a duration of 24 h, the Mg_2Sn undergoes a dissolution into the matrix. Some fraction of Mg_2Sn was still retained in the microstructure on T4 treatment, as shown in **Fig. 2.26**. As a result, due to the combined effect of solid solution strengthening and precipitate strengthening, the tensile and creep properties of the aged alloy are significantly improved. The mechanism for the higher tensile and creep properties of the solutionized alloy is related to the dispersive distribution of the retained Mg2Sn phase in the α-Mg matrix, retarding the dislocation movement during creep deformation.

Several other studies are also available discussing the effect of heat treatment on the microstructural evolution and mechanical properties of Mg alloys [34-40, etc.].

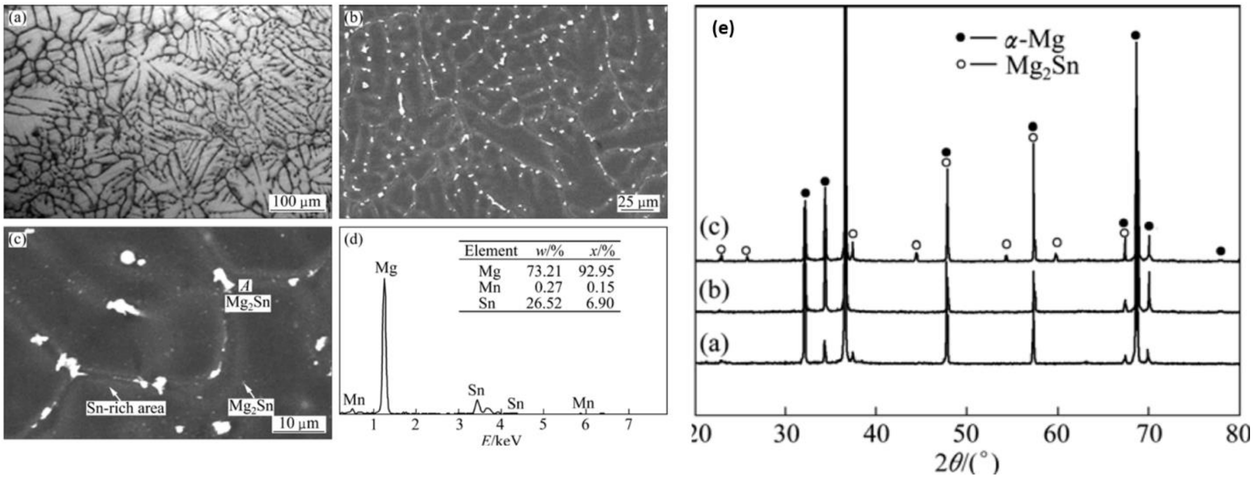

Element	w/%	x/%
Mg	73.21	92.95
Mn	0.27	0.15
Sn	26.52	6.90

Fig. 2.25: Optical and SEM images of as-cast alloy: (a) Optical image; (b), (c) SEM image; (d) EDS results of position *A* in (c), and e) XRD patterns of experimental alloys: (a) As-cast alloy; (b) Alloy solutionized at 420 °C for 24 h; (c) Alloy aged at 250 °C for 16 h [46].

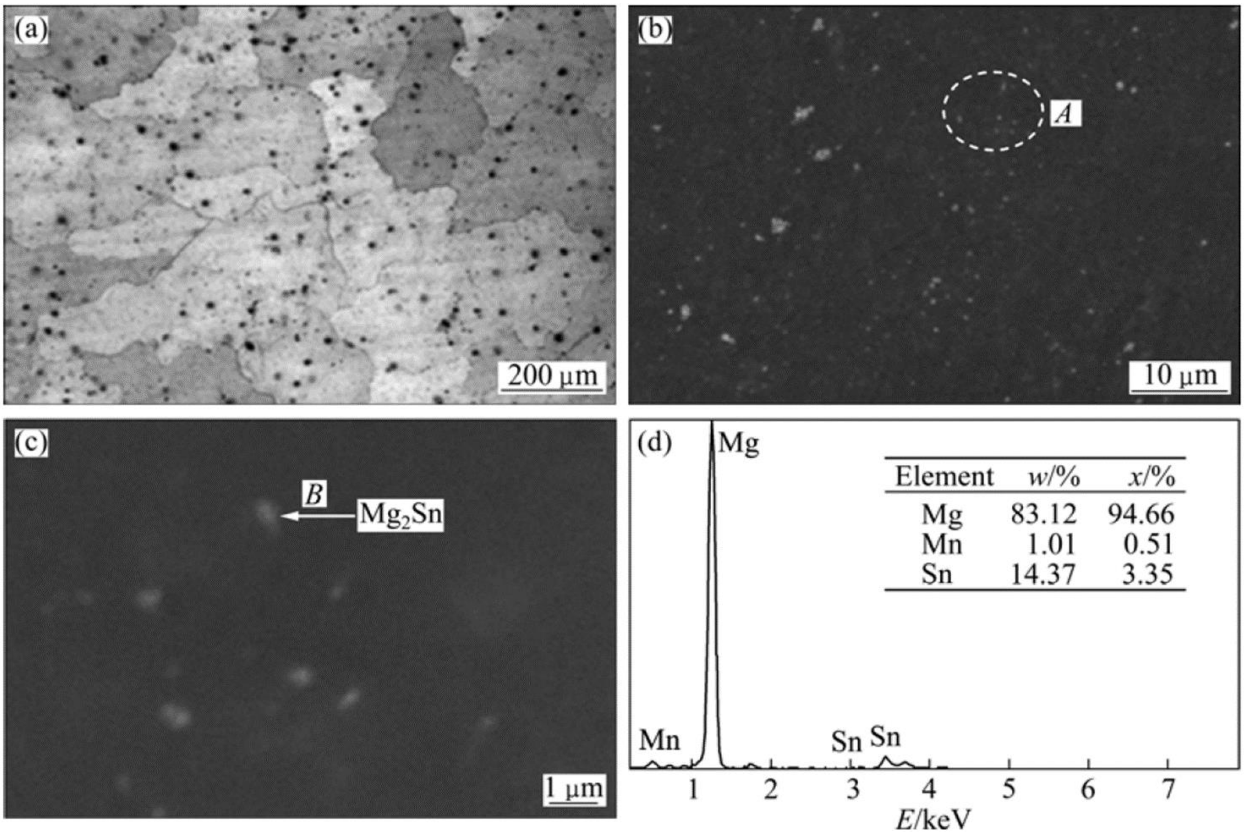

Element	w/%	x/%
Mg	83.12	94.66
Mn	1.01	0.51
Sn	14.37	3.35

Fig. 2.26: Optical and SEM images of alloy solutionized at 420 °C for 24 h: (a) Optical image; (b) SEM image; (c) Local magnification of area *A* in (b); (d) EDS results of position *B* in (c) [46].

The present thesis work deals with the investigation of the AZ91 Mg alloy creep properties, which are comprised of its creep performance and underlying creep mechanism during the creep deformation that occurs under the specific range of temperatures and stresses of interest. AZ91 alloy has been selected due to its remarkable properties discussed above. The poor creep performance of the AZ91 alloy can be taken care of by suitable alloying addition. Apart from this, the route of alloy fabrication also influences the mechanical and creep performance of the Mg alloys. The AZ91 alloy prepared using a die-casting technique involves a higher amount of porosity that allows easy crack initiation and growth during creep tests. Also, the volume fraction of the thermally unstable β-$Mg_{17}Al_{12}$ phase is the highest in the AZ91 alloy prepared via gravity casting (GC), leading to its poor creep performance [33]. Most of the studies investigating the creep performance of the Mg alloy include the alloy prepared using die-casting only, as shown in **Table 2.3**. Therefore, it is favorable to change the fabrication route of the AZ91 alloy in order to overcome the problems associated with die-casting efficiently. At present, squeeze casting is increasing rapidly due to the benefits of high productivity, high precision, high-quality surface, good machinability, and high fluidity of melt achieved. Also, squeeze-cast components do not show porosity and produce a fine and consistent β-phase network, which may improve the mechanical and wear properties of the AZ91 alloy. In addition, the volume fraction of the thermally unstable β-$Mg_{17}Al_{12}$ phase is observed to be the lowest in the AZ91 alloy prepared via squeeze-casting (SC) [33]. At the same time, significant grain refinement in the alloy can be achieved. The details on squeeze casting and its advantages over die-casting have been explained in **section 2.5.1**.

A detailed understanding of the governing creep mechanism of the Mg-Al-Zn alloy system is crucial for developing new creep-resistant materials. A number of studies have been conducted to identify the creep mechanism in the AZ91 Mg alloy. *Nakaura et al.* [126] studied the creep performance of die-cast Mg-Al alloys in the temperature range of 150°C-200°C and a stress range of 25-70 MPa. They reported grain boundary sliding and dislocation motion as the creep mechanism. *Kim et al.* [127] performed the creep study for the die-cast Mg-Al-Sn system with the temperature and stress range of 150 °C-200°C and 50-80 MPa, respectively, and could not specify the governing creep mechanism due to the value of activation energy (116 kJ/mol). This value of activation energy lies in between the activation energy for grain boundary diffusion or cross slip for Mg alloy deformed by grain boundary sliding and lattice self-diffusion for Mg alloy deformed by dislocation climb. At lower stresses, *Kaveh Meshinchi Asl* [119] reported the stress exponent n=5.7 for AZ91 Mg alloy prepared via die-casting, which is in the range of dislocation climb mechanism; however, the activation energy (Q) was measured 119 kJ/mol, which lies between that for self-diffusion and grain boundary diffusion. Moreover, among the few studies discussing the creep mechanism of the die-cast Mg-Al alloy, there is non-uniformity in specifying the creep mechanism at different stresses and temperatures, as listed in **Table 2.3**. Also, no study involves the investigation of the creep mechanism of the AZ91 alloy prepared via the squeeze casting route. Therefore, the initial work in the thesis investigates the underlying creep mechanism prevalent in squeeze-cast AZ91 Mg alloy at different stresses and temperatures, as detailed in **Chapter 4**.

Table 2.3: Summary of creep mechanisms for AZ91 Magnesium alloys.

Alloy (Wt.%)	*Processing route*	*Temp. (°C)*	*Stress (MPa)*	*n (Stress exponent)*	*Q (KJ/mol) (Activation energy)*	*Proposed Mechanisms*
AZ91 [17]	Die-cast	85-125	<60	2	42-100	Grain boundary diffusion
			>60	2.5-5	42-100	Dislocation climb
AZ91 [47]	Die-cast	125-175	50	2	30-45	Grain boundary migration and sliding
			>50	5	95	Activated cross slip, as well as grain boundary diffusion for Mg
AZ91 [76]	Thixomolding	200	100	7.5	-	Grain boundary effect
AZ91 [76]	Die-cast	150	100	~ 7	135 (Q_L)	Dislocation climb controlled
		180		5.4		
AZ91 [77]	Die-cast	135-200	48-96	5.7	119	Dislocation climb along with self-diffusion and grain boundary diffusion (Mixed mode of behaviour)

AZ91 [18]	Die-cast	150	70	-	-	Dislocation creep
AZ91 [67]	Die-cast	125	26-60	1.5	-	Grain boundary sliding
			60-100	5	-	Dislocation climb
AZ91 [67]	Die-cast	150	20-40	1.6	-	Grain boundary sliding
			40-80	5.7	-	Dislocation climb
AZ91 [67]	Die-cast	125-175	30	-	44	Grain boundary sliding
AZ91 [11]	Die-cast	125	26-60	1.5	-	Grain boundary sliding
Present Study (AZ91)	Squeeze cast	150 & 175	50 & 65	~6	135-137	Dislocation climb controlled by lattice diffusion

Furthermore, the poor creep performance of the AZ91 alloy arises due to a dramatic loss of strength and creep resistance at service temperatures, which needs attention in order to improve its commercialization. It is widely accepted that the root cause for the poor creep performance of the AZ series alloys is the low thermal stability of the secondary β-$Mg_{17}Al_{12}$ phase [9], [10], [54], [78]. Therefore, the low creep resistance of host Mg is dependent on other alloy constituents. As such, it is possible to increase the high-temperature creep resistance of AZ91 alloys through careful solute selections without sacrificing its other properties. In terms of the applications and manufacturing process, the common strategies to improve the creep resistance of Mg alloys include two approaches [27]. One is to modify the AZ91 alloy through small additions of other alloying elements, and another is to develop entirely new alloys that are age hardenable and can be used as cast or wrought alloys. To date, the AZ91 (Mg-Al) system has been introduced with alloying elements like rare earth (RE), calcium (Ca), antimony (Sb), strontium (Sr), silicon (Si), bismuth (Bi), and others [3], [4], [16], [69], [79-82]. The addition of these alloying elements to Mg-Al alloys results in the precipitation of thermally stable intermetallic phases at the grain boundaries, which may hinder the dislocation motion and grain boundary migration at elevated temperatures. The decrease in the phase fraction of the thermally unstable β-$Mg_{17}Al_{12}$ phase is also reported after incorporating these elements into the Mg-Al system. All these factors are expected to enhance the creep performance of the alloy. *Wei et al.* [17] reported the increasing creep resistance of die-cast AZ91 Mg alloy with the addition of RE elements. In this study, tensile creep behavior was studied in a temperature range of 85°-200°C and a stress range of 30-100 MPa. From the creep curve demonstrated in **Fig. 2.28**, it can be seen that the AE42 alloy is showing a lower minimum creep rate compared to that of the AZ91 alloy at both tested conditions. The reduced Aluminum content in AE42 minimizes the formation of Al supersaturated zones near the dendrite boundaries, and when combined with the stable interdendritic phase $Al_{11}RE_3$ (melting point ~640°C), this contributes to the superior creep resistance of AE42. Phases with a bright contrast and surrounded by high Al-segregated eutectic α-Mg are the β-$Mg_{17}Al_{12}$ phase, **Fig. 2.27a**. The dominant interdendritic phase is $Al_{11}RE_3$. Mn-containing phases also formed during solidification in both AZ91 and AE42 die-cast alloy, **Fig. 2.27b**.

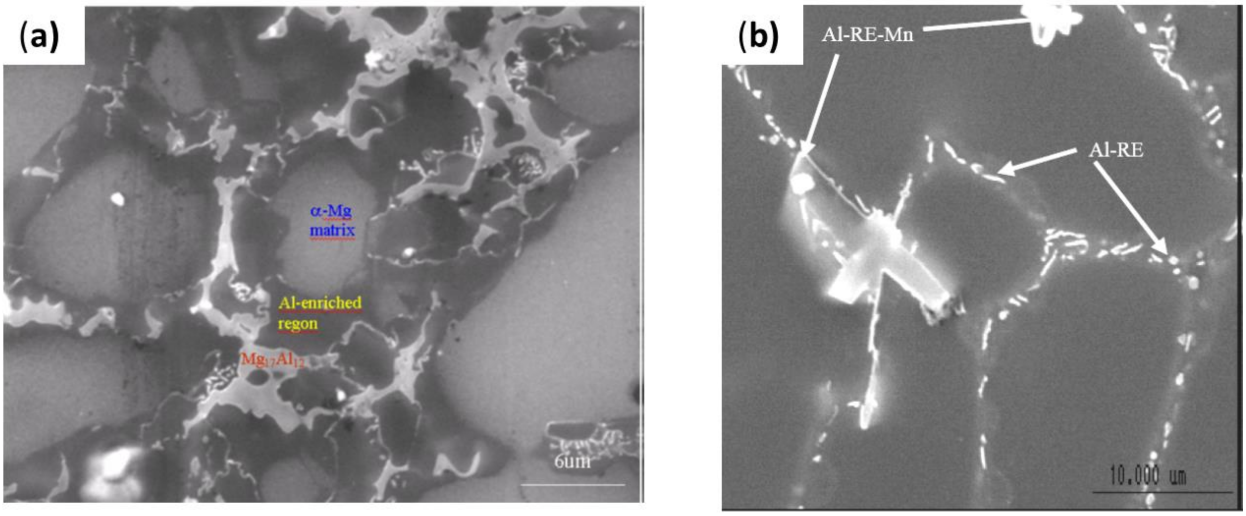

Fig. 2.27: SEM micrographs of the die-cast alloys (a) AZ91D; (b) AE42 [17].

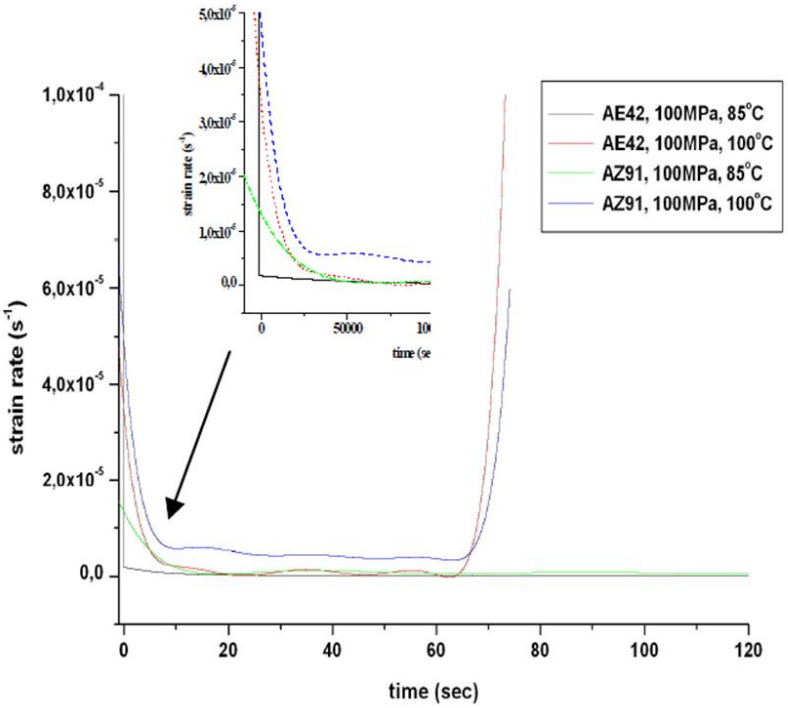

Fig. 2.28: Creep rate vs. time for die cast AZ91D and AE42 (85 °C and 100 °C, 100 MPa) [17].

The same results are depicted by *Srinivasan et al.* [4] after adding Si & Sb in AZ91 Mg alloy. From **Fig. 2.29**, it can be seen that the addition of Sb to AZ91 alloy has introduced the block needle shape phase at grain boundaries, **Fig. 2.29c**. The EDS analysis confirms these phases as Mg_3Sb_2 intermetallic phases, **Fig. 2.29d.** With the addition of Si to AZ91 alloy, massive Chinese script phases are seen at grain boundaries in addition to $Mg_{17}Al_{12}$ intermetallic phases (**Fig. 2.29a)**. The EDS spectrum of the phase presented in **Fig. 2.29b** clearly shows that it contains only Mg and Si and is identified as the Mg_2Si intermetallic phase. Changes in the morphology of the Mg_2Si intermetallic phase can be observed with the combined addition of Si and Sb (**Fig. 2.30c &d**), where the massive Chinese script morphology of Mg_2Si (**Fig. 2.29a**) has been changed into a fine polygon shape. Such a morphological change in the Mg_2Si intermetallic phase is due to a small amount of Sb addition. The alloying additions have little effect on the grain size of the AZ91 alloy castings. The measured grain size (in heat-treated condition) of the base alloy AZ91 is 80 ± 10μm, whereas 0.5% Si, 0.5% Sb, and 0.5% Si + 0.2% Sb added alloys have a grain size of 73 ± 10μm, 70 ± 15μm and 60 ± 10μm respectively. The results from the creep curves shown in **Fig. 2.31** clearly show that the Si and Sb added AZ91 alloys exhibit relatively superior creep resistance than that of the base alloy. The creep rate observed with the Sb addition is one order of magnitude lower than that of the base alloy.

The reason for such improvements, in all cases, is attributed to the presence of hard and thermally stable Mg_3Sb_2 and Mg_2Si intermetallic phases, which strengthen the grain boundaries against sliding even at high temperatures [4]. The coarse Chinese script morphology of the Mg_2Si phase is detrimental to the tensile properties (both at room as well as high temperatures). The addition of Sb to the AZ91+Si alloy brings a morphological change in the Mg_2Si phase from the Chinese script to the polygonal shape. The creep behavior of AZ91 + 0.5% Si and AZ91 + 0.5% Si + 0.2% Sb alloys indicates that the morphological change of the Mg_2Si intermetallic phase has not effectively altered the creep behavior at 150 °C.

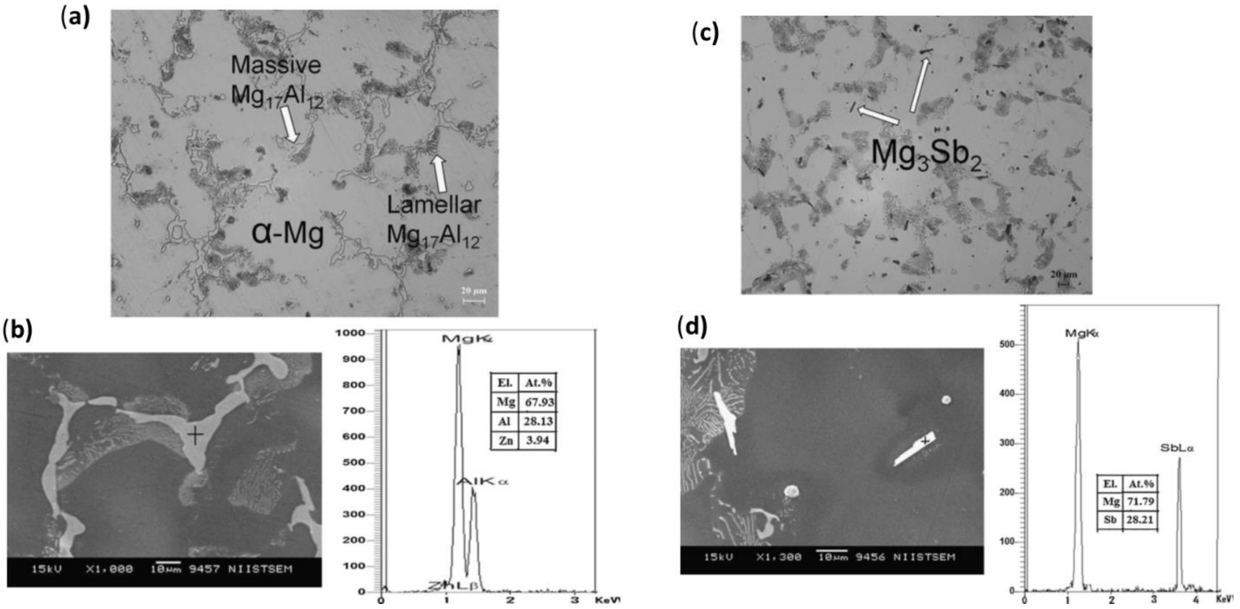

Fig. 2.29: As cast microstructure of AZ91 alloy. (a) Optical (b) SEM with EDS analysis of the intermetallic phase. As cast microstructure of AZ91 + 0.5% Sb alloy. (a) Optical (b) SEM with EDS analysis of the intermetallic phase [4].

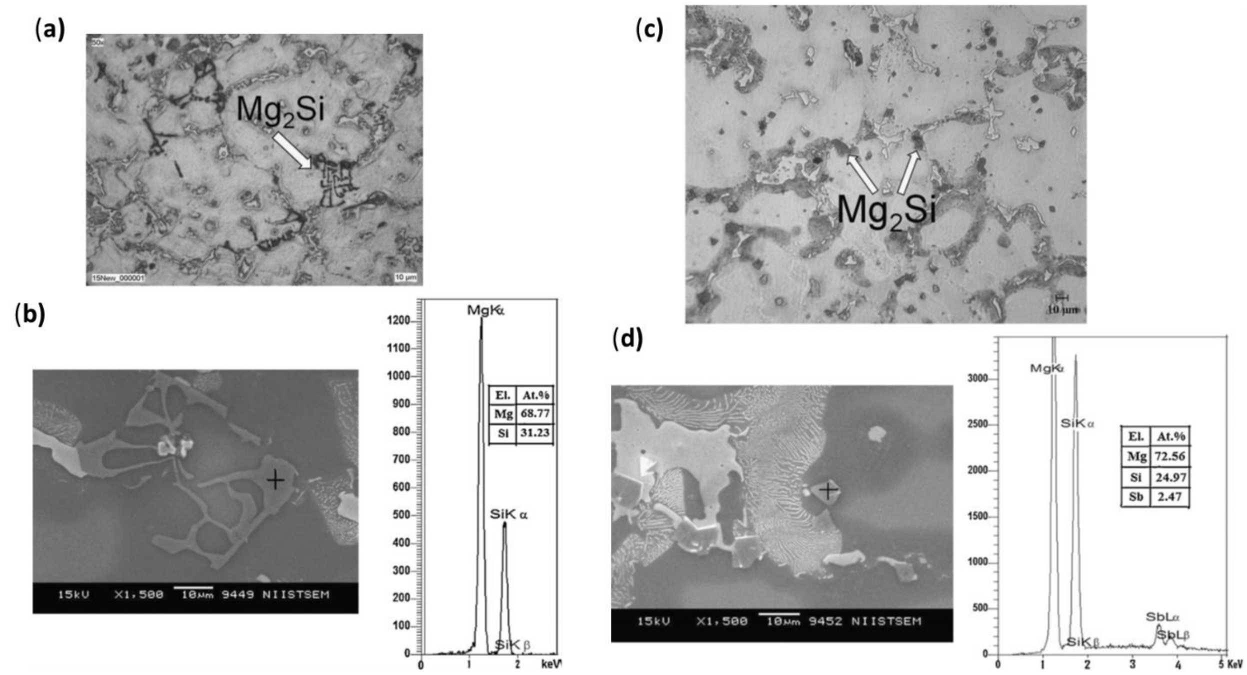

Fig. 2.30: As cast microstructure of AZ91 + 0.5% Si alloy. (a) Optical (b) SEM with EDS analysis of the intermetallic phase. As cast microstructure of as-cast microstructure of AZ91 + 0.5% Si + 0.2% Sb alloy. (a) Optical (b) SEM with EDS analysis of the intermetallic phase [4].

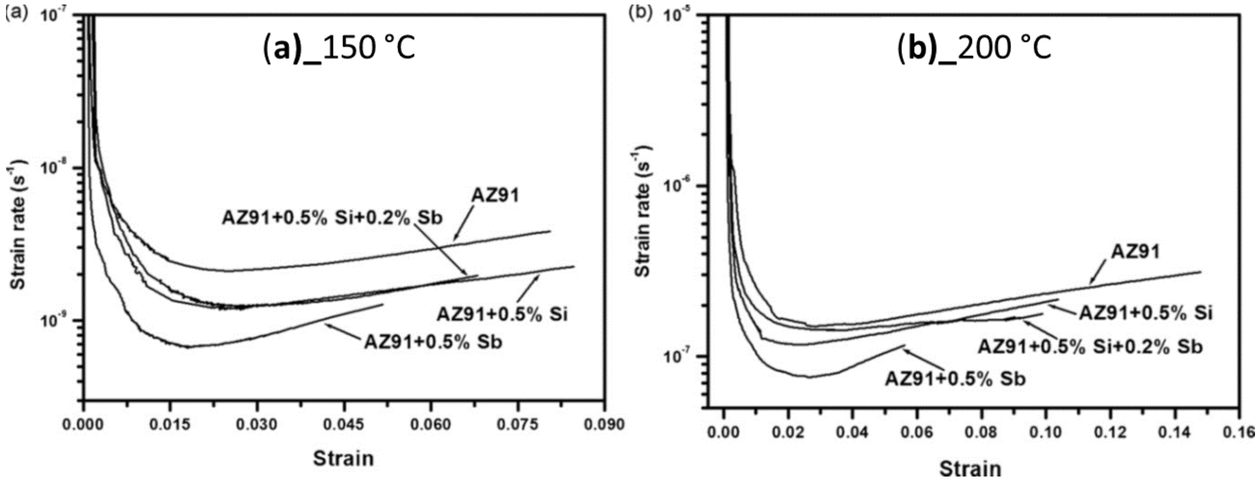

Fig. 2.31: Creep data in strain rate-true strain plot (a) at 150 ºC (b) at 200 ºC [4].

Several other studies are available explaining the importance of alloying addition on the creep performance of the base AZ91 alloy. The author *Bankoti et al.* [80] reported the improved mechanical properties at elevated temperatures of 200 °C after Ca and Sb combined addition in AZ91 Mg alloy. Author *Majhi et al*. [12] observed better creep resistance in the case of AZ91 Mg alloy with the combined addition of Sr and Bi. Although the addition of rare earth elements in AZ91 alloy promotes precipitation with higher thermal stability, their commercialization in automobile industries is limited because they are too expensive [6], [7]. The addition of low-cost Si to the Mg alloy leads to the formation of Mg_2Si intermetallic having coarse ‘Chinese-script’ morphology, leading to the stress concentration during deformation [8], [85]. Therefore, low-cost alkaline earth metals, such as Sr and Ca, are alternatively used as suitable additives in AZ91 alloy. The formation of the thermally stable Al-Sr and Al-Ca compounds in those AZ91-modified alloys is beneficial for improving elevated temperature properties. *Amberger et al.* [25] and *Qudong et al.* [26] reported the precipitation of thermally stable Al_2Ca phase post-Ca addition, and a simultaneous decrease in phase fraction of the β-$Mg_{17}Al_{12}$ phase, thus contributing to the improved creep performance of the AZ91 Mg alloy.

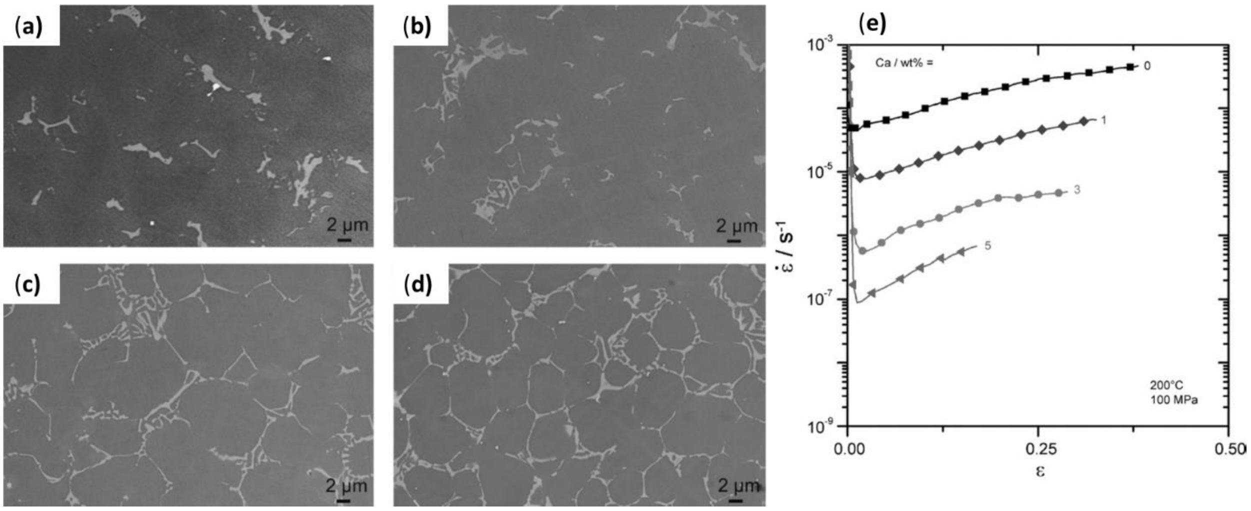

Fig. 2.32: Scanning electron microscopy images of the alloys in as-cast condition (a) AZ91, (b) AXZ911, (c) AXZ931, (d) AXZ951, and e) Creep curves for the alloys AZ91, AXZ911, AXZ931 and AXZ951 tested at 200 °C and 100MPa [25].

However, poor die castability is an important drawback of the Ca-modified AZ91 alloys [19]. The die-cast AZ91 (Mg-Al) alloys containing Ca are observed to be prone to hot cracking and die sticking. The small casting cracks resulting from stress concentration during solidification shrinkage are also observed post-Ca addition [18], [19], [67]. Applying the squeeze casting technique to fabricate the Mg alloy containing Ca may overcome the problem associated with die casting. The detailed literature on the die castability of Ca-containing AZ91 alloy has been explained in **section 2.5.1**. Moreover, the addition of Sr along with Ca in the AZ91 alloy may also help in reducing the hot cracking during die-casting [18], [31], as shown in **Fig. 2.33**. Very few studies are available that have utilized the squeeze-casting technique for the preparation of the Mg-Al-Ca (MRI 153) alloy [31]. Furthermore, only a few studies describing the governing creep mechanism in the case of Mg-Al + Ca (AZX) alloys are available, and there has been no study on these alloys fabricated via squeeze casting. Moreover, among the few available studies concerning the creep mechanism of Mg-Al alloy + Ca alloy (and especially AZ91-Ca alloy) fabricated via different routes, operating creep deformation mechanisms have been found to be different at creep conditions, as listed in **Table 2.4**. A detailed understanding of the creep mechanism is crucial for developing new Mg-Al-based creep-resistant materials. Also, it is interesting to investigate the effect of heat treatment on the creep resistance and microstructure prior to and post-creep of the AZ91-Ca alloy. However, no study has been found in the literature for the same.

Table 2.4: An overview of the creep mechanisms in the AZ91+Ca Magnesium alloy.

Alloy (Wt.%)	**Fabrication route**	**Type of creep testing**	**Temp. (°C)**	**Stress (MPa)**	**n, stress exponent**	**Q, activation energy (kJ/mol)**	**Proposed mechanisms**
AM50+Ca [67]	Die-casting	Tensile	100-200	< 70 > 70	1.5 8.5	40 120	Grain boundary sliding and dislocation creep.
AZ91+Ca [25]	Thixomolding	Impression	150-200	70-200	8.2	-	NA
AM50+Ca [19]	Die-casting	Tensile	150-200	25-50	2.3	40	Grain boundary sliding.
AZ91+Ca [19]	Squeeze-Cast	Impression	150-250	300-480	4.2-5.6	106	Dislocation climbed creep governed by pipe diffusion.
AM60+Ca [67]	Die-Casting	Impression	150 250	150 750	5 >8	100 165	Dislocation climb controlled by pipe

							diffusion & Power law breakdown.
The present study (AZ91+Ca)	Squeeze-casting	Tensile	150 175	50 65	3.49 8.97	187 177	Dislocation-climb & Power law breakdown

Therefore, the second objective of the thesis work is aimed at investigating the effect of 1% Ca addition on the tensile creep properties of AZ91 Mg alloy fabricated via squeeze casting. The detailed results and discussion of the second objective are reported in **Chapter 5.** Similarly, based on the literature, no study has described the tensile creep properties of the squeezed cast AZ91 alloy having individual Sr or combined Sr& Ca addition. Although a few studies investigated the creep performance of AZ91 or similar alloy combined with Sr in addition to Ca/Bi/ RE elements, as mentioned with the operative creep mechanism in **Table 2.5**, in none of these studies, the tensile creep performance was evaluated in squeezed cast AZ91 alloys. Therefore, the third objective of the thesis work is to investigate the effect of individual Sr and combined Sr-Ca addition on the tensile creep properties of the AZ91 alloy fabricated via the squeeze casting technique. The detailed results and discussion based on the third objective are reported in **Chapter 6.**

Table 2.5: An overview of the creep mechanisms in the reported (Mg-Al) + (Sr, Ca) Magnesium alloys.

Alloy (Wt.%)	**Fabrication route**	**Type of creep testing**	**Temp. (°C)**	**Stress (MPa)**	**n, stress exponent**	**Q, activation energy (kJ/mol)**	**Proposed mechanisms**
AZ91-1.07Ca-0.48Sr [18]	Die-casting	Tensile	175	47-117	5	-	Dislocation climb
AM50-1.63Ca-0.22Sr [19]	Die-casting	Tensile	150	50	1.7	60	Grain boundary sliding
AZ91-0.5RE-1Sr [94]	Die-casting	Tensile	150	50	5.23	118	Dislocation climb

The present study **1. AZ91-1Sr**	Squeeze-casting	Tensile	150	50	7.9	208	Climb-controlled dislocation creep governed by lattice diffusion
2. AZ91-1Ca-0.6Sr	Squeeze-casting	Tensile	225	50	8	158	Climb-controlled dislocation creep governed by lattice diffusion

Though the suitable alloying addition in order to improve the creep performance of the AZ91 Mg alloy appears to be a potential technique, it involves higher production costs and a longer cycle time [46]. This led to the strategy that includes a heat treatment process to achieve the desired creep performance of the Mg-Al alloys under investigation. On solutionizing heat treatment, the β-$Mg_{17}Al_{12}$ phase responsible for the poor creep performance of the AZ91 alloy is expected to dissolve homogeneously into the α-Mg matrix, which perhaps enhances the mechanical properties of the alloy at both ambient and elevated temperatures [34-37]. In the majority of studies conducted over the past decade, numerous researchers have concentrated on investigating the impact of different heat treatment processes, such as solutionizing and aging, on the mechanical properties of Mg-Al alloys. However, there has been a scarcity of studies examining the effect of different heat treatment processes on the creep performance of the Mg-Al alloy. Yeoh et al. [44] reported an improvement in the ultimate tensile strength, yield strength, and elongation of the AZ80 Mg alloy on solution treatment and age hardening treatment. A similar observation is made by Wang et al. [95] and Kang et al. [39] [40]on the mechanical properties in the case of Mg-3Al-1Si-0.3Mn-xSr and Al-Si-Mg alloy, respectively. Pu et al. [39] reported the improved comprehensive mechanical properties and corrosion resistance of the AZ91 Mg alloy attributed to the decomposition of the eutectic structure following solution treatment. In addition, Ming-bo et al. [44] experienced both improved mechanical and creep properties in the Mg-3Sn-1Mn alloy as a result of aging treatment. The detailed literature discussion based on the investigation of the effect of heat treatment on the mechanical and creep performance of the Mg-Al alloy is explained in the current section at the start. To the best of the author’s knowledge, investigations on the tensile creep performance of squeeze-casted AZ91 (Mg-Al-Zn) alloy having the addition of Sr and Ca followed by heat treatment are not available. Therefore, the fourth objective of the present thesis work aims to preliminarily investigate the influence of solutionizing heat treatment on the microstructure evolution, hardness, and tensile creep properties of the squeeze-casted AZ91-based alloys and compare them with those alloys in as-cast condition. The detailed results and discussion based on the fourth objective are reported in **Chapter 7.**

2.5.1 Squeeze casting

Squeeze casting is a manufacturing process that combines the advantages of both casting and forging to produce high-quality metal components [98]. In this method, molten metal is poured into a preheated die, which is then subjected to high pressure as it solidifies [99]. This pressure ensures that the molten metal fills all the cavities and eliminates porosity. Moreover, the high applied pressure eliminates air gaps at the liquid-mold interface, leading to enhanced heat transfer across the die surface and thereby increasing solidification and cooling rates, resulting in a dense, fine-grained structure with excellent mechanical properties [100], [101]. In AZ91 alloy, the squeeze casting technique ensures a fine and consistent β-phase network over the eutectic lamellar β-phase, which may further improve the mechanical and creep properties of the AZ91 alloy [10]. The authors Shastri et al. [33] and Mordike et al. [27] reported the best creep resistance in the case of the AZ91 alloy fabricated using a squeeze casting (SC) technique compared to other die casting (DC) and high-pressure die casting techniques (HPDC). The negligible porosity and continuous network of the eutectic phase contribute to the superior creep resistance of the SC alloy. One of the authors, *Zhu et al*. [31], also reported improved creep resistance for the squeeze-cast Mg-Al-Ca (MRI153) alloy, while lower creep resistance was experienced in the die-cast alloy. Similarly, Chadwick et al. [102] showed the highest values of yield strength, ultimate tensile strength, and elongation to failure for AZ91 alloy prepared by squeeze casting technique over other methods, such as sand casting, gravity die casting, and high-pressure die casting, in both as-cast and heat-treated conditions. Therefore, the squeeze casting process has been established as superior to conventional casting methods.

Furthermore, the die-cast Mg-Al alloys containing Ca are observed to be prone to hot cracking and die sticking. The small casting cracks resulting from stress concentration during solidification shrinkage are also observed post-Ca addition [18], [19]. The authors, *Nakaura et al.* [19] and *Hirai et al.* [18], reported the emergence of casting cracks during solidification in the die-casted AZX911 Mg alloy. Also, the porosity in the die-cast Mg alloy may lead to diffusion in Mg alloy [31]. Author *Nakaura et al.* evaluated the die castability of the alloys in terms of casting crack. For each alloy, at least 70 die-casting test specimens were made for die-castability evaluation. For the casting crack evaluation, the total length of the cracks on each specimen was measured, and the average crack length was obtained as the evaluation value, as represented in **Fig. 2.33**.

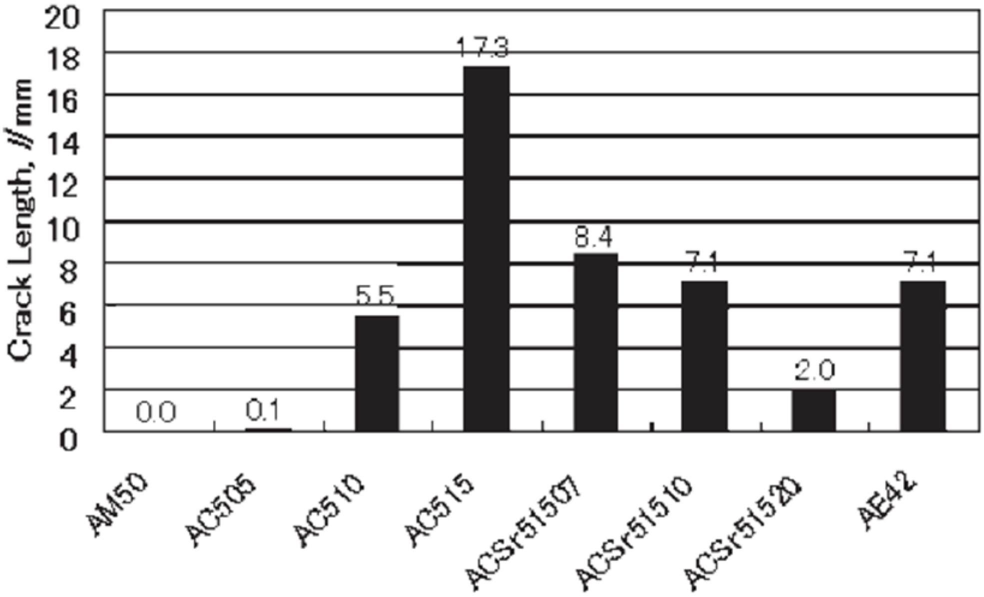

Fig. 2.33: Effect of Ca and Sr addition on the average crack length of AM50-based alloys [19].

Applying the squeeze casting technique to fabricate the Mg alloy containing Ca has overcome the problem associated with die casting, which will be explained and reported in the upcoming chapters (5-6) based on manuscripts of the present thesis work.

Squeeze casting is particularly beneficial for producing components with intricate shapes and thin walls, as it enhances dimensional accuracy and surface finish. It is widely used in the automotive and aerospace industries for producing lightweight, high-strength parts such as pistons, wheels, and structural components. This process not only improves the performance and durability of the parts but also offers significant cost savings by reducing the need for secondary machining operations [99], [103].

2.6 Automotive applications of Mg alloys

Currently, there remains a substantial gap between the use of Magnesium (Mg) alloys in automotive applications and the projected demand for 2030. This gap highlights a strong potential for expanding Mg alloy use in the automotive industry. Mg alloys offer excellent casting properties, making them well-suited for structural components. Automotive applications of Mg alloys include structural parts, high-temperature-resistant components, and moving parts. The evolution of Mg alloy use in automotive components over recent years is illustrated based on the study reported by Liu et al. [1] in **Fig. 2.34**.

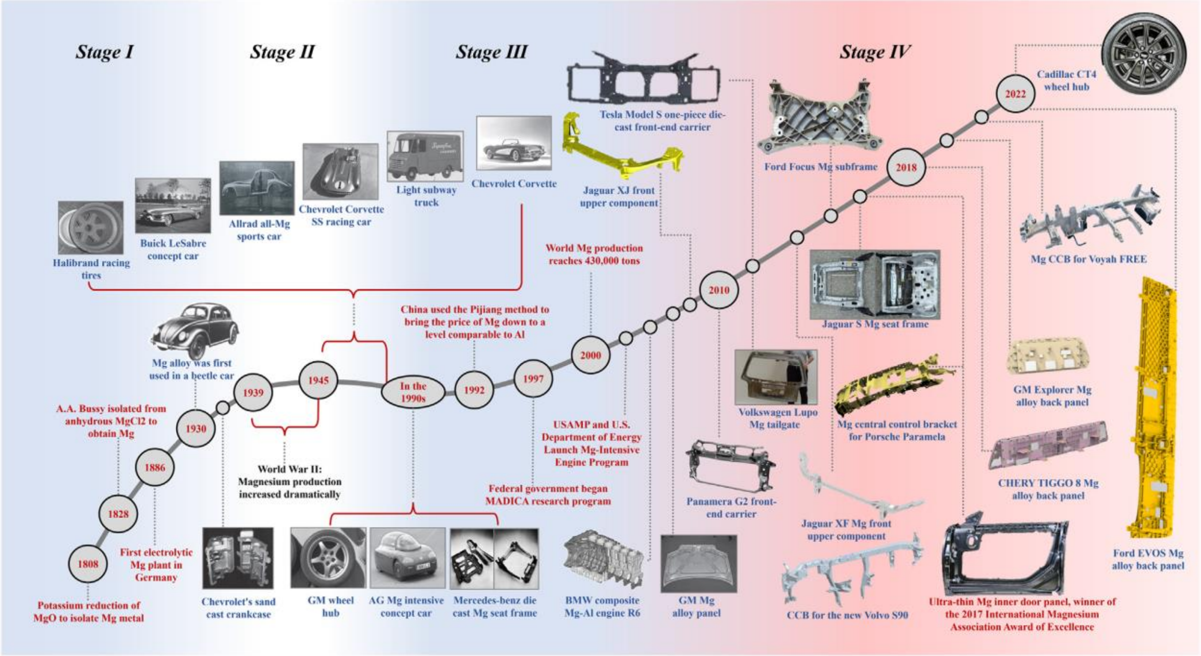

Fig. 2.34: Mg alloy in the development of automotive parts of the historical process [1].

A) Car door and Steering wheel

An assessment by Lotus Engineering on the 2009 Toyota Venza crossover revealed that over 26 kg of Magnesium castings were incorporated within the side doors and lift gate, achieving a weight reduction of 41% [1]. To prevent corrosion, which Magnesium alloys are prone to, the door joints were bolted instead of welded.

Fig. 2.35: Development and application of Mg alloys in car doors: (a) Aston Martin Vanquish S with cast Mg side door inner; (b) All-new 2018 Jeep Wrangler produced with a die-cast Mg rear swing gate; (c) Chrysler Pacifica showing the liftgate assembly highlighted by an Mg die-cast inner; (d) The rear end of the Mercedes-Benz E-Class T-Model featuring the hybrid Mg-Al hatchback; (e) Inner door frame of the Daimler-Chrysler SL Roadster; (f) Ford's concept die-cast Mg door inner with an open architecture; (g) Integrated Mg die-cast door inner designed (h) Ultra-thin and ultra-light Mg alloy door inner[1].

B) Steering wheel

The use of Magnesium (Mg) alloys in steering wheels is widely recognized and valued globally for its energy absorption and vibration-damping capabilities. These properties make Magnesium alloy steering wheels a vital component for driver safety, especially in protecting the head and chest during severe collisions. Currently, die-cast molding is the predominant manufacturing technique for Mg alloy steering wheels. For instance, the Chery AM50A model uses cold chamber die casting, which enables a weight reduction of over 25%.

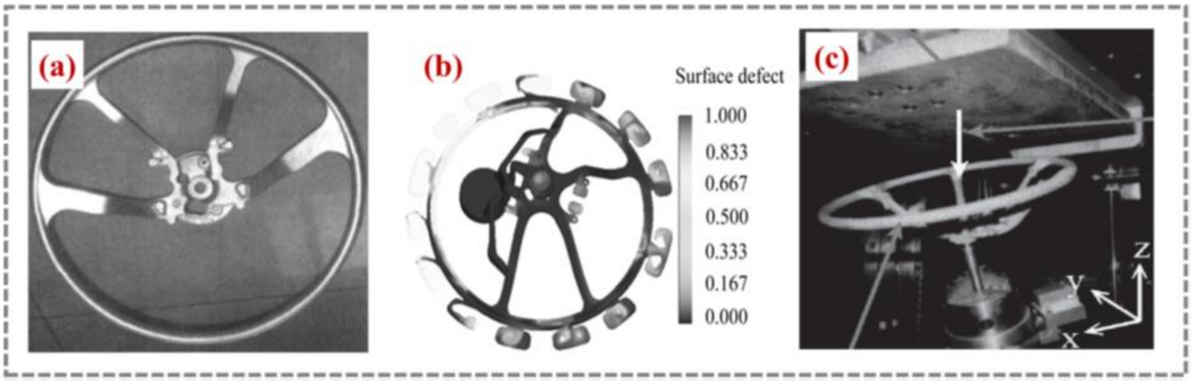

Fig. 2.36: The development and application of Mg alloy in the steering wheel: (a) Mg alloy steering wheel frame produced by Chongqing Mg Industry; (b) Surface defect probability simulation result; (c) Mg alloy steering wheel crash test [1].

C) Seat frame

In vehicles, the front seats typically have more complex structures and greater functionality, while the rear seats are simpler and less functional, as illustrated in **Fig. 2.37**. Currently, Mg alloys are primarily used in the backrest and seat basin skeletons of seats. Materials such as AM50 and AM20 are well-suited for these applications, offering both high rigidity and excellent ductility for frame components. A Magnesium alloy front seat skeleton, with a 1 kg backrest and a 1.2 kg seat basin, results in a total weight reduction of 2.8 kg compared to traditional steel frames.

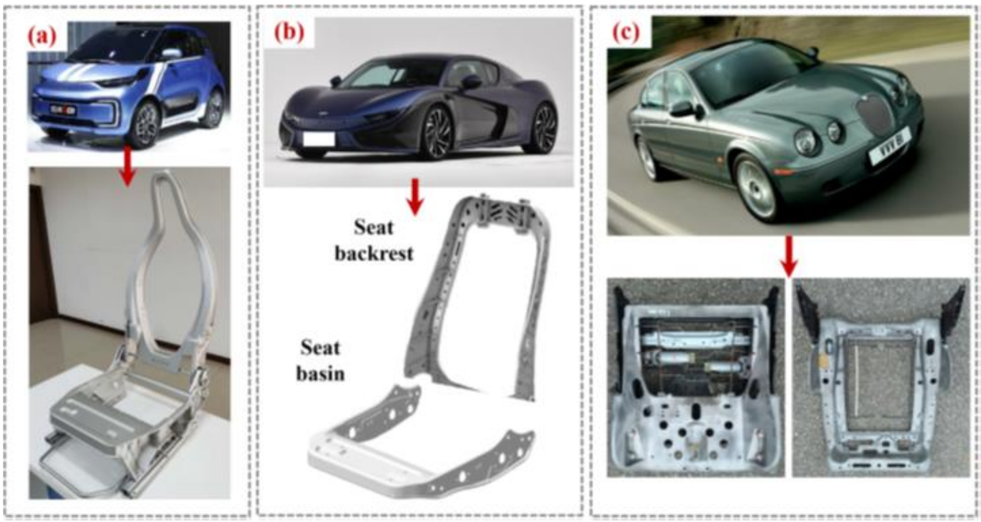

Fig. 2.37: Application of Mg alloy on seat frame: a) Changan E01 Mg alloy seat frame, b) Future K50 Mg alloy seat frame, and c) Jaguar S Type’s Mg alloy seat frame [1].

2.6.1 Powertrain applications

The high castability and favorable properties of Magnesium (Mg) alloys make them particularly well-suited for powertrain components, including engine blocks, oil pans, cylinder heads, transmission cases, and gearboxes.

A) Engine and transmission housing

The powertrain of the German VW Beetle used approximately 20 kg of Magnesium (Mg) castings for components such as the crankcase and transmission housing. Models like the VW Passat, Audi A4, and A6, as well as Ford’s truck gearboxes, utilize the AZ91D Mg alloy. In 2004, Changan introduced Mg-based transmission parts and cylinder heads, which successfully passed both bench and road tests, leading to weight reduction of approximately 33% and widespread market adoption. **Figure 2.38f** illustrates various Mg alloy cylinder head covers.

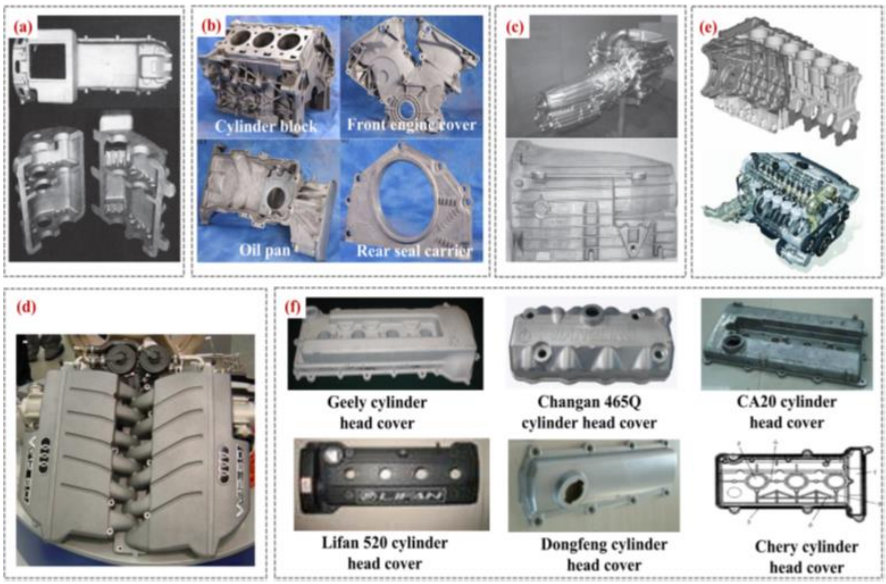

Fig. 2.38: Mg alloy in powertrain applications: a) Mg alloy in the 1930s crankcase and transmission housing, b) Mg cast powertrain components, c) The Mercedes 7-speed automatic transmission case, d) Audi A8 (12-cylinder) intake manifold cover, e) BMW 6-cylinder R6 engine, and f) Engine cylinder head cover typical cases [1].

B) Oli pan

Engine radiation noise at low to medium speeds is a significant contributor to overall vehicle noise. In addition to this, noise from components like the oil pan, timing gear head, and cylinder head cover also plays a notable role. To minimize vibration and noise, it's essential to explore lighter materials and Magnesium (Mg) alloys are often preferred in this regard. For instance, the oil pan made from heat-resistant Mg alloys can reduce weight by up to 33% compared to Aluminum alloys. Die-cast AJ alloys have been identified as ideal for components like the oil pan and valve cover.

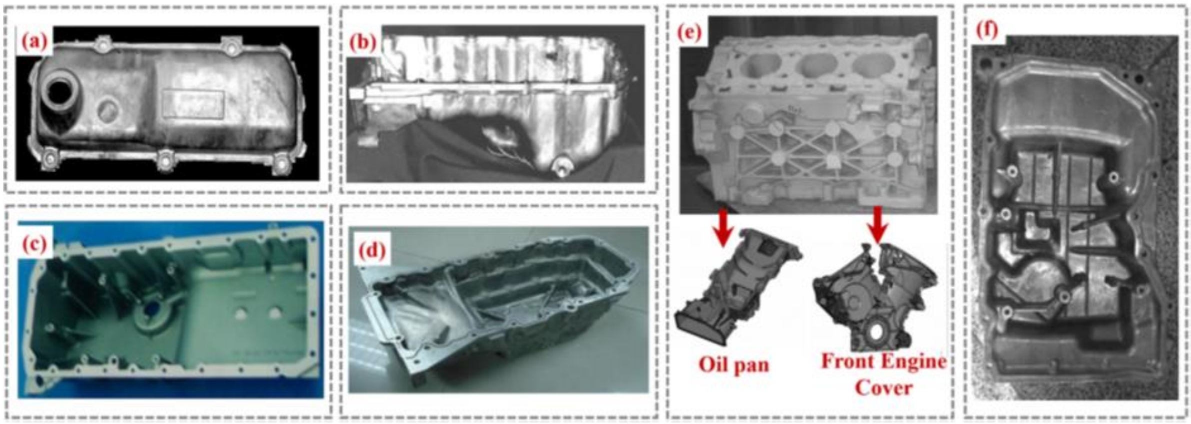

Fig. 2.39: Application of Mg alloy in oil pan: a) Valve cover cast in AJ52x, b) oil pan cast in AJ52x, c) Honda insight Mg alloy oil pan, d) CA20 Mg alloy oil pan, e) USAMP Mg engine oil pan and engine cover, and f) High-temperature creep resistant die-cast Mg alloy oil pan for FAW Beston car [1].

2.7 Summary

Nowadays, fuel efficiency is a major concern in the automobile industry, which demands the use of lightweight materials in automotive components. Low-density die-cast AZ91 (Mg-Al-Zn) alloy is mostly used in automotive components in both cast and wrought conditions because of its lower cost, excellent die-castability, and adequate room-temperature mechanical properties. However, the lack of creep strength restricts its applications beyond the service temperature of 120 °C, making them inefficient for the automotive powertrain components. Several efforts have been undertaken to improve the creep performance of AZ91 alloy by adding suitable alloying elements such as rare earth (RE), Sn, Bi, Si, and Ca. The addition of these alloying elements to AZ91 alloy incorporates the thermally stable intermetallic phases into the alloy and substitutes the β-$Mg_{17}Al_{12}$ phase, improving the creep performance at elevated temperatures. Although the addition of rare earth elements in AZ91 alloy promotes precipitation with higher thermal stability, their commercialization in automobile industries is limited because they are too expensive. On the other hand, the other low-cost additives like Si to the Mg alloy lead to the formation of Mg_2Si intermetallic having coarse ‘Chinese-script’ morphology, leading to the stress concentration during deformation. Therefore, low-cost and easily accessible alkaline earth metals, such as Sr and Ca, are expected to be a better choice as suitable additives in AZ91 alloy. At present, the use of squeeze casting is increasing rapidly due to the benefits of high productivity, high precision, high-quality surface, good machinability, and high fluidity of melt achieved. Also, squeeze-cast components do not show porosity and produce a fine and consistent β-phase network with reduced volume fraction, which may improve the creep performance of the AZ91 alloy. Further, poor die castability associated with the Ca-modified AZ91 alloy can also be overcome using the squeeze-casting technique. All these together are expected to favorably contribute to the creep performance of the AZ91 alloy.

In this study, AZ91-Ca/Sr alloys were produced using the squeeze casting technique. Moreover, the combined addition of Ca and Sr has also been investigated. The study also included an in-depth characterization to examine the microstructure modification that occurred as a result of precipitation of secondary phases in the alloy on alloying addition. The morphology of the precipitated intermetallic phases and their influence on the creep performance of the alloy was also explored. On the other hand, the understanding of the creep mechanism of the alloy is crucial in order to design the new creep resistant Mg-Al alloys. There is a lack of literature reporting the underlying creep mechanism of the squeeze cast AZ91 Mg alloys with Ca and Sr addition. Therefore, in this study, the governing creep deformation mechanism of the investigated AZ91 alloys within the stress and temperature range of interest has also been examined.

Though the suitable alloying addition in order to improve the creep performance of the AZ91 Mg alloy appears to be a potential technique, it involves higher production costs and a longer cycle time. This led to the strategy that includes a heat treatment process to achieve the desired properties of the Mg-Al alloys under investigation. In the majority of studies conducted over the past decade, numerous researchers have concentrated on investigating the impact of different heat treatment processes, such as solutionizing and aging, on the mechanical properties of Mg-Al alloys. However, there has been a scarcity of studies examining the effect of different heat treatment processes on the creep performance of the Mg-Al alloy. Therefore, the impact of the heat treatment process on achieving the desired creep performance of the AZ91-based alloys has been investigated in the present study.

Chapter 3

Experimental Procedure

A brief overview of experimental techniques employed in the present details is provided in this chapter, followed by detailed information in individual results chapters (Chapters 4-7). Each chapter describes the experimental procedures specific to its manuscript.

The flow chart shown below demonstrates the major experimental steps followed in the present research methodology:

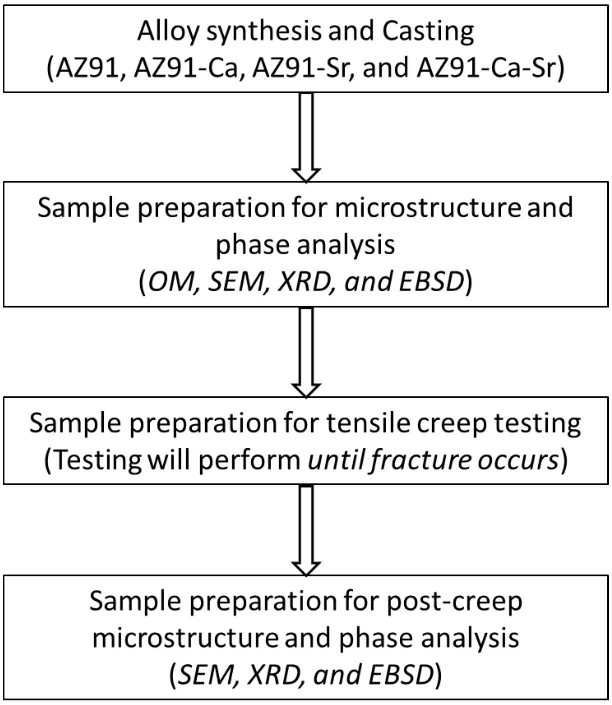

Fig. 3.1: Flow chart demonstrating the experimental steps followed in order to conclude the present work.

3.1 Alloy synthesis and casting

As squeeze casting offers several advantages over die-casting in terms of mechanical properties and lower shrinkage porosity, it is considered the primary technique for the preparation of desired castings in the present work. The detailed steps followed during the operation of squeeze casting are demonstrated in the flow chart shown in **Fig. 3.3** below. The commercial AZ91 alloy ingot received from the supplier (*SURESH METALS, An ISO 9001:2015 Certified Company, Mumbai)* was used as raw material to fabricate the desired castings in the present work. In order to fabricate the different compositions of the AZ91 alloy with the addition of Ca and Sr, the Mg-Ca (Mg-20 wt% Ca) and Mg-Sr (Mg-20 wt% Sr) master alloys were used. The casting setup includes an electrical resistance furnace to melt the material. The melting of the material is carried out in the graphite crucible of 2 kg capacity. Once the melting is done, the molten material is poured into the mold through the runway using a bottom pouring setup. As soon as the molten material fills the mold, the pressure, with the help of a piston connected to the squeeze casting set-up, is applied to the molten metal. For a detailed understanding, the bottom pouring type stir casting machine equipped with a squeeze casting setup is shown in **Fig. 3.2**.

At the initial stage of the casting, the empty furnace was kept at a temperature of 700 °C for the purpose of preheating. Once the preheating was done, the required amount of AZ91 alloy blocks was added to the crucible kept inside the melting furnace. After the initial melting of the AZ91 blocks, the measured quantity of Mg-Ca and Mg-Sr master alloys were added to the melt and waited for 15 mins. The molten mixture was stirred at 300 rpm for the next 10 minutes at least in order to achieve uniform mixing. A complete procedure of melting was carried out under the protective environment of argon or SF6 gas to minimize oxidation. Once the melting was done, the molten metal at 700 °C was poured into a cylindrical cast iron mold through the bottom pouring arrangement consisting of a runway, whose one end is just kept below the bottom pouring valve and the other end is touched to the entrance of mold. The runway was kept at the temperature of 750 °C in order to allow the smooth passing of the molten metal. Before pouring the melt, the mold was coated with a thin layer of graphite oil and allowed to preheat at 200 °C by using an external heater provided. As soon as the melt was poured into the mold, the squeezing pressure of 100 MPa was applied for 30 seconds using the piston from the squeeze casting setup (**see Fig. 3.2**). The list of casting parameters used for the successful casting is shown in **Table 3.1**. The actual chemical composition of the prepared castings was carried out using optical emission spectroscopy.

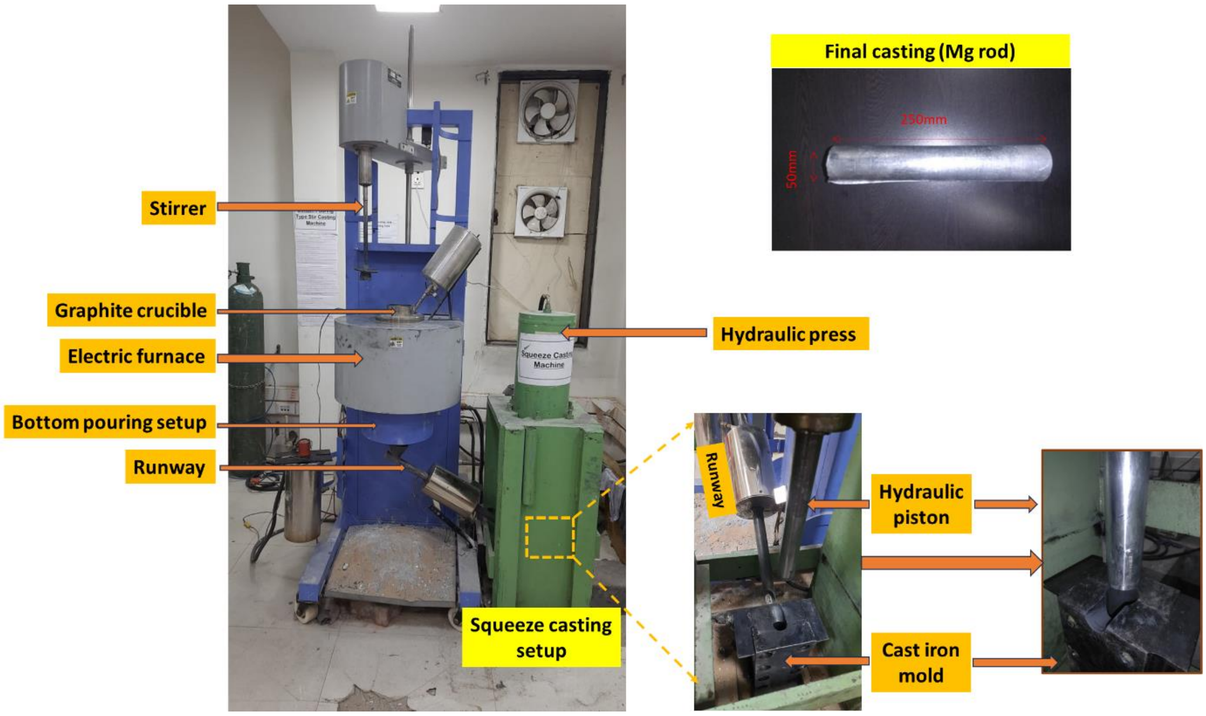

Fig. 3.2: Figure indicates the bottom pouring type stir casting machine equipped with a squeeze casting setup utilized for the preparation of the desired castings.

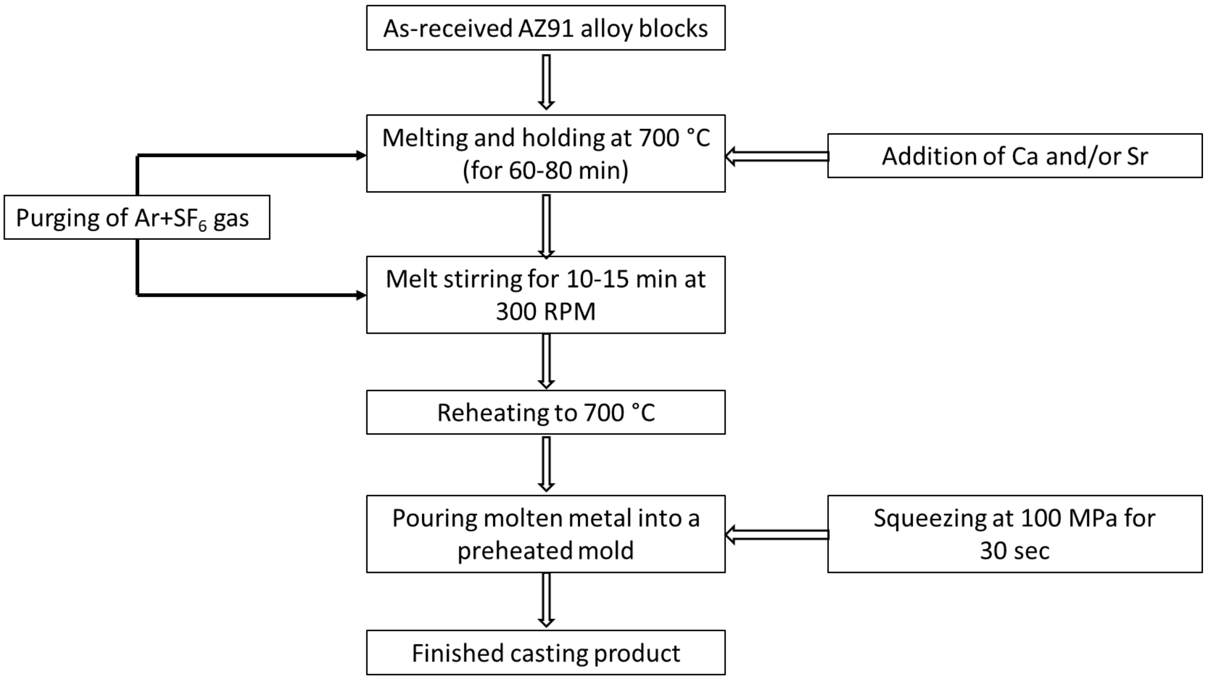

Fig 3.3: Flow chart explaining the steps followed during the casting of the product.

Table 3.1: Squeeze casting parameters used for the castings.

Parameters	Set values
Size of the melting (graphite) crucible	1200 cm^3
Furnace temperature	700 °C
Melt temperature	700 °C
Mold pre-heating temperature	200 °C
Runway temperature	750 °C
Stirrer speed	300 rpm
Stirring time	10 min
Applied squeezing pressure	100 MPa

3.2 Microstructural characterization

3.2.1 Sample preparation

The samples characterized for microstructural examination are first sectioned and polished on grit-size papers ranging from 600 to 4000, followed by cloth polishing with diamond suspensions from 3 microns to 1 micron in order to get a mirror finish surface. Subsequently, the polished sample was then subjected to etching using a solution named acetic picral, composed of 1.5 gm picric acid, 1 ml acetic acid, 25 ml ethanol, and 5 ml distilled water to reveal microstructure. The etched sample for a duration of 1-2 s was immediately rinsed using distilled water and dried using hot air. The dried sample was then considered for the microstructural examination.

3.2.2 Optical Microscopy (OM) and field emission scanning electron microscopy (FE-SEM)

A detailed microstructural examination was carried out using optical and scanning electron microscopy. Optical microscopy was carried out using a Zeiss axiovert a 1 inverted microscope, whereas scanning electron microscopy was carried out using a JEOL-JSM-6500 F Plus FESEM microscope. In SEM, the existing phases and their morphologies in the as-cast alloys were examined. The distinct phases of the alloy samples are sometimes characterized using a back scattered mode (BSE) available with the SEM. In addition, a phase elemental composition and its distribution were analyzed using a point scan and elemental mapping through an energy dispersive spectroscopy (EDS) equipped with scanning electron microscopy. In the thesis, the elemental distribution maps should be interpreted qualitatively rather than as absolute quantitative values due to limitations such as beam size effects, interaction volume, and matrix corrections. The quantification provided in the maps is an approximation and subject to uncertainties arising from signal delocalization, detector efficiency, and X-ray generation depth.

3.2.3 Electron back scattered diffraction (EBSD)

Due to the presence of secondary phases over the grain boundaries of the as-cast alloys, it is very difficult to visualize the grains and estimate the grain size of the specimen associated with the respective alloy. Therefore, in the present work, EBSD was carried out in order to obtain information regarding the grain size of the specimens associated with the respective alloy. The specimen subjected to the EBSD analysis was prepared with the help of mechanical polishing using colloidal silica for 1 h just after the mirror polishing with diamond suspension (**see section 3.2.1**). During polishing with a colloidal silica solution, a white layer may develop on the specimen surface. To remove this layer, intermittent polishing with distilled water between colloidal silica polishing sessions is recommended. After the final polishing step, the specimen is cleaned using ultrasonication in acetone and then air-dried. Finally, the prepared specimen is stored in a vacuum desiccator to prevent atmospheric contamination and oxidation until it is required for EBSD examination. The polishing with colloidal silica aimed to relieve the stresses and strains induced at the surface of the specimen due to prior mirror polishing. Also, while polishing, it is important to ensure the flat surface of the specimen to get a perfect focusing and high-quality scan. The EBSD was carried out using a JEOL-JSM-6500 F Plus FESEM microscope at a 20 kV accelerating voltage with a working distance of 25 mm and a tilt angle of 70°. The area of the scan is selected in such a way that the scan can accommodate a sufficient number of grains. Similarly, the step size (2 μm) of the scan was determined to cover 100,000 to 150,000-pixel points for a good-quality scan. The EBSD data was collected and analyzed using the HKL channel 5 system software. The analysis software transforms the data into images, which helps in understanding the crystallography of the sample on the basis of certain color codes. The sample direction for the EBSD orientation maps has been considered in the normal direction (ND).

3.2.4 X-ray diffraction (XRD)

X-ray diffraction (XRD) is widely used to identify and characterize the phases present in a material. In the present work, the phases that exist in the microstructure of the as-cast alloys are identified using a PANalytical EMPYREAN x-ray diffractometer with CuKα (k = 1.541 Å) radiation. The peaks indexed at respective 2θ diffraction angles demonstrate phases associated with the peak. The existing phases were confirmed by comparing the peak position with the inorganic crystal structure database (ICSD).

3.3 Thermodynamic and thermal analysis

Thermodynamic calculations for the prepared alloy compositions were conducted using the computational materials engineering Thermo-Calc® software, specifically employing the TCMG6 database for Magnesium alloys. These calculations were based on the chemical compositions of the respective alloys. The thermodynamic analysis included estimating the evolution, type, and stability of potential equilibrium phases within the alloys over a range of temperatures, as well as determining the phase composition. Additionally, to confirm the precipitation of the required equilibrium phases in the alloys, thermal analysis was performed using a differential scanning calorimetry (DSC) instrument, model STA8000 by Perkin Elmer, in a purified argon atmosphere. A detailed explanation of the evolved phases and their DSC analysis will be presented in the chapters containing manuscripts.

3.4 Tensile creep test

The tensile creep testing of the specimens from the respective alloys was performed using a creep testing machine manufactured by Star Testing Systems (STS) with a lever ratio of 20:1. The complete creep testing set-up is shown in **Fig. 3.4**. The maximum load capacity and temperature associated with the set-up is 20 KN and 1000 °C, respectively. The sample used for creep testing is prepared using a wire-cut EDM machine following ASTM E-139 standards, as shown in **Fig. 3.5**. The prepared sample was subjected to a constant load creep test within the stress and temperature range of interest. The specific range of stress and temperature considered in the present work has been reported in the chapters containing manuscripts. The creep specimen was maintained at the desired temperature using a three-zone heating furnace attached to the creep machine. The displacement at the gauge length of the specimen during creep testing was measured using a dial gauge mounted in the extensometer attached to the gauge length of the specimen (25mm). The least count of the dial indicator is 1 micron. The strain reading was continuously recorded through a Eurotherm data logging system. Once the load is applied thoroughly, the strain reading is taken at an interval of 1 minute until the fracture occurs. Sometimes, a specimen will take a long time to undergo fracture for the lower combination of stress and temperature. For such cases, the test was continued until the starting point of the tertiary creep regime and was then stopped.

In the present work, the minimum creep rate (s^{-1}) is used as the parameter for assessing the creep performance of the AZ91 alloys to avoid the impact of unavoidable casting defects. The minimum creep rate reported is calculated by estimating the average strain rate observed in the steady-state region. The average strain rate of the steady-state region of each creep curve is estimated by constructing a straight line at the average position and marking its intersection point at the strain rate (Y) axis.

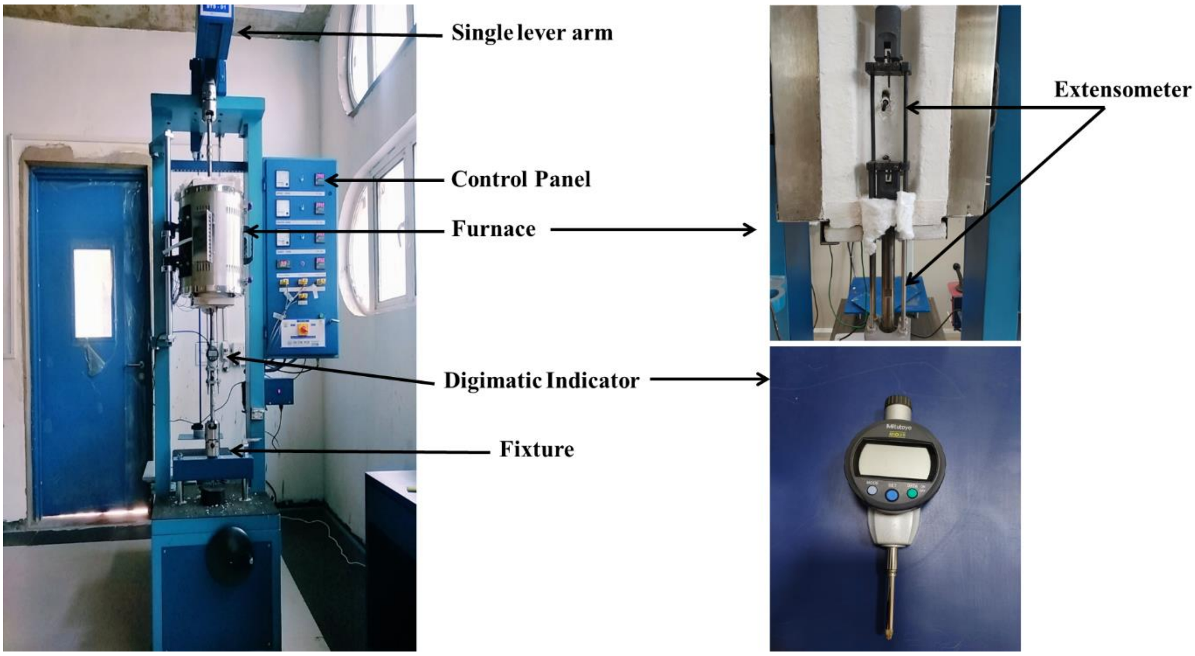

Fig. 3.4: Single lever creep testing machine.

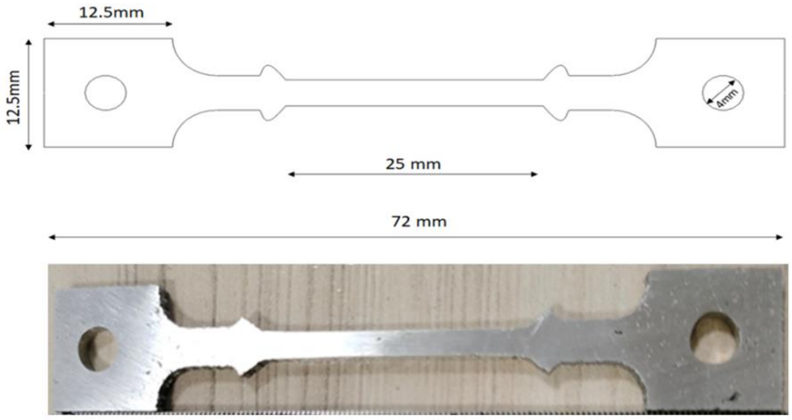

Specimen before creep test

Specimen after creep test

Fig. 3.5: Tensile creep specimen before and after creep test.

Chapter 4

Creep Deformation Study of Squeeze Cast AZ91 Magnesium Alloy

As the literature illustrated, the creep behavior of the squeeze cast AZ91 Mg alloy has not been explored yet in detail; the present chapter investigates the correlation between the microstructure and creep performance of the squeeze cast AZ91 alloy. In addition, the post-creep microstructure has also been studied in order to understand the effect of creep parameters on the thermal stability of the microstructure of the alloy during the creep process. Further, the governing creep mechanism associated with the alloy during the creep deformation is also determined. Attempts have also been made to estimate the dislocation density and threshold stress associated with the creep-deformed AZ91 alloy under applied creep temperature and stress.

Chapter 4

Creep Deformation Study of Squeeze Cast AZ91 Magnesium Alloy

The work in this chapter has been published as: Hitesh Patil, Akshay Jain, Ankush S. Marodkar, Piyush Kumar, Abhijit Ghosh, Hemant Borkar, "Creep deformation study of squeeze cast AZ91 Magnesium alloy", *Materials Science and Technology*, Vol 39, Issue 15, 1926–1938 (2023).

4.1 Introduction

Magnesium alloys are of tremendous interest as a structural material in the automotive and aerospace industries owing to their high specific strength and stiffness, good castability, and machinability. Mg cast alloys have comprised 85-90% of all commercial Mg alloy products due to their advantages over wrought alloys in terms of cost and the challenges associated with Mg formability [9]. The commercial AZ91 (Mg-Al-Zn) alloy is the most intensively used Mg alloy in the automotive industry, owing to its good mechanical properties and excellent die castability. The microstructure of AZ91 Mg alloy comprises two phases (α-Mg and intermetallic β-$Mg_{17}Al_{12}$ phase). β-$Mg_{17}Al_{12}$ phase in AZ91 alloy results in good mechanical performance (at room temperature) except ductility but poor creep performance at elevated temperature. The poor creep resistance of Mg-Al alloys is generally related to the formation of the β-$Mg_{17}Al_{12}$ phase, which has poor thermal stability at elevated temperatures. Not only has β-$Mg_{17}Al_{12}$ a low melting temperature (458 ºC), but the Mg-$Mg_{17}Al_{12}$ lamellar eutectic structure is also associated with a low eutectic temperature (437 ºC), which tends to soften and starts dissolving above 120 ºC -125 ºC, thus causes substantial grain boundary sliding at elevated temperatures. The poor creep performance of the AZ91 alloy can be taken care of by suitable alloying addition, which will result in the precipitation of the thermally stable intermetallic phases by suppressing the thermally unstable β-$Mg_{17}Al_{12}$ phase and also leads to grain refinement in the alloy.

The route of alloy fabrication also influences the mechanical and creep performance of the Mg alloys. As the AZ91 alloy prepared using a die-casting technique involves a higher amount of porosity that allows easy crack initiation and growth during creep tests. Also, the volume fraction of the thermally unstable β-$Mg_{17}Al_{12}$ phase is the highest in the AZ91 alloy prepared via gravity casting (GC), leading to its poor creep performance [33]. At present, squeeze casting is increasing rapidly due to the benefits of high productivity, high precision, high-quality surface, good machinability, and high fluidity of melt achieved. Also, squeeze-cast components do not show porosity and produce a fine and consistent β-phase network, which may improve the mechanical and wear properties of the AZ91 alloy [13], [27], [33], [101]. In addition, the volume fraction of the thermally unstable β-$Mg_{17}Al_{12}$ phase is observed to be the lowest in the AZ91 alloy prepared via squeeze-casting (SC) [27]. The squeeze-casting process also provides significant grain refinement. So, there is a potential for improvement of creep resistance by changing the production method from die casting to squeeze casting. Most of the studies investigating the creep performance of the Mg alloy include the alloy prepared using die-casting only, as shown in **Table 2.2**. The refined microstructure and reduction of defects in squeeze-cast products are expected to improve creep resistance in Mg alloys, including AZ91 alloys.

A detailed understanding of the creep mechanism of the Mg-Al-Zn alloy system is crucial for developing new creep-resistant materials. Moreover, among the few studies discussing the creep mechanism of the die-cast Mg-Al alloy, there is non-uniformity in specifying the creep mechanism at different stresses and temperatures, as listed in **Table 2.2**. Also, no study involves the investigation of the creep mechanism of the AZ91 alloy prepared via the squeeze casting route. Therefore, the present work investigates the underlying creep mechanism prevalent in squeeze-cast AZ91 Mg alloy at different stresses and temperatures. Also, an attempt has been made to determine the threshold stress for the creep deformation at the selected stresses and temperatures.

4. 2 Chemical composition of the AZ91 alloy

The chemical composition of the squeeze-cast AZ91 alloy estimated using an optical emission spectrometer in the present work is listed in **Table 4.1**.

Table 4.1: Chemical composition of squeeze-cast AZ91 Mg alloy.

Elements	Al	Zn	Mn	Si	Mg
wt(%)	9.01±0.142	1.57±0.002	0.17±0.002	0.022±0.011	balance

4.3 Microstructure characterization of squeeze cast AZ91 Mg alloy

The optical and scanning electron micrographs of the as-received and squeeze-cast AZ91 Mg alloy are shown in **Fig. 4.1& 4.2**, respectively. The microstructure shows the presence of α-Mg matrix and intermetallic β-$Mg_{17}Al_{12}$ phase. The EDS analysis (**Fig. 4.2c**) confirms the presence of these phases. It is observed that the β- $Mg_{17}Al_{12}$ phase exists in two morphologies, i.e., either as a massive phase or in the form of a lamellar network. After squeeze casting, only a massive β-$Mg_{17}Al_{12}$ phase is obtained in the microstructure. The microstructure of squeeze cast AZ91 Mg alloy **(Fig. 4.2a)** is more refined than that of as-received alloy **(Fig. 4.1a)** due to the squeezing action during solidification. The volume fraction of the β-$Mg_{17}Al_{12}$ phase in **Fig. 4.2b** is observed to be 14±2%, estimated using Image J software.

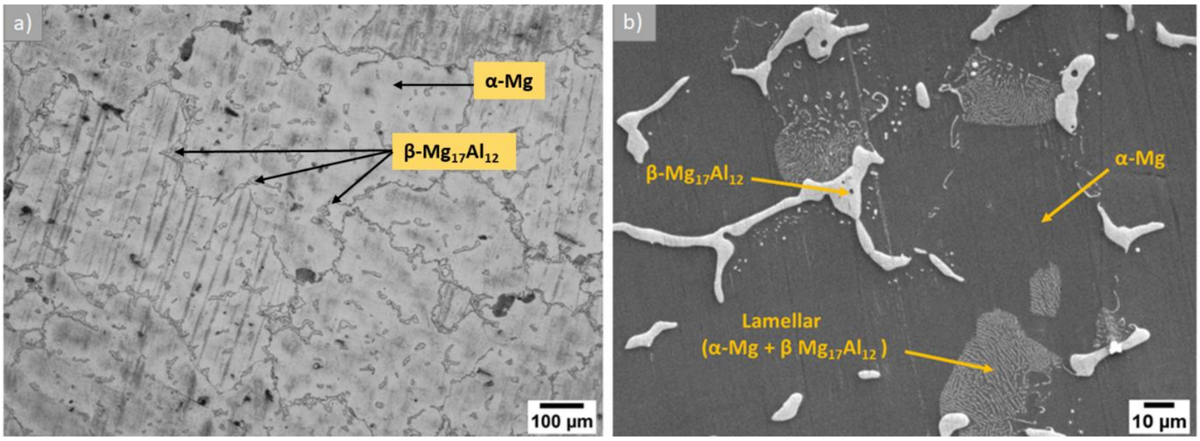

Fig. 4.1: a) Optical and b) SEM micrograph of as-received AZ91 Mg alloy.

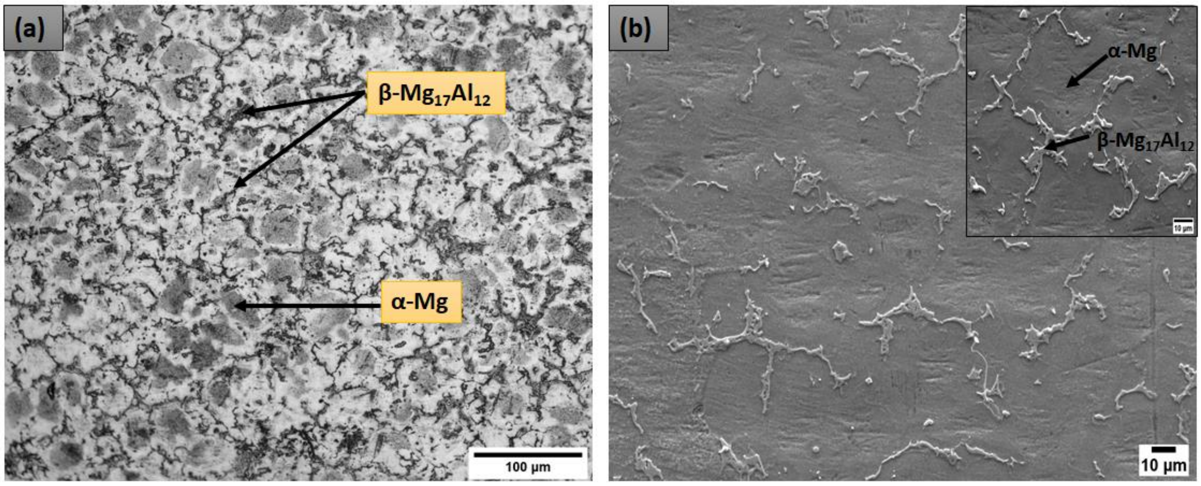

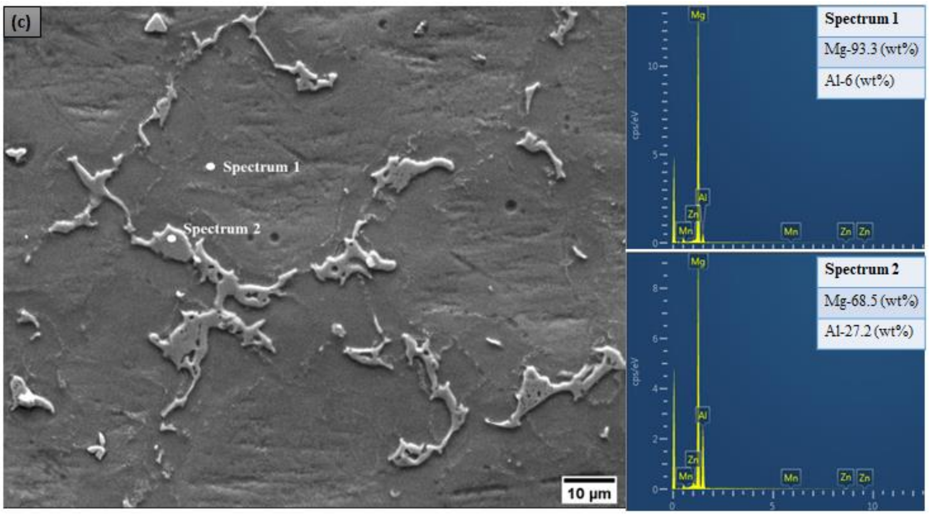

Fig. 4.2: a) Optical and b) SEM micrograph of squeeze cast AZ91 Mg alloy with c) EDS analysis.

4.4 Creep properties

The typical tensile creep curves (strain%-time plot) for the squeeze cast AZ91 Mg alloy at a temperature range of 150-200°C and stress range of 50-80 MPa are shown in **Fig. 4.3**. All the curves exhibit three well-defined stages of creep i.e., short primary region, a secondary region of almost constant strain rate, and a tertiary stage. The strain rate vs. time plot at different testing conditions is shown in **Fig. 4.4** to demonstrate the creep behavior of squeeze cast AZ91 Mg alloy.

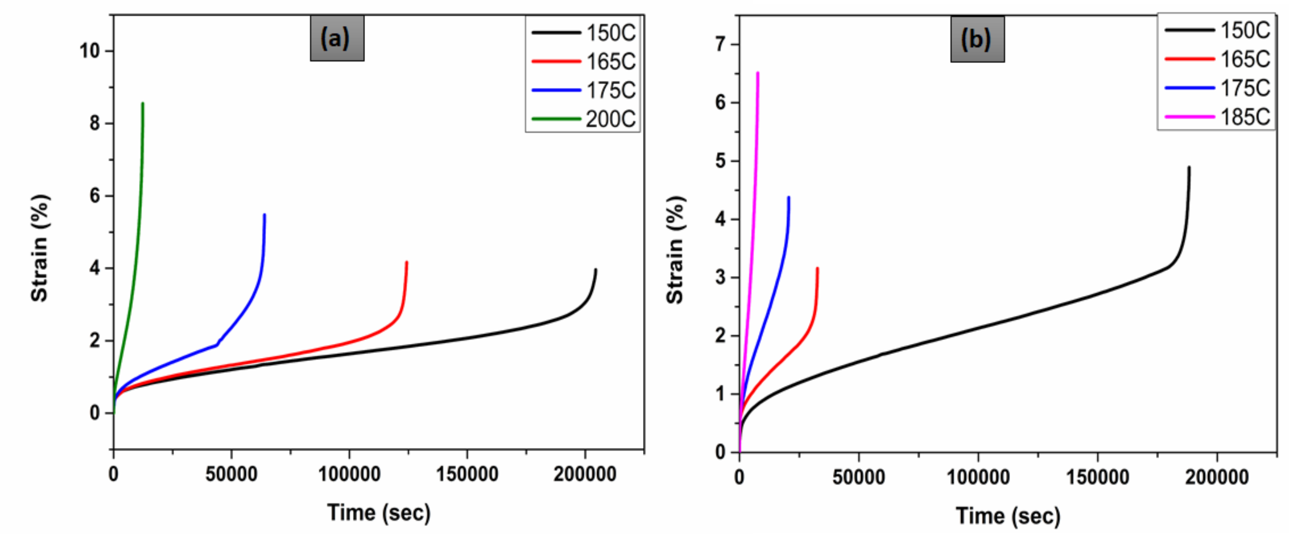

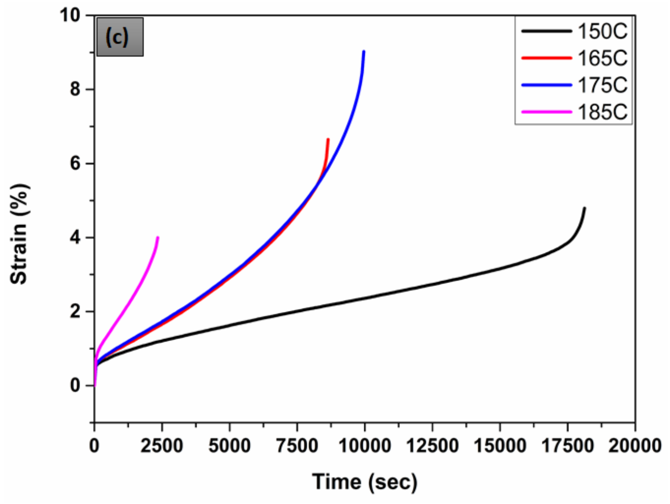

Fig. 4.3: Creep curves at different temperatures under the applied stress of (a) 50 MPa, (b) 65 MPa, and (c) 80 MPa.

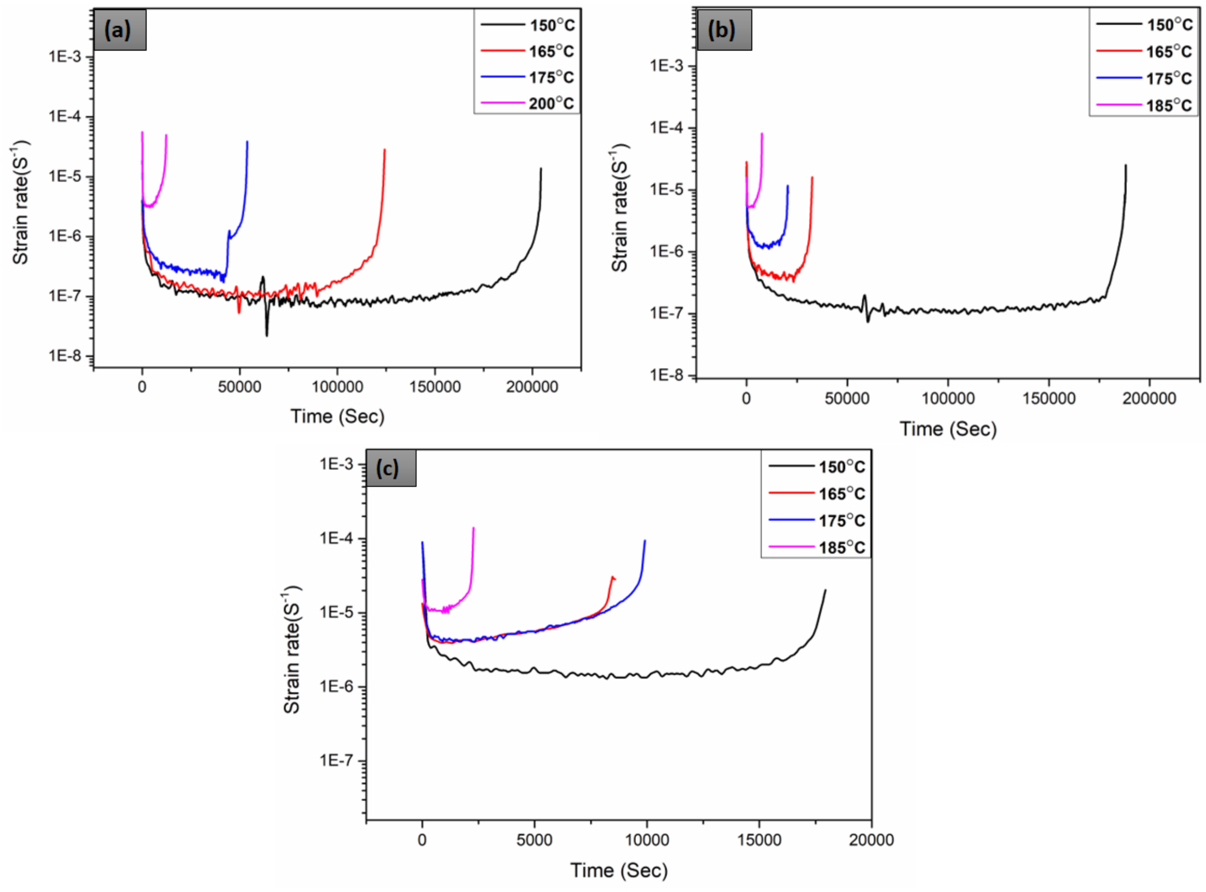

Fig. 4.4: Creep strain rate vs time curves using semi-log scheme at stress (a) 50 MPa (b) 65 MPa & (c) 80 MPa.

In all the curves, the general trend is that the strain rate decreases with time in the initial primary stage, then reaches an almost constant strain rate during the intermediate secondary stage, followed by an increasing strain rate in the tertiary stage. As expected, the strain rate increases with increased applied load and temperature. The steady-state strain rates are found to be varied in the range from a minimum of 7.73×10-8 (s-1) under 50 MPa stress at 150oC to a maximum of 2.22×10^{-5} (S^{-1}) under 80 MPa stress at 200°C. Approximately, the minimum creep rate increases by order 1 or 2 (10^2 to 10^1) when the temperature increases from 150 °C to 200 °C under constant stress. In contrast, the stress variation from 50 MPa to 80 MPa at constant temperature increases the creep strain rate by factor 2 to 4.

4.5 Post-creep microstructure

Microstructural stability at the application temperature is essential to have better creep resistance. The optical and scanning electron micrographs of the crept samples tested at different temperatures under 50 MPa stress are shown in **Fig. 4.5 and 4.6,** respectively. The β-$Mg_{17}Al_{12}$ precipitate is observed to undergo coarsening in crept samples as compared to the unexposed sample. Further, with an increase in test temperature, the interparticle distance increases. Additionally, the second phase fraction is found to decrease with an increase in test temperature. The area fraction of the β-$Mg_{17}Al_{12}$ phase reduces from 11.40% to 8.9% on the increment of test temperature from 150 °C to 200 °C, as estimated by image analysis. Therefore, the β-$Mg_{17}Al_{12}$ is expected to be thermally unstable and dissolve on increments of test temperature from 150 °C to 200 °C.

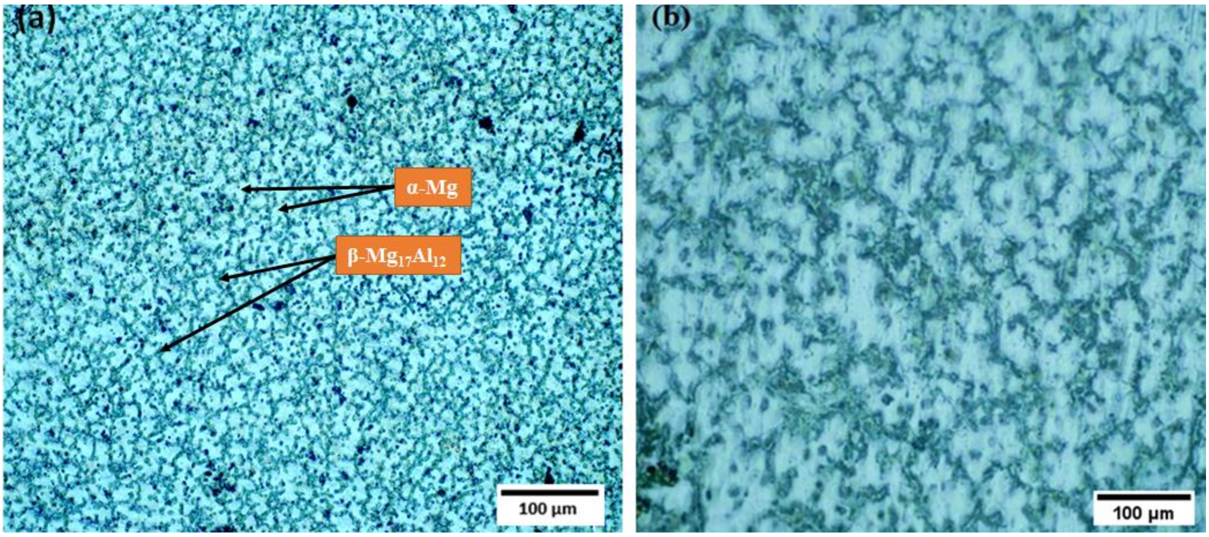

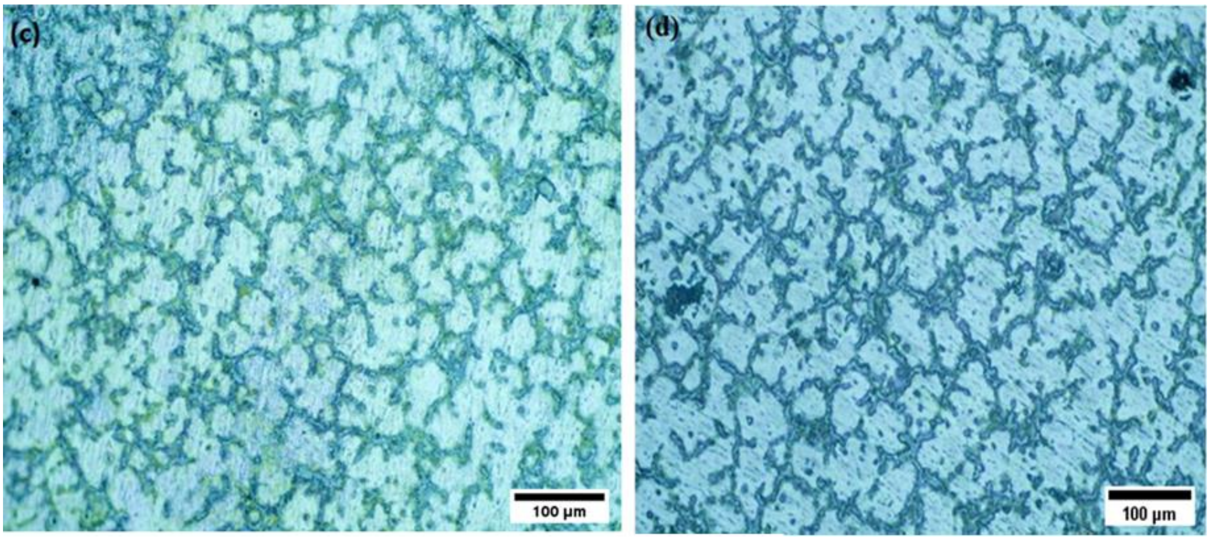

Fig. 4.5: Optical microstructure (OM) of (a) without creep and crept sample of AZ91 at 50 MPa (b) 150 °C (c) 175 °C (d) 200 °C.

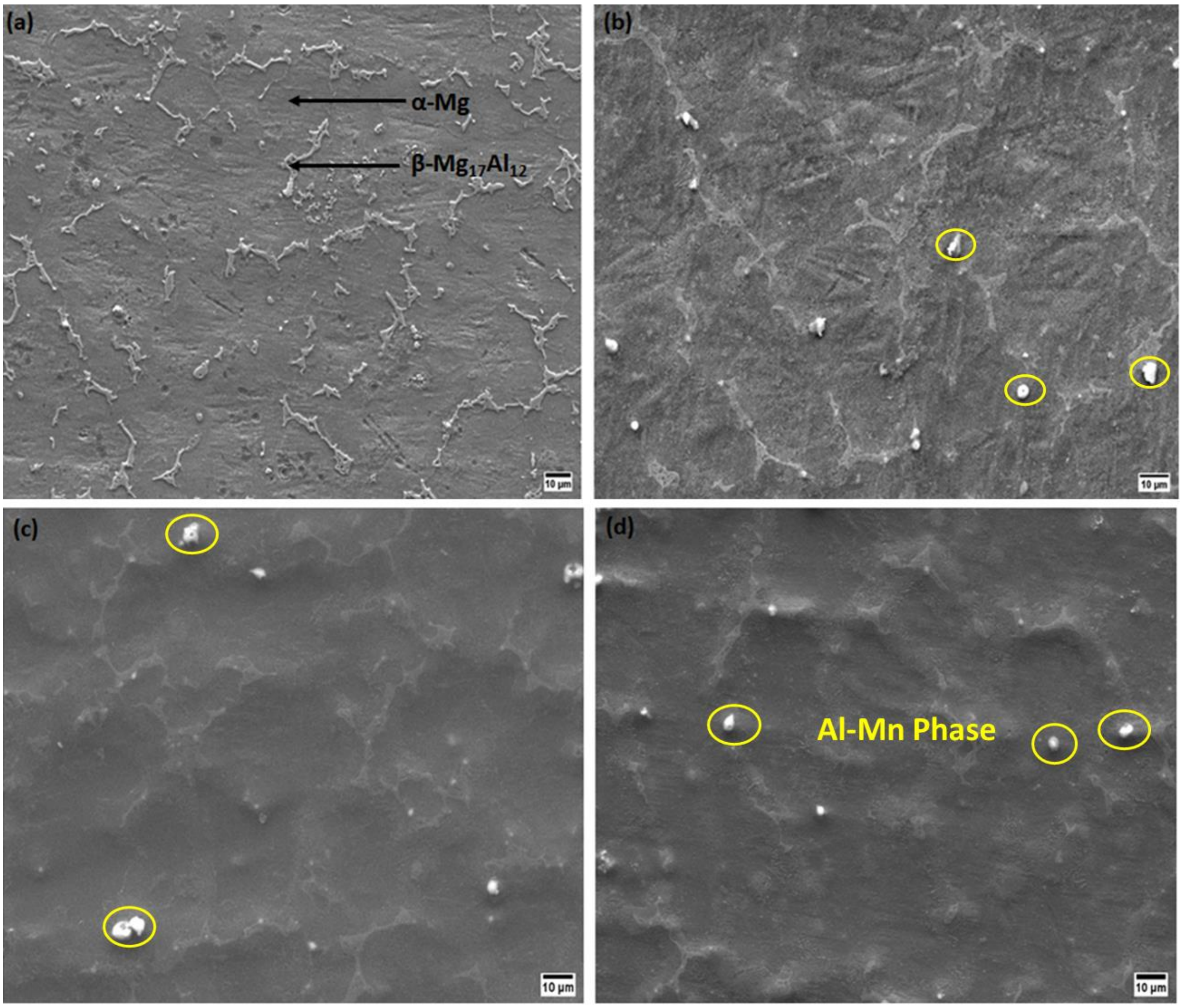

Fig. 4.6: SEM images of a) fresh and crept sample of AZ91 at 50 MPa (b) 150 ℃ (c) 175 ℃ (d) 200 ℃.

4.5.1 Cavity formation

Figure 4.7 represents the SEM micrograph of the transverse cross-section near the fracture surface of crept samples tested at 150 °C under 50 MPa stress and 185 °C under 80 MPa stress. The presence of cracks in most of the β-$Mg_{17}Al_{12}$ intermetallic phase particles is observed **(Fig. 4.7(a))**. In some of the cases, as shown in (Figure 4.7(b)), the breakdown of the continuous β-$Mg_{17}Al_{12}$ phase has also been noticed. β-$Mg_{17}Al_{12}$ phase is incoherent with the α-Mg matrix since the Magnesium matrix has a hexagonal closed packed (hcp) lattice, whereas the β-$Mg_{17}Al_{12}$ phase has a cubic lattice [2]. Such incoherency (lattice mismatch), which exists between the α-Mg matrix and β-$Mg_{17}Al_{12}$ phase interface, leads to easy cavity formation **(Fig. 4.7(a-c))**. Further, these cavities join and form a continuous network along the grain boundaries **(Fig. 4.7(d))**. These cavities promote dislocations to surpass the bulk of the grain to the free surface without being blocked by obstacles [85], [126] and thus promote softening.

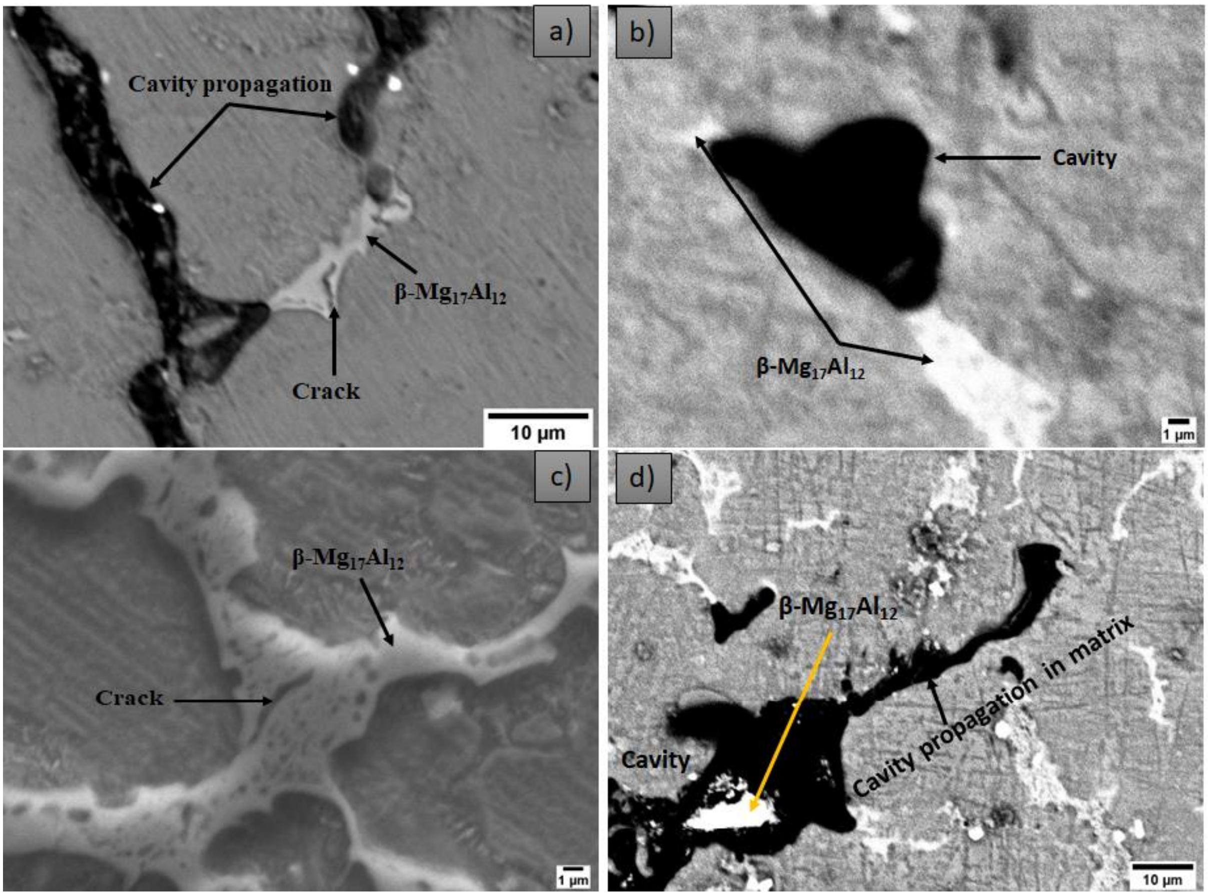

Fig. 4.7: SEM micrograph of transverse cross-section near the fracture area of crept AZ91 alloy tested at a) & b) 50 MPa_150 °C, c) & d) 80 MPa_185 °C.

4.5.2 Fractography of crept sample

The fracture surface of the crept sample has been investigated in detail to understand the origin and mode of fracture. The SEM images of the fracture surface at different test conditions are shown in Fig. 4.8. The mode of fracture is completely cleavage, as shown in Fig. 4.8a in the unexposed sample, which is fractured at room temperature in quasi-static loading. Cleavage fracture is attributed to the limited plasticity of AZ91 Mg alloy owing to less number of active slip systems at room temperature [32, 117]. The crept samples exhibit ductile fracture with the presence of large dimples in low magnification, as shown in **Fig. 4.8b**. The dimple size varies in the range of 50 to 100 μm. However, a closer look inside the dimples reveals the intergranular fracture, as shown in **Fig. 4.8c**. This intergranular fracture has initiated at the grain boundary triple junction in the form of a wedge-type pore or cavity. The presence of hard precipitates or the second phase at the grain boundary triple junction may have played a crucial role. Overall, the mode of fracture for the crept samples is "intergranular then ductile," and a similar report has been made in some recent studies in AZ91 Mg alloy [32]. The fracture initiates in the form of the intergranular cavity at the grain/sub-grain boundaries, followed by the growth and coalescence of these cavities in a ductile mode.

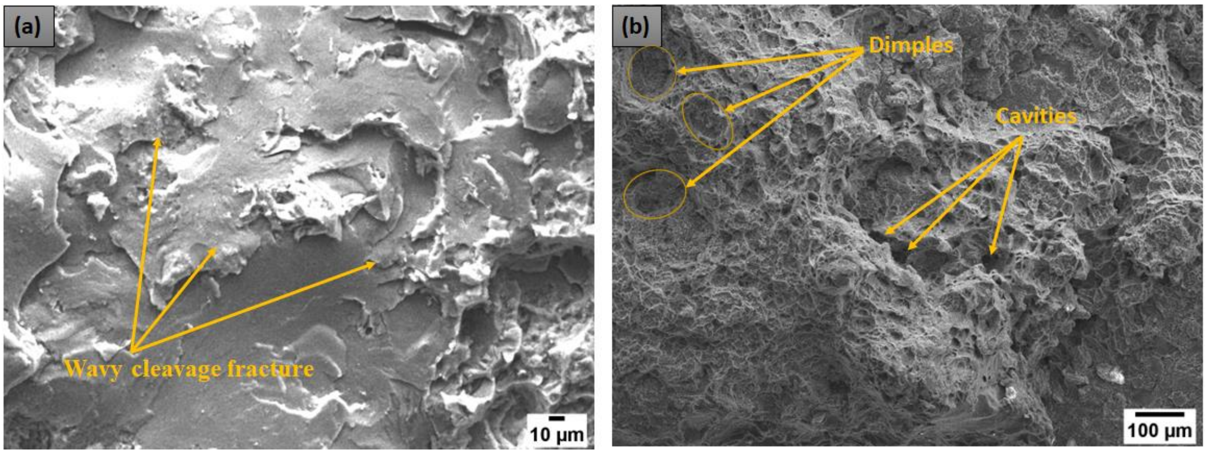

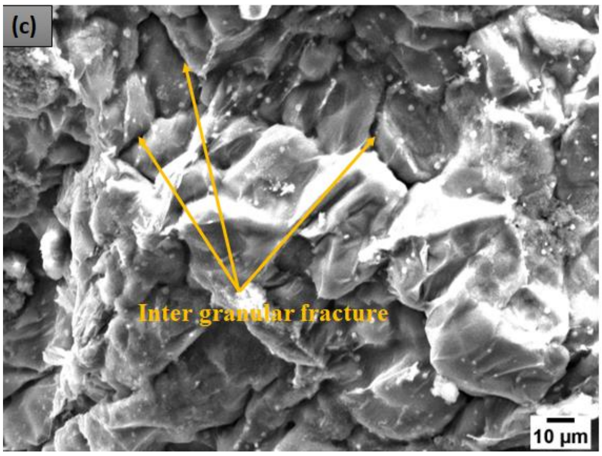

Fig. 4.8: SEM images of the fracture surface of a) unexposed sample, showing flat cleavage facet, b) creep tested specimen (80 MPa & 185 °C) at low magnification, showing ductile dimple, c) creep tested specimen at high magnification, showing intergranular fracture.

4.6 Creep parameters

In order to identify the governing creep mechanism, stress exponent (n) and activation energy (Q) have been calculated under different test conditions. The values of n and Q vary with the change in the operative creep mechanism. For n=1, the diffusional creep mechanism predominates, and it generally occurs at high temperatures and low stress. The creep mechanism changes to dislocation controlled as the n value increases to 3-8. The power-law breakdown mechanism is the rate-controlling mechanism in creep deformation, where the n value is greater than 8. Similarly, the Q value represents the activation energy of the rate-controlling physical process associated with the creep deformation.

The temperature dependency of minimum creep rate for squeeze cast AZ91 Mg alloy under different stress is shown in the Arrhenius type plot, **Fig. 4.9.** The activation energy (Q) at different stress levels is calculated from the slope of the fitted straight line at different stress levels as shown in **Fig. 4.9**. The estimated activation energies at different stress levels are listed in **Table 4.2**. The activation energy for grain boundary sliding in Mg alloys is reported to be between 30-45 kJ/mol (Q value for β-phase) [118]. On the other hand, the Q values are 80 kJ /mol and 135 kJ/mol for grain boundary diffusion and self-diffusion, respectively. Further, the activation energy increases to 143 kJ/mol if the diffusion of Aluminum atoms becomes the rate-controlling step [118]. In the present study, the activation energy values for AZ91 Mg alloy at 50 MPa of stress is estimated to be 117 kJ/mol, which are close to the self-diffusion activation energy values for Magnesium lattice, i.e., 135 kJ/mol. The estimated activation energy increases to 180 kJ/mol at 65 MPa stress. However, activation energy decreases to 92 kJ/mol at 80 MPa stress. The observed reduction in activation energy with an increase in stress value is in line with an earlier work by Spigarelli et al. for AZ91 Mg alloy [118].

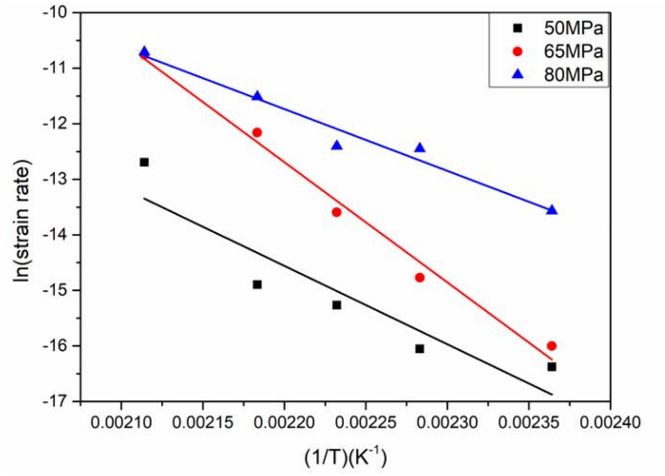

Fig. 4.9: Relationships between creep rate and inverse of temperature for AZ91.

Table 4.2. Activation energy values for different stresses.

Stress (MPa)	Slope	Activation energy (kJ/mol)
50	14107±3277	117±27
65	21650±1406	180±11
80	11123±1161	92±9

Stress dependence of the minimum steady-state creep rate for the same alloy is represented in a log-log plot in **Fig. 4.10**. The stress exponent (n) of creep is obtained from the slope of fitted straight lines as shown in **Fig. 4.10**, and their respective values are listed in **Table 4.3**. The stress exponent (n) values are 7.21 & 5.90 for both the test temperatures of 150 °C and 175 °C, respectively. Therefore, the dislocation-based 5 power law creep mechanism is expected to be the governing mechanism in the temperature range of 150 °C and 175 °C.

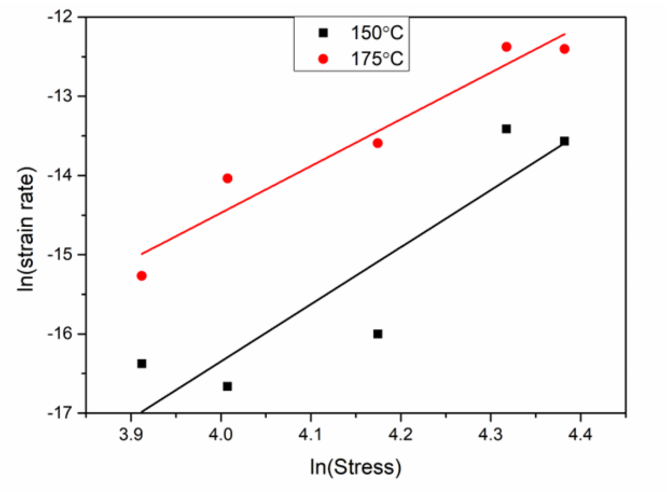

Fig. 4.10: Relationships between creep rate and applied stress for AZ91.

Table 4.3. Creep Stress Exponent values for different temperatures.

Temperature (°C)	Stress exponent (n)
150	7.21±1.91
175	5.90±0.83

The estimated creep parameters in the present study can be compared with those in the other studies in the literature in **Table 2.2**. It has been widely accepted that the activation energy in creep corresponds to self-diffusion in power-law creep, where the creep mechanism is dislocation creep and dislocation climb is controlled by lattice diffusion at 50 MPa stress [119, 19]. The activation energy at 65 MPa stress is 180 kJ/mol, much larger than the activation energy corresponding to self-diffusion. At 80 MPa stress, it is 92 kJ/mol, close to the activation energy for grain boundary diffusion. On the other hand, the obtained stress exponent value n suggests the governing creep mechanism is dislocation climb controlled. However, the grain boundary diffusion cannot generally be the rate-controlling mechanism in dislocation climb controlled creep. A further study is required to confirm this aspect.

4.7 Role of microstructural stability

Microstructural stability is another crucial aspect that can influence the overall creep behavior. Microstructural analysis dictates that the area fraction of β-$Mg_{17}Al_{12}$ precipitates reduces with an increase in testing temperature. Further, the reduction in β-$Mg_{17}Al_{12}$

precipitates results in an increment in the interparticle distance. Dissolution of the thermally unstable β-$Mg_{17}Al_{12}$ phase can be quantified by employing thermodynamic analysis. The variation in the equilibrium wt. fraction of the β-$Mg_{17}Al_{12}$ phase with temperature as predicted using the Thermo-Calc® database is presented in **Fig. 4.11**. The wt. fraction of the thermally unstable β-Mg17Al12 phase is expected to decrease with an increase in equilibrium temperature and finally dissolve completely in the primary α-Mg phase at 300 ° C. An increase in equilibrium temperature from 150 °C to 200 °C results in a 2.1 wt % reduction of the β-$Mg_{17}Al_{12}$ phase. The dissolution of the hard and brittle β-$Mg_{17}Al_{12}$ phase contributes to the softening of the microstructure by reducing the hindrance to the dislocation motion. Some other studies [111, 117] have also reported similar observations in AZ91 alloy.

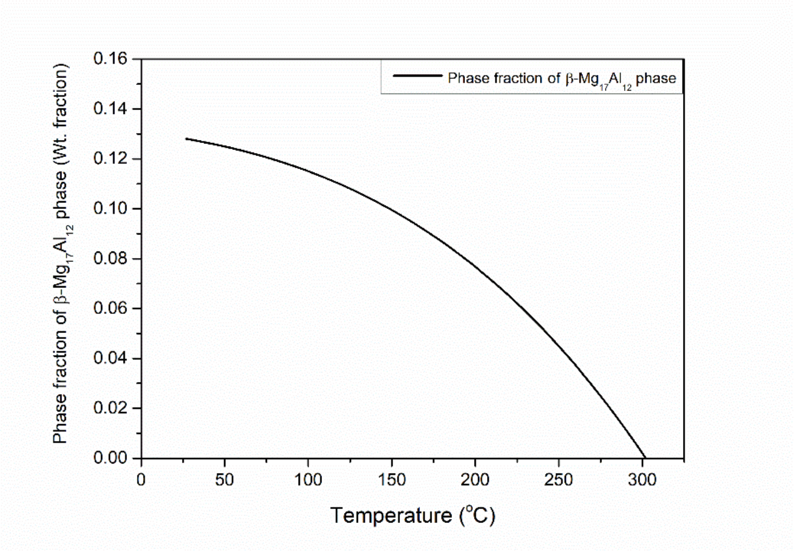

Fig. 4.11: Variation in equilibrium phase fraction of β-$Mg_{17}Al_{12}$ with temperature.

4.8 Effect of creep on the evolution of dislocations

The evolution of dislocation density during the creep deformation has been investigated following the modified Williamson-Hall method [85], [132] using the X-ray diffraction technique. The crept samples tested under 55 MPa to 80 MPa stress at 150 °C are considered for this study. The samples were prepared carefully from a region far from the fracture surface but within the gauge length section so that the microstructural changes associated with tertiary creep do not reflect in the result. The obtained XRD patterns from the different testing conditions are shown in **Fig. 4.12**.

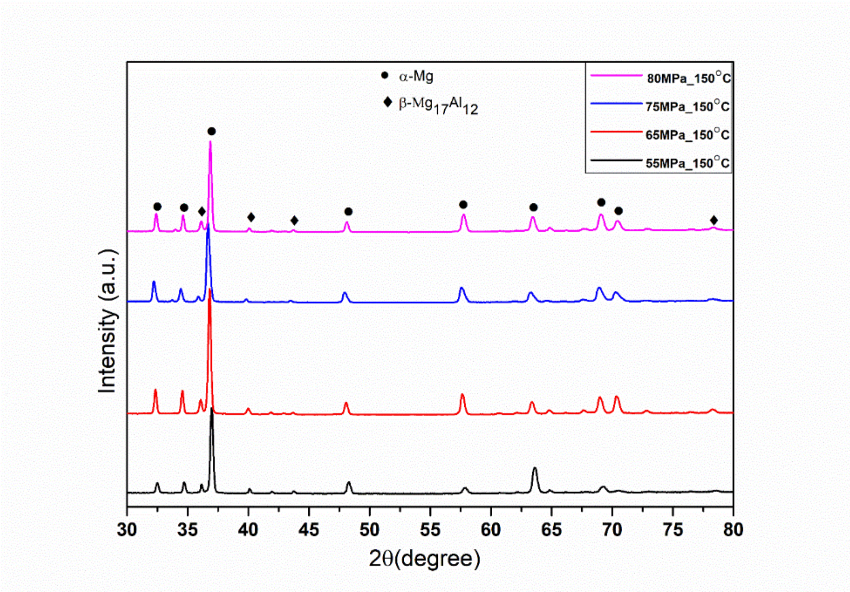

Fig. 4.12: X-ray diffraction patterns for crept samples tested at 150 °C & 55, 65, 75, and 80 MPa.

Full-width half maxima (FWHM), which represents the broadening of the peak (β) has been measured for all the peaks belonging to the α-Mg phase. Williamson-Hall method [120, 122, 123] relates the peak broadening (β) with the microstrain (Ɛ) and crystallite size (Dv) using the following relation:

$$\frac{\beta Cos\theta}{\lambda} = \frac{1}{D} + 2\mathcal{E}(\frac{2Sin\theta}{\lambda}) \tag{4.1}$$

where θ is the angle between the incident beam and sample, and λ is the wavelength (0.154 nm for CuKα). Microstrain (Ɛ) of the investigated specimen can be obtained from the slope of the straight-line fitted for (βCosθ) vs. (4Sinθ) plot as shown in **Fig. 4.13**.

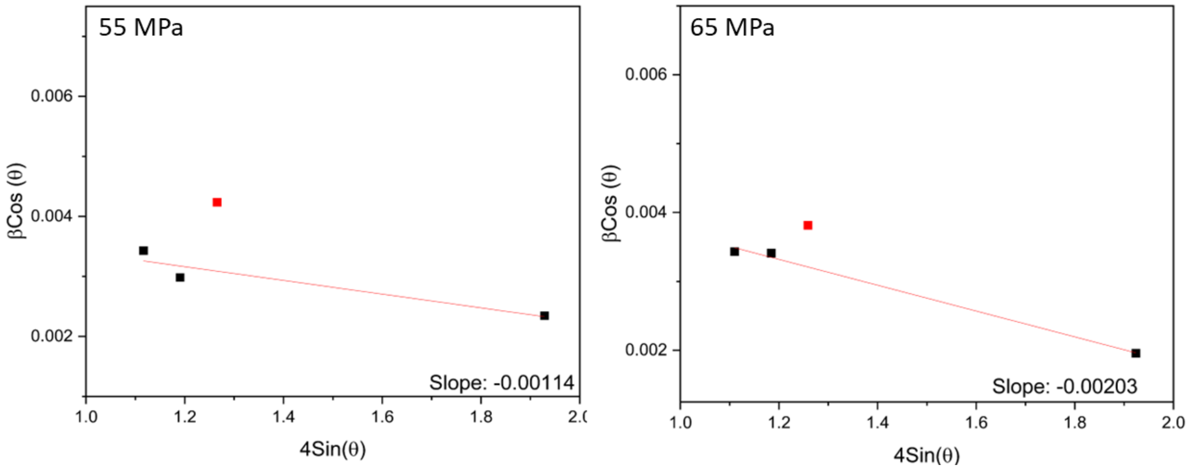

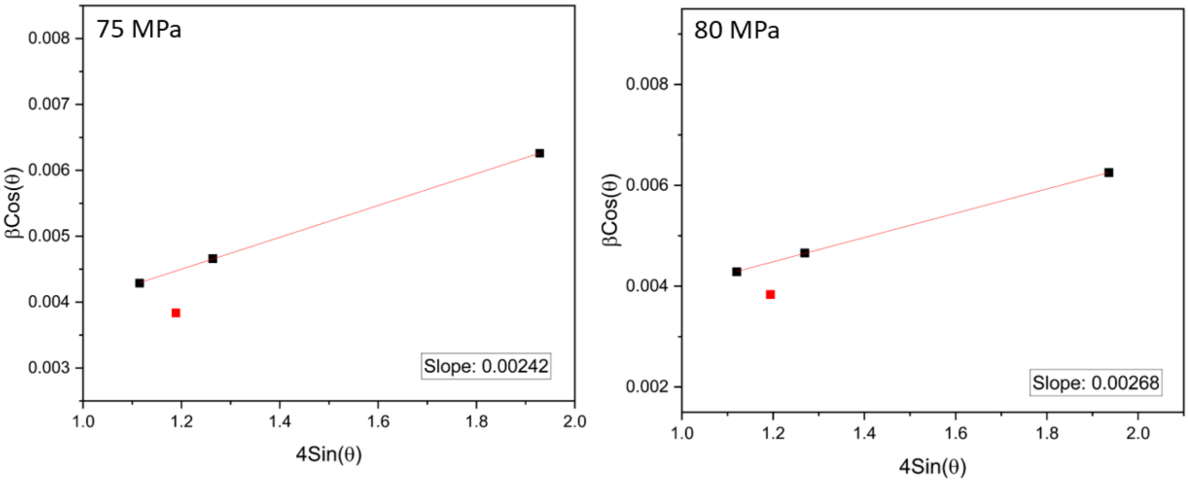

Fig. 4.13: Williamson-Hall plot for crept samples at 150 °C& (a) 55 MPa, (b) 65 MPa, (c) 75 MPa, &(d) 80 MPa.

Dislocation density (ρ) has been calculated from measured microstrain (Ɛ) and crystallite size (Dv) following the Williamson and Smallman approach given below:

$$\rho = \frac{2\sqrt{3}\varepsilon}{Dvb^2} \tag{4.2}$$

where b is the magnitude of the Burgers vector of the basal slip system. The value of b is 3.2 A° for Mg alloys [120]. Measured dislocation densities of investigated samples tested under different stresses at 150 °C are shown in **Fig. 4.14**.

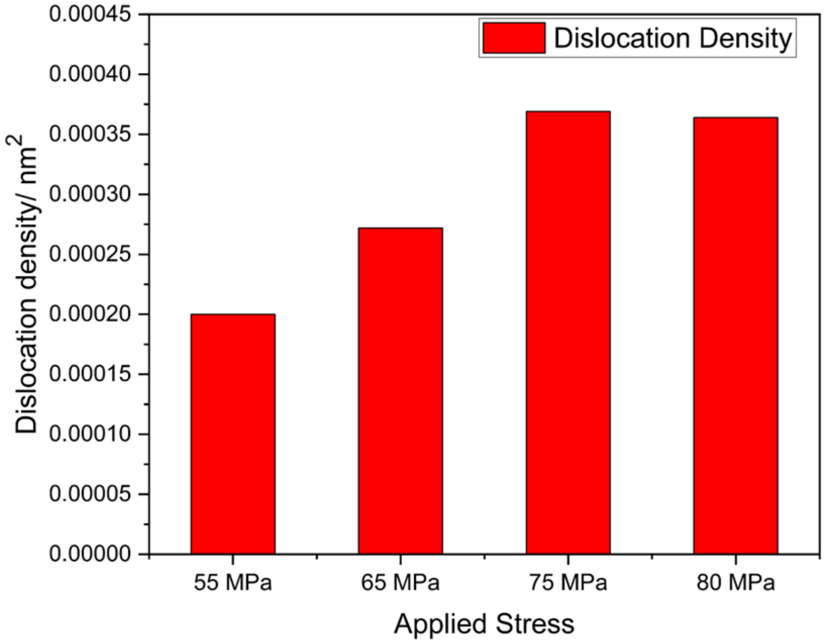

Fig. 4.14: Dislocation densities of AZ91 Mg alloy for crept samples at 150 °C at different stresses.

Dislocation density is found to increase by a factor of 1.85 with an increase in stress from 55 MPa to 80 MPa. In power law creep, the dislocation density is expected to be proportional to the square of the applied stress. Dislocation density is expected to increase by a factor of 2.11 (i.e. square of (80/55)) for stress increment from 55 MPa to 80 MPa. In the present investigation, the measured dislocation density values show good agreement with the expected dislocation density in the power law creep mechanism.

4.9 Threshold stress determination in the creep of AZ91 alloy

In the present work, an attempt has been made to estimate the threshold stress of squeeze-cast AZ91 alloy. The creep strain is expected to be negligible below the threshold stress at a given exposed temperature. It defines the safe usage limit of an alloy under certain temperatures. A simplified relation of steady-state strain rate and threshold stress in power-law creep can be given as follows [118]:

$$\dot{\varepsilon} = K(\sigma - \sigma_0)^{n'} \tag{4.3}$$

where K is a constant, $\dot{\varepsilon}$ is minimum steady-state strain rate, stress, n' is the stress exponent, and σ_o is the threshold stress. The threshold stress (σ_0) is determined by plotting $\varepsilon^{\cdot(1/n')}$ against σ. The σ_0 depends on the choice of stress exponent (n') value [136], [137]. In the present case, the n' equals to 5 is chosen since the underlying creep mechanism was found to be dislocation-controlled. The plot between σ vs $\varepsilon^{\cdot\,(1/5)}$ gives the linear fit to the data, as shown in **Fig. 16**. Threshold stress has been estimated by extrapolating the fitted straight line to the zero-strain rate in σ vs $\varepsilon^{\cdot\,(1/5)}$ plot, and values are listed in **Table 4.4**. The reduced threshold stress with increased temperature may be due to the easier dislocation motion and enhanced diffusivity at higher temperatures [111, 118].

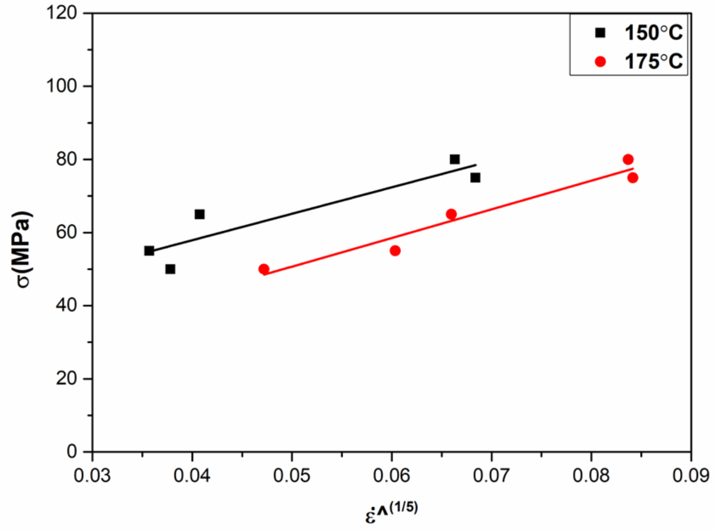

Fig. 4.15: σ vs. $\dot{\varepsilon}^{(1/5)}$ extrapolating curve

Table 4.4. Threshold values of stresses for two working temperatures.

Temperature (°C)	σ_o (Threshold Stress)
150	28 MPa
175	11 MPa

4.10 Conclusion

In the present work, squeeze cast AZ91 alloy was subjected to tensile creep tests at varying temperatures in the range of 150 °C to 200 °C and stresses in the range of 50 MPa to 80 MPa. The major conclusions from this work are summarized below:

1. The microstructure of squeezed cast AZ91 alloy consists of the primary α-Mg phase and massive continuous β-$Mg_{17}Al_{12}$ phase, distributed uniformly all over the microstructure.

2. In the present work, creep is found to follow power law behavior with stress exponent n of 7.21 for 150 C and 5.9 for 175 C. The activation energy for creep under 50 MPa stress is estimated to be around 117 kJ/mol, which is close to the self-diffusion of Mg. Overall, the governing creep mechanism is found to be dislocation creep at 50 MPa stress at 150 °C to 175 °C, and dislocation climb is governed by lattice diffusion.

3. The contribution of β- $Mg_{17}Al_{12}$ phase in providing creep resistance reduces significantly with temperature due to its dissolution from 150 °C to 200 °C.

4. Fractographic study reveals that the creep fracture initiates in the form of the intergranular cavity at the interface of α-Mg matrix and β-$Mg_{17}Al_{12}$ precipitate, followed by growth and coalescence of the cavities. The mode of fracture for the crept samples is "intergranular then ductile."

Chapter 5

Study on the Investigation of Creep Behaviour in Squeeze Cast Ca-Modified AZ91 Magnesium Alloy

In Chapter 4, it is shown that dislocation climb, governed by lattice diffusion, is a governing creep mechanism affecting the deformation of the AZ91 base alloy. Enhanced creep resistance may be achievable by incorporating a thermally stable intermetallic into the microstructure to inhibit dislocation movement. Additionally, the literature suggests that adding alloying elements to the base alloy can improve both mechanical and creep performance. Consequently, Chapter 5 focuses on examining the effect of low-cost calcium (Ca) additions on the microstructure evolution and tensile creep properties of squeeze-cast AZ91 alloy. Furthermore, the post-creep microstructure of the AZ91+Ca (AZX911) alloy is investigated and compared to that of the base AZ91 alloy. The thermostability of precipitated phases in the AZX911 alloy is also analyzed using thermodynamic analysis. Finally, an effort is made to identify the governing creep mechanism in the AZX911 alloy during creep deformation, comparing it to the mechanism identified for the base AZ91 alloy (Chapter 4) under similar stress and temperature conditions.

Chapter 5

Study on the Investigation of Creep Behaviour in Squeeze Cast Ca-Modified AZ91 Magnesium Alloy

The work in this chapter has been published as: Hitesh Patil, Ankush Marodkar, Abhijit Ghosh, and Hemant Borkar, “Study on the investigation of creep behaviour in squeeze cast Ca-modified AZ91 Magnesium alloy”, *Philosophical Magazine*.

5.1. Introduction

AZ91 alloy is the most widely used Mg alloy in the automotive industry. However, the poor creep resistance limits its powertrain applications. The poor creep performance of the AZ91 alloy is attributed to the thermally unstable β-$Mg_{17}Al_{12}$ phase, which starts dissolving above the temperature of 120°-125 °C [10]. One of the approaches could be the addition of suitable alloying elements, which results in the precipitation of thermally stable intermetallic phases at the grain boundaries, which may hinder the dislocation motion and grain boundary migration at elevated temperatures. The decrease in the phase fraction of the thermally unstable β-$Mg_{17}Al_{12}$ phase is also reported after incorporating these elements into the AZ91 system [67]. All these factors are expected to enhance the creep performance of the alloy.

In this chapter, Ca (alkaline earth metal) has been selected as a suitable additive to the AZ91 alloy because of its low cost and easy availability. However, die-casting of the AZ91 alloy containing Ca is prone to hot cracking and die sticking. The small casting cracks resulting from stress concentration during solidification shrinkage are also observed post-Ca addition [25], [26]. Therefore, the squeeze casting technique (discussed in **section 2.3.3**) has been utilized instead of die casting, which may overcome the problems associated with the fabrication of Ca-containing AZ91 alloy via die-casting. To the best of the author’s knowledge, tensile creep behavior has not been studied in detail in Ca-added AZX911 alloy after squeeze casting. Moreover, there is a disagreement that persists in existing literature regarding the governing creep mechanism in Ca-added Mg-Al alloy fabricated via different routes, as listed in **Table 2.3**. Therefore, a detailed study on the creep behavior of Ca-added squeeze cast AZX911 alloy and correlating the creep mechanism with microstructure is necessary to establish its applicability at elevated temperatures.

The present study is aimed at investigating the effect of 1% Ca addition on the creep behavior and operating creep mechanisms in squeeze-casted AZ91+Ca alloy under tensile loading. Simultaneously, the underlying creep mechanism of AZX911 alloy has been compared with the AZ91 alloy investigated previously. An attempt has also been made to understand the relative stability of different precipitates evolved in the investigated alloy.

5.2 Chemical composition of the investigated alloys

The chemical composition of the squeeze-cast *AZ91* and *AZ91+Ca* alloy estimated using an optical emission spectrometer in the present work is listed in **Table 5.1**.

Table 5.1. Chemical composition of squeeze-cast alloys (Weight%).

Alloy	Chemical Composition (wt%)					
	Al	Zn	Mn	Si	Ca	Mg
AZ91	9.01±0.142	1.57±0.002	0.17±0.002	0.022±0.011	-	Bal.
AZX911 **(AZ91+1%Ca)**	8.86±0.146	0.83±0.002	0.17±0.002	0.018±0.009	1.18±0.004	Bal.

5.3 Microstructure characterization of investigated alloys

5.3.1. As-Cast Microstructure

The scanning electron micrographs (SEM) of the as-cast a) AZ91 alloy and b) AZX911 Mg alloy are shown in **Fig. 5.1.** The microstructure of AZ91 alloy **(Fig. 5.1a)** is comprised of a primary α-Mg (Mg-Al solid solution) matrix phase and a secondary massive β-$Mg_{17}Al_{12}$ phase, having an irregular morphology, dispersed in the α-Mg matrix [10]. The Ca addition in the AZ91 alloy i.e., AZX911 alloy, promotes the precipitation of the thermally stable Al_2Ca (C-15 laves, AB2) phase along with the β-$Mg_{17}Al_{12}$ phase **(Fig. 5.1b)** [9]. The Al_2Ca phase appears in the microstructure with skeleton morphology and is expected to cause microstructure refinement [3], [67]. The elemental distribution in different phases has been analyzed using energy dispersive spectroscopy, which is shown in **Fig. 5.1c**. Further, XRD analysis confirms the precipitation of the thermally stable Al_2Ca laves phase in the AZX911 alloy, **Fig. 5.1d**. The intensity of the β-phase (peak (4 1 1), $2\theta=36°$) in the XRD graph (**Fig. 5.1d**) is found to decrease after the addition of Ca. Similarly, thermodynamic analysis using Thermocalc$^{®}$, as shown in **Fig. 5.2a,** predicts a reduction in the mole% of the β-phase from 19.5% to 16 % at room temperature after Ca addition. In the same way, almost equal observation regarding the volume fraction of the intermetallic phases in the α-Mg matrix has been made using Image J software. It indicates almost 13±2% of the intermetallic phases comprised 10.7±1% of β-$Mg_{17}Al_{12}$ and the remaining 2.3±0.6% of the Al_2Ca phase in AZ91+1%Ca alloy. The variation of mol % of different phases evolved in AZX911 alloy with equilibrium temperature is shown in **Fig. 5.2b**. As per the thermodynamic prediction carried out through thermodynamic calculations resulting from the computational thermodynamic software Thermo-Calc® TCMG6 database, the C15 laves phase, along with the α-Mg and β-Mg17Al12 phases, are expected in the microstructure at room temperature. The composition and quantity of different phases in the AZX911 alloy, as estimated by thermodynamic calculation, are listed in **Table 5.2**. In the C15-laves phase, the mole % of the Al at room temperature is almost double that of Ca, which helps to read this composition as the Al_2Ca phase. Also, with the increase in equilibrium temperature from R.T. to working temperature (250 °C), the quantity (mol%) of the β-$Mg_{17}Al_{12}$ phase is reduced by 52%, whereas it is only a 9% reduction in the case of the Al_2Ca phase. This implies that the Al-Ca phase is more thermally stable compared to the β-$Mg_{17}Al_{12}$ phase. Further, DSC analysis was carried out to confirm the dissolution temperatures of these phases, as shown in **Fig. 5.2c.** The dissolution temperature associated with the Al_2Ca phase (515 °C) is observed to be higher than the β-$Mg_{17}Al_{12}$ phase (435 °C). The DSC analysis was carried out using a differential scanning calorimetry (DSC) instrument (model no. STA8000 by Perkin Elmer) in a purified argon atmosphere.

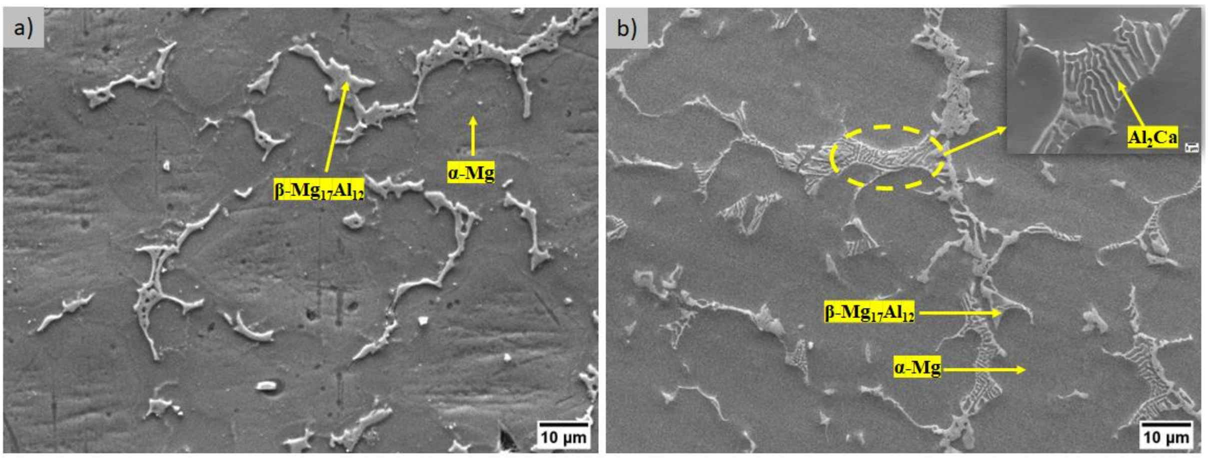

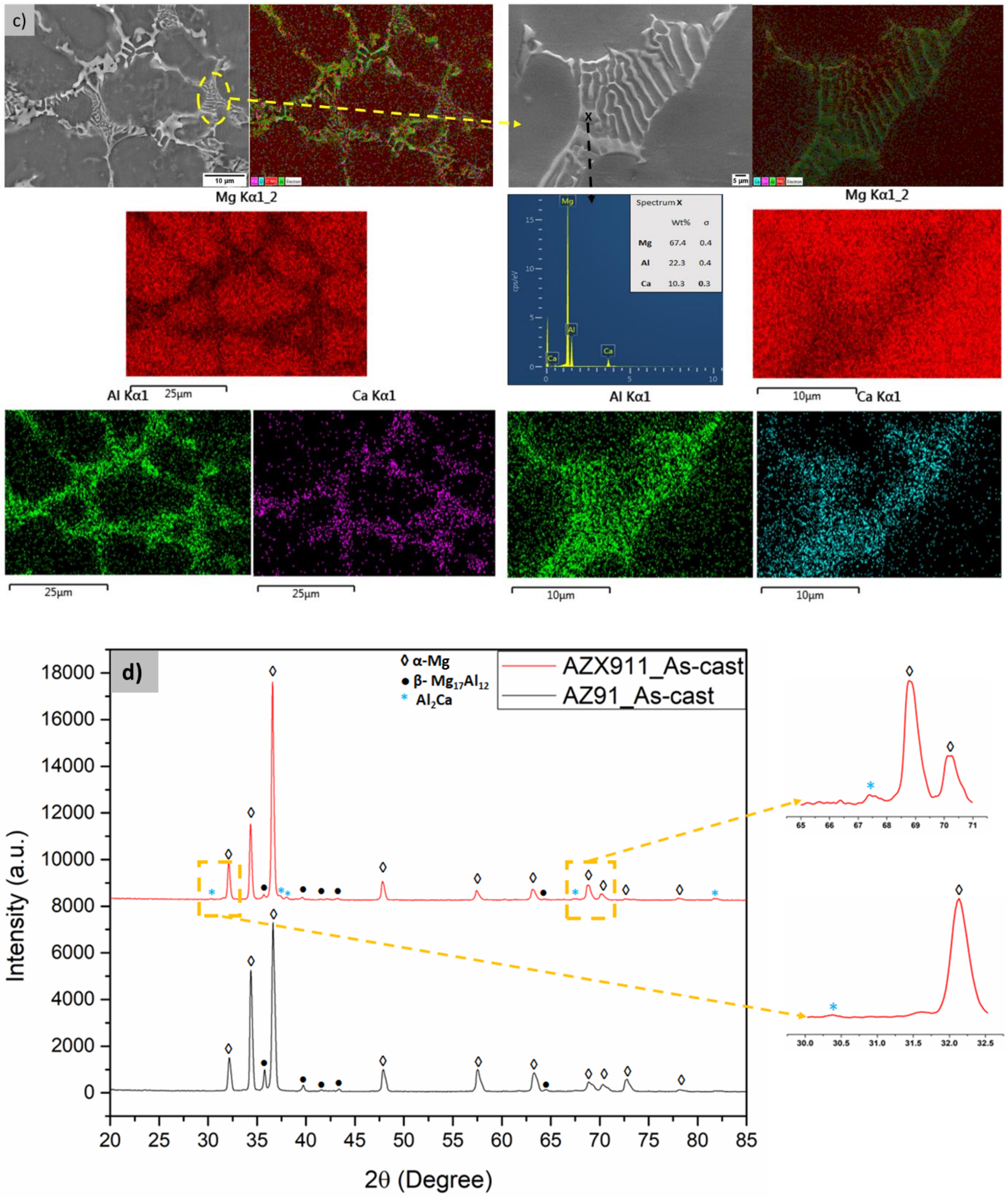

Fig. 5.1: SEM Micrographs of as-cast a) AZ91, b) AZX911 Mg alloy with c) elemental mapping and EDS analysis, and d) x-ray diffraction pattern of as-cast AZ91 & AZX911 Mg alloy.

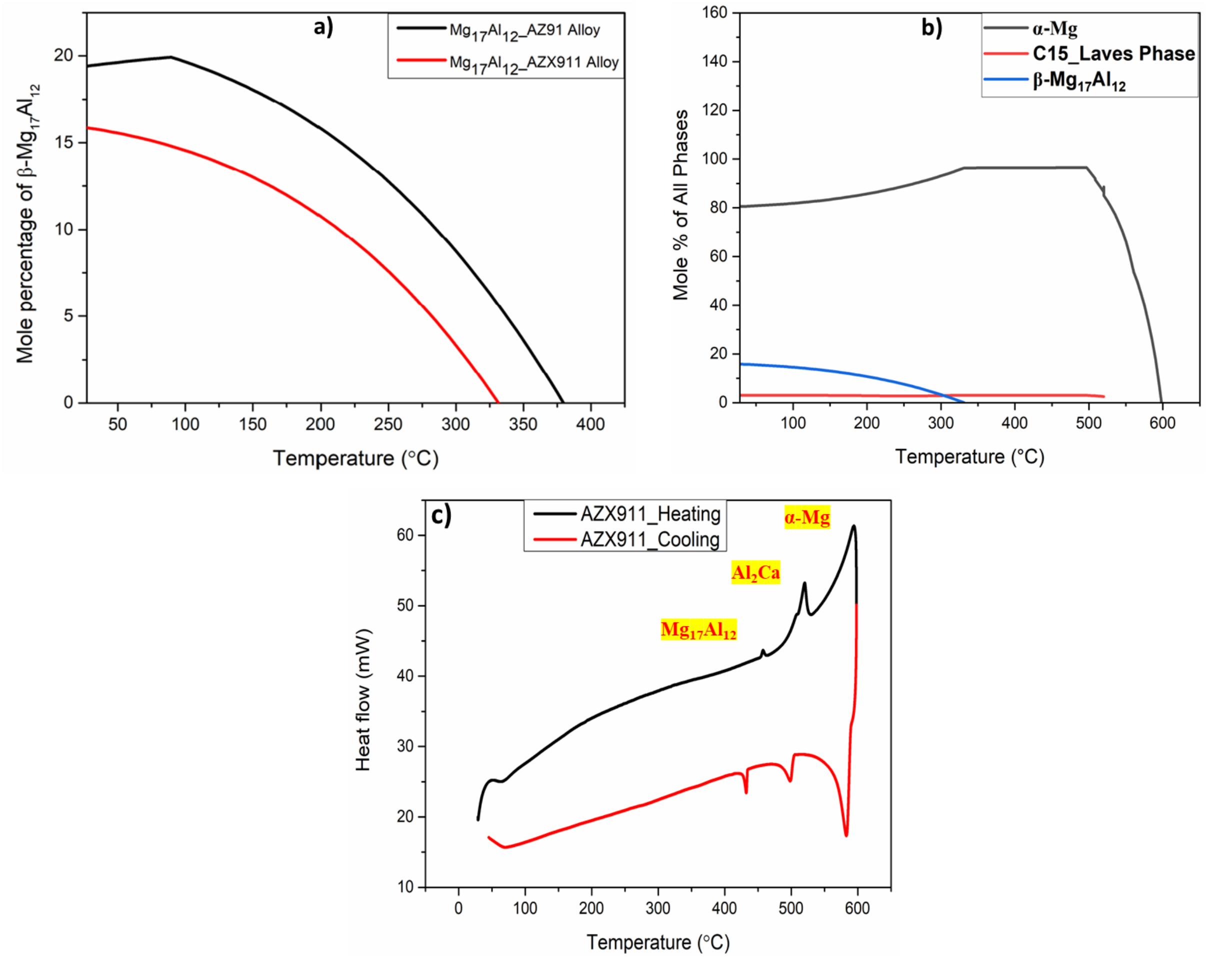

Fig. 5.2: The variation in equilibrium mole% of a) β-$Mg_{17}Al_{12}$ and b) all the possible phases in AZX911 Mg alloy with temperature. c) DSC curve (at 5 °C/min heating rate) of AZX911 Mg alloy.

Table 5.2: The composition and amount of the phases present in the microstructure of AZX911 Mg alloy.

Phases present at R.T.	Composition (mole %) of the phases at R.T.						Mole% of the phase at R.T.	Mole% of the phase at 250°C
	Al	Ca	Mg	Mn	Zn	Si		
C15-laves phase	55.5	33.3	2.03E-6	6.67E-11	11.2	1E-10	3.07	2.78
β-$Mg_{17}Al_{12}$	41.4	9.1E-3	58.6	-	9E-4	-	15.9	7.58

α-Mg	0.299	1E-10	99.7	1E-10	0.239 E-4	1E-10	80.5	88.9

5.3.2. Heat-treated Microstructure

In order to confirm that the Al_2Ca phase has higher thermal stability compared to the β-$Mg_{17}Al_{12}$ phase, both AZ91 and AZX911 alloys are subjected to heat treatment at 450 °C for 24 hours, followed by water quenching. The SEM micrographs of heat-treated AZ91 and AZX911 alloy specimens are shown in **Fig. 5.3**. There was no trace of the β-$Mg_{17}Al_{12}$ phase in the microstructure of the heat-treated AZ91 alloy, **Fig. 5.3a**. However, in the heat-treated AZX911 alloy, a second phase is found to be present in the microstructure, **Fig. 5.3b**. EDS analysis, as shown in **Fig. 5.3c**, confirms that the second phase that appeared in heat-treated AZX911 is Al_2Ca. The dissolution of the β-$Mg_{17}Al_{12}$ phase after the heat treatment in both alloys is further confirmed by XRD analysis, as shown in **Fig. 5.4**. Moreover, the experimental results obtained are in good agreement with the thermodynamic prediction, as shown in **Fig. 5.2b**. The β-$Mg_{17}Al_{12}$ phase was predicted to be dissolved completely at 331 °C (< 450 °C), while the Al_2Ca phase was expected to be stable up to 521 °C. Therefore, it is confirmed that the Al_2Ca phase has higher thermal stability compared to the β-$Mg_{17}Al_{12}$ phase.

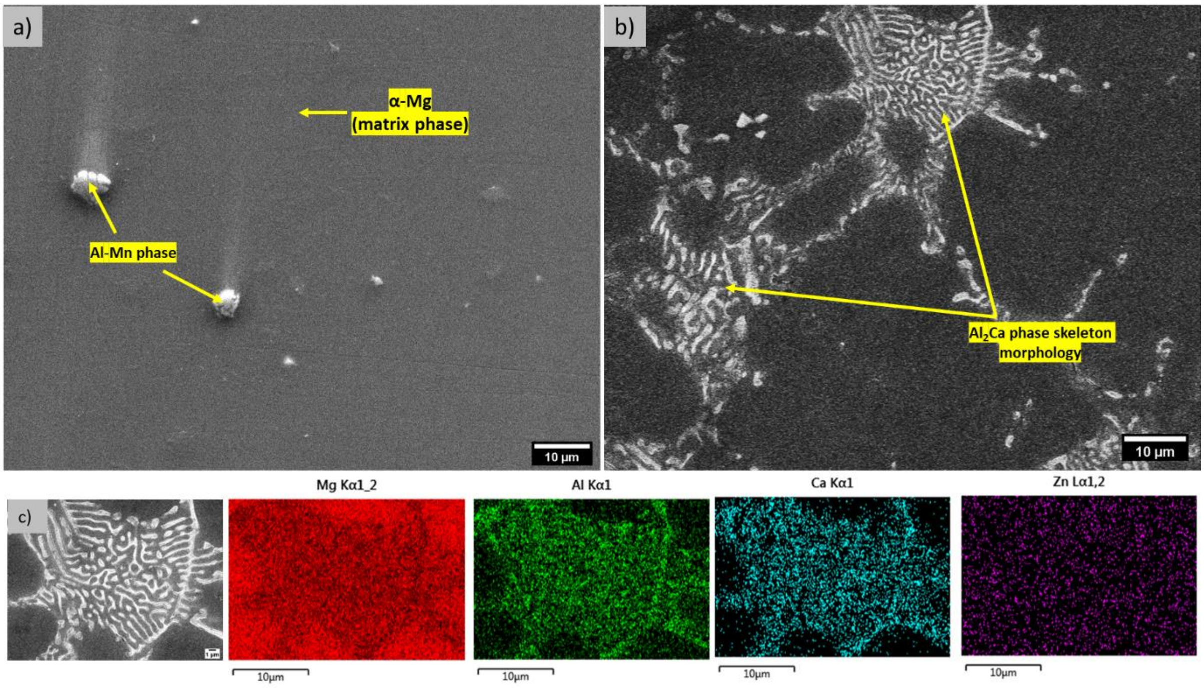

Fig. 5.3: SEM micrograph showing the heat-treated a) AZ91 and b) AZX911 Mg alloy with c) elemental mapping of a magnified image of heat-treated AZX911 Mg alloy.

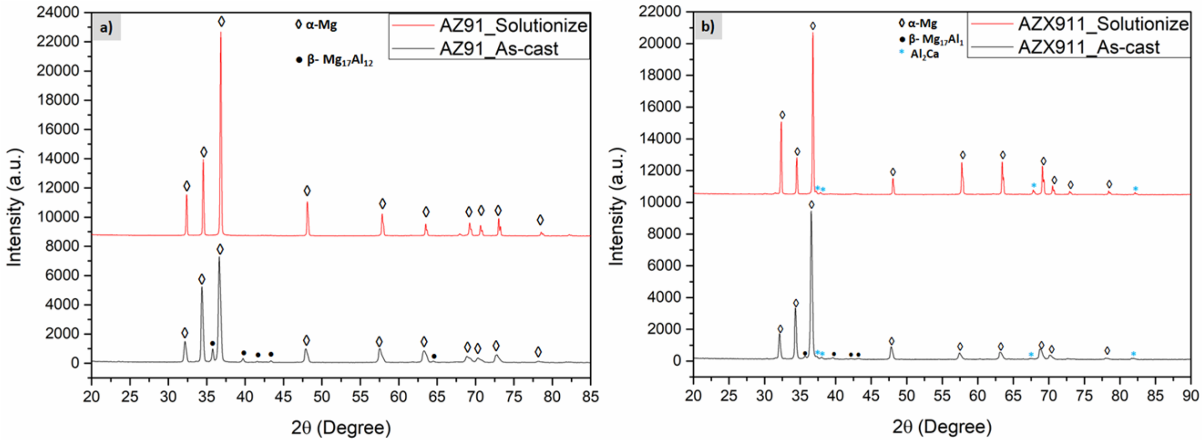

Fig. 5.4: X-ray diffraction pattern of heat-treated a) AZ91 and b) AZX911 Mg alloy.

5.4. Creep Properties

In the present study, tensile creep tests have been carried out in AZX911 alloy at a temperature range of 150 °C to 250 °C under 65 and 80 MPa stresses. Additionally, to compare the creep performance of the presently investigated AZX911 alloy with the base AZ91 alloy, some initial tensile creep test results of both alloys, which were previously reported by the author of the present work [4], [10], have been considered in this study. The characteristic tensile creep curves of both alloys are depicted in **Fig. 5.5.** All the creep curves exhibit three stages: primary, secondary, followed by tertiary. The minimum creep rate was estimated at varied testing conditions from the bucket-type curve plotted between the strain rate (s^{-1}) and time (t), as shown in **Fig. 5.6**. As expected, in all the cases, the strain rate is found to increase with the increase in applied load and temperature. The comparison of the minimum creep rate between AZ91 and AZX911 alloys shows that the minimum creep rate is reduced by approximately one order of magnitude at 50 MPa_150 °C and 80 MPa_200 °C testing conditions in AZX911 alloys, as mentioned in **Table 5.3**.

The decrease in creep rate after the addition of Ca in the AZ91 alloy may be attributed to the formation of a thermally stable intermetallic Al_2Ca phase [4], [25]. The high-temperature stability and high elastic modulus associated with the Al_2Ca phase may effectively obstruct the dislocation motion during the deformation at elevated temperatures [13], [25], [138]. Some studies reported that the addition of alkaline earth elements, i.e., Ca, to the AZ91 alloy may not result in a considerable improvement in the creep performance beyond the working temperature of 200 °C [9]. However, in the present study, the AZX911 alloy shows a lower steady-state creep rate at 250 °C and 50 MPa stress than the AZ91 alloy tested at 200 °C temperature and 50 MPa stress, as shown in **Fig. 5.5d and 5.6d**. The resistance to creep deformation further improves at 150 °C and 50 MPa stress after the heat treatment at 450 °C when compared to the as-cast specimen of the same alloy, as shown in **Fig. 5.7,** and a similar observation has been reported in another Mg alloy [126]. Specifically, the heat treatment delays the onset of the tertiary stage of the creep deformation, thus improving the overall creep life of the alloy.

Table 5.3: Creep properties of alloys at 50 MPa stress and 150 °C temperature, and 80 MPa stress and 200 °C temperatures.

Alloy	Minimum Creep Rate (s^{-1})		Creep Strain %	
	50 MPa-150ºC	80 MPa-200ºC	50 MPa-150ºC	80 MPa-200ºC
AZ91[139]	7.73E-8	2.22E-5	3.96	3.16
AZX911	4.23E-9	6.97E-6	0.92	2.25

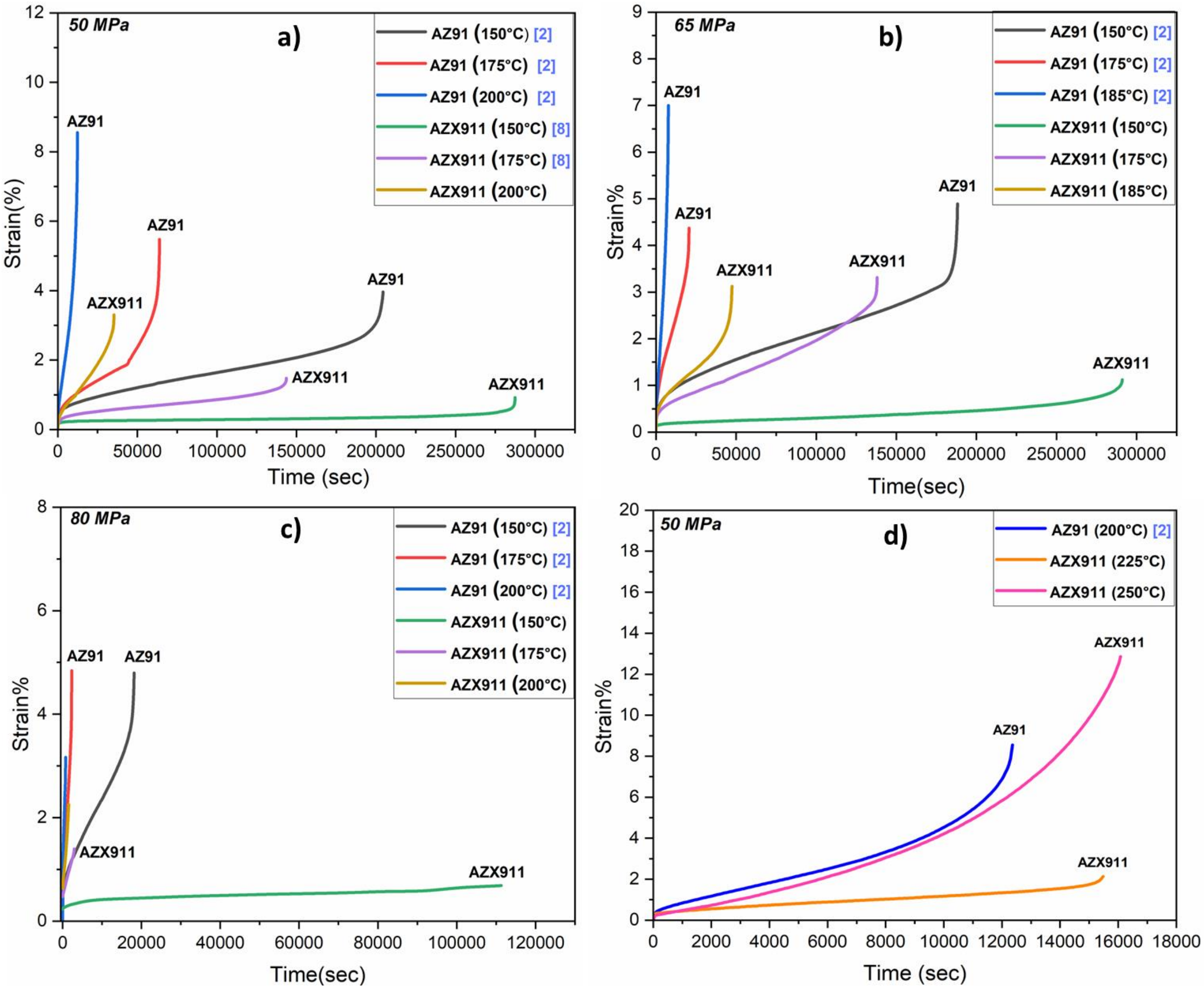

Fig. 5.5: Creep curves of AZ91 and AZX911 alloy at different creep temperatures (a-c at 150 °C -200 °C) under the applied stress of (a) 50 MPa, (b) 65 MPa, (c) 80 MPa, and (d) at 200 °C -250 °C at 50 MPa.

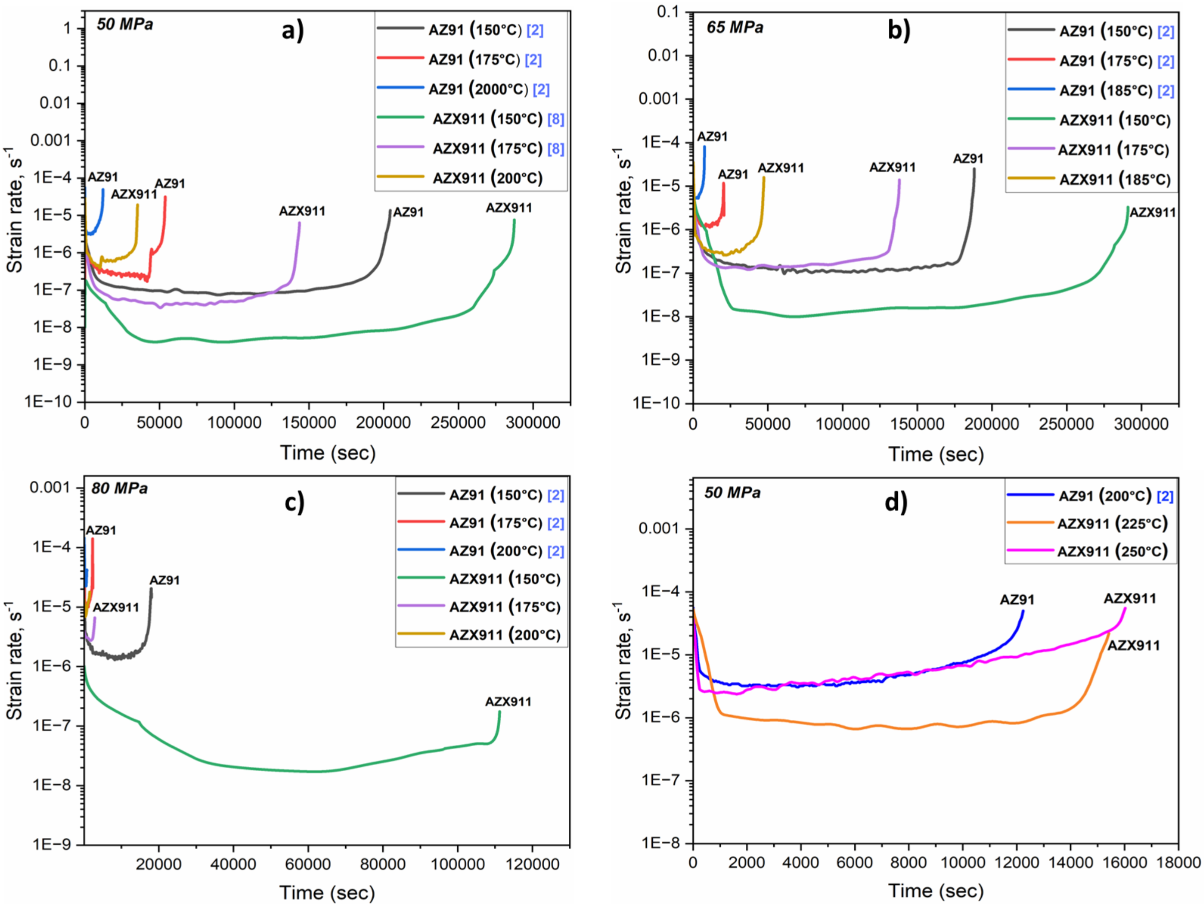

Fig. 5.6: Creep strain rate vs. time curves of AZ91 and AZX911 alloy using semi-log scheme at different temperatures (a-c at 150 ˚C -200 ˚C) under the applied stress of (a) 50 MPa, (b) 65 MPa, (c) 80 MPa, and (d) at 200 ˚C -250 ˚C at 50 MPa.

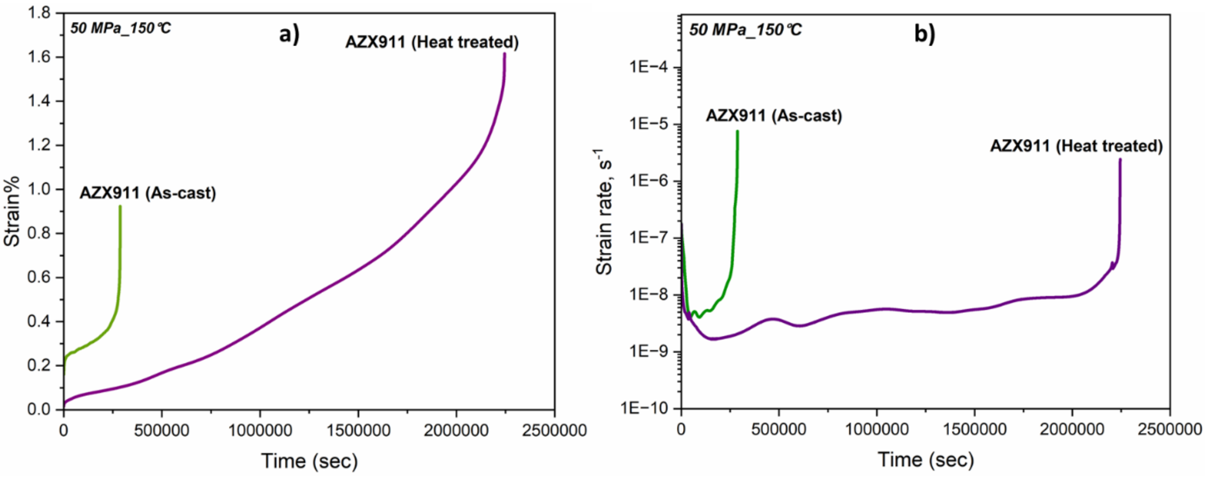

Fig. 5.7: a) The typical creep curve and b) The strain rate vs. time curve of the investigated as-cast and heat-treated AZX911 alloys at 50 MPa stress and 150 ˚C temperature.

5.5. Post-Creep Microstructure

Microstructure stability is the major factor determining the creep resistance of the alloy at elevated temperatures. In the case of AZ91 Mg alloy, the microstructure is reported to be thermally unstable at and above the temperature of 150°C, causing the β-$Mg_{17}Al_{12}$ phase to undergo partial dissolution in the matrix with increasing temperature [3], [10]. In the present investigation, the post-creep microstructures of the AZX911 alloy samples, which ruptured at two different creep testing conditions such as (a) at 200 °C temperatures under 80 MPa stress, and (b) at 250 °C temperature under 50 MPa stress, are shown in **Fig. 5.8**. The specimen for the examination is taken from the transverse section adjacent to the fracture surface of the alloys. The micrograph, as shown in **Fig. 5.8a and b,** suggests that the Al_2Ca phase in AZX911 alloy appears to be stable in the crept microstructure with increasing temperature. The morphology and volume fraction of the Al_2Ca phase are observed to be unaffected after creep deformation. The Al_2Ca phase in the AZX911 samples is found to be stable even up to a testing temperature of 250 °C under 50 MPa stress, as shown in **Fig. 5.8c**. In addition, further investigation illustrates that similar to the AZ91 alloy, the β-$Mg_{17}Al_{12}$ phase in AZX911 alloy is also found to be unstable. The dissolution of the preexisting β-$Mg_{17}Al_{12}$ phase in AZX911 alloy is indicated by yellow arrows in **Fig. 5.9a**. Further, EDS analysis confirms that the dissolution phase (sites 1 and 2 in **Fig. 5.9b**) belongs to the β-$Mg_{17}Al_{12}$ phase. However, some fraction of the β-$Mg_{17}Al_{12}$ phase remains undissolved in the crept microstructure (site 3 in **Fig. 5.9b**) along with the unaffected Al_2Ca phase (site 4 in **Fig. 5.9b**).

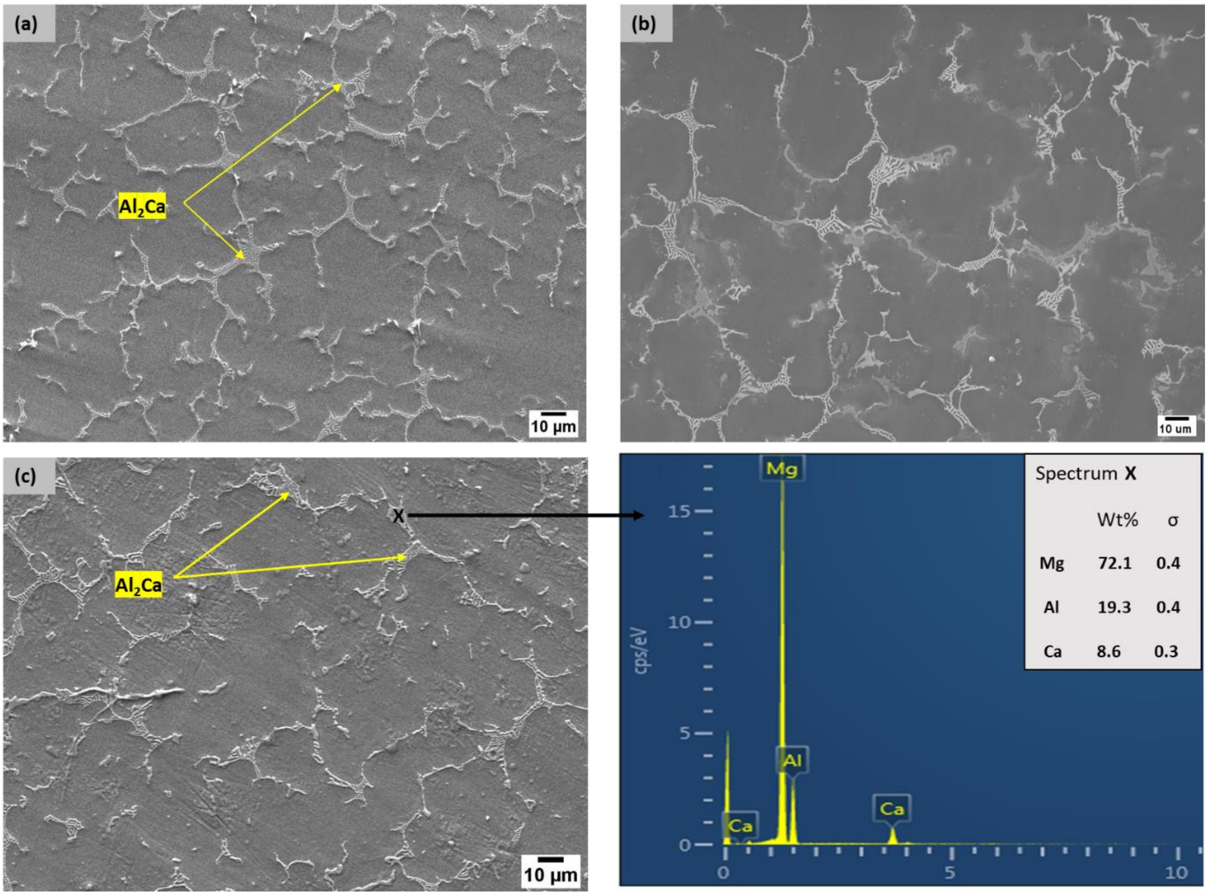

	Wt%	σ
Mg	72.1	0.4
Al	19.3	0.4
Ca	8.6	0.3

Fig. 5.8: SEM Micrograph of the a) as-cast AZX911 alloy, b) crept AZX911 alloy at 80 MPa_200 °C, and c) crept AZX911 alloy at 50 MPa_250 °C with EDS analysis.

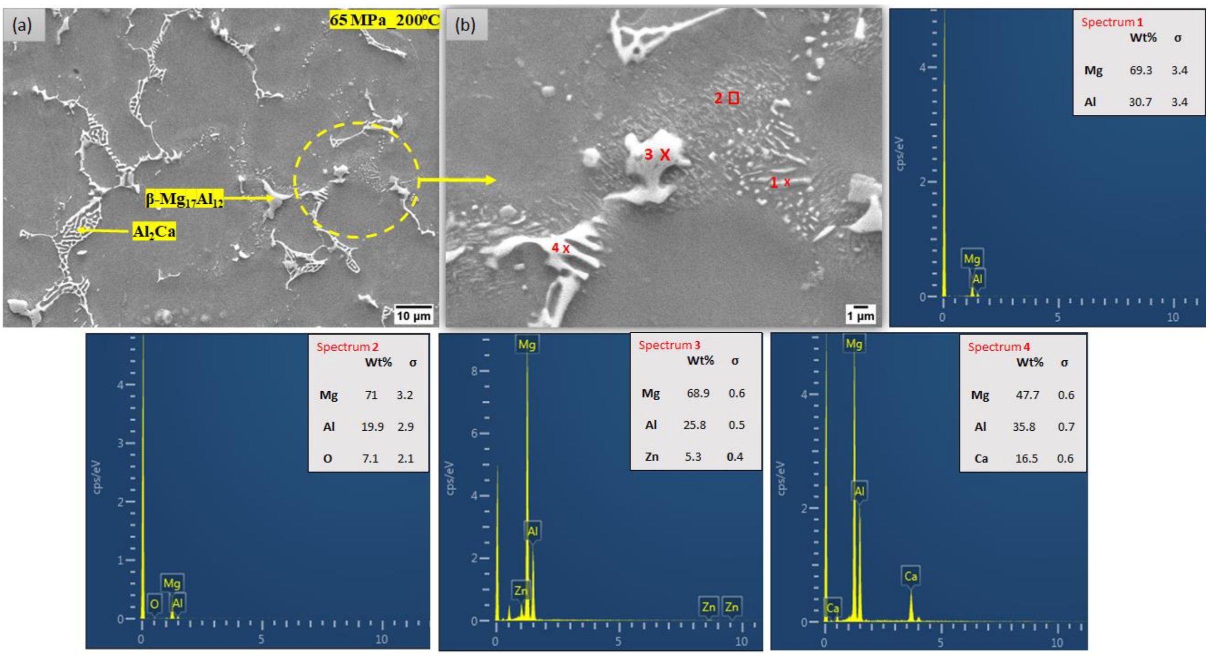

Spectrum 1

	Wt%	σ
Mg	69.3	3.4
Al	30.7	3.4

Spectrum 2

	Wt%	σ
Mg	71	3.2
Al	19.9	2.9
O	7.1	2.1

Spectrum 3

	Wt%	σ
Mg	68.9	0.6
Al	25.8	0.5
Zn	5.3	0.4

Spectrum 4

	Wt%	σ
Mg	47.7	0.6
Al	35.8	0.7
Ca	16.5	0.6

Fig. 5.9: a) SEM micrograph showing the dissolution of the β-$Mg_{17}Al_{12}$ phase during the creep deformation in AZX911 Mg alloy at 65 MPa_200 °C, and b) respective EDS analysis of a crept sample of AZX911 Mg alloy tested at 65 MPa_200 °C.

5.6 Creep Mechanism

To understand the governing creep mechanism, the steady state strain rates recorded during the creep tests under different conditions have been considered. The steady-state strain rate can be represented by the following power-law equation [79]:

$$\dot{\varepsilon} = A\sigma^n \exp\left(-\frac{Q}{RT}\right) \tag{5.1}$$

Where A is a material constant, R-gas constant, T- creep temperature, Q represents apparent activation energy related to the governing diffusion process during creep deformation, and n-stress exponent. The creep parameters, such as n and Q, indicate the governing creep mechanism [61], [137], [140].

Following Eq. **5.1**, the activation energy (Q) is obtained from the Arrhenius plot between log ($\dot{\varepsilon}$) vs. (1/T) at a specific stress, as shown in **Fig. 5.10a**. The estimated activation energy at 50 MPa and 65 MPa of stress is 187 kJ/mol and 177 kJ/mol, respectively, as shown in **Table 5.4**. The estimated values are much higher than the Mg self-diffusion (135 kJ/mol) activation energy. However, the activation energy of AZX911 alloy is very close to the reported activation energy of AZ91 alloy at 65 MPa **(Table 5.4)**.

The stress exponent (n) of the investigated AZX911 alloy has been estimated from the slope of the plot between log ($\dot{\varepsilon}$) vs log (σ) at 150 °C and 175 °C temperature in the stress range of 50 to 85 MPa in **Figure 5.10b.** In order to crosscheck if any threshold stress is involved in the creep deformation of the AZX911 alloy, the relationship between the steady-state strain rate ($\dot{\varepsilon}$) and stress (σ) in a double logarithmic plot have been plotted and analyzed [137], as shown in **Fig. 5.11**. The plot indicates the linear relationship between the stress (σ) and steady-state strain rate ($\dot{\varepsilon}$) in the log-log plot, which reveals that the creep deformation of the present as-cast AZX911 alloy is not associated with threshold stress. Similarly, another study by Naghdi et al. [141], [142] also reported the absence of threshold stress in the creep deformation of as-cast Mg-Zn-Ca alloy. Therefore, the n value calculated in the present manuscript can be used to identify the governing creep mechanism. The stress exponent (n) values are 3.49 and 8.97 for 150 °C and 175 °C temperatures, respectively, as shown in **Table**

5.5. Therefore, the dislocation-based (dislocation climb) creep mechanism is expected to be the governing creep mechanism at a temperature of 150 °C, which is consistent with the AZ91 Mg alloy investigated in the previous study at 150 °C temperature [10]. However, power law breakdown (n>8) is expected at 175 °C. *Kondori et al*. [90] reported the power law breakdown with the stress exponent (n>8) and activation energies of about 130-165 kJ/mol in similar Mg alloys.

In summary, the AZX911 Mg alloy shows improved creep resistance compared to the AZ91 Mg alloy without altering the governing creep mechanism at 150 °C [10].

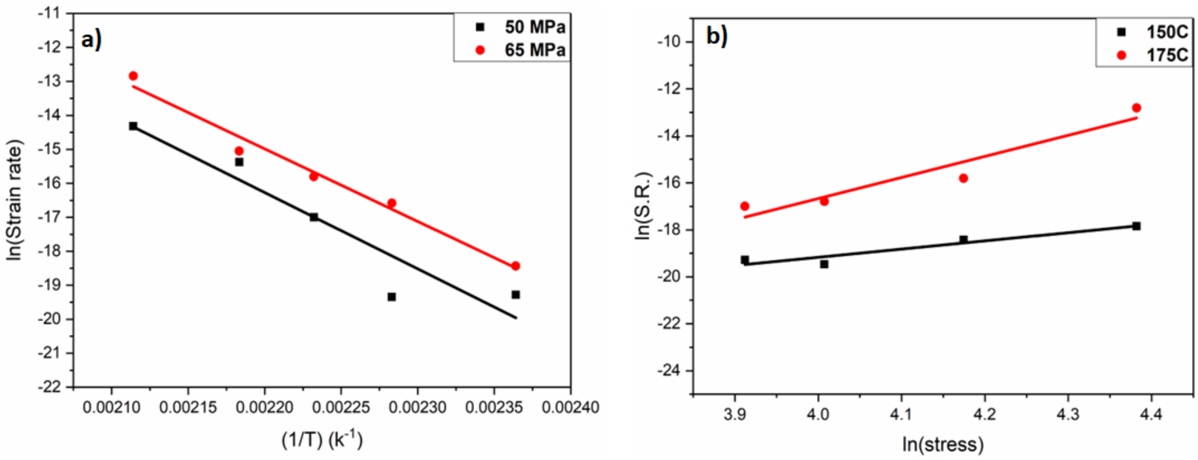

Fig. 5.10: a) The relationship between strain rate and inverse of temperature, and b) the relationship between strain rate and applied stress for AZX911 alloy.

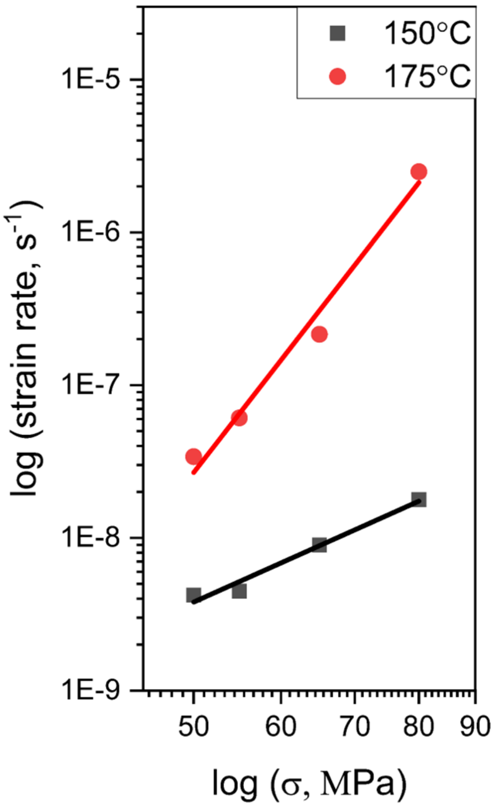

Fig. 5.11: Relations between the steady-state strain rate ($\dot{\varepsilon}$) and applied stress (σ) in double logarithmic coordinates.

Table 5.4. Activation energy values for AZ91 and AZX911 Mg alloys at different stresses.

Stress (MPa)	Activation energy (Q, kJ/mol)	
	AZX911	AZ91 [10]
50	187	117
65	177	180

Table 5.5. Creep stress exponent values for AZ91 and AZX911 Mg alloys at different temperatures.

Temperature (°C)	Stress exponent (n)	
	AZX911	AZ91 [10]
150	3.49	7.21
175	8.97	5.90

5.7. Role of the Second Phases on Creep Performance

The microstructure of AZX911 alloy mainly consists of two secondary phases, such as β-$Mg_{17}Al_{12}$ and Al_2Ca phases, as shown in **Fig. 5.1b**. The addition of Ca in AZ91 Mg alloy reduces the fraction of the β-$Mg_{17}Al_{12}$ phase and introduces the Al_2Ca phase. Thermodynamic analysis shows that the Al_2Ca phase is precipitated at a higher temperature compared to the β-$Mg_{17}Al_{12}$ phase (**Fig. 5.2b)**. Due to the advantage of early precipitation, Al_2Ca phases consume most of the Al available in the microstructure. Therefore, a very low fraction of Al remains for the precipitation of the β-$Mg_{17}Al_{12}$ phase, resulting in the reduction of the phase fraction of the thermally unstable β-$Mg_{17}Al_{12}$ phase in the microstructure at room temperature. The superior creep performance observed in AZX911 Mg alloy is despite the reduced fraction of the β-$Mg_{17}Al_{12}$ phase. The preferential microstructural site for crack and cavity formation in AZX911 Mg alloys has been studied in detail, as shown in **Fig. 5.12**. In most of the cases, the β-$Mg_{17}Al_{12}$ intermetallic phases are found to be cracked, as shown in **Fig. 5.12a-b.** Further, the microcrack propagated into the matrix, **Fig. 5.12c,** or followed the interface between the α-Mg matrix and β-$Mg_{17}Al_{12}$ intermetallic, **Fig. 5.12d,** and resulted in a cavity. In some cases, cavity formation along a continuous network of β-$Mg_{17}Al_{12}$ intermetallic phases has also been observed, **Fig. 5.12e**. On the other hand, no evidence of crack formation has been noticed either in the Al_2Ca phase or at the interface between α-Mg and Al_2Ca, **Fig. 5.12f**. The tendency of cavity formation at the α-β interface is explained by the difference between the crystallographic lattices associated with the α-matrix and β-precipitate. The α-Mg matrix has an hcp lattice, while the β-precipitate has a cubic lattice [4], [126]. The lattice mismatch causes incoherency at the interphase and results in cavity formation. These cavities encourage the dislocation to overstep the bulk of the grain without being obstructed and thus result in softening [10], [126]. Whereas thermally stable Al_2Ca phase and α-Mg matrix share a strong coherent interface [27], [143]; hence, the cavity formation is not observed at the interface **(Fig. 5.12f).**

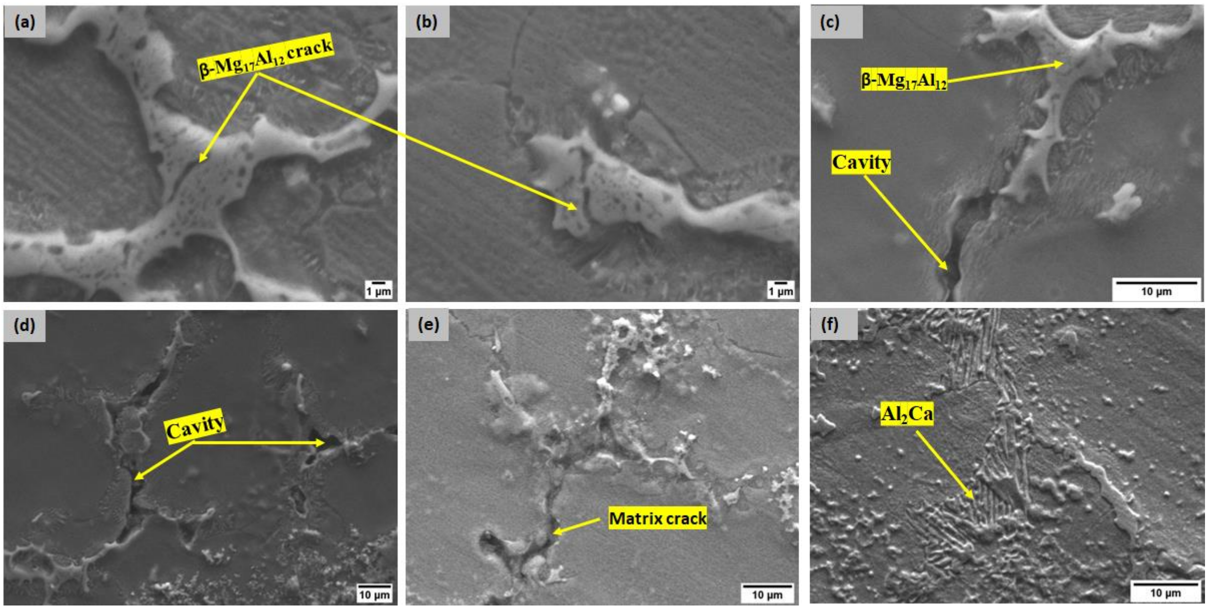

Fig. 5.12: SEM micrograph showing the transverse cross-section adjacent to the fracture surface of crept AZX911 Mg alloy tested at 65 MPa stress and 150 °C temperature.

In order to completely remove the β-$Mg_{17}Al_{12}$ phase, the as-cast AZX911 alloy was heat treated at 450 °C for 24 hours, followed by water quenching. As a result, the thermally unstable β-$Mg_{17}Al_{12}$ phase gets entirely dissolved in the matrix. However, the Al_2Ca phase remained stable in the microstructure, as verified through the microstructural and XRD analysis shown in **Fig. 5.3 and 5.4**. As a result of the β-$Mg_{17}Al_{12}$ phase dissolution, Al concentration in the Mg matrix increases, which adds to solid solution strengthening [144] in heat-treated AZX911 alloy. Hence, the creep resistance of the alloy further improved after the heat treatment, **Fig. 5.7**.

The post-creep microstructure of the heat-treated AZX911 alloy specimen, as represented in **Fig. 5.13a and b,** shows the distribution of thermally stable Al_2Ca phase mostly along the grain boundaries. This Al_2Ca phase not only resists the dislocation motion but also restricts grain boundary migration at high temperatures, thereby improving the creep performance. However, no trace of the β-$Mg_{17}Al_{12}$ phase has been noticed even after creep deformation. Importantly, a considerable delay in the onset of tertiary creep has been noticed in the heat-treated AZX911 alloy specimen, as shown in **Fig. 5.7**. Most probably, the nonexistence of the β-$Mg_{17}Al_{12}$ phase is the primary reason behind a delayed tertiary creep.

The formation of these precipitates at the expense of solid solution strengthening leads to severe stress concentration in the matrix, thus deteriorating the creep resistance of the alloy [145]. On the other hand, unlike the β-$Mg_{17}Al_{12}$ phase, Al_2Ca is expected to maintain a coherent interface with the α-Mg matrix, and therefore, intragranular Al_2Ca is not likely to contribute to the cavity formation [146], [147]. As a result, the cavities are mostly evolving at the grain boundary triple points and grain boundaries in the heat-treated AZX911 sample, as shown in **Fig. 5.13c**. EBSD analysis shown in **Fig. 5.13d** further confirms the evolution of the cavity at the grain boundary region.

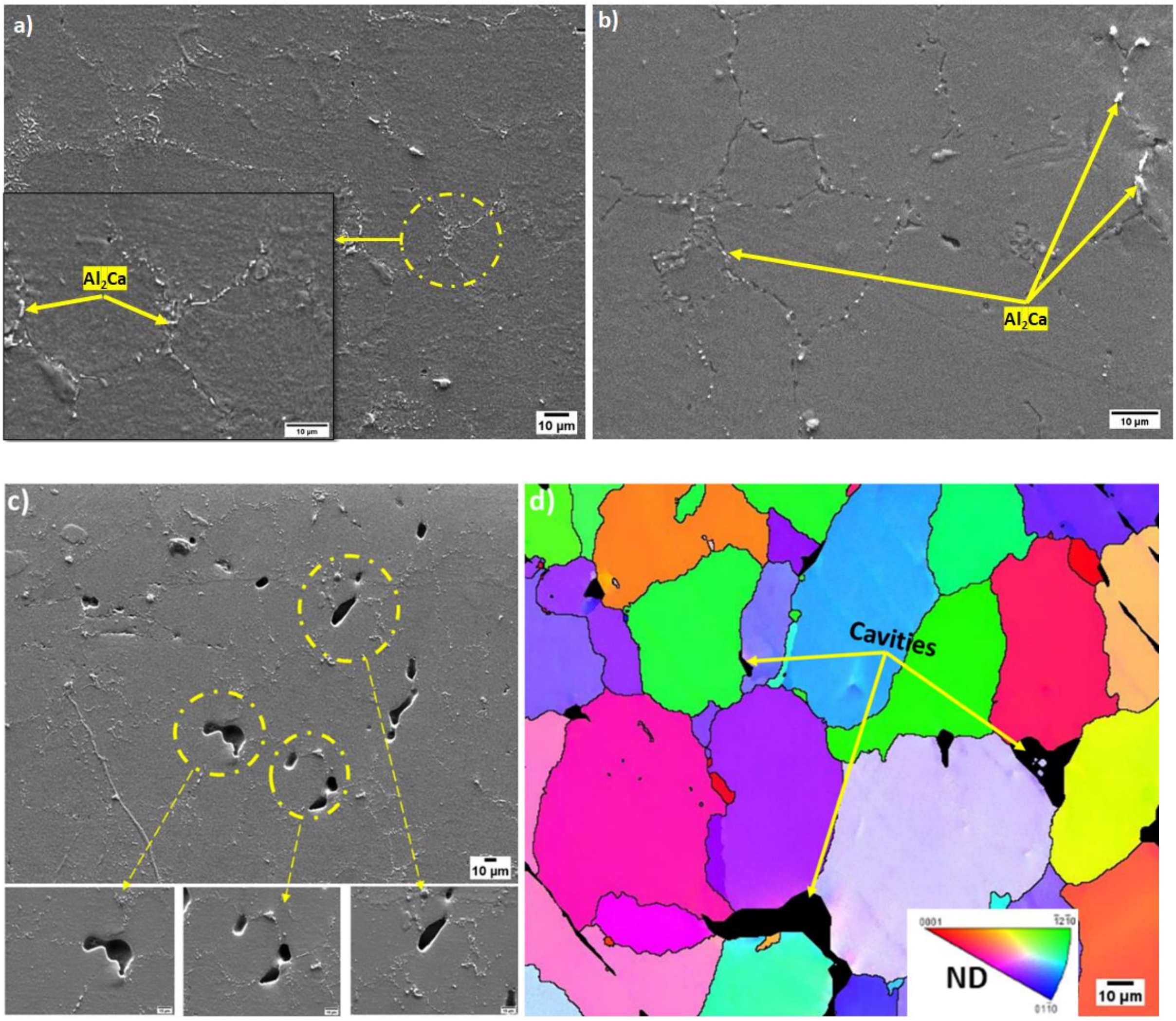

Fig. 5.13: Post-creep micrograph of heat-treated a) AZX911 alloy with b) higher magnification image, c) micrographs showing the evolution of cavities and voids during the creep deformation, further confirmed with d) EBSD micrographs.

The superior creep performance of AZX911 alloy is due to the presence of a thermally stable Al_2Ca phase. In the Mg matrix, the precipitation of the Al_2Ca phase occurs on the basal plane; they effectively hinder the dislocation gliding on non-basal planes and provide significant matrix strengthening by delaying the onset of basal slip [9], [147]. In addition, the higher dissolution temperature and higher elastic modulus associated with the Al_2Ca phase act as an obstacle against the matrix deformation and dislocation motion at elevated temperatures [148]. All these factors together enhance the creep resistance of the AZX911 alloy.

5.8. Dissolution kinetics of Al_2Ca and β-$Mg_{17}Al_{12}$ phase

In order to estimate the activation energy (E_a) required for the dissolution of the β-$Mg_{17}Al_{12}$ and Al_2Ca phases in AZX911 Mg alloy, the non-isothermal kinetic technique known as the Kissinger method has been employed. The Kissinger equation for determining the activation energy (E_a) is as follows [149]:

$$\ln\left(\frac{\beta}{T_m{}^2}\right) = \ln\left(\frac{AR}{E_a}\right) - \frac{E_a}{RT_m} \tag{5.2}$$

Where β is the heating rate, T_m is the peak temperature at which maximum decomposition occurs, A is a constant, R is the gas constant, and Ea represents the activation energy of decomposition. In order to estimate the activation energy associated with the dissolution of different precipitates, samples are subjected to different heating rates (β) in the DSC study. The peak temperature of dissolution (T_m) is recorded from the DSC curve at the different heating rates. Then, the obtained results are plotted in a $\ln\left(\frac{\beta}{Tm^2}\right)$ vs $\frac{1}{T_m}$ plot, and the best-fit straight line is constructed. The slope and intercept of the fitted straight line are equal to ($-\frac{E_a}{R}$) and $\ln\left(\frac{AR}{E_a}\right)$, respectively.

In the present study, the as-cast AZX911 Mg alloy specimens were subjected to heating at different rates (5, 10, 15, and 20 °C/min) using a DSC instrument. The obtained DSC curves with endothermic decomposition peaks are shown in **Fig. 5.14a**. The dissolution temperatures of β-$Mg_{17}Al_{12}$ and Al_2Ca phase are found to be 460 °C and 515 °C at a 5 °C/min heating rate, which is in good agreement with the Thermocalc® prediction as shown in **Fig. 5.2b**. Kissinger plot has been constructed using the experimental results and is shown in **Fig. 5.14b**. The activation energy associated with the dissolution of the β-$Mg_{17}Al_{12}$ and Al_2Ca phases is estimated to be 664 and 923 kJ/mol, respectively. The activation energy for the dissolution of the Al_2Ca phase is observed to be higher than that of β-$Mg_{17}Al_{12}$, which indicates that the Al_2Ca phase is more thermally stable compared to the β-$Mg_{17}Al_{12}$ phase [149]. Hence, the Al_2Ca phase is expected to provide higher creep resistance compared to the β-$Mg_{17}Al_{12}$ phase of the AZX911 Mg alloy. Similarly, following the same procedure, the activation energy associated with the dissolution of the β-$Mg_{17}Al_{12}$ phase in AZ91 alloy has been estimated to be 652 kJ/mol, which is very close to the activation energy of β-$Mg_{17}Al_{12}$ phase of the AZX911 Mg alloy. This result indicates that the addition of Ca does not have any influence on the activation energy of β-$Mg_{17}Al_{12}$ phase dissolution.

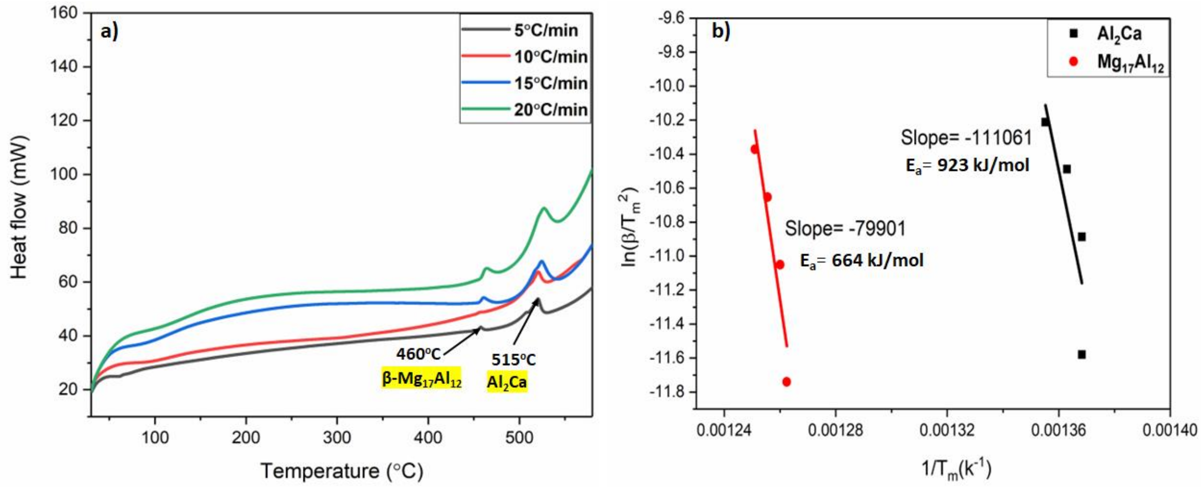

Figure 5.14: a) DSC endothermic curves for the AZX911 Mg alloy at different heating rates, and b) Kissinger plot of ln (β/T_m^2) versus 1/ T_m for AZX911 Mg alloy.

5.9 Conclusions

In the present investigation, the AZX911 Mg alloy is subjected to microstructural and creep study within the temperature range of 150 °C -250 °C under 65 and 80 MPa stress. The primary conclusions drawn from the present investigation are mentioned below:

1. The addition of Ca resulted in the development of thermally stable Al_2Ca intermetallic in AZ91 alloy with a simultaneous decrease in the volume fraction of the thermally unstable β-$Mg_{17}Al_{12}$ phase.

2. The presence of thermally stable Al_2Ca precipitate alloy contributes to the significant improvement in creep resistance of AZ91+Ca (AZX911) alloy as compared to AZ91

alloy. However, the governing creep mechanism is dislocation climb in both alloys, AZX911 and AZ91, at 150 °C.

3. Further, heat treatment at 450 °C on the as-cast AZX911 alloy exhibits a delay in the onset of tertiary creep because of the complete dissolution of the β-$Mg_{17}Al_{12}$ phase and subsequent increments in solid solution strengthening.

4. A non-isothermal kinetic analysis employing the Kissinger method reveals that the activation energies for dissolution of the Al_2Ca phase and β-$Mg_{17}Al_{12}$ phase in AZX911 alloy are 923 and 664 kJ/mol, respectively, implying higher thermal stability of Al_2Ca compared to β-$Mg_{17}Al_{12}$ phase.

Chapter 6

Role of Intermetallics in the Creep Behaviour of Squeezed Cast Ca and Sr Modified AZ91 Magnesium Alloy

In Chapter 5, it is demonstrated that the addition of individual Ca into the AZ91 alloy successfully enhanced the creep resistance of the alloy. Therefore, in a similar way, in Chapter 6, the attempt has been made to further investigate the compatibility of another alkaline earth element, ‘Sr’ with the AZ91 alloy for its creep performance. It is expected that the incorporation of Al-Sr intermetallic into the alloy will also favorably contribute to the creep performance of the alloy. The creep performance of the AZ91 alloy can be further improved by increasing the concentration of individual Ca/Sr, but it may compromise the alloy’s ductility and castability. Therefore, in the present study, an attempt has been made to further improve the creep performance of the AZ91 alloy without sacrificing its ductility and castability through the combined addition of Ca and Sr. Therefore, in Chapter 6, the effect of individual Sr and combined Ca-Sr addition on the microstructure evolution and tensile creep properties of the squeezed cast AZ91 alloy has been investigated. Further, the results from the current chapter are compared with the creep performance of the base AZ91 (Chapter 4) and AZ91-1Ca (Chapter 5) alloys.

Chapter 6

Role of Intermetallics in Creep Behaviour of Squeezed Cast Ca and Sr Modified AZ91 Magnesium Alloy

The work in this chapter has been published as: Hitesh Patil, Abhijit Ghosh, and Hemant Borkar, “Role of intermetallics in creep behaviour of squeezed cast Ca and Sr modified AZ91 Magnesium Alloy”, *Advanced Engineering Materials*.

6.1 Introduction

As we know, the creep performance of AZ91 alloy can be effectively improved by adding suitable elements to it. Therefore, low-cost and easily accessible alkaline earth metals, such as Sr and Ca, are expected to be a better choice as suitable additives in AZ91 alloy. The formation of the thermally stable Al-Sr and Al-Ca compounds in those AZ91-modified alloys is beneficial for improving elevated temperature properties. To the best of the author’s knowledge, no study has described the tensile creep properties of the squeezed cast AZ91 alloy having individual Sr or combined Sr-Ca addition. Although a few studies investigated the creep performance of AZ91 or similar alloy combined with Sr in addition to Ca/Bi/ RE elements, as mentioned with the operative creep mechanism in **Table 2.4**, in none of these studies, the tensile creep performance was evaluated in squeezed cast AZ91 alloys. Therefore, in the present study, the effect of individual Sr and combined Sr-Ca addition on the creep properties (creep performance and creep mechanism) of the AZ91 alloy fabricated via the squeeze casting technique. Further, the comparison of the creep properties after the Sr and /Ca addition with the base AZ91 alloy is necessary to demonstrate the advantages of alloying addition.

6.2 Chemical composition of the investigated alloys

The chemical composition of the squeeze-cast investigated *AZ91* Mg alloys estimated using an optical emission spectrometer in the present work is listed in **Table 6.1**.

Table 6.1: Material designation and chemical composition of the investigated AZ91 alloys (Weight%).

Designation	Alloy	Al (wt%)	Zn (wt%)	Mn (wt%)	Si (wt%)	Ca (wt%)	Sr (wt%)	Mg
A	AZ91	9.01 ± 0.142	1.57 ± 0.002	0.17 ± 0.002	0.022 ± 0.011	-	-	Bal.
B	AZ91-1Sr	8.72 ± 0.138	0.511 ± 0.002	0.234 ± 0.002	0.021 ± 0.009	-	0.998 ± 0.002	Bal.
C	AZ91-1Ca-0.3Sr	8.5 ± 0.140	0.50 ± 0.002	0.17 ± 0.002	0.015 ± 0.014	1.04 ± 0.002	0.4 ± 0.001	Bal.
D	AZ91-1Ca-0.6Sr	8.21 ± 0.136	0.49 ± 0.002	0.18 ± 0.002	0.014 ± 0.019	1.06 ± 0.004	0.8 ± 0.002	Bal.

6.3 Microstructure characterization of investigated alloys

The Scanning electron micrograph of the investigated alloys, Alloy A, B, C, and D, are illustrated in **Fig. 6.1**. The microstructure of the squeezed cast AZ91 alloy (alloy A) consists of an α-Mg matrix with a massive continuous network of the β-$Mg_{17}Al_{12}$ phase as shown in Fig. **Fig. 6.1a**. The needle-shaped (length 6.5±1.3μm) Al_4Sr phase, along with the refined discontinuous β-$Mg_{17}Al_{12}$ phase in an α-Mg matrix, evolved on the addition of *1wt% Sr* in as-received AZ91, alloy B, as shown in Fig. **Fig. 6.1b**. Similarly, the addition of Ca and Sr combined into the AZ91 alloy, i.e., alloy C and D *(AZ91-1Ca-0.3Sr and AZ91-1Ca-0.6Sr)*, promotes the precipitation of both Al_2Ca and Al_4Sr phases in the microstructure, Fig. **Fig. 6.1 (c, d)**. An attempt has been made to quantify the volume fraction of Al_4Sr using Image J software, and it is observed to be 4.2±1% in the total intermetallic phase fraction of 14±2% in alloy B. The Al_2Ca phase has a skeleton morphology, as indicated in the offset of Fig. **Fig. 6.1 (c, d)**. However, Al_4Sr could not be distinguished from the Al_2Ca phase based on their morphology in alloys C and D. The formation of this Al_2Ca and Al_4Sr phase is due to the higher chemical affinity of Ca and Sr with the Al [7], [20], [141]. The elemental distribution in different precipitates is characterized by elemental mapping using EDS analysis, as shown in **Fig. 6.2**. Figure **Fig. 6.2a** confirms that the needle shape second phase in alloy B is rich in Sr. On the other hand, the precipitates in alloy D are found to be rich in Al along with either Ca or Sr, **Fig. 6.2b**. In some cases, the Sr-rich phase is observed to be co-precipitated with the Ca-rich phase. Further, the existence of these phases mentioned above is confirmed by conducting X-ray diffraction and by comparing the peak position with the inorganic crystal structure database (ICSD) as shown in **Fig. 6.3**. ICSD identification numbers for α-Mg, β-$Mg_{17}Al_{12}$, Al_2Ca, and Al_4Sr are 654648, 158247, 57530, and 107887, respectively. Al_4Sr phase is found to be present in all the alloys containing Sr, i.e., alloys B, C, and D. Similarly, the

Al_2Ca phase is present in alloys C and D. On the other hand, the intensity of β-$Mg_{17}Al_{12}$ phase peak decreases with the addition of Sr and Ca indicating a reduction in the β-$Mg_{17}Al_{12}$ phase fraction [5], [23], [150]. The amount of β-$Mg_{17}Al_{12}$ phase fraction becomes almost negligible in alloy D, so the β-$Mg_{17}Al_{12}$ phase peak could not be identified.

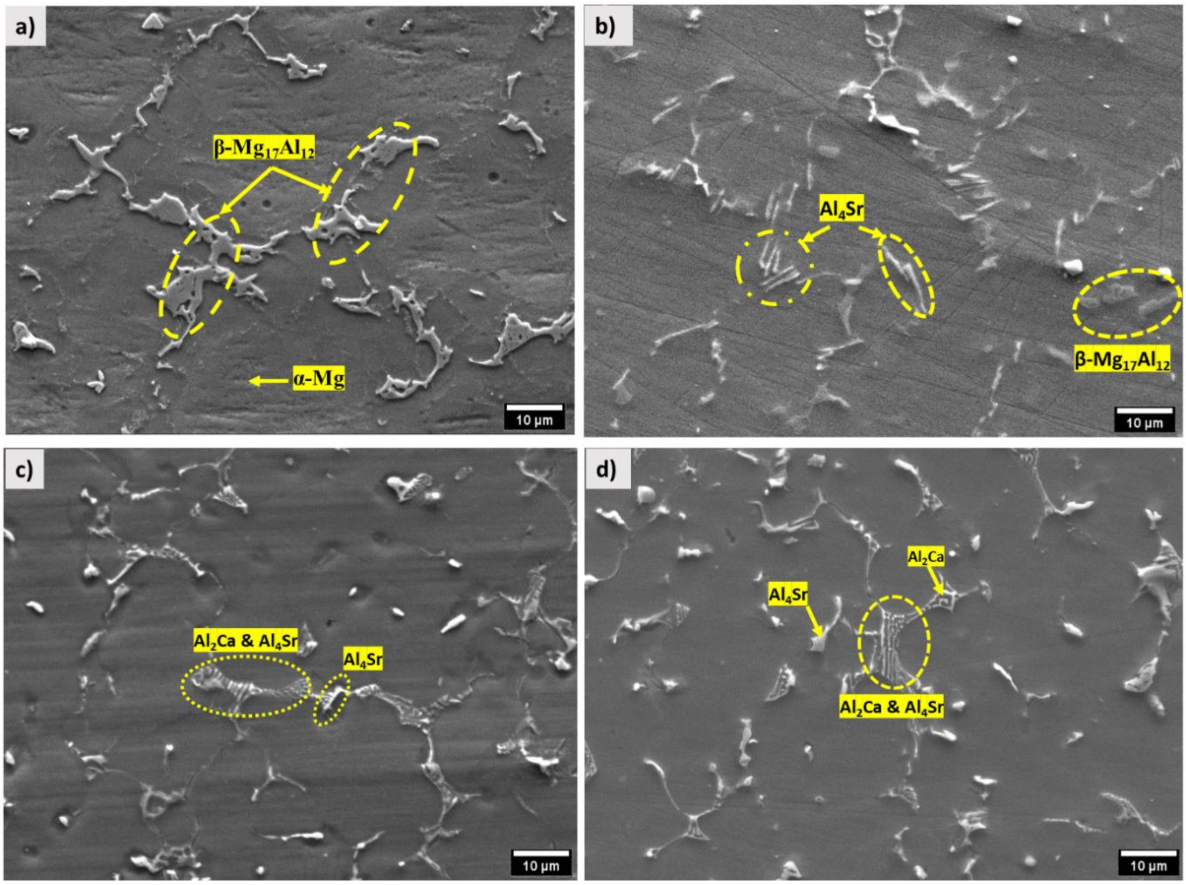

Fig. 6.1: SEM micrograph of squeeze-cast a) *AZ91* alloy (alloy A), b) *AZ91-1Sr* alloy (Alloy B), c) *AZ91-1Ca-0.3Sr* alloy (Alloy C), and d) *AZ91-1Ca-0.6Sr* alloy (Alloy D).

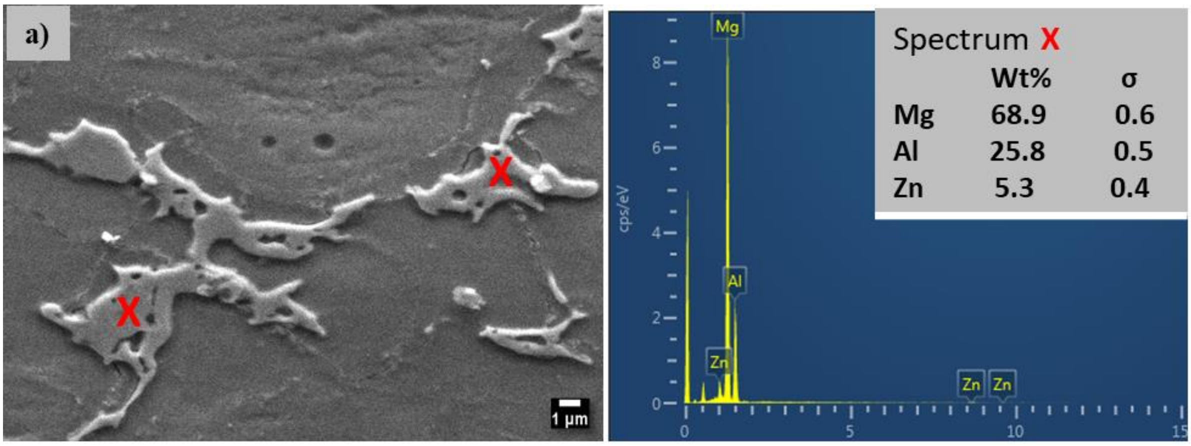

Spectrum X

	Wt%	σ
Mg	68.9	0.6
Al	25.8	0.5
Zn	5.3	0.4

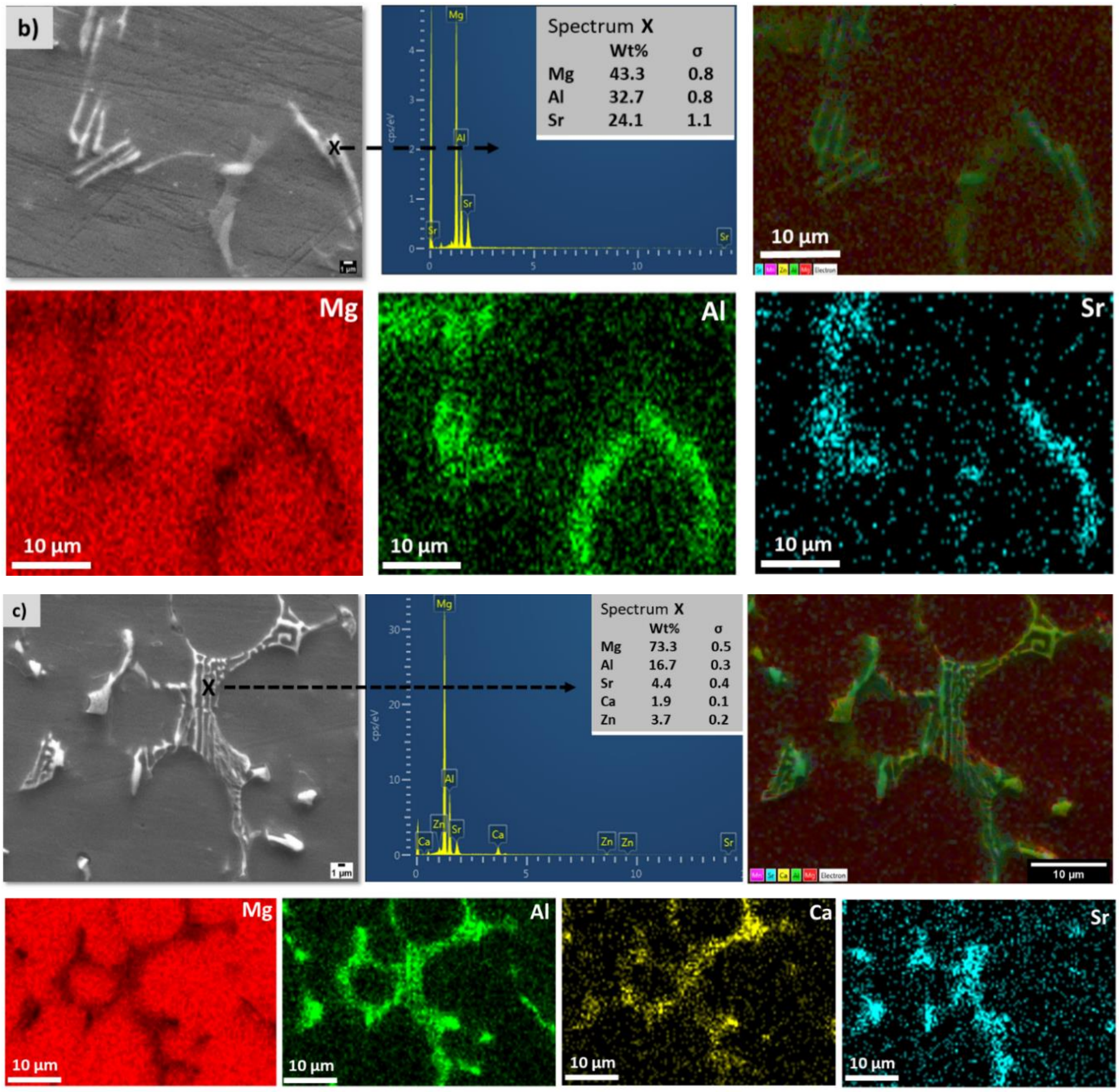

Spectrum X

	Wt%	σ
Mg	43.3	0.8
Al	32.7	0.8
Sr	24.1	1.1

Spectrum X

	Wt%	σ
Mg	73.3	0.5
Al	16.7	0.3
Sr	4.4	0.4
Ca	1.9	0.1
Zn	3.7	0.2

Fig. 6.2: Elemental distribution in squeeze-cast a) AZ91 alloy, b) *AZ91-1Sr* alloy (Alloy B), and c) *AZ91-1Ca-0.6Sr* alloy (Alloy D).

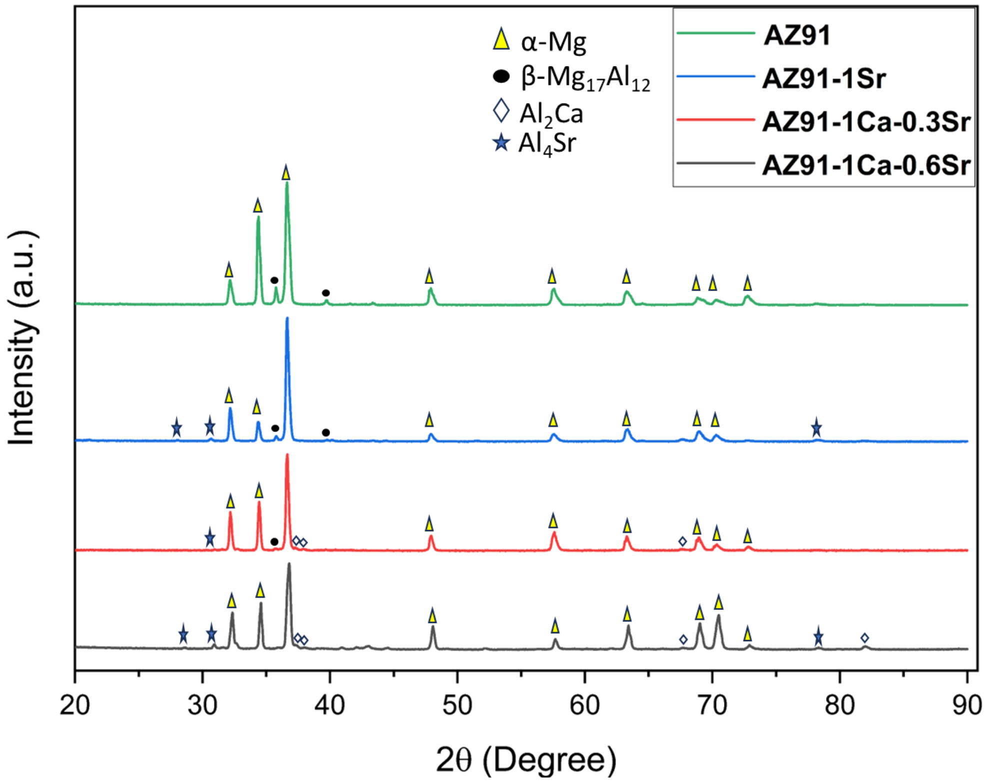

Fig. 6.3: X-ray diffraction profile of the investigated AZ91 alloys.

6.4 Thermodynamic and thermal analysis

The existence of the equilibrium phases at room temperature and the reduction in the amount of the β-phase in alloys B, C, and D is further ascertained by the thermodynamic analysis carried out through thermodynamic calculations resulting from the computational thermodynamic software Thermo-Calc® TCMG6 database. The predicted variation in mole% of equilibrium phases with respect to temperature is shown in **Fig. 6.4(a-d)**. The equilibrium composition of different phases evolved at room temperature in alloys A, B, C, and D is listed in **Table 6.2**.

In line with thermodynamic prediction, the Al_4Sr and C15-Al_2Ca phase, along with the α-Mg & β-$Mg_{17}Al_{12}$, are expected in alloy C and D at room temperature, as shown in **Fig. 6.4 (b, c)**. However, the amount of equilibrium β-$Mg_{17}Al_{12}$ phase is expected to reduce drastically by 71% on increasing temperature from 27 °C to 250 °C, **Table 6.2**. In contrast, the intermetallic phases, such as Al_4Sr and Al_2Ca, experience an almost negligible change in the amount with a similar increase in temperature, **Table 6.2**. During solidification, the C15-Al_2Ca phase evolves first, followed by Al_4Sr and then the β-$Mg_{17}Al_{12}$ phase, as shown in **Fig. 6.4d**. On the other hand, the amount of β-phase is expected to reduce from 16.41% in alloy A to 10.68 % in alloy D at room temperature due to the addition of 1 mol % Ca and 0.6 mol

%Sr, **Fig. 6.4e**. The single Sr atom consumes four Al atoms in the Al_4Sr phase. In contrast, only two Al atoms are consumed by the Ca atom in the case of the C15-Al_2Ca phase, **Table 6.2**. Therefore, Sr addition in the AZ91 alloy results in a higher reduction in the volume fraction of the β-$Mg_{17}Al_{12}$ phase; the remaining Al in the α-Mg matrix is low enough to suppress the formation of the β-$Mg_{17}Al_{12}$ phase [5]. Further, the dissolution temperature (on heating) of the β-$Mg_{17}Al_{12}$ phase also decreases simultaneously with the reduction in the phase fraction from above 375 °C to below 300 °C with the addition of Ca and/Sr, as shown in **Fig. 6.4e**. The reduction in the dissolution temperature of the β-$Mg_{17}Al_{12}$ phase could be due to the restricted availability of Zn, as listed in **Table 6.2**. Similarly, the mole % of the Al_4Sr phase was also reduced after the addition of Ca with Sr (alloy C & D), as shown in **Fig. 6.4f**. However, it has little effect on the dissolution temperature of the Al_4Sr phase. Overall, in alloy D, the β- $Mg_{17}Al_{12}$ phase is expected to be present up to a maximum temperature of 300 °C with a continuous reduction in phase fraction with an increase in temperature above room temperature, and therefore it is considered to be thermally unstable. On the other hand, the Al_4Sr phase and C15- Al_2Ca phase are expected to be stable up to a higher temperature of 515 °C and 540 °C respectively, and more importantly, unlike β- $Mg_{17}Al_{12}$ phase, the Al_4Sr and Al_2Ca phase fractions are expected to be almost insensitive to the equilibrium temperature up to 500 °C. Therefore, the Al_4Sr and C15-Al_2Ca are more stable compared to the β-$Mg_{17}Al_{12}$ phase.

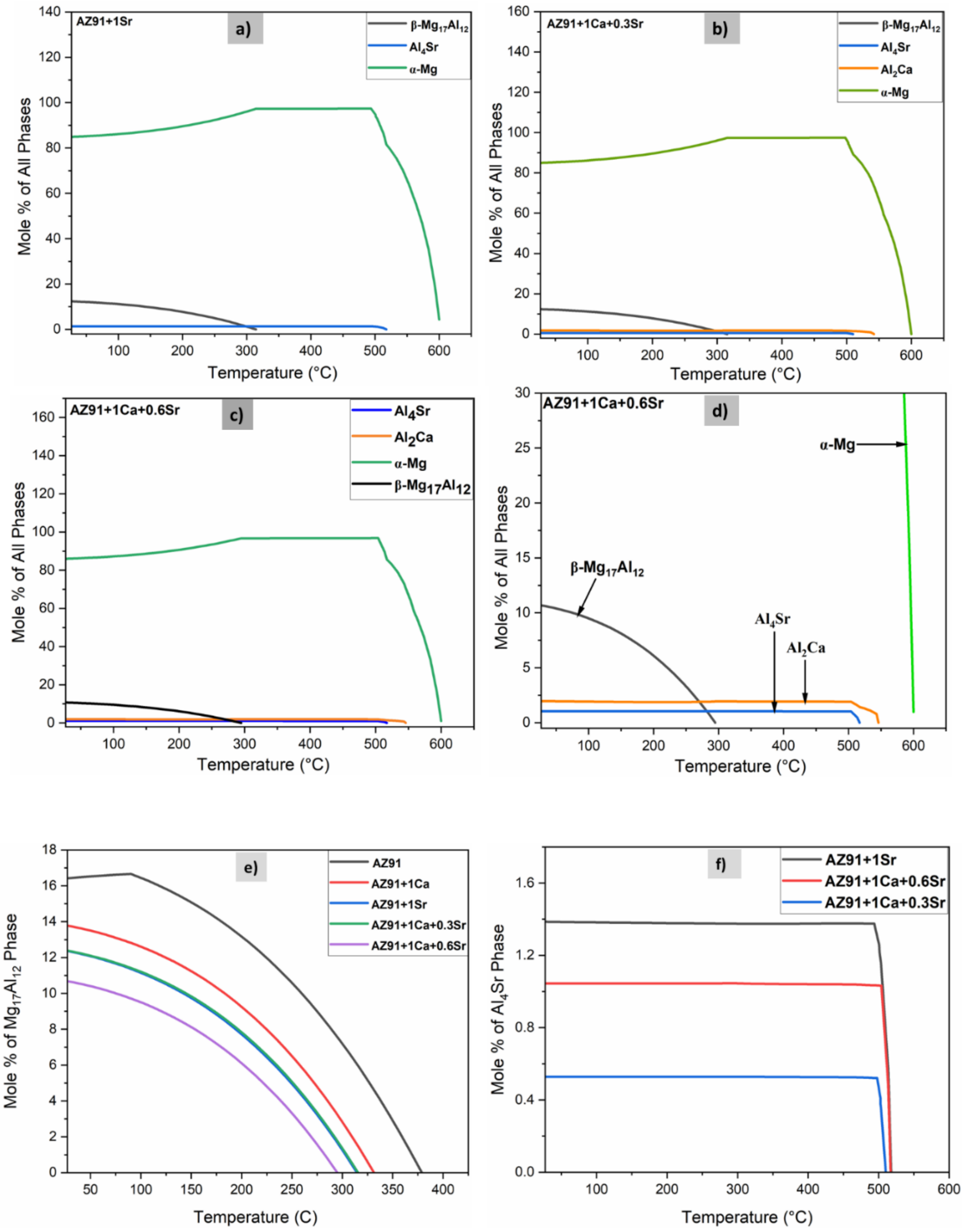

Fig. 6.4: The thermodynamic plot indicating the precipitation characteristics of the $Mg_{17}Al_{12}$, Al_4Sr, and Al_2Ca phase in the alloy a) *AZ91-1Sr*, b) *AZ91-1Ca-0.3Sr*, c) *AZ91-1Ca-0.6Sr*, d) magnified view of (c), e) change in β-$Mg_{17}Al_{12}$ phase volume fraction with temperature, and f) change in Al_4Sr phase volume fraction with temperature.

Further, the dissolution of Al_2Ca and Al_4Sr phases during heating has been examined experimentally by thermal analysis using differential scanning calorimetry (DSC) instrument (model no. STA8000 by Perkin Elmer) in a purified argon atmosphere. The respective DSC curve of the investigated AZ91 alloys is shown in **Fig. 6.5**. In alloy B, only one endothermic peak at 515 °C has been detected. In comparison, the Al_4Sr phase is expected to dissolve completely around 520 °C as per thermodynamic analysis, **Fig. 6.4a**. Similarly, in alloy D, the peak dissolution temperature of Al_4Sr and C15-Al_2Ca phases is found to be 515 °C and 540 °C respectively (**Fig. 6.5**), which are in good agreement with thermodynamic analysis, **Fig. 6.4c**. However, no peak associated with the β-$Mg_{17}Al_{12}$ phase dissolution appeared in the DSC analysis (heating) of both alloys B and D. The SEM images and XRD plot also indicate the almost complete suppression of the β-$Mg_{17}Al_{12}$ phase in alloy D. However, the thermodynamic analysis presented in **Table 3** demonstrates a phase fraction of the β-$Mg_{17}Al_{12}$ phase above 10% in both alloys B and D. Here, the discrepancy between the thermodynamic prediction and DSC observation in alloy D may be due to the non-equilibrium cooling during squeezed casting. However, in alloy B, the β-$Mg_{17}Al_{12}$ phase peak in DSC could not be traced, although both SEM and XRD analysis confirmed its presence in small quantities. Therefore, in addition to the non-equilibrium cooling, the small phase fraction and the low sensitivity of DSC analysis might have resulted in the non-occurrence of the β-$Mg_{17}Al_{12}$ phase peak in alloy B. In addition, the Al_2Ca and Al_4Sr phases have higher thermal stability compared to the β-$Mg_{17}Al_{12}$ phase.

Table 6.2: The composition and volume fraction of the phases present in the microstructure of investigated AZ91 alloys at room temperature and 250 °C of creep temperature.

Alloy	Phases present	Composition (mole %) of the phases at R.T.						Mole% of the phase at **R.T.**	Mole% of the phase at **250°C**
		Al	**Ca**	**Sr**	**Mg**	**Mn**	**Zn**		
AZ91 *(As-received)* (Alloy A)	**α-Mg**	0.28	-	**-**	99.66	1E^{-10}	0.058	84.91	92.58
	β-$Mg_{17}Al_{12}$	39.97	-	-	58.24	-	1.77	16.41	10.76
AZ91-1Sr (Alloy B)	**α-Mg**	0.29	-	**1E^{-10}**	99.67	1E^{-10}	0.033	84.91	92.58
	β-$Mg_{17}Al_{12}$	40.56	-	-	58.35	-	1.08	12.36	4.72
	Al_4Sr	79.95	-	20	0.046	-	-	1.386	1.377

AZ91-1Ca-0.3Sr (Alloy C)	**α-Mg**	0.299	**1E^{-10}**	**1E^{-10}**	99.70	1E-10	4.90E^{-06}	84.969	92.606
	β-$Mg_{17}Al_{12}$	41.39	-	-	58.58	-	0.00018	12.38	4.83
	Al_2Ca or C15-Laves Phase	56.58	33.33	-	2.05E-06	-	10.07	1.821	1.73
	Al_4Sr	79.95	0.070	19.92	0.044	-	-	0.528	0.528
AZ91-1Ca-0.6Sr (Alloy D)	**α-Mg**	0.299	**1E^{-10}**	**1E^{-10}**	99.70	1E-10	1.29E^{-06}	84.969	92.606
	β-$Mg_{17}Al_{12}$	41.39	-	-	58.58	-	5E^{-05}	10.68	3.082
	Al_2Ca or C15-Laves Phase	57.50	33.33	-	2.73E-06	-	9.16	1.83	1.756
	Al_4Sr	79.95	0.103	19.89	0.044	-	-	1.045	1.045

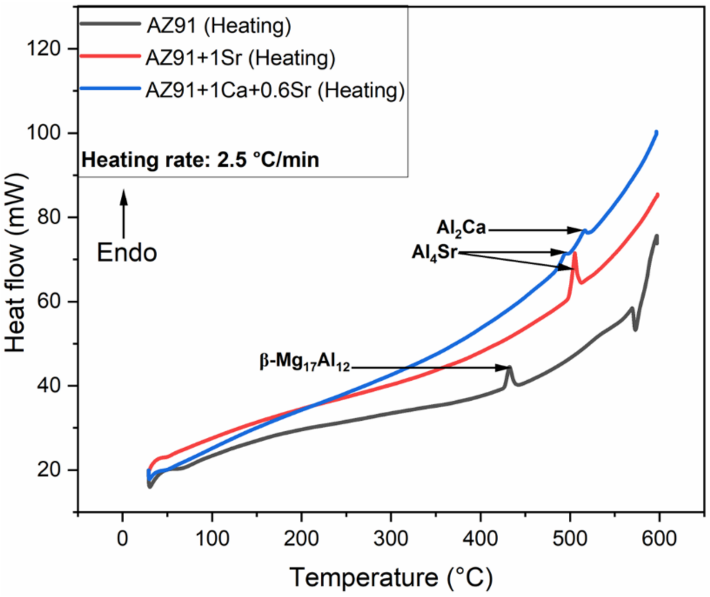

Fig. 6.5: DSC curve (at 2.5 °C/min heating rate) of investigated AZ91 alloys.

6.5 Creep properties

The characteristic tensile creep curves of the alloys B, C, and D under 50 MPa stress and 150 °C-250 °C temperatures are demonstrated in **Fig. 6.6**. In addition, the tensile creep curves associated with alloy B at 150 °C and alloy D at 225 °C temperature under the stress range of 50 MPa to 80 MPa are also reported in the present investigation, **Fig. 6.7**. The selected temperatures for the creep tests were chosen to investigate the performance of the specimens under the operating temperatures of various automotive powertrain components, such as transmission gears (up to 150 °C), engine blocks (175 to 200 °C), and engine pistons (up to 250 °C). The creep performance investigated in the present alloys (Alloy B, C, and D) is compared with previously reported squeeze cast *AZ91* and *AZ91-1Ca* (AZX911) alloys [3], [10]. The steady-state creep rates of all alloys in **Fig. 6.6** are listed in **Table 6.3**. For convenience, the minimum creep rate $(\dot{\varepsilon})$ during secondary creep is considered to represent the creep resistance of the concerned alloy. Under applied stress of 50 MPa and 150 °C creep temperature, alloy B *(AZ91-1Sr)* showed a lower creep rate compared to the squeezed cast AZ91 base alloy, **Fig. 6.6a**. However, the improvement in creep resistance after 1% Sr addition (alloy B) is not significant above 150 °C, **Fig. 6.6 (b, c)**. On the other hand, *AZ91-1Ca* alloy was reported to demonstrate a much lower creep rate than alloy B, **Fig. 6.6 (a-c)**. Irrespective of the creep deformation temperature, the creep performance after the individual addition of Sr (alloy B) is found to be worse than *AZ91-1Ca* alloy under 50 MPa stress. However, with the addition of 0.3 % Sr in the *AZ91-1Ca* alloy (alloy C), the creep resistance is improved compared to *AZ91-1Ca* at 50 MPa stress and 175 °C temperature, **Fig. 6.6b**. A further increase in Sr content to 0.6 % provides better creep resistance, as observed in alloy D at 175 °C-250 °C temperatures, **Fig. 6.6 (b-e)**. Overall, with the combined addition of *1%Ca* and *0.6%Sr*, alloy D demonstrates the best creep performance among all the investigated alloys.

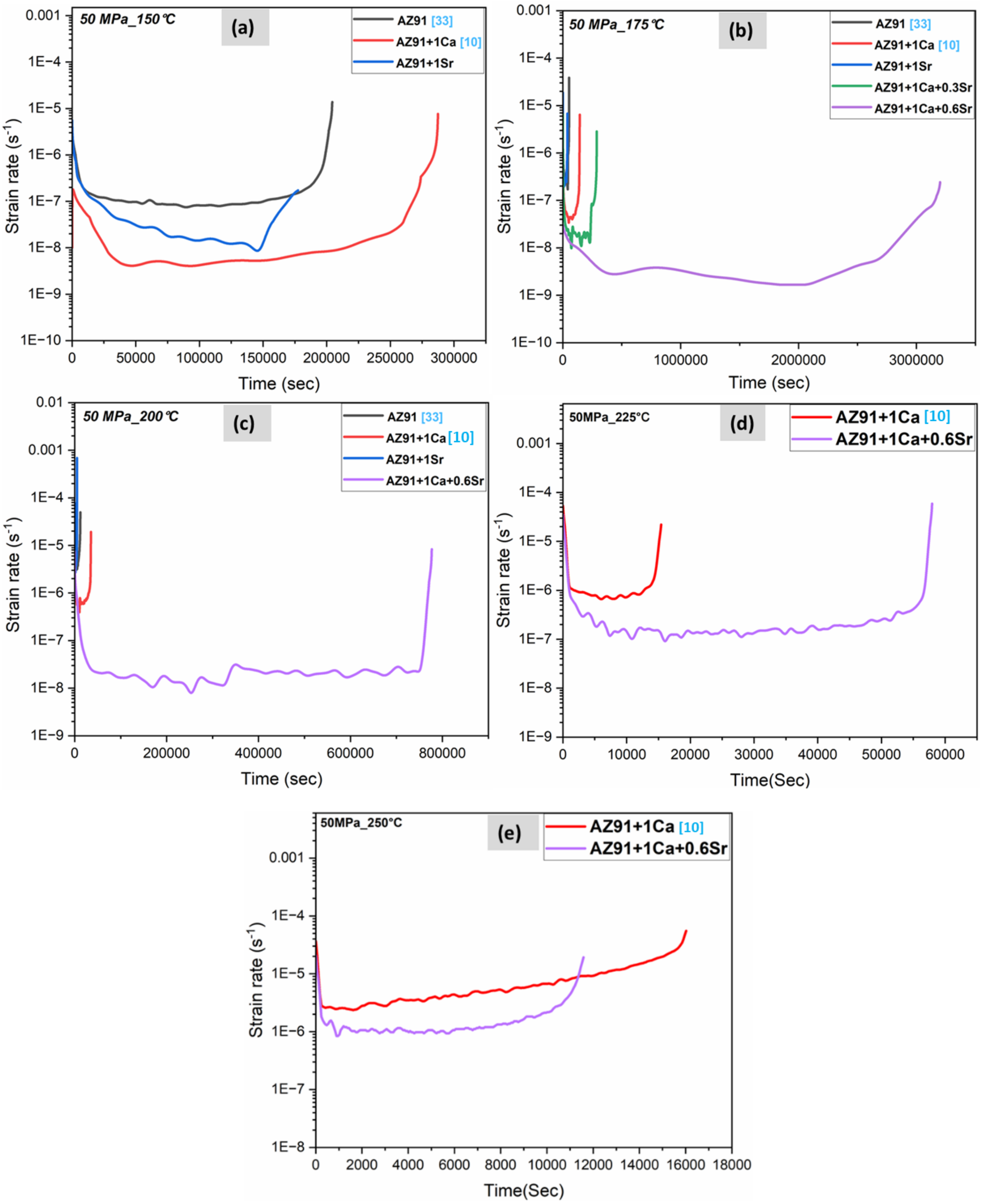

Fig. 6.6: Creep strain rate vs. time curves of AZ91 alloys tested at 50 MPa stress and different creep temperatures of (a) 150 °C, (b) 175 °C, (c) 200 °C, (d) 225 °C, and e) 250 °C.

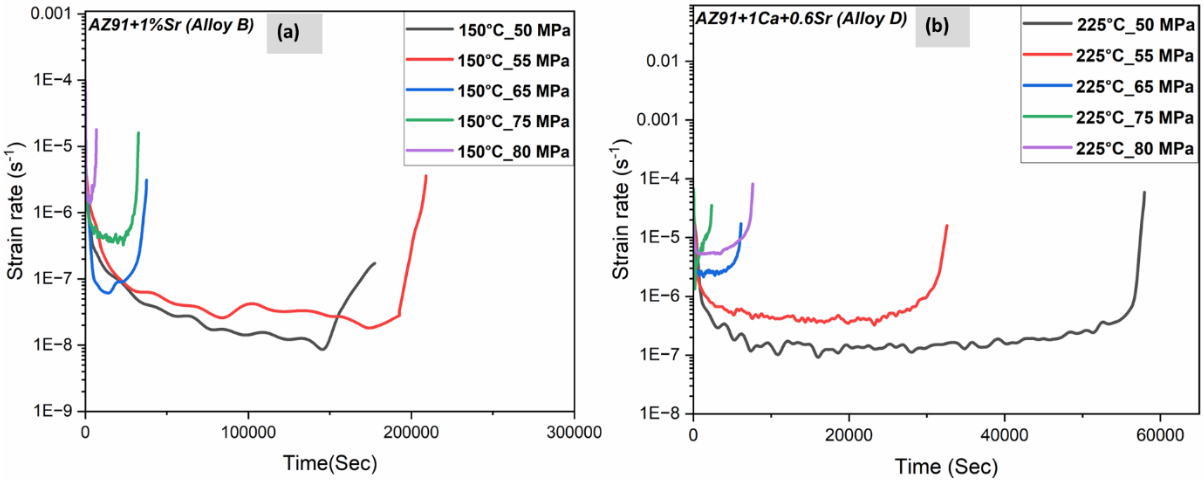

Fig. 6.7: Creep strain rate vs. time curves of a) alloy B *(AZ91-1Sr)* at 150 °C under 50-80 MPa stress and b) alloy D *(AZ91-1Ca-0.6Sr)* at 225 °C under 50-80 MPa stress.

Table 6.3: Minimum creep rate of the investigated alloys under all tested conditions.

Stress (MPa)	Temperature (°C)	Minimum Creep Rate (s^{-1})			
		AZ91 [10]	AZ91-1Ca [3]	AZ91-1Sr *(Alloy B)*	AZ91-1Ca-0.6Sr *(Alloy D)*
50	150	7.73E-08	4.23E-09	1.359E-08	-
	175	2.34E-07	4.14E-08	2.27E-07	2.23E-09
	200	3.07E-06	6.03E-07	3.48E-06	1.60E-08
	225	-	7.47E-07	-	1.36E-07
	250	-	2.55E-06	-	9.71E-07

Further, attempts have been made to investigate the governing creep mechanism associated with the creep deformation of the alloys B and D. The minimum steady-state creep rate ($\dot{\varepsilon}$) is related to the applied stress (σ) and temperature (T), as per the conventional power law equation [151].

$$\dot{\varepsilon} = A\frac{D_0 Gb}{kT}\left(\frac{\sigma}{G}\right)^{n} \exp\left(-\frac{Q}{RT}\right) \tag{6.1}$$

Where D_0 is the frequency factor, k is Boltzmann's constant, b is the length of the burgers vector, σ the applied stress, T is the creep temperature, and R is the gas constant. n and Q are the material parameters characterizing the creep-controlling mechanism of the alloys.

The steady-state strain rates obtained from the creep tests conducted at different stresses and temperatures **(Fig. 6.6 and 6.7)** have been considered to estimate stress exponent (n) and activation energy (Q). The stress exponent (n) values of the alloy B *(AZ91-1Sr, n =8)* and D *(AZ91-1Ca-0.6Sr, n=7.9)* have been estimated from the slope of the logarithmic plot between $\dot{\varepsilon}$ versus σ at 150 °C and 225 °C, respectively, with the variation of stress in the range of 50 MPa to 80 MPa, **Fig. 6.8a**. These calculated stress exponent values represent a dislocation-based power law creep mechanism [7], [12]. In some other studies [141], power law breakdown in Mg alloy with n value greater than 10-12 has been reported under high stress (Impression test, 350-700 MPa). In such cases, the strain rate varied exponentially with the applied stress rather than following the power law. The evolution of excess vacancy concentration at high stress is reported to be responsible for such behavior. However, the applied stress in the present investigation varied in the range of 50-80 MPa, and a stress exponent greater than 12 is necessary to establish the exponential relationship between strain rate and stress.

The activation energy (Q) has been estimated in the temperature range of 150 °C-200 °C for alloy B *(AZ91-1Sr)* and 175 °C-250 °C for alloy D *(AZ91-1Ca-0.6Sr)* from the slope of the logarithmic plot between $\dot{\varepsilon}$ versus 1/T at 50 MPa stress for both alloys, **Fig. 6.8b**. For alloy B, the activation energy is calculated to be 208 kJ/mol, while for alloy D, it is 158 kJ/mol, which is close to the activation energy of self-diffusion in Mg i.e., 135 kJ/mol. The activation energy (208 kJ/mol) in alloy B significantly surpasses the activation energy for self-diffusion in Mg. It is well known that the dislocation climb mechanism within the lattice relies on atomic diffusion, and Ca and Sr atoms have significantly higher activation energy for dislocation climb than that needed for self-diffusion in pure Mg. Therefore, these alloys have a higher activation energy compared to the self-diffusion activation energy of Mg. Thus, the dominant creep mechanism in these alloys, B and D, on the basis of estimated n and Q values, is considered to be dislocation climb controlled by the lattice diffusion (Q_L), which is consistent with the AZ91 Mg alloy investigated in the previous study at 50 MPa stress, 150 °C temperature [10]. The creep mechanisms of AZ91 alloy with Sr and Ca addition, fabricated by the different techniques in other studies, are listed in **Table 2.4**.

In summary, alloys B *(AZ91-1Sr)* and D *(AZ91-1Ca-0.6Sr)* demonstrate an improved creep resistance compared to squeeze cast AZ91 alloy while maintaining the dominant creep mechanism of dislocation climb at 150 °C and 225 °C temperature, respectively.

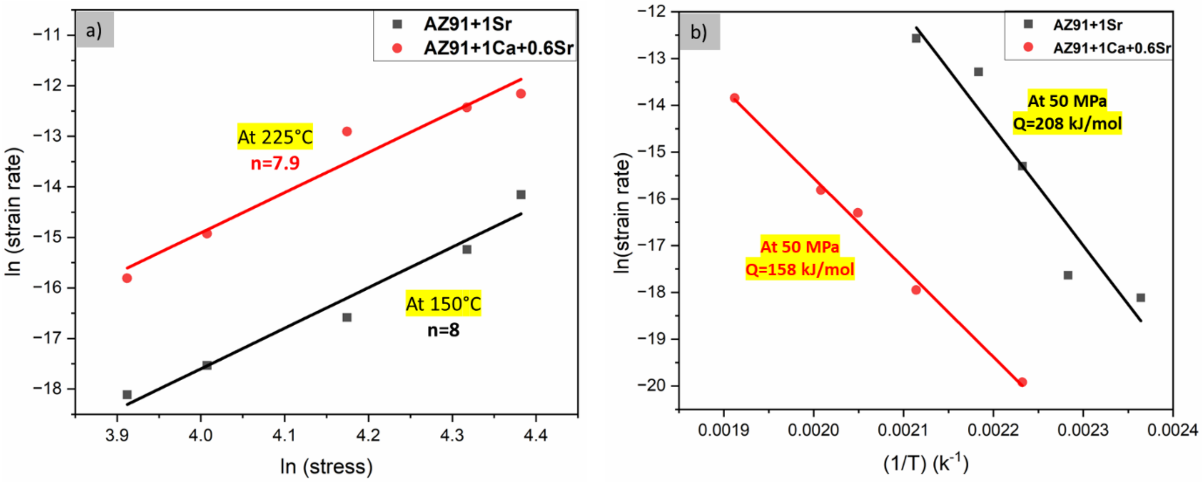

Fig. 6.8: a) The plot between strain rate and applied stress, and b) the plot between strain rate and inverse of temperature for alloys B *(AZ91-1Sr)* and D *(AZ91-1Ca-0.6Sr)*.

6.6 Post-creep microstructure

In order to achieve superior creep resistance, the microstructure needs to be stable at elevated temperatures. In the present study, the creep ruptured microstructures of alloy B *(AZ91-1Sr)* at 200 °C and alloy D *(AZ91-1Ca-0.6Sr)* at 250 °C, under the same stress of 50 MPa, are shown in **Fig. 6.9(a, b)**. The area adjacent to the fracture surface of the crept specimen, parallel to the loading direction, up to a distance of 3 mm, was chosen for the microstructural examination. In the case of alloy B, partial dissolution of precipitates is noticed in the microstructure. Further elemental mapping using EDS analysis confirms that the precipitates taking part in dissolution belong to the β-Mg$_{17}$Al$_{12}$ phase, which is lean in Sr. However, the precipitates rich in Sr, Al$_4$Sr, with needle-shaped morphology, are found to be completely unaffected, as indicated by a yellow arrow in **Fig. 6.9a**. Some traces of undissolved β-Mg$_{17}$Al$_{12}$ phases are also noticed and are indicated by the red arrow. On the other hand, in the case of alloy D, the dissolution of precipitates is rarely observed, **Fig. 6.9b**. In addition, the presence of the undissolved β-Mg$_{17}$Al$_{12}$ phase, which is lean with both Ca and Sr, has also not been detected. The fraction of undissolved precipitates present after the creep rupture is higher in alloy D compared to alloy B. Further, the unaffected precipitates observed in the microstructure of alloy D are rich in Ca and Sr, indicating it to be either Al$_2$Ca or Al$_4$Sr. However, the Al$_4$Sr phase in alloy D is supposed to have a different morphology than needle-shaped as observed in alloy B, and it is difficult to distinguish the Al$_4$Sr and Al$_2$Ca phases, both of them being a part of an interconnected second phase network as seen in **Fig. 6.9b**.

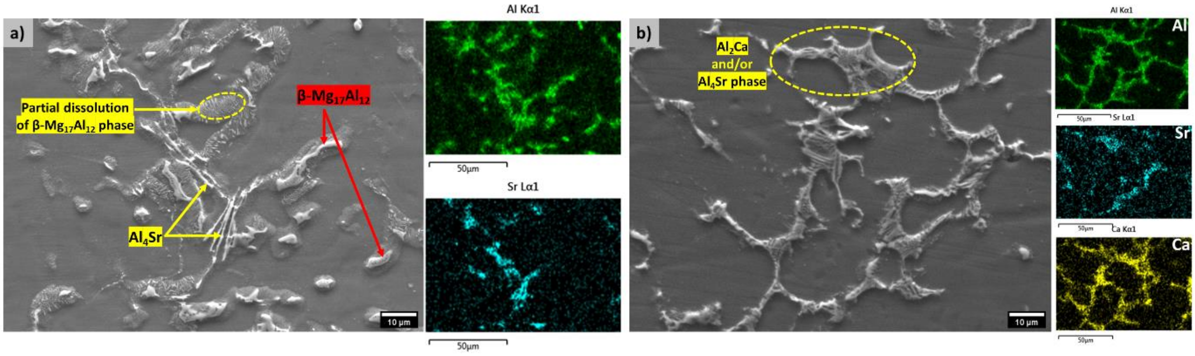

Fig. 6.9: Scanning electron micrograph with EDS analysis of creep ruptured a) alloy B *(AZ91-1Sr)* at 50 MPa stress under 200 °C temperature and b) alloy D *(AZ91-1Ca-0.6Sr)* at 50 MPa stress under 250 °C temperature.

Further, an attempt has been made to investigate the behavior of crack and cavity formation in the creep-ruptured specimen of alloys B and D. The microstructure demonstrating cracks and cavities in both alloys is shown in **Fig. 6.10 (a-d)**. In most of the cases, the crack and cavity observed in alloy B are longer and continuous, **Fig. 6.10 (a, b)**, whereas the cracks are found to be smaller and obstructed by skeleton shape interconnected second phase (Al_2Ca and/or Al_4Sr) in alloy D, **Fig. 6.10 (c, d)**. In alloy B, cracks and cavities are found to initiate adjacent to the needle-shaped Al_4Sr phase, as indicated in **Fig. 6.10 (a, b)**. The needle-shaped Al_4Sr phase in alloy B might have acted as a stress concentrator and promoted crack and cavity formation [94], [150], [152].

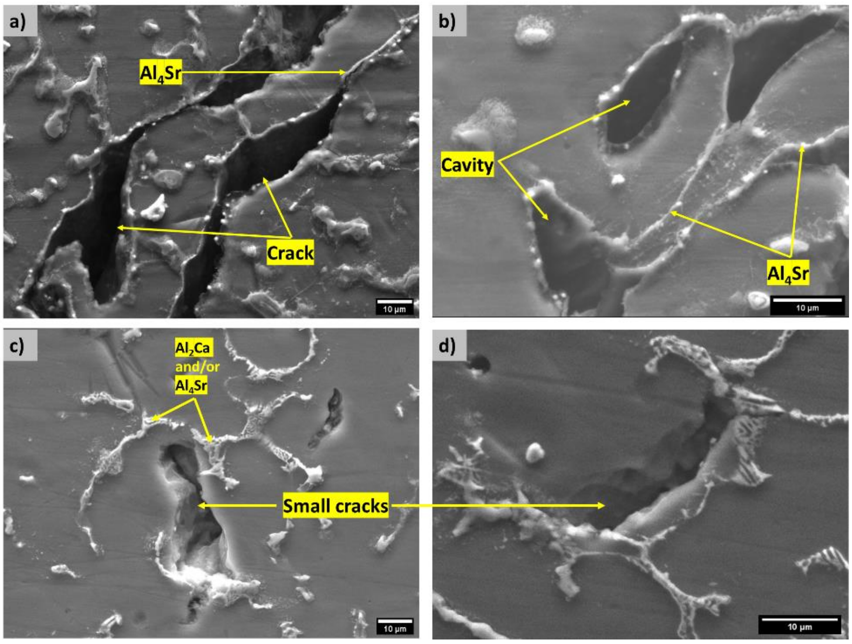

Fig. 6.10: Scanning electron micrograph indicating crack behavior of creep ruptured a, b) alloy B *(AZ91-1Sr)* at 50 MPa stress under 200 °C temperature and c, d) alloy D *(AZ91-1Ca-0.6Sr)* at 50 MPa stress under 250 °C temperature.

6.7 Role of stable phases on creep performance

Variation in the microstructure of the alloys leads to different creep properties. In AZ91 alloy, the β-$Mg_{17}Al_{12}$ phase is observed to be thermally unstable because of the initiation of its dissolution above 125 °C temperature [7]. The improvement in the creep performance of the AZ91 alloys post Sr and Ca addition is attributed to the precipitation of the Al_4Sr and Al_2Ca intermetallic phases. Their precipitation suppresses the formation of the β-$Mg_{17}Al_{12}$ phase in the microstructure [153], especially in alloy D *(AZ91-1Ca-0.6Sr)*, **Fig. 6.3 &6.4e**. Also, the Al_4Sr and Al_2Ca intermetallic phases are observed to be associated with higher dissolution temperatures [94]. According to the thermo-Calc® data presented in **Fig. 6.4(a-d)**, these Al_4Sr and Al_2Ca intermetallic phases are expected to remain thermally stable till 515 °C. The thermal stability of the intermetallic phases at elevated temperatures is further described by considering the thermodynamic property, especially Gibbs free energy (G). In the investigated alloys B *(AZ91-1Sr)* and D *(AZ91-1Ca-0.6Sr)*, the Gibbs free energy associated with the possible phases at the elevated temperatures has been estimated using the Thermo-Calc® database. The variation in Gibbs free energy (G) of the phases (β-$Mg_{17}Al_{12}$, Al_4Sr, Al_2Ca, α-Mg phases, and the whole system) in the temperature range of 27 °C to 515 °C are plotted in **Fig. 6.11**. In all the cases, the free energy of the phases decreases as the temperature increases. The smaller Gibbs free energy (G) indicates the better the thermal stability of the phases [154-156]. The Al_4Sr phase with lower free energy is observed to be the most stable phase over the temperature range of interest in alloy B, **Fig. 6.11a**. On the other hand, the Al_2Ca phase appears to be more thermally stable with much lower free energy than those of Al_4Sr and other phases in alloy D, **Fig. 6.11b**. This is in agreement with the DSC results of the alloy D, exhibiting a lower dissolution temperature of the Al_4Sr phase compared to the Al_2Ca phase (See **Fig. 6.5**).

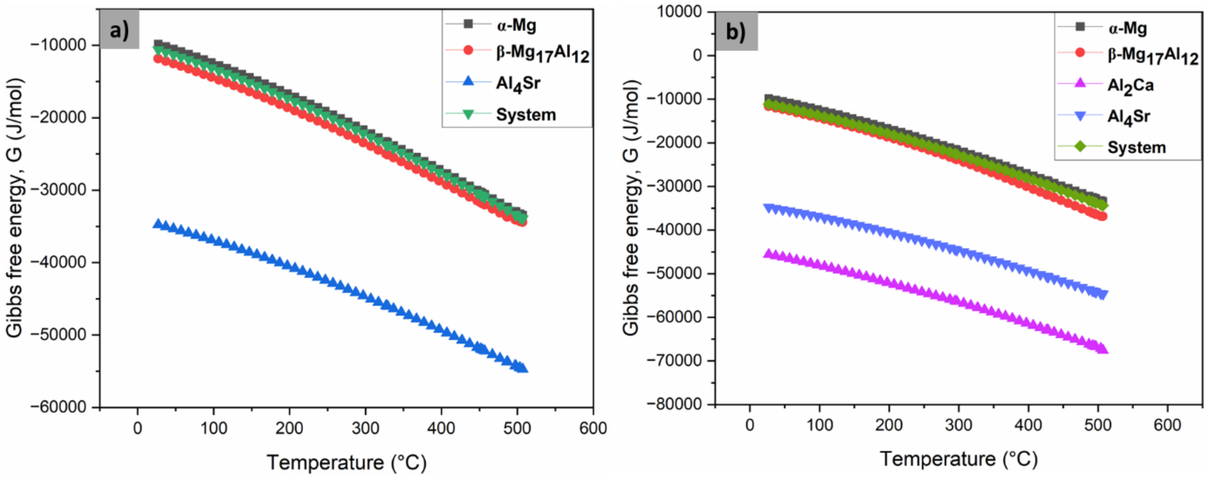

Fig. 6.11: Thermodynamic properties of α-Mg, β-$Mg_{17}Al_{12}$, Al_2Ca, and Al_4Sr phases: a) Gibbs free energy vs. temperature plot for all discussed phases in alloy B *(AZ91-1Sr)* over the temperature range of interest and b) Gibbs free energy vs. temperature plot for all discussed phases in alloy D *(AZ91-1Ca-0.6Sr)* over the temperature range of interest.

The role of these thermally stable precipitates on the overall creep performance of the investigated alloys is twofold. At first, the precipitation of thermally stable Al_2Ca and Al_4Sr phases within the matrix effectively impedes the movement of dislocations, as illustrated in the schematic shown in **Fig. 6.12**a. These precipitates exhibit a higher elastic modulus compared to the β-$Mg_{17}Al_{12}$ phase [148] and are expected to provide modulus strengthening. In addition, during creep deformation at elevated temperatures and stress, these thermally stable precipitates are also effective in restricting grain boundary migration. Several other studies have shown that the dislocations pile up at the interface of the secondary phase and generate back stress during the creep deformation, resulting in the improved creep resistance of the alloy [32], [144], [157-160]. Majhi et al. [12] reported a higher creep resistance of AZ91 alloy modified with the combined addition of Bi and Sr, where the secondary phases cause the dislocations to pile up and undergo tangling at the interface. Similarly, in the present study, the steady state creep rate of alloy D *(AZ91-1Ca-0.6Sr)*, having the combined addition of Ca and Sr, was one or two orders lower compared to the other investigated alloys. The improved creep resistance of the alloy D could be mainly attributed to the existence of the most thermally stable Al_2Ca phase in addition to the Al_4Sr phase in the alloy.

On the other hand, the Ca and Sr have almost zero solubility in the α-Mg matrix, even at 500 °C. As a result, insoluble Ca and Sr combine with Al and precipitate as Al_2Ca and Al_4Sr intermetallic phases during the final stage of solidification from the liquid state. These thermally stable precipitates along the grain boundaries pin the grain growth at elevated temperatures [19] [153]. Therefore, these precipitates are expected to play a significant role in grain refinement by hindering grain growth during solidification. In addition to the precipitates, the grain refinement in the alloys can be further expected to result from the squeeze casting process. A smaller grain size leads to an increased number of grain boundaries, which in turn is expected to restrict the motion of dislocations during creep deformation, as illustrated in the schematic shown in **Fig. 6.12**b, and enhances creep resistance. Several authors have noted enhancements in both room and elevated temperature mechanical properties of the Mg-Al alloy due to grain refinement [15], [162] [15]. The electron backscattered (EBSD) orientation maps demonstrating the grain refinement in alloys A to D are shown in **Fig. 6.13**. Mainly, in alloy D, where Ca and Sr are added together, the grain refinement is more evident, as shown in **Fig. 6.13d**. As discussed in section 3.3, alloys B *(AZ91-1Sr)* and D *(AZ91-1Ca-0.6Sr)* exhibit a dislocation-based creep mechanism. A smaller grain size leads to an increased number of grain boundaries, which in turn restricts the motion of dislocations during creep deformation and enhances creep resistance. Therefore, alloy D, with a minimum grain size of 32 μm, is expected to contribute to higher creep resistance in accordance with its governing creep mechanism.

Furthermore, as shown in section 3.4, the crack susceptibility of the AZ91 alloy grows with the addition of Sr, i.e., in alloy B *(AZ91-1Sr)*. Generally, the precipitation of the needle-shaped Al_4Sr phase on the Sr addition plays a significant role in stress concentration cracking during the creep process, thus resulting in long matrix crack formations. However, in alloy D *(AZ91-1Ca-0.6Sr),* the precipitation of the Al_2Ca phase interconnected with the Al_4Sr phase in a network of skeleton morphology is observed to retard the crack propagation, thus improving the creep performance of alloy D. The higher thermal stability and elastic strength associated with the Al_2Ca phase provides it enough strength to restrict the crack propagation inside the matrix. In addition, the change in the morphology of the Al_4Sr phase from needle shape to irregular shape, which is less detrimental to crack initiation and propagation **(**see **Fig 6.1d)**, reduces the probability of stress concentration cracking in the alloy D. Also, the precipitation of Al_2Ca phase in addition to Al_4Sr phase in alloy D reduces the fraction of Al_4Sr in the microstructure. As a result, the presence of thermally stable Al_2Ca and Al_4Sr phases, the smallest grain size, and change in the needle-shaped morphology of the Al_4Sr phase with reduced fraction in alloy D *(AZ91-1Ca-0.6Sr)* resulted in the best creep performance of alloy D *(AZ91-1Ca-0.6Sr)* among all the investigated alloys.

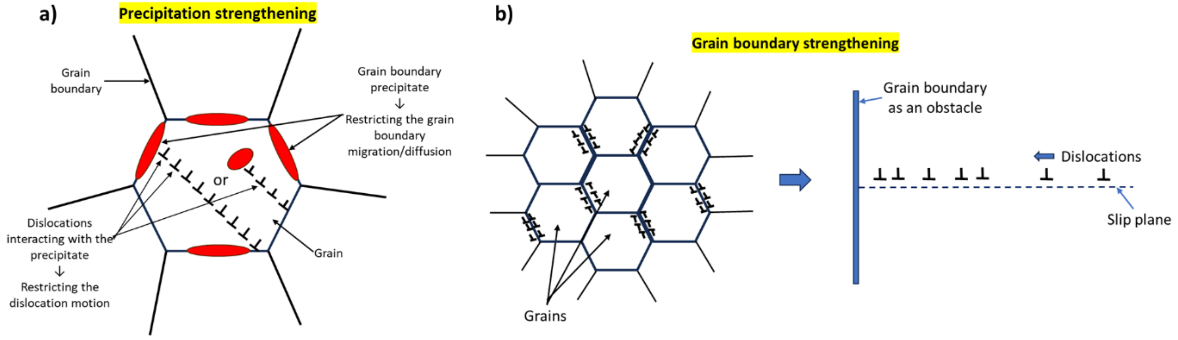

Fig. 6.12: The schematic illustrates a) precipitation strengthening and b) grain boundary strengthening governing the creep performance of the AZ91 Mg alloys.

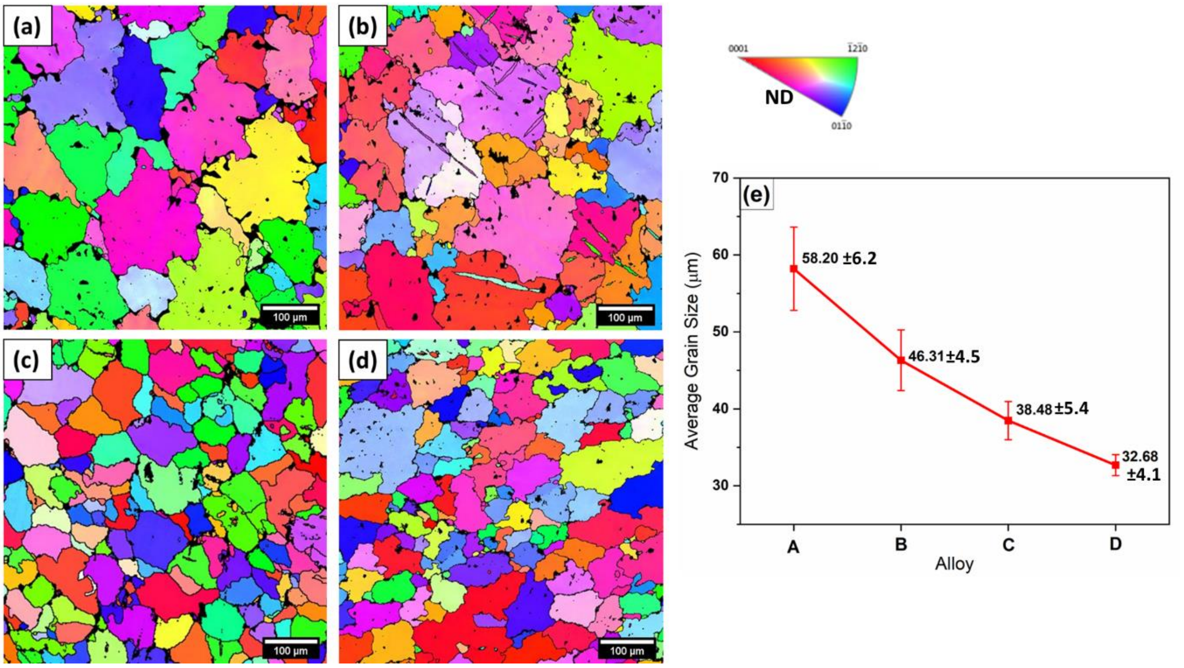

Fig. 6.13: EBSD orientation maps of squeeze-cast a) *AZ91*, b) *AZ91-1Sr*, c) *AZ91-1Ca-0.3Sr*, and d) *AZ91-1Ca-0.6Sr* Mg alloys with e) average grain size plot.

6.8 Conclusion

In the present investigation, the AZ91 Mg alloy with individual Sr and combined Sr-Ca addition is subjected to microstructural and creep study within 150 °C-250 °C temperature range under 50-80 MPa stress. The primary conclusions drawn from the present investigation are outlined below:

1. Incorporating Sr and Ca into the AZ91 alloy facilitates the formation of thermally stable Al_2Ca and Al_4Sr intermetallic phases, suppressing the thermally unstable β-$Mg_{17}Al_{12}$ phase precipitation and hence improving the creep resistance. Alloy D *(AZ91-1Ca-0.6Sr)*, which contains both Al_2Ca and Al_4Sr, exhibits superior creep performance (at 175 °C-250 °C under 50 MPa stress) compared to the other investigated alloys. The steady-state strain rate of alloy D is found to be $1.36*10^{-7}$ s^{-1} and $9.71*10^{-7}$ $s^{-1,}$ respectively, at 225 °C and 250 °C under 50 MPa stress.
2. Dislocation climb dominates the creep deformation process in both alloy compositions of B *(AZ91-1Sr)* at 150 °C (n=8) and D *(AZ91-1Ca-0.6Sr)* at 225 °C (n=7.9) under 50 MPa stress.
3. The morphology of the Al_4Sr intermetallic phase in Sr-containing AZ91 alloy was found to serve a critical role. The needle-shaped Al_4Sr intermetallic phase serves as a potential site for both crack initiation and cavity formation in alloy B *(AZ91-1Sr)*. Whereas, Al_2Ca and/or Al_4Sr phases with an interconnected network of skeleton morphology in alloy D *(AZ91-1Ca-0.6Sr)* are found to impede the crack propagation effectively.

Chapter 7

Effect of Heat Treatment on the Microstructure Evolution and Creep Performance of Squeezed Cast AZ91-Based Alloys

As discussed in Chapter 6, suitable alloying addition appears to be a potential technique in order to improve the creep performance of the AZ91 Mg alloy. Though it is a potential technique, it involves higher production costs and a longer cycle time. Therefore, in the study reported in Chapter 7, an attempt has been made to investigate the influence of heat treatment on the creep performance of the present squeezed cast AZ91 alloys. The present chapter investigates the microstructure, hardness, and creep performance of the squeeze-cast AZ91 base alloy (*Alloy A*), AZ91 with 1wt.% Sr addition (*Alloy B*), and AZ91 with 1wt.%Ca-0.6wt.%Sr addition (*Alloy C*) subjected to heat treatment. These alloys on heat treatment (solution treatment at 415 °C for 24 h) are expected to encounter a change in their microstructures, thus influencing the creep performance and hardness.

Chapter 7

Effect of Heat Treatment on the Microstructure Evolution and Creep Performance of Squeezed Cast AZ91-Based Alloys

---

The work in this chapter has been submitted for publication as: Hitesh Patil, Ankush Marodkar, Abhijit Ghosh, and Hemant Borkar, "Effect of heat treatment on the microstructure evolution and creep performance of squeezed cast AZ91-based alloys", *The Journal of The Minerals, Metals & Materials Society (Under Revision)*.

7.1 Introduction

Though the suitable alloying addition in order to improve the creep performance of the AZ91 Mg alloy appears to be a potential technique, it involves higher production costs and a longer cycle time [46]. This led to the strategy that includes a heat treatment process to achieve the desired creep performance of the Mg-Al alloys under investigation. On solutionizing heat treatment, the β-$Mg_{17}Al_{12}$ phase responsible for the poor creep performance of the AZ91 alloy is expected to dissolve homogeneously into the α-Mg matrix, which perhaps enhances the mechanical properties of the alloy at both ambient and elevated temperatures [1], [2], [8], [9], [20]. In the majority of studies conducted over the past decade, numerous researchers have concentrated on investigating the impact of different heat treatment processes, such as solutionizing and aging, on the mechanical properties of Mg-Al alloys [7], [22-24]. However, there has been a scarcity of studies examining the effect of different heat treatment processes on the creep performance of the Mg-Al alloy. To the best of the author's knowledge, specifically, investigations on the tensile creep performance of squeeze-casted AZ91 (Mg-Al-Zn) alloy that has the addition of Sr and Ca followed by heat treatment are not available. Therefore, the present study aims to preliminarily investigate the influence of heat treatment on the microstructure evolution, hardness, and tensile creep properties of the squeeze-casted AZ91-based alloys. The alloys considered in the present study for the heat treatment are the same alloys investigated for creep performance in the squeeze-cast conditions in Chapter 6, i.e., AZ91 base alloy (*Alloy A*), AZ91 with 1wt.% Sr addition (*Alloy B*), and AZ91 with 1wt.%Ca-0.6wt.%Sr addition (*Alloy C*). The creep properties of the heat-treated alloys will be compared to the same alloys investigated previously in the squeeze-cast condition. In addition, the activation energy of the creep deformation has also been estimated in the case of heat-treated alloys and compared with the same alloys in as-cast conditions.

7.2 Chemical composition of the investigated alloys

The chemical composition of the squeeze-cast investigated *AZ91* Mg alloys estimated using an optical emission spectrometer in the present work is listed in **Table 7.1**.

Table 7.1: Material designation and chemical composition of the investigated AZ91 alloys (Weight%).

Designation	Alloy	Al (wt%)	Zn (wt%)	Mn (wt%)	Si (wt%)	Ca (wt%)	Sr (wt%)	Mg
A	AZ91	9.01 ± 0.142	1.57 ± 0.002	0.17 ± 0.002	0.022 ± 0.011	-	-	Bal.
B	AZ91-1Sr	8.72 ± 0.138	0.511 ± 0.002	0.234 ± 0.002	0.021 ± 0.009	-	0.998 ± 0.002	Bal.
D	AZ91-1Ca-0.6Sr	8.21 ± 0.136	0.49 ± 0.002	0.18 ± 0.002	0.014 ± 0.019	1.06 ± 0.004	0.8 ± 0.002	Bal.

7.3 Microstructure Characterization of the heat-treated AZ91 alloys

As we have seen in Chapter 6, the addition of Sr and Ca to the squeeze-cast AZ91 alloy leads to the precipitation of thermally stable Al_4Sr and Al_2Ca intermetallic phases in the microstructure by suppressing the thermally unstable β-$Mg_{17}Al_{12}$ phase. Among the investigated alloys, the AZ91, with the combined addition of Ca and Sr, demonstrates a superior creep performance. The as-cast specimens considered in the present chapter are subjected to heat treatment. The heat treatment follows the heating of the specimen at 415 °C for a soaking time of 24 h. On completion of soaking time, the specimen was subjected to immediate water quenching to room temperature. From the microstructure and respective elemental mapping using EDS analysis of the heat-treated AZ91 alloys (alloys A, B, and C) shown in **Fig. 7.1**, it is observed that the β-$Mg_{17}Al_{12}$ phase has undergone a complete dissolution into the Mg matrix in alloys A, B, and C, as shown in **Fig. 7.1a-c**, whereas the other secondary phases like Al_4Sr and Al_2Ca are retained in the microstructure of the alloys B and C, as shown in **Fig. 7.1b, c**. Thus, these Al_4Sr and Al_2Ca phases can be considered thermodynamically stable compared to the β-$Mg_{17}Al_{12}$ phase. From the micrograph shown in **Fig. 7.1b, c**, the morphology of the Al_4Sr phase was observed to be altered on heat treatment from needle shape to small particulate shape distributed over the grain boundaries, whereas the skeleton morphology of the Al_2Ca phase is unaffected, **Fig. 7.1c**. The dissolution of the β-$Mg_{17}Al_{12}$ phase and thermal stability of the remaining Al_2Ca and Al_4Sr phases on heat treatment can also be further confirmed using a thermoCalc® plot shown in **Fig. 7.2a**. In the plot representing alloy C, the β-$Mg_{17}Al_{12}$ phase is observed to be experiencing complete dissolution at the temperature of 300 °C since the other Al_2Ca and Al_4Sr phases are observed to be consistent till the temperature of 515 °C. The identification of the precipitates in all as-cast and heat-treated alloys was further characterized by XRD analysis, as shown in **Fig. 7.2b**. The X-ray diffraction analysis confirms the existence of all the above-mentioned phases in as-cast conditions and the simultaneous dissolution of the β-$Mg_{17}Al_{12}$ phase on heat treatment in alloys A and B. On the other hand, the β-$Mg_{17}Al_{12}$ phase has almost been suppressed in alloy C on the combined addition of Ca and Sr in AZ91 alloy. Therefore, the peak for the β-$Mg_{17}Al_{12}$ phase has not been detected in alloy C in both as-cast and heat-treated conditions.

Furthermore, the investigated as-cast alloys A, B, and C subjected to heat treatment experienced grain growth, as demonstrated by their EBSD plots, as shown in **Fig. 7.3(a-f)**. The comparison of the average grain size of the as-cast and heat-treated alloys for respective alloys compositions is represented in the plot shown in **Fig. 7.3g**. When an alloy is subjected to elevated temperature heat treatment, the atom's kinetic energy increases, which is responsible for the grain boundaries of the individual grains to migrate and merge into one larger grain [168]. The grain growth in the alloy significantly influences the strength and hardness of the alloys under consideration [169] [170].

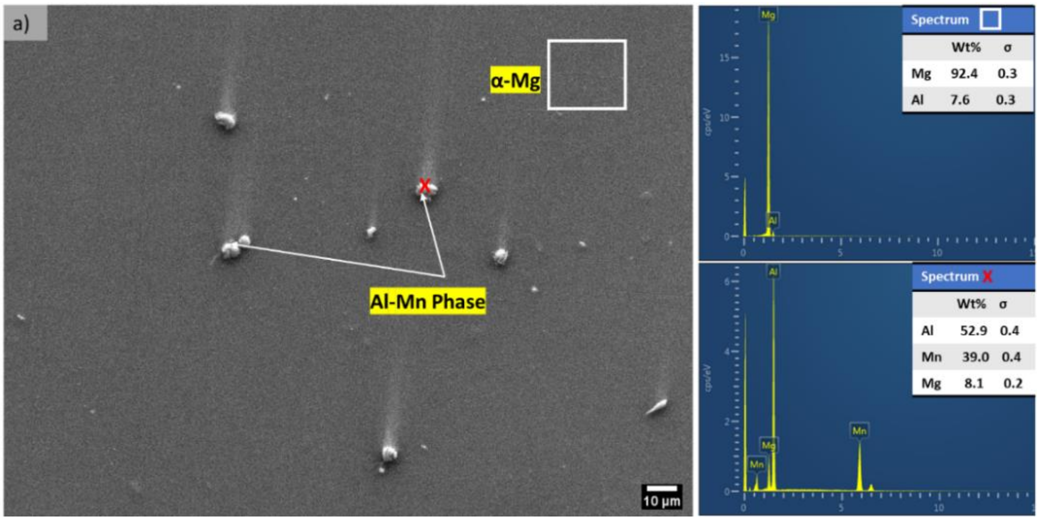

Spectrum ☐	Wt%	σ
Mg	92.4	0.3
Al	7.6	0.3

Spectrum X	Wt%	σ
Al	52.9	0.4
Mn	39.0	0.4
Mg	8.1	0.2

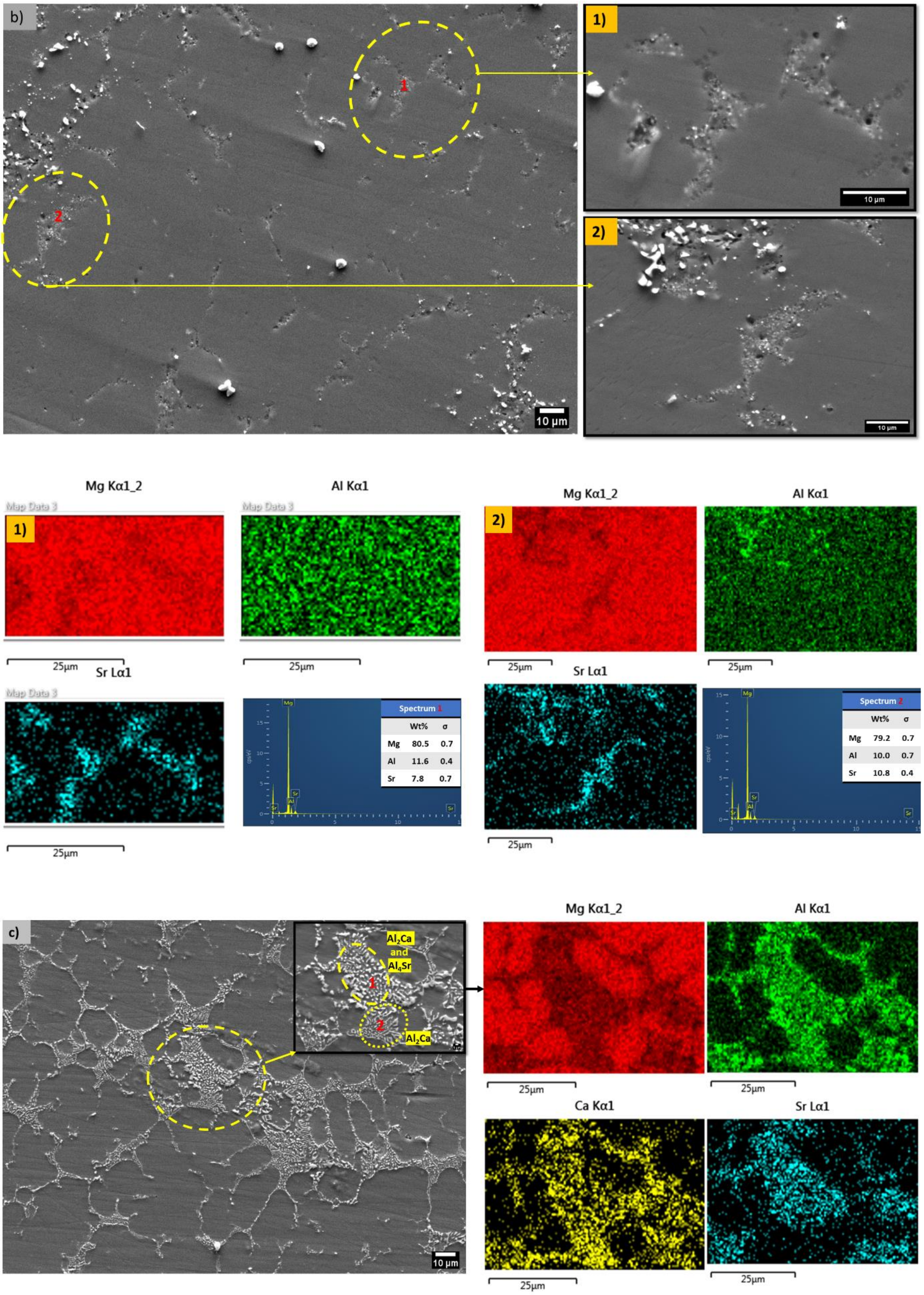

Spectrum 1	Wt%	σ
Mg	80.5	0.7
Al	11.6	0.4
Sr	7.8	0.7

Spectrum 2	Wt%	σ
Mg	79.2	0.7
Al	10.0	0.7
Sr	10.8	0.4

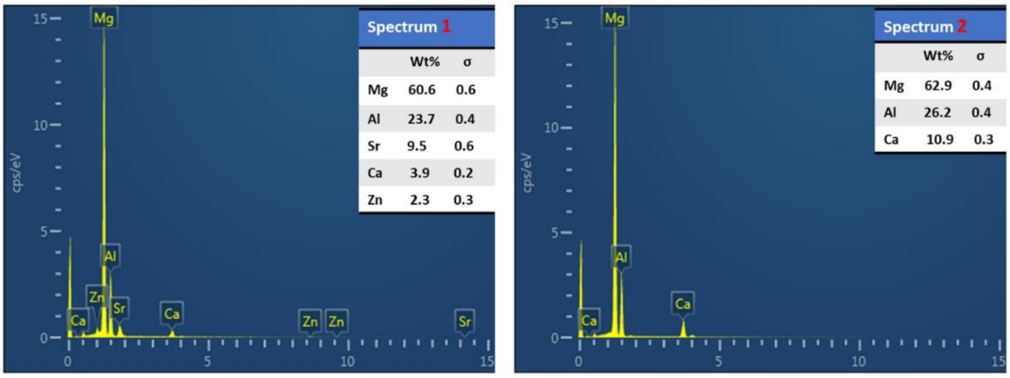

Spectrum 1

	Wt%	σ
Mg	60.6	0.6
Al	23.7	0.4
Sr	9.5	0.6
Ca	3.9	0.2
Zn	2.3	0.3

Spectrum 2

	Wt%	σ
Mg	62.9	0.4
Al	26.2	0.4
Ca	10.9	0.3

Fig. 7.1: Heat-treated scanning electron micrograph and respective EDS analysis of the a) alloy A (AZ91), b) alloy B (AZ91-1Sr), and c) alloy C (AZ91-1Ca-0.6Sr).

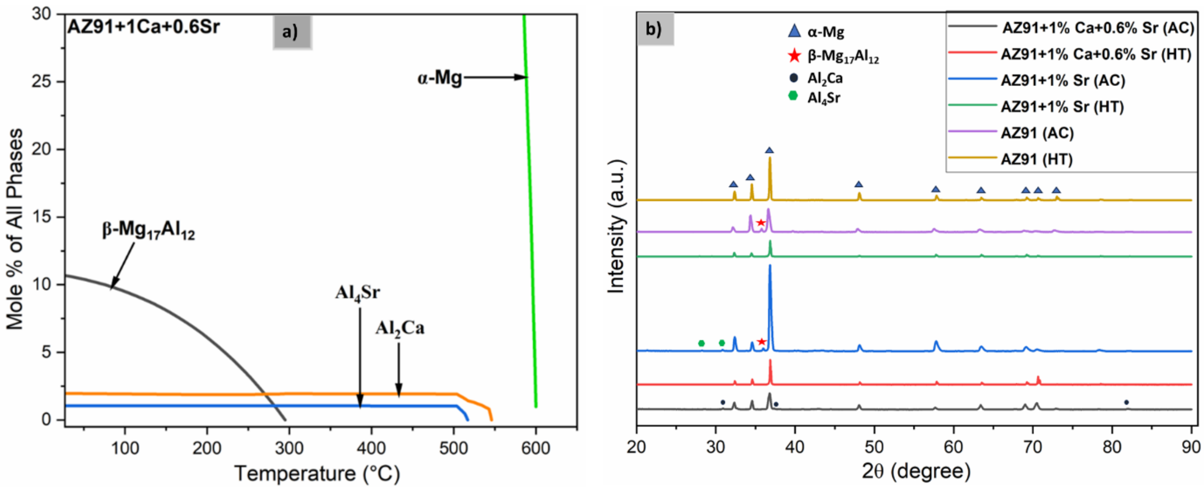

Fig. 7.2: a) Thermodynamic plot indicating the change in the mole % of precipitated phases with temperature and b) X-ray diffraction profile of the investigated AZ91 Mg alloys (AC-as-cast and HT- heat-treated).

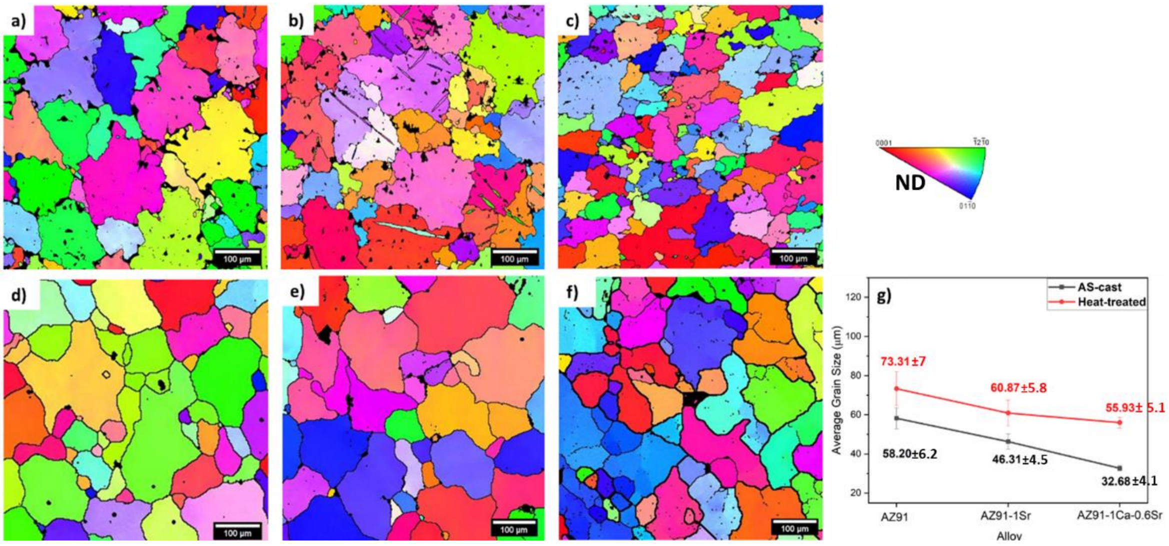

Fig. 7.3: EBSD orientation maps of the squeeze-casted a) AZ91, b) AZ91-1Sr, c) AZ91-1Ca-0.6Sr alloy, and heat-treated d) AZ91, e) AZ91-1Sr, f) AZ91-1Ca-0.6Sr alloy with g) average grain size plot associated with both squeeze-cast and heat-treated alloys.

7.4 Hardness

The hardness of the investigated squeeze-cast and heat-treated AZ91 alloys has been accessed with the Rockwell-B macro hardness test. The test was performed according to the E18-18a standard, was performed using a digital Rockwell hardness tester (Model: TRH-150 D) with a 1/16” steel ball-type indentor. The indentor was forced into the sample surface using an applied load of 15 kgf. Here, the hardness values reported are estimated as an average of five measurements.

The macro hardness test was carried out to study the bulk property of the AZ91 alloys, which includes the combined effect of the Mg matrix and secondary phases on hardness. The hardness of the AZ91 alloys A (AZ91), B (AZ91-1Sr), and C (AZ91-1Ca-0.6Sr) with their respective estimated values are illustrated in **Fig. 7.4**. By comparing only squeeze-cast alloys, the variation in hardness observed is in the order of $H_{(alloy\ C)} > H_{(alloy\ B)} > H_{(alloy\ A)}$. On the other hand, after heat treatment, the respective hardness values of the AZ91 alloys A and B are increased, but the hardness of alloy C is reduced after heat treatment, as shown in **Fig. 7.4**.

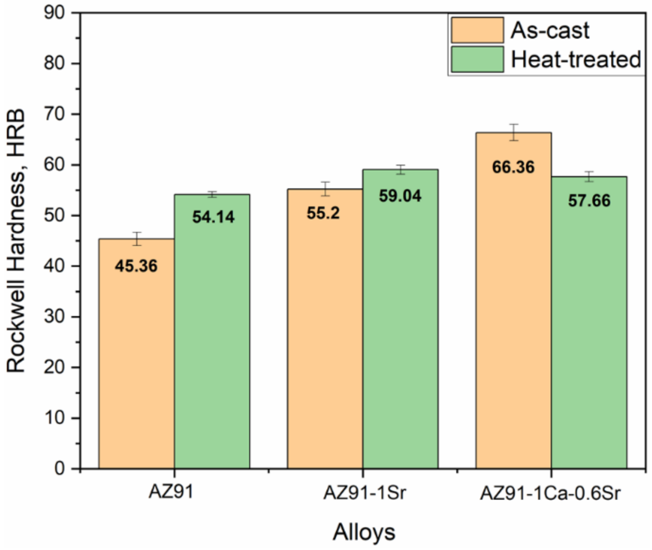

Fig. 7.4: Comparison of hardness of squeezed-cast and heat-treated AZ91 alloys.

7.5 Creep Properties

In this work, all three compositions of AZ91 alloys A, B, and C subjected to specified heat treatment are tested under tensile creep test at 50 MPa stress within the temperature range of 150 °C-200 °C for alloys A and B, while 175 °C-250 °C for alloy C. The higher creep test temperature was selected for alloy C because of its lower creep rate, even at higher temperatures compared to other alloys A and B. All the tests were run till the rupture of the specimen. To demonstrate the creep behavior of the heat-treated AZ91 alloys, the typical bucket-type tensile creep curves plotted from the creep test data are shown in **Fig. 7.5.** The secondary minimum creep rate values associated with the creep curves are summarized in **Table 7.2.** For convenience, the minimum creep rate ($\dot{\varepsilon}$) during secondary creep is considered to represent the creep performance of the concerned alloys. Furthermore, the creep performance of the present heat-treated alloys is compared with the same alloys in as-cast conditions, as shown in **Fig. 7.6**. From the creep curves shown in **Fig. 7.5a-c**; it is observed that the creep rate of the heat-treated alloys increases with increasing creep temperature under the same applied stress. Also, the addition of Ca and Sr in AZ91 alloy further improves the creep performance by decreasing the creep rate of the alloys in both as-cast and heat-treated conditions, **Fig. 7.6 (a-c)**. Meanwhile, when comparing the heat-treated alloys A, B, and C with the same alloys in as-cast condition, further considerable improvement in the creep performance of heat-treated alloys A and B has been observed with decreasing creep rate, **Fig.**

7.6 (a, b). In contrast, a small decrease in the creep performance of alloy C with increasing creep rate has been observed post-heat-treatment, **Fig. 7.6c**.

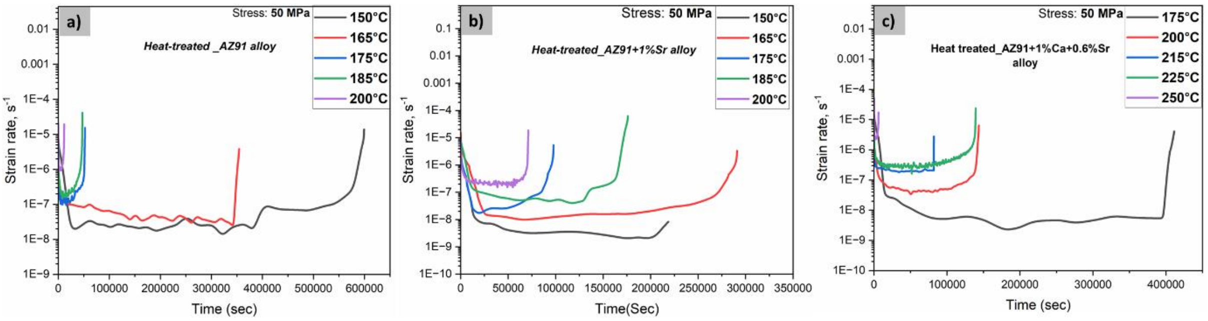

Fig. 7.5: Strain rate vs. time creep curve of the heat-treated a) *AZ91* alloy, b) *AZ91-1Sr* alloy, and c) *AZ91-1Ca-0.6Sr* alloy at applied stress and different temperatures.

Table 7.2: The estimated secondary creep rate values of the heat-treated AZ91 Mg alloys.

Alloys	**Secondary minimum creep rate, s^{-1}**							
	150 °C	**165 °C**	**175 °C**	**185 °C**	**200 °C**	**215 °C**	**225 °C**	**250 °C**
A *(AZ91)*	2E-08	3.9E-08	6.27E-08	1.41E-07	9.71E-07	-	-	-
B *(AZ91-1Sr)*	3E-09	9.90E-09	2.55E-08	5.80E-08	2E-07	-	-	-
C *(AZ91-1Ca-0.6Sr)*	-	-	4.8E-09	-	4.14E-08	1.78E-07	2.70E-07	2.48E-06

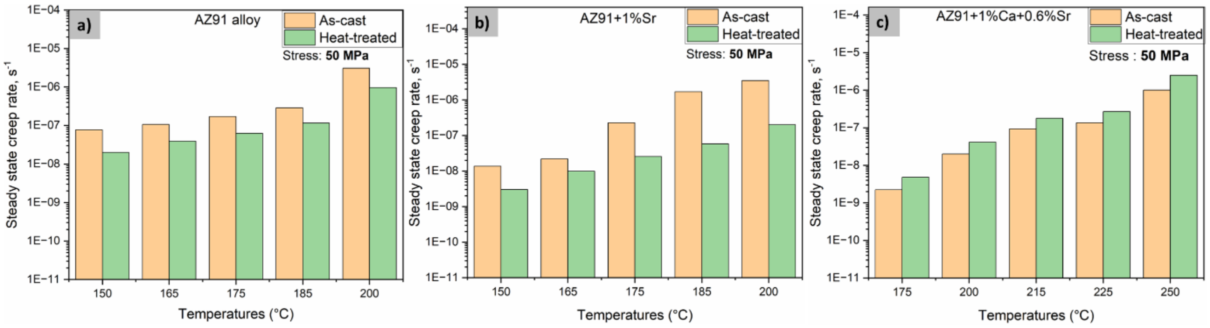

Fig. 7.6: Bar chart comparing the steady state creep rate between as-cast and heat-treated a) *AZ91* alloy, b) *AZ91-1Sr* alloy, and c) *AZ91-1Ca-0.6Sr* alloy at applied 50 MPa stress and different temperatures.

Further, an attempt has been made to estimate the apparent activation energy (Q) of the creep deformation in present heat-treated alloys. The steady-state secondary creep rate $\dot{\varepsilon}$ of the Mg alloy is represented by the power-law equation in the stress (σ) and temperature (T) range of interest [10]:

$$\dot{\varepsilon} = A\,(\sigma)^{n} \exp\left(-\frac{Q}{RT}\right) \qquad (7.1)$$

Where A is a material-related constant, σ the applied stress, T is the creep temperature, R is the gas constant, Q is the apparent activation energy for creep, and n is the stress exponent. Based on **Eq. (7.1)**, an Arrhenius plot of $\dot{\varepsilon}$ vs. 1/T at a specific stress will yield the apparent activation energy (Q) value. The apparent activation energy (Q) values of creep deformation in the case of heat-treated alloys A *(AZ91)*, B *(AZ91-1Sr)*, and C *(AZ91-1Ca-0.6Sr)* are estimated in the temperature range of 150 °C-200 °C for alloy A and alloy B, whereas 175 °C-225 °C for alloy C from the slope of the logarithmic plot of $\dot{\varepsilon}$ vs. 1/T at the same 50 MPa stress, as shown in **Fig.7.7**. In the case of alloys A *(AZ91)* and B (*AZ91-1Sr)*, the apparent activation energy (Q) is estimated to be 125 kJ/mol and 140.6 kJ/mol, respectively, which are in good agreement with the activation energy required for the self-diffusion of Mg lattice (135 kJ/mol). Whereas the apparent activation energy (Q) is estimated to be 160.64 kJ/mol for the alloy C *(AZ91-1Ca-0.6Sr)*, which is much higher than the activation energy of Mg lattice self-diffusion. The apparent activation energy of the investigated alloys is observed to be increasing in the following manner, $Q_C > Q_B > Q_A$, indicating a higher resistance to the creep deformation in the case of alloy C than alloy B and then A. The increased value of activation energy associated with the investigated alloys is perhaps attributed to the alloying addition and heat treatment. The activation energies of the alloys A, B, and C in both as-cast and heat-treated conditions are illustrated in **Table 7.3**. The activation energy in the case of alloy A increases on heat treatment from 117 to 125 kJ/mol, whereas it decreases for alloy C from 208 to 160 kJ/mol, which is in good agreement with the demonstrated creep rates of these alloys, as shown in **Fig. 7.6**. In contrast, in alloy B, on the basis of its enhanced creep performance on heat treatment, the activation energy of creep deformation is expected to increase in comparison to the squeeze cast alloy. However, it decreased from 158 to 140 kJ/mol, **Table 7.3**. A further thorough investigation is necessary to address this anomaly.

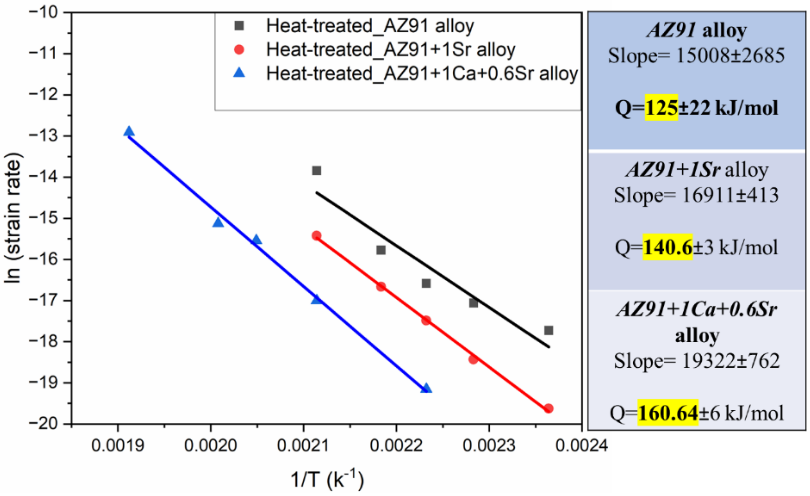

Fig. 7.7: Logarithmic plot of strain rate ($\dot{\varepsilon}$) versus the inverse of temperature (1/T) at the same 50 MPa stress for investigated heat-treated AZ91 alloys.

Table 7.3: The apparent activation energy values of creep deformation of investigated squeezed cast and heat-treated Mg alloys.

Apparent activation energy (Q, kJ/mol)		
Investigated alloys	Heat-treated	Squeeze-cast
AZ91	125	117
AZ91-1Sr	140	158
AZ91-1Ca-0.6Sr	160	208

7.6 Microstructure evolution post-creep deformation

The present heat-treated AZ91 alloys A *(AZ91)*, B *(AZ91-1Sr)*, and C *(AZ91-1Ca-0.6Sr)* post-creep rupture are further subjected to the microstructural examination in order to investigate the microstructure modification during the creep deformation. A specimen for the microstructure analysis is taken from the area parallel to the tensile axis and adjacent to the rupture surface at a distance of 3 mm. The scanning electron micrographs of alloys A, B, and C creep ruptured at 50 MPa stress under 200 °C are shown in **Fig. 7.8-7.10**. In the micrographs, the precipitation of the β-$Mg_{17}Al_{12}$ phase during the creep deformation has been observed in **Fig. 7.8b, 7.9b, and 7.10b**. On heat treatment, the dissolved β-$Mg_{17}Al_{12}$ phase increases the Al concentration in the Mg matrix, which provides a solid solution strengthening at the initial stage of the creep. Later on, during creep deformation, the concentrated Al from the matrix precipitates out again in the form of a β-$Mg_{17}Al_{12}$ phase, preferentially along the grain boundaries [4] [126] [171]. Such precipitation of the β-$Mg_{17}Al_{12}$ phase during the creep deformation is attributed to the presence of heterogeneous nucleation sites like dislocations [4], [10], [40]. The precipitated β-$Mg_{17}Al_{12}$ phase has appeared in two different morphologies, such as lamellar and small particulate in alloy A, **Fig. 7.8(a, b)**, while in alloy B, the lamellar precipitates of the β-$Mg_{17}Al_{12}$ phase, in addition to a small particulate of the Al_4Sr phase, are observed along the grain boundaries, **Fig. 7.9(a,b)**. The microstructure of alloy C comprised both Al_2Ca and Al_4Sr phases in the form of small particulates along with lamellar β-$Mg_{17}Al_{12}$ phase, as shown in **Fig.** 7.**10(a,b)**. The existence of these phases in the respective alloys mentioned above is confirmed using an EDS analysis, which is additionally demonstrated using X-ray diffraction (XRD) analysis, as shown in **Fig. 7.11**. The XRD plots of all three heat-treated alloys A, B, and C subjected to creep rupture indicate β-$Mg_{17}Al_{12}$ phase peaks (marked by a red dotted circle) in addition to other Al_2Ca and Al_4Sr phases. On the other hand, the disintegration of the skeleton morphology of the Al_2Ca phase (**see Fig. 7.1c**) has been observed in the post-creep microstructure of the alloy C, which is attributed to the elevated temperature exposure during the creep process, **Fig. 7.10a**. Such a disintegration of the skeleton morphology of the Al_2Ca phase may adversely affect the creep performance of the alloy C [172]. Further, the occurrence of intergranular crack as a result of applied load and temperature during the creep deformation, as shown in **Fig. 7.8(b-d), 7.9b,** also results in accelerated creep.

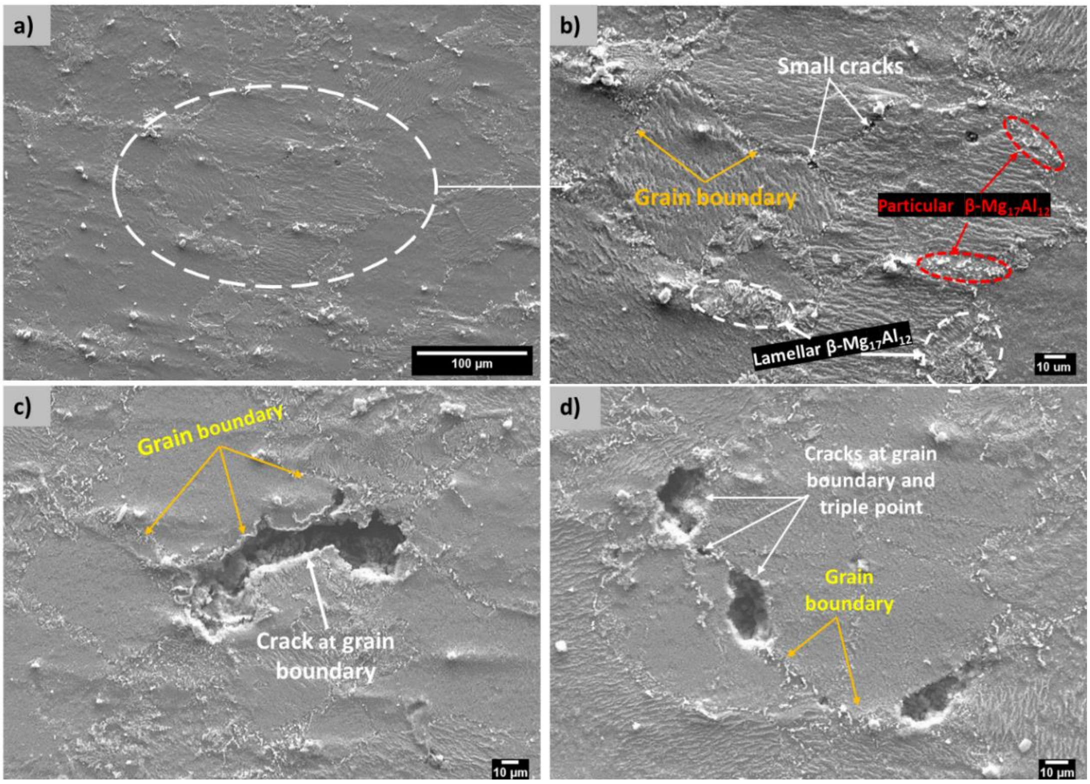

Fig. 7.8: SEM micrograph of the heat-treated *AZ91* alloy subjected to creep rupture at 50 MPa stress under 200 °C temperature.

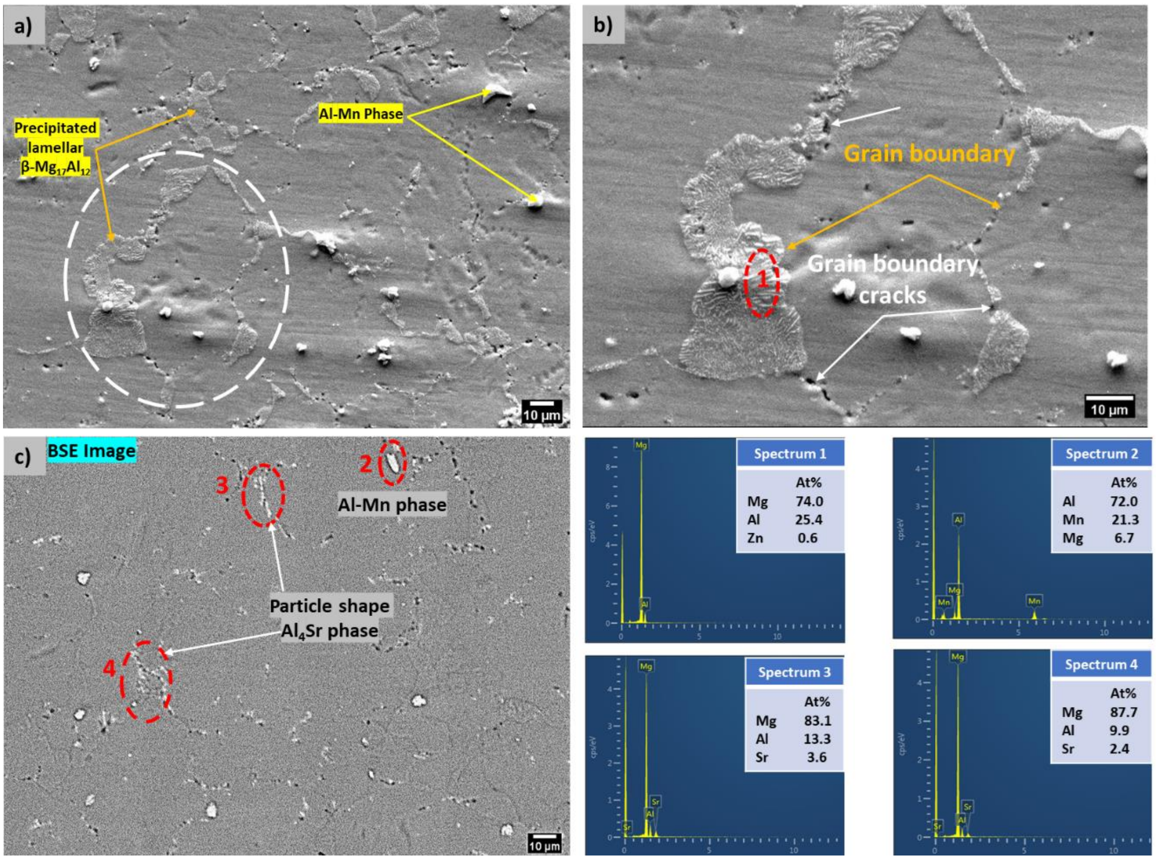

Fig. 7.9: SEM micrograph of the heat-treated *AZ91-1Sr* alloy subjected to creep rupture at 50 MPa stress under 200 °C temperature.

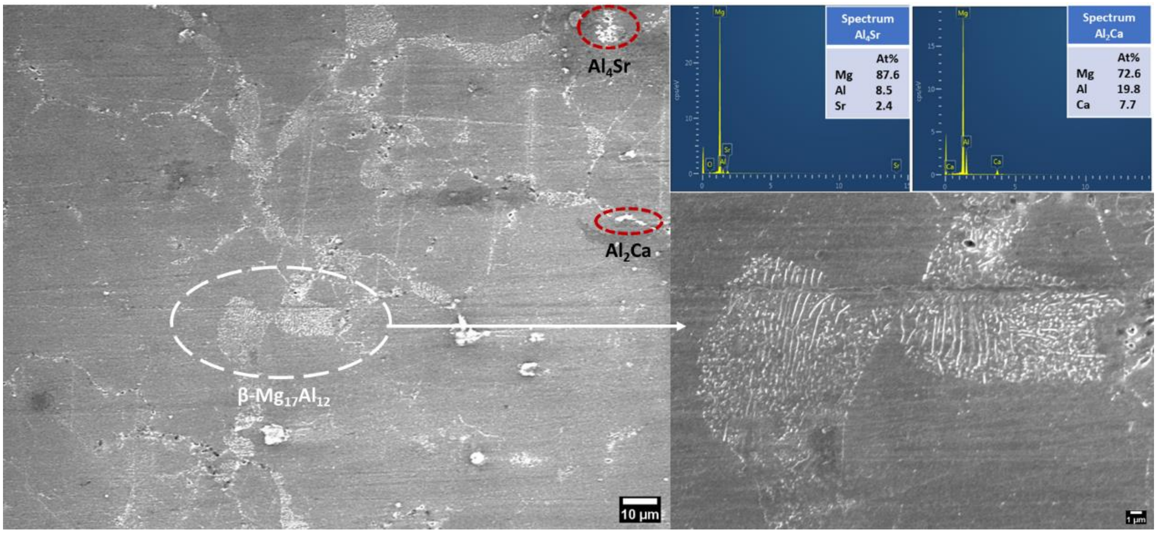

Fig. 7.10: SEM micrograph of the heat-treated *AZ91-1Ca-0.6Sr* alloy subjected to creep rupture at 50 MPa stress under 200 °C temperature.

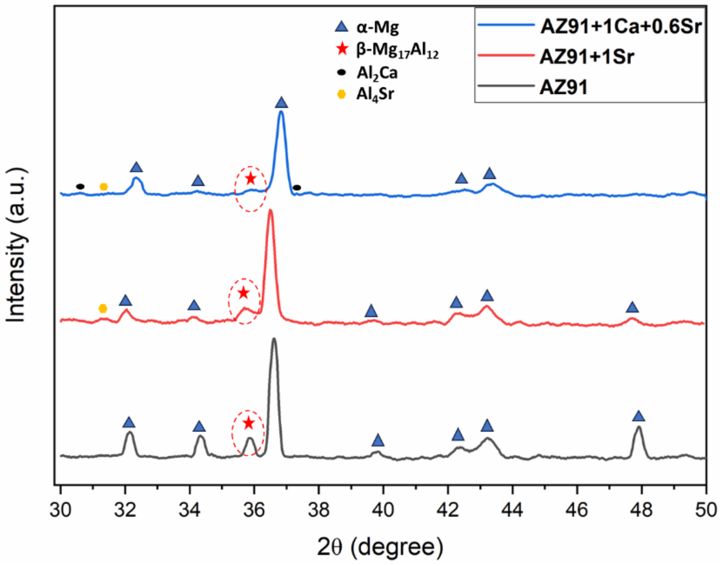

Fig. 7.11: X-ray diffraction profile of heat-treated creep ruptured AZ91 alloys.

7.7 *Effect of heat-treatment on creep performance and hardness*

As discussed in Chapter 6, the poor creep performance of the as-cast AZ91 alloy is attributed to the thermally unstable β-$Mg_{17}Al_{12}$ phase. The improved creep performance of the AZ91 alloy on the addition of Ca and Sr is attributed to the precipitation of Al_4Sr and Al_2Ca intermetallic grain boundary phases. These phases are observed to be thermally stable phases, thus effectively obstructing the dislocation motion during creep deformation. In addition, these phases are also effective in restricting grain boundary migration during creep deformation at elevated temperatures, thus improving creep performance. However, the needle-shaped morphology of the Al_4Sr phase is likely to incorporate stress concentration cracking, which may introduce an adverse effect on the creep performance. The as-cast AZ91 alloy, containing both Ca and Sr, is observed to exhibit a superior creep performance compared to other alloys. The improvement in creep performance of this alloy is attributed to the combined precipitation of both Al_4Sr and Al_2Ca phases and the change in needle-shaped morphology of the Al_4Sr phase to irregular-shaped morphology, which is less detrimental to the crack formation and propagation. In addition, almost complete suppression of the thermally unstable β-$Mg_{17}Al_{12}$ phase with the precipitation of Al_4Sr and Al_2Ca phases strengthens alloy *AZ91-1Ca-0.6Sr* against creep deformation.

In the present chapter, the creep performance of the heat-treated AZ91 alloys is influenced by various strengthening and softening effects that arise due to the dissolution of the β-$Mg_{17}Al_{12}$ phase, grain coarsening, increase in Al concentration in the matrix, reduction in the density of pre-existed cracks. Upon heat treatment, the investigated as-cast alloys A (AZ91), B (AZ91-1Sr), and C (AZ91-1Ca-0.6Sr) experience the complete dissolution of the thermally unstable β-$Mg_{17}Al_{12}$ phase into the α-Mg matrix. The complete dissolution of the β-$Mg_{17}Al_{12}$ phase incorporates a solid solution strengthening due to increased Al concentration in the matrix. As solute (Al) content increases, the pinning effect of solute atoms on dislocations strengthened [40], [95]. In addition, the dissolution of the β-$Mg_{17}Al_{12}$ phase almost eliminates the weakest site for the cracks and cavity initiation [4], [10], [37]. As a result, the creep performance of AZ91 alloy is observed to improve on heat treatment (see **Fig. 7.6**). On the other hand, in heat-treated alloy B *(AZ91-1Sr)*, the improved creep performance might be attributed to the alteration in the morphology of the thermally stable Al_4Sr phase from needle-shaped to particulate-shaped and their distribution over the grain boundaries, as shown in **Fig.7.1b**. The current particulate-shaped morphology of the Al_4Sr phase may not experience high-stress concentration on creep loading. Further, their existence over the grain boundaries provides strengthening against the grain boundary migration. Besides, the dissolved β-$Mg_{17}Al_{12}$ phase into the Mg-matrix further provides a solid solution strengthening in the alloy B. Therefore, in summary, the improved creep performance of heat-treated alloy B is due to solid solution strengthening and altered morphology of the Al_4Sr phase.

The minimum creep rate in alloy C *(AZ91-1Ca-0.6Sr)* is almost one order lower than alloy B *(AZ91-1Sr)* at 175 °C after the heat treatment. However, on comparison of creep behavior with the as-cast sample, alloy C demonstrates little increase in the creep rate after heat treatment. The point worth mentioning here is that unlike alloys A and B, the presence of the β-$Mg_{17}Al_{12}$ phase is negligible in alloy C in the as-cast condition. The Al_2Ca and Al_4Sr phases evolved before the β-$Mg_{17}Al_{12}$ phase in alloy C during solidification, as confirmed by the thermodynamic analysis, **Fig. 7.2a**. Consequently, most of the Al is already consumed by these phases; thereafter, the remaining Al in the α-Mg matrix is low enough to suppress the formation of the β-$Mg_{17}Al_{12}$ phase. On the other hand, the dissolution temperature of Al_2Ca and Al_4Sr is above 515 °C. Consequently, a heat treatment at 415 °C in alloy C did not cause the dissolution of any precipitate [173]. Therefore, the specified heat treatment did not provide any additional solid solution strengthening in alloy C. As a result, the creep performance of alloy C on heat treatment is solely due to the precipitation strengthening, which is attributed to the existence of undissolved high-strength thermally stable Al_4Sr and Al_2Ca intermetallic phases.

On the other hand, the governing creep mechanism for alloys A, B, and C in the as-cast condition, as identified in the previous study, is dislocation creep. According to this mechanism, a small grain size is beneficial as it incorporates grain boundary strengthening in the alloy. The smaller grains likely restrict the motion of dislocations during creep deformation, thereby enhancing creep resistance. However, upon heat treatment, these alloys A, B, and C undergo significant grain growth, as shown in **Fig. 7.3**, which reduces the grain boundary region. This reduction minimizes the restriction on dislocation motion during creep deformation. Consequently, the easier movement of dislocations during creep deformation leads to an increased creep rate in heat-treated alloy C [172]. However, in heat-treated alloys A and B, the additional solid solution strengthening arises due to the dissolution of the β-$Mg_{17}Al_{12}$ phase, which counteracts the adverse effect of grain growth on the creep rate. Consequently, despite grain growth, the creep rate of alloys A and B decreases upon heat treatment, as shown in **Fig. 7.6**. In summary, heat treatment causes grain growth, which negatively impacts the creep performance of alloy C. However, in alloys A and B, the adverse effect of grain growth is dominated by solid solution strengthening.

Furthermore, in terms of the mechanisms to enhance the creep performance of the heat-treated alloys, the precipitation of the β-$Mg_{17}Al_{12}$ phase during the creep deformation contributes an additional strengthening to the creep performance, **Fig. 7.8-7.11**. Srinivasan et al. [4], Regev et al. [126], and Chen et al. [145] reported a similar observation on the formation of β-$Mg_{17}Al_{12}$ precipitates near the grain boundary during creep, which in turn restricts the creep deformation in AZ91 alloy. Kunst et al. [171], observed the continuous precipitation of coherent β-$Mg_{17}Al_{12}$ lamellae during creep, which interacts with dislocations and hence causes strengthening of the matrix. In addition, Yang et al. [40] reported the β-$Mg_{17}Al_{12}$ phase precipitation in Mg-Al-Nd-Gd alloy on age hardening, which in turn increases the resistance to the dislocation motion, thus increasing the creep resistance. The formation of the β-$Mg_{17}Al_{12}$ phase during the creep process restricts the dislocation motion and grain boundary migration, which, as a result, provides an additional improvement in the creep performance of the respective heat-treated alloys A, B, and C. But, in the case of alloy C, the detrimental effect of grain growth may have dominated the additional strengthening provided by the β-$Mg_{17}Al_{12}$ phase precipitation during creep deformation. As a result, no further improvement in the creep performance was observed in alloy C post-heat treatment. Instead, the creep rate has slightly increased on heat treatment. Further, due to exposure to the applied load and high temperature, these β-$Mg_{17}Al_{12}$ phase precipitates at the final stage of the creep coarsen and lose their ability to further restrict both dislocation motion and grain boundary migration, thus leading to an accelerated creep [4].

Like a creep performance, the as-cast hardness of alloy C, as demonstrated in section 3.2, is estimated to be highest compared to alloy B and is lowest in the case of alloy A. The hardness in the investigated alloys A, B, and C is a result of the hardening effect that arises due to the existence of secondary phases in the alloys [174]. The highest hardness of alloy C is attributed to the presence of both Al_2Ca and Al_4Sr phases combined in the alloy, as these phases exhibited higher elastic strength and hardness compared to other β-$Mg_{17}Al_{12}$ phases [148]. Upon heat treatment, the dissolved β-$Mg_{17}Al_{12}$ phase in alloys contributes to solid solution strengthening, while the undissolved Al_2Ca and Al_4Sr phases in alloys B and C provide a precipitation hardening to the alloys. However, these alloys on heat treatment experience grain growth (**Fig.7.3**), which adversely affects their hardness [172]. Despite the effect of grain growth, an increase in hardness was observed in alloys A and B on heat treatment, likely due to solid solution strengthening in alloy A and the combined effect of solid solution strengthening and precipitation hardening in alloy B. In contrast, as discussed above, alloy C does not experience solid solution strengthening. Additionally, the undissolved Al_2Ca and Al_4Sr precipitates alone may not be strong enough to counterbalance the detrimental impact of grain growth, leading to a reduction in hardness after heat treatment.

7.8 Conclusions

The conclusions made from the present investigation are outlined below:

1. Adding Ca and Sr to the AZ91 alloy introduced thermally stable intermetallic phases into the microstructure of the alloys B and C, such as needle-shaped Al_4Sr and skeleton-shaped Al_2Ca, alongside the thermally unstable β-$Mg_{17}Al_{12}$ phase.
2. The precipitation of thermally stable phases in the alloys B and C suppressed the formation of the thermally unstable β-$Mg_{17}Al_{12}$ phase on solidification, whereas the suppression is prominent in the case of alloy C, exhibiting the combined precipitation of Al_2Ca and Al_4Sr phases.

3. The microstructure of the investigated alloys is altered on heat treatment, indicating the complete dissolution of the β-$Mg_{17}Al_{12}$ phase in each alloy since Al_4Sr and Al_2Ca phases are undissolved in the microstructure of the alloys B and C. In addition, the alloys on heat treatment experience considerable grain growth, which has an adverse effect on the hardness and creep performance of alloy C.
4. Dissolution of the β-$Mg_{17}Al_{12}$ phase in alloys A and B provides a solid solution strengthening into the Mg matrix, which is less pronounced in alloy C due to the near complete suppression of the β-$Mg_{17}Al_{12}$ phase. In addition, the undissolved precipitates in alloys B and C on heat treatment provide additional strengthening to the alloys. Moreover, the evolution of the β-$Mg_{17}Al_{12}$ phase during the creep deformation of the heat-treated alloys occurred, which is further expected to provide a strengthening to the alloys.
5. Despite the adverse effect of grain growth observed during the heat treatment, the combined effect of solid solution strengthening in alloy A and both solid solution and precipitation strengthening in alloy B increased hardness and creep performance. In contrast, the reduced creep performance of alloy C on heat treatment is attributed to the absence of solid solution strengthening and significant grain growth.

Chapter 8

Conclusions and Future Scope of Work

8.1 Conclusions

The present research study has successfully explored the effect of squeeze casting, alloying addition, and heat treatment on the microstructure evolution and creep properties of the AZ91 (Mg-Al-Zn) alloy. The fraction of secondary phases in the investigated alloys and their thermal stability have been estimated using thermodynamic and thermal analysis. The major conclusions of the present study are summarized below:

Microstructure and creep behaviour of squeezed cast AZ91 alloy

1. The cost-effective commercial die-cast AZ91 (Mg-Al-Zn) alloy, which is most widely used in automotive components, experiences severe loss of strength or creep resistance at service temperatures above 120 °C. The poor creep performance is due to the unstable microstructure, which is attributed to the presence of a thermally unstable β-$Mg_{17}Al_{12}$ phase which starts dissolving above 120 °C. In addition, the cracks and cavities at the interface of the Mg matrix and β-$Mg_{17}Al_{12}$ phase further lower the creep performance of the AZ91 alloy.

2. The application of squeeze casting instead of die-casting eliminates the porosity and produces a fine and consistent β-$Mg_{17}Al_{12}$ phase network.

3. The initial contribution of the β-$Mg_{17}Al_{12}$ phase in providing creep resistance reduces significantly with temperature due to its dissolution and increase in interparticle distance from 150 °C to 200 °C

4. Threshold stress of the squeezed cast AZ91 alloy has been found to reduce with increased temperature, owing to easier dislocation motion and increased diffusivity at higher temperatures.

Effect of alloying addition of Ca and Sr on the microstructure and creep behavior of squeezed cast AZ91 alloy

5. The creep performance of AZ91 alloy effectively improved by adding low-cost and easily accessible alkaline earth metals, such as Sr and Ca, to AZ91 alloy. The addition of Ca to the AZ91 alloy, i.e., AZX911 alloy, resulted in the precipitation of skeleton-shaped Al_2Ca intermetallic in the alloy with a simultaneous decrease in the volume fraction of the thermally unstable β-$Mg_{17}Al_{12}$ phase. The presence of Al_2Ca precipitate alloy contributes to the significant improvement in creep resistance of AZX911 alloy as compared to AZ91 alloy. Furthermore, the post-creep microstructure indicates cracks and cavities at the interface of the β-$Mg_{17}Al_{12}$ phase and Mg matrix. However, the cavity formation is not observed at the interface of the Al_2Ca phase and α-Mg matrix.

6. Similarly, the individual addition of Sr to the AZ91 alloy also resulted in the precipitation of needle-shaped Al_4Sr intermetallic in the alloy by partially suppressing the thermally unstable β-$Mg_{17}Al_{12}$ phase precipitation. Moreover, the simultaneous precipitation of both Al_2Ca and Al_4Sr in alloy *AZ91-1Ca-0.6Sr* provides superior creep performance compared to other alloy *AZ91-1Sr* and *AZ91-1Ca*. The creep performance of the AZ91 alloy on alloying addition can be concluded in the order: *AZ91-1Ca-0.6Sr > AZ91-1Ca-0.3Sr > AZ91-1Ca > AZ91-1Sr > AZ91*.

7. The needle-shaped Al_4Sr intermetallic phase serves as a critical site for both crack initiation and cavity formation in alloy *AZ91-1Sr*. However, the thermally stable Al_2Ca and/or Al_4Sr phases with an interconnected network of skeleton morphology and change in morphology of the Al_4Sr phase to an irregular shape in alloy *AZ91-1Ca-0.6Sr* are found to impede the crack propagation effectively. In addition, the reduced fraction of the Al_4Sr phase on precipitation of the Al_2Ca phase in alloy *AZ91-1Ca-0.6Sr* also effectively reduces the probability of crack initiation.

8. A non-isothermal kinetic analysis employing the Kissinger method reveals that the activation energies for dissolution of the Al_2Ca phase and β-$Mg_{17}Al_{12}$ phase in AZX911 alloy are 923 and 664 kJ/mol, respectively, implying higher thermal stability of Al_2Ca compared to β-$Mg_{17}Al_{12}$ phase. Further, DSC analysis also indicates the higher dissolution temperature associated with the Al_2Ca and Al_4Sr phases compared to the β-$Mg_{17}Al_{12}$ phase. On the other hand, thermodynamic analysis with the Thermo-Calc® database further confirms the lower

negative free energy (higher thermal stability) associated with Al_2Ca and Al_4Sr phases than other investigated phases.

9. All the investigated AZ91 alloys containing Ca and Sr are observed to follow the power law behavior. The governing creep mechanism is found to be dislocation creep involving dislocation climb governed by lattice diffusion. It indicates that the AZ91 alloy containing Ca and Sr shows improved creep resistance compared to the AZ91 base alloy without altering the governing creep mechanism.

Effect of heat treatment on the microstructure and creep behaviour of squeezed cast AZ91-based alloys

10. The microstructure of the investigated AZ91 alloys is altered on heat treatment (solution treatment at 415 °C for 24 h), indicating the complete dissolution of the β-$Mg_{17}Al_{12}$ phase in each alloy since Al_4Sr and Al_2Ca phases are undissolved in the microstructure of the AZ91 alloys containing Ca and Sr. In addition, the alloys in heat treatment experience considerable grain growth, which has an adverse effect on their hardness and creep performance.

11. Dissolution of the β-$Mg_{17}Al_{12}$ phase in alloys *AZ91* and *AZ91-1Sr* provides a solid solution strengthening into the Mg matrix, which is less pronounced in alloy *AZ91-1Ca-0.6Sr* due to the near complete suppression of the β-$Mg_{17}Al_{12}$ phase during solidification. In addition, the undissolved precipitates in alloys *AZ91-1Sr* and *AZ91-1Ca-0.6Sr* on heat treatment provide additional strengthening to the alloys. Moreover, the evolution of the β-$Mg_{17}Al_{12}$ phase during the creep deformation of the heat-treated alloys occurred, which is further expected to provide strengthening to the alloys.

12. Despite the adverse effect of grain growth observed during the heat treatment, the effect of solid solution strengthening in alloy *AZ91* and both solid solution and precipitation strengthening in alloy *AZ91-1Sr* increased hardness and creep performance. In contrast, the reduced creep performance of alloy *AZ91-1Ca-0.6Sr* on heat treatment is attributed to the absence of solid solution strengthening and significant grain growth.

8.2 Future scope of work

Based on the current work, the following studies can be further carried out for future work:

- The proposed creep mechanism in the investigated AZ91 alloys needs to be further confirmed by characterizing the dislocation structure and its interactions with precipitates, grain boundaries, etc., employing a transmission electron microscope (TEM). Here, studying the intermittent creep-tested specimens may provide further insight.
- Further prolonged creep testing may be carried out at lower temperature and stress range to eliminate the possibility of change in creep deformation mechanism at actual service condition.
- The creep performance of the investigated alloy composition in the present thesis work can be studied in the industrial setup with full-size standard specimen where enhanced melt quality control is practiced, which reduces the probability of casting defects.
- There is a scope to investigate the creep performance of AZ91-based composites, which can be a more suitable material for elevated-temperature automotive applications compared to AZ91 alloys.
- Change in the fabrication technique of the Mg alloys to additive manufacturing can be favorable in order to reduce the cost and processing time associated with the casting route.
- The modeling and simulation approaches can be explored to complement the experimental findings.

Chapter 9

Novelty and Contribution to Original Knowledge

This research work addresses several critical aspects pertaining to the microstructure, creep properties, and processing techniques of AZ91 Magnesium alloy, particularly focusing on the effects of alloying additions of Calcium and Strontium and microstructural modifications on its creep properties.

Application of squeeze casting technique to prepare AZ91 Magnesium alloy:

- For the first time, the influence of the squeeze-casting method on the creep properties of the AZ91 alloy containing Ca and Sr elements is explored, highlighting a gap in the existing literature.
- Squeeze casting of AZ91 alloy produced higher-quality rods with significantly reduced porosity and defects, leading to a more uniform microstructure and refined grains. Consequently, this enhanced the creep properties of the investigated alloys.

Alloying the squeeze-cast AZ91 Magnesium alloy with calcium (Ca) and strontium (Sr), both individually and in combination:

- This study represents the first examination of Ca and Sr addition in squeeze-cast AZ91 alloy. It investigates the impact of individual and combined Ca and Sr addition on the microstructural modification and creep properties of squeeze-cast AZ91 alloy, involving the precipitation of new phases, their volume fraction and morphologies, their thermal stability, and finally, grain size.

- In general, the creep performance of the AZ91 alloy was found to be superior with combined Ca and Sr addition, containing 1% Ca and 0.6% Sr.

Application of the heat treatment process to the squeeze cast AZ91-based Magnesium alloys:

- Since no previous studies have explored the effect of heat treatment on the creep performance of the Ca and Sr-containing AZ91 alloy, the present study investigates the microstructure evolution in the same alloys on heat treatment and its subsequent impact on creep performance. The microstructure modification on heat treatment involves phase stability, alteration in phase morphology, and grain size modification.

- As a result of the heat treatment, the creep performance was improved in the AZ91 base alloy and AZ91-1Sr alloy, whereas a decrease in creep performance was observed in the AZ91-1Ca-0.6Sr alloy.

This work established new knowledge on the effect of alloying addition of Ca and Sr on squeezed-cast AZ91 Mg alloy, with a detailed study on their microstructural evolution and tensile creep behaviour.

APPENDIX

- **Bulk-texture of the as-cast and creep deformed AZ91 Mg alloy specimens**

In the thesis work, for all the investigated alloys, the governing creep mechanism is confirmed with the stress exponent (n) and activation energy (Q) values. Further, an attempt has also been made to confirm it with the estimated dislocation density using the X-ray diffraction technique in Chapter 4. Here, through both techniques, the governing creep mechanism is observed to be dislocation-based.

Moreover, studying the crystallographic texture of the creep-deformed samples could also provide some insights into the underlying creep mechanisms. Therefore, a macro texture study has been carried out on a few crept samples with similar creep strain (up to secondary stage) of 6-8% as shown below. In line with the dislocation-based creep mechanism, the preliminary results indicate the evolution of weak deformation texture after creep, while the variation in texture index is negligible. However, further thorough study with more samples is necessary before reaching any conclusion.

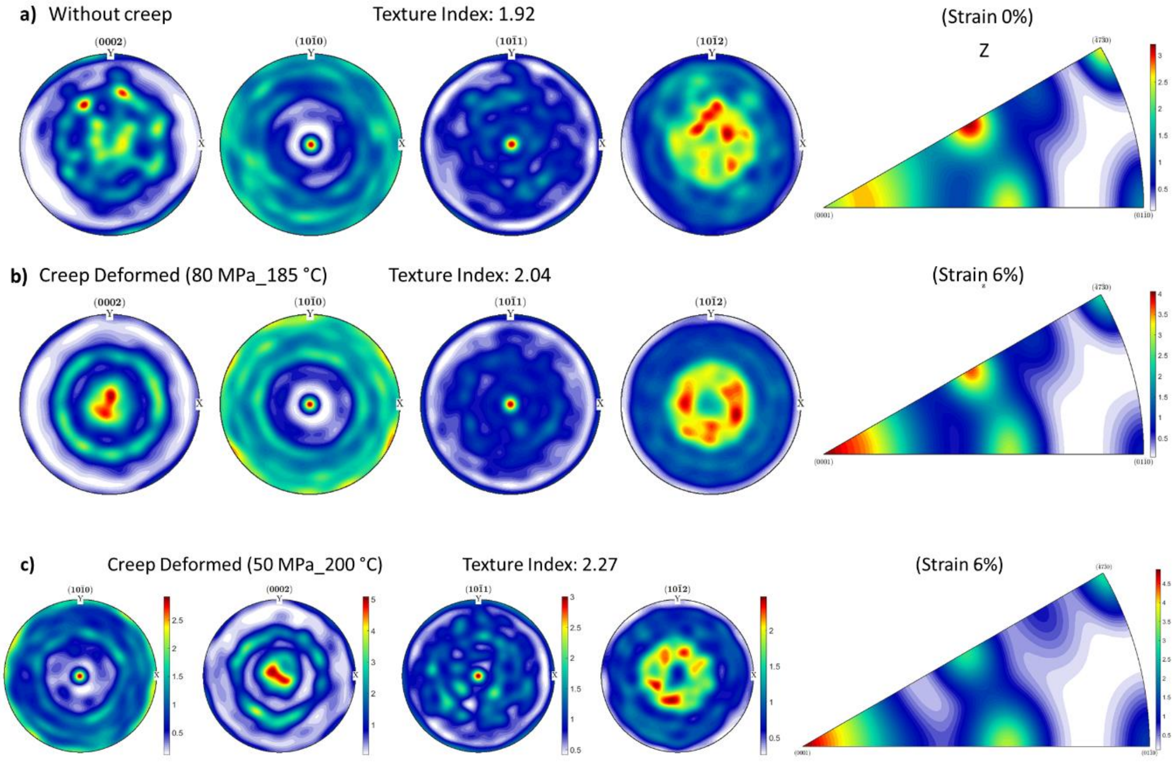

Figure. Pole figure and Inverse Pole figure (IPF) of a) As-cast, b) Creep deformed (80 MPa-185 °C), and Creep deformed (50 MPa-200 °C) AZ91 Mg alloy.

REFERENCES

[1] B. Liu, J. Yang, X. Zhang, Q. Yang, J. Zhang, and X. Li, "Development and application of magnesium alloy parts for automotive OEMs: A review," *Journal of Magnesium and Alloys* (2023), vol. 11, pp. 15-47. (DOI: 10.1016/j.jma.2022.12.015)

[2] A. Luo and M. O. Pekguleryuz, "Review Cast magnesium alloys for elevated temperature applications," *Journal of Materials Science* (1994), vol. 29, PP. 5259-5271.

[3] H. Patil, A. Marodkar, A. Ghosh, and H. Borkar, "Effect of Ca addition on the microstructure and creep behaviour of AZ91 Mg alloy," *Materials Today Proceedings* (2023). (DOI: 10.1016/j.matpr.2023.03.056).

[4] A. Srinivasan, J. Swaminathan, M. K. Gunjan, U. T. S. Pillai, and B. C. Pai, "Effect of intermetallic phases on the creep behavior of AZ91 magnesium alloy," *Materials Science and Engineering: A* (2010), vol. 527, no. 6, pp. 1395–1403. (DOI: 10.1016/j.msea.2009.10.00)

[5] E. Baril, P. Labelle, and M. O. Pekguleryuz, "Elevated Temperature Mg-Al-Sr: Creep Resistance, Mechanical Properties, and Microstructure," *The Journal of The Minerals, Metals & Materials Society* (2003), vol. 55, pp. 34-39. (DOI: https://doi.org/10.1007/s11837-003-0207-7)

[6] B. H. Kim, K. C. Park, Y. H. Park, and I. M. Park, "Microstructure and creep properties of Mg-4Al-2Sn-1(Ca, Sr) alloys," *Transactions of Nonferrous Metals Society of China (English Edition)* (2010), vol. 20, no. 7, pp. 1184–1191. (DOI: 10.1016/S1003-6326(09)60276-4)

[7] J. Kubásek, D. Vojtěch, and M. Martínek, "Structural characteristics and elevated temperature mechanical properties of AJ62 Mg alloy," *Mater Charact* (2013), vol. 86, pp. 270–282. (DOI: 10.1016/j.matchar.2013.09.018)

[8] Z. W. Wang, H. X. Wang, J. L. Gong, M. Li, W. L. Cheng, and W. Liang, "Modification and refinement effects of Sb and Sr on Mg17Al12and Mg2Si phases in Mg-12Al-0.7Si alloy," *China Foundry* (2016), vol. 13, no. 5, pp. 310–315. (DOI: 10.1007/s41230-016-5112-0)

[9] N. Mo *et al.*, "Current development of creep-resistant magnesium cast alloys: A review," *Materials Design* (2018), vol. 155, pp. 422–442. (doi: 10.1016/j.matdes.2018.06.032)

[10] H. Patil, A. Jain, A. Marodkar, P. Kumar, A. Ghosh, and H. Borkar, "Creep deformation study of squeeze cast AZ91 magnesium alloy," *Materials Science and Technology (United Kingdom)* (2023), vol. 39, no. 15, pp. 1926–1938. (DOI: 10.1080/02670836.2023.2186055)

[11] U. K. Karl, H. Yuanding, D. Hajo, and H. Norbert, "Status of the development of creep resistant magnesium materials for automotive applications," *Materials Science Forum*, *Trans Tech Publications Ltd* (2010), vol. 638-642, pp. 73–80. (DOI: 10.4028/www.scientific.net/MSF.638-642.73)

[12] J. Majhi, T. Das, A. Basu, and A. K. Mondal, "An analysis of microstructure and impression creep response of squeeze-cast AZ91–xBi–ySr alloys," *Materials Science and Technology (United Kingdom) (2020)*, vol. 36, no. 6, pp. 731–742. (DOI: 10.1080/02670836.2020.1736763)

[13] Y. Zhang *et al.*, "Effects of processing parameters and Ca content on microstructure and mechanical properties of squeeze casting AZ91-Ca alloys," *Materials Science and Engineering: A* (2014), vol. 595, pp. 109–117. (DOI: 10.1016/j.msea.2013.12.014)

[14] J. Yan, Y. Sun, F. Xue, S. Xue, Y. Xiao, and W. Tao, "Creep behavior of Mg-2 wt.%Nd binary alloy," *Materials Science and Engineering: A* (2009), vol. 524, no. 1–2, pp. 102–107. (DOI: 10.1016/j.msea.2009.06.008)

[15] S. Lee, H. Seung, D. O. Lee, and K. Hyang, "Effect of Y, Sr, and Nd Additions on the Microstructure and Microfracture Mechanism of Squeeze-Cast AZ91-X Magnesium Alloys," *Metallurgical and Materials Transactions A* (1998), vol. 29A, pp. 1221-1235. (DOI: https://doi.org/10.1007/s11661-998-0249-0)

[16] H. Patil, A. Ghosh, and H. Borkar, "Effect of Individual Alloying Addition on the Microstructure and Creep Behavior of Squeeze Cast AZ91 Magnesium Alloy," *Key Engineering Materials* (2024), vol. 973, pp. 45-50. (DOI: 10.4028/p-iX5Z1E)

[17] K. Wei, L. Y. Wei, and R. Warren, "Creep Behaviour and Microstructure of Magnesium Die Cast Alloys AZ91 and AE42," *Materials Science Forum* (2007), vol. 546–549, pp. 73–76. (DOI: 10.4028/www.scientific.net/msf.546-549.73)

[18] K. Hirai, H. Somekawa, Y. Takigawa, and K. Higashi, "Effects of Ca and Sr addition on mechanical properties of a cast AZ91 magnesium alloy at room and elevated temperature," *Materials Science and Engineering: A* (2005), vol. 403, no. 1–2, pp. 276–280. (DOI: 10.1016/j.msea.2005.05.028)

[19] Y. Nakaura, A. Watanabe, and K. Ohori, "Effects of Ca,Sr Additions on Properties of Mg-Al Based Alloys," *Materials Transactions* (2006), vol. 47, no. 4, pp. 1031-1039.

[20] U. K. Karl, H. Yuanding, D. Hajo, and H. Norbert, “Status of the development of creep resistant magnesium materials for automotive applications,” *Materials Science Forum*, Trans Tech Publications Ltd (2010), vol. 638-642, pp. 73–80. (DOI: 10.4028/www.scientific.net/MSF.638-642.73)

[21] P. Shahbeigi Roodposhti, A. Sarkar, K. L. Murty, and R. O. Scattergood, “Effects of Microstructure and Processing Methods on Creep Behavior of AZ91 Magnesium Alloy,” *Journal of Materials Engineering and Performance* (2016), vol. 25, pp. 3697-3706. (DOI: 10.1007/s11665-016-2222-1)

[22] M. Pekguleryuz and M. Celikin, “Creep resistance in magnesium alloys,” *International Materials Reviews* (2010), vol. 55, pp. 197-217. (DOI: 10.1179/095066010X12646898728327)

[23] H. L. Zhao, S. K. Guan, and F. Y. Zheng, “Effects of Sr and B addition on microstructure and mechanical properties of AZ91 magnesium alloy,” *J Mater Res* (2007), vol. 22, no. 9, pp. 2423–2428. (DOI: 10.1557/jmr.2007.0331.)

[24] F. Wang, T. Hu, Y. Zhang, W. Xiao, and C. Ma, “Effects of Al and Zn contents on the microstructure and mechanical properties of Mg-Al-Zn-Ca magnesium alloys,” *Materials Science and Engineering: A* (2017), vol. 704, pp. 57–65. (DOI: 10.1016/j.msea.2017.07.060)

[25] D. Amberger, P. Eisenlohr, and M. Göken, “Microstructural evolution during creep of Ca-containing AZ91,” *Materials Science and Engineering: A* (2009), vol. 510–511, no. C, pp. 398–402. (DOI: 10.1016/j.msea.2008.04.115)

[26] W. Qudong *et al.*, “Effects of Ca addition on the microstructure and mechanical properties of AZ91magnesium alloy,” *Journal of Materials Science* (2001), vol. 36, pp. 3035-3040. (DOI: https://doi.org/10.1023/A:1017927109291)

[27] B. L. Mordike and T. Ebert, “Magnesium Properties-applications-potential,” *Materials Science and Engineering: A* (2001), vol. 302, 1, pp. 37-45. (DOI: https://doi.org/10.1016/S0921-5093(00)01351-4)

[28] A. A. Luo, “Recent magnesium alloy development for elevated temperature applications,” *International Materials Reviews* (2004), vol. 49, pp. 13-30. (DOI: 10.1179/095066004225010497)

[29] Xixi Dong et al., "On the exceptional creep resistance in a die-cast Gd-containing Mg alloy with Al addition," *Acta Materialia* (2022), vol. 232, Issues 1-2, pp. 117957. (DOI: https://doi.org/10.1016/j.actamat.2022.117957)

[30] K. Hirai, H. Somekawa, Y. Takigawa, and K. Higashi, “Effects of Ca and Sr addition on mechanical properties of a cast AZ91 magnesium alloy at room and elevated temperature,” *Materials Science and Engineering: A* (2005), vol. 403, no. 1–2, pp. 276–280. (DOI: 10.1016/j.msea.2005.05.028)

[31] S. M. Zhu, B. L. Mordike, and J. F. Nie, “Creep properties of a Mg-Al-Ca alloy produced by different casting technologies,” *Materials Science and Engineering: A* (2008), vol. 483–484, no. 1-2 C, pp. 583–586. (DOI: 10.1016/j.msea.2006.09.154)

[32] A. S. Marodkar, H. Patil, H. Borkar, and A. Behl, “Effect of Squeeze Casting and Combined Addition of Calcium and Strontium on Microstructure and Mechanical Properties of AZ91 Magnesium Alloy,” *International Journal of Metalcasting* (2023), vol. 17, no. 3, pp. 2252–2270. (DOI: 10.1007/s40962-022-00943-1)

[33] H. Shastri, A. K. Mondal, K. Dutta, H. Dieringa, and S. Kumar, “Microstructural correlation with tensile and creep properties of AZ91 alloy in three casting techniques,” *J Manuf Process* (2020), vol. 57, pp. 566–573. (DOI: 10.1016/j.jmapro.2020.07.010)

[34] K. B. Nie, X. J. Wang, K. Wu, M. Y. Zheng, and X. S. Hu, “Effect of ultrasonic vibration and solution heat treatment on microstructures and tensile properties of AZ91 alloy,” *Materials Science and Engineering: A* (2011), vol. 528, no. 25–26, pp. 7484–7487. (DOI: 10.1016/j.msea.2011.06.072)

[35] J. U. Lee, S. H. Kim, Y. J. Kim, and S. H. Park, “Effects of homogenization time on aging behavior and mechanical properties of AZ91 alloy,” *Materials Science and Engineering: A* (2018), vol. 714, pp. 49–58. (DOI: 10.1016/j.msea.2017.12.061)

[36] J. H. Jun, “Effect of solution treatment on mechanical properties of cast AZ91-(Ca) alloys,” *Archives of Metallurgy and Materials* (2019), vol. 64, no. 1, pp. 265–269. (DOI: 10.24425/amm.2019.126247)

[37] M. C. Zhao, M. Liu, G. L. Song, and A. Atrens, “Influence of homogenization annealing of AZ91 on mechanical properties and corrosion behavior,” *Adv Eng Mater* (2008), vol. 10, no. 1–2, pp. 93–103. (DOI: 10.1002/adem.200700234)

[38] X. Xia, W. Zhao, X. Feng, H. Feng, and X. Zhang, “Effect of homogenizing heat treatment on the compressive properties of closed-cell Mg alloy foams,” *Mater Des* (2013), vol. 49, pp. 19–24. (DOI: 10.1016/j.matdes.2013.01.064)

[39] Z. Pu, H. Liu, K. Zhang, and X. Li, “The Influence of Solution Treatment on Structure and Performance of AZ91 Magnesium Alloy,” 2016. (DOI:10.2991/icimm-16.2016.51)

[40] J. Yang, W. Wang, M. Zhang, J. Liu, and S. Qin, “The effects of continuous and discontinuous β-Mg17Al12 on compression creep properties of Mg-8.0Al-1.0Nd-1.0Gd alloys,” *Materials Science and Engineering: A* (2022), vol. 858, 144191. (DOI: 10.1016/j.msea.2022.144191)

[41] L. Čížek, M. Greger, L. Pawlica, L. A. Dobrzański, and T. Tański, “Study of selected properties of magnesium alloy AZ91 after heat treatment and forming,” in *Journal of Materials Processing Technology* (2004), pp. 466–471. (DOI: 10.1016/j.jmatprotec.2004.07.149)

[42] Y. Li, Y. Chen, H. Cui, B. Xiong, and J. Zhang, “Microstructure and mechanical properties of spray-formed AZ91 magnesium alloy,” *Mater Charact* (2009), vol. 60, no. 3, pp. 240–245. (DOI: 10.1016/j.matchar.2008.09.007)

[43] S. N. Chen, W. Yang, H. Yu, and Y. L. Zhang, “Effects of microstructure modification and pressurized solidification on mechanical property of AZ91 alloy,” *J Alloys Compd* (2014), vol. 611, pp. 1–6. (DOI: 10.1016/j.jallcom.2014.05.033)

[44] M. K. Yeoh, X. H. Tan, P. H. N. Cheang, T. C. Lim, and R. W. O. Kwok, “Effect of Solutionizing Time on Improving the Microstructure and Mechanical Properties of Aged AZ80 Mg Alloy,” *J Mater Eng Perform* (2019), vol. 28, no. 11, pp. 6836–6852. (DOI: 10.1007/s11665-019-04382-8)

[45] N. Loukil, “Alloying Elements of Magnesium Alloys: A Literature Review,” in *Magnesium Alloys Structure and Properties*, *IntechOpen* 2022. (DOI: 10.5772/intechopen.96232)

[46] M. B. Yang, C. Y. Qin, and F. S. Pan, “Effects of heat treatment on microstructure and mechanical properties of Mg-3Sn-1Mn magnesium alloy,” *Transactions of Nonferrous Metals Society of China (English Edition)* (2011), vol. 21, no. 10, pp. 2168–2174. (DOI: 10.1016/S1003-6326(11)60990-4)

[47] M. O. Pekguleryuz and A. A. Kaya, "Creep resistant magnesium alloys for powertrain applications," *Advanced Engineering materials* (2003), vol. 5, Issue 12, pp. 866-878. (DOI: 10.1002/adem.200300403)

[48] M. Goede, M. Stehlin, L. Rafflenbeul, G. Kopp, and E. Beeh, "Super Light Car-lightweight construction thanks to a multi-material design and function integration," *European Transport Research Review* (2009), vol. 1, no. 1, pp. 5–10. (DOI: 10.1007/s12544-008-0001-2)

[49] E. G. S. Cole and A. M. Sherman, "Lightweight Materials for Automotive Applications." (1995). (DOI: https://doi.org/10.1016/1044-5803(95)00063-1)

[50] M. K. Kulekci, "Magnesium and its alloys applications in automotive industry," *International Journal of Advanced Manufacturing Technology* (2008), vol. 39, no. 9–10, pp. 851–865. (DOI: 10.1007/s00170-007-1279-2)

[51] L. Tian, L. Wang, H. Wu, H. Wang, L. Zheng, and K. S. Shin, "Recent research advances in Mg single crystal based on the crystal orientations：A review," *Journal of Materials Research and Technology* (2023), vol. 27, pp. 5572–5593. (DOI: 10.1016/j.jmrt.2023.10.273)

[52] A. Yamashita, Z. Horita, and T. G. Langdon, "Improving the mechanical properties of magnesium and a magnesium alloy through severe plastic deformation," Materials Science and Engineering: A (2001), vol. 300, Issues 1-2, pp. 142-147. (DOI: https://doi.org/10.1016/S0921-5093(00)01660-9)

[53] H. Borkar, "Texture and Microstructure Studies on Magnesium-Manganese-Strontium (Mg-Mn-Sr) Extrusion Alloys," 2012.

[54] Z. Yang, J. P. Li, J. X. Zhang, G. W. Lorimer, and J. Robson, "Review on Research and Development of Magnesium Alloys," *Acta Metallurgica Sinica (English Letters)* (2008), vol. 21, no. 5, pp. 313–328. (DOI: 10.1016/S1006-7191(08)60054-X)

[55] D. S. Kumar, C. T. Sasanka, K. Ravindra, and K. N. S. Suman, "Magnesium and Its Alloys in Automotive Applications – A Review," *American Journal of Materials Science and Technology* (2015), vol. 4, no. 1, pp. 12-30. (DOI: 10.7726/ajmst.2015.1002)

[56] A. Baghani, H. Khalilpour, and S. M. Miresmaeili, "Microstructural evolution and creep properties of Mg-4Sn alloys by addition of calcium up to 4 wt.%," *Transactions of Nonferrous Metals Society of China (English Edition* (2020), vol. 30, no. 4, pp. 896–904. (DOI: 10.1016/S1003-6326(20)65263-3)

[57] N. Hort, Y. D. Huang, T. A. Leil, K. P. Rao, and K. U. Kainer, “Properties and processing of magnesium-tin-calcium alloys,” *Kovove Materialy-Metallic Materials*

(2011), vol. 49, pp. 163–177, 2011. (DOI: 10.4149/km)

[58] Y. Huang, H. Dieringa, K. U. Kainer, and N. Hort, “Understanding effects of microstructural inhomogeneity on creep response - New approaches to improve the creep resistance in magnesium alloys,” *Journal of Magnesium and Alloys* (2014), vol. 2, no. 2, pp. 124–132. (DOI: 10.1016/j.jma.2014.03.003)

[59] M. C. Flemings, “Solidification Processing,” *Metallurgical transactions* (1974), vol. 5, pp. 2121-2134. (DOI: https://doi.org/10.1007/BF02643923)

[60] M. Regev, E. Aghion, and A. Rosen, “Creep studies of AZ9lD pressure die casting,” *Materials Science and Engineering A (*1997), vol. 234-236, 123-126, pp. 1–6. (DOI: 10.1016/j.msea.2009.06.048)

[61] K. R. Athul, U. T. S. Pillai, A. Srinivasan, and B. C. Pai, “A review of different creep mechanisms in Mg alloys based on stress exponent and activation energy,” *Advanced Engineering Materials* (2016), vol. 19, no. 5, pp. 770-795. (DOI: 10.1002/adem.201500393)

[62] G. Vander Voort, “Solutions for Materials Preparation, Testing and Analysis Metallography of Magnesium and its Alloys.” Tech Note, Vol. 2, Issue 4, pp. 1-5.

[63] I. J. Polmear, “Magnesium alloys and applications Production of magnesium,” 1994.

[64] Andure MW, Jirapure SC, and Dhamande LP, “ Advance Automobile Material for Light Weight Future-A Review,” IJCA (2012).

[65] A. I. Taub and A. A. Luo, “Advanced lightweight materials and manufacturing processes for automotive applications,” *MRS Bull* (2015), vol. 40, no. 12, pp. 1045–1053. (DOI: 10.1557/mrs.2015.268)

[66] W. J. Joost and P. E. Krajewski, “Towards magnesium alloys for high-volume automotive applications,” *Scr Mater* (2017), vol. 128, pp. 107–112. (DOI: 10.1016/j.scriptamat.2016.07.035)

[67] A. A. Luo, “Recent magnesium alloy development for elevated temperature applications,” International Materials Reviews (2004), vol. 49, pp. 13-30. (DOI: 10.1179/095066004225010497)

[68] B. Prasad. and P. Bhingole., “Critical assessment of strengthening mechanism of magnesium alloys: Review,” *Advanced Materials Proceedings* (2021), vol. 2, no. 11, pp. 734–744. (DOI: 10.5185/amp.2017/859)

[69] A. Kielbus and T. Rzychon, “Microstructure and creep properties of AJ62 and AE44 Diecasting magnesium alloys,” in *Materials Science Forum*, Trans Tech Publications Ltd, (2010), pp. 1546–1551. (DOI: 10.4028/www.scientific.net/MSF.638-642.1546)

[70] Horst E. Friedrich, Barry. L. Mordike, “Magnesium Technology.” (2006). (DOI: https://doi.org/10.1007/3-540-30812-1)

[71] W. Chen, J. Kong, and W. J. Chen, “Effect of rare earth Ce on the microstructure, physical properties and thermal stability of a new lead-free solder,” *Journal of Mining and Metallurgy, Section B: Metallurgy* (2011), vol. 47, no. 1, pp. 11–21. (DOI: 10.2298/JMMB1101011C)

[72] Y. Huang, H. Dieringa, N. Hort, T. A. Leil, K. U. Kainer, and Y. Liu, “Effects of segregation of primary alloying elements on the creep response in magnesium alloys,” *Scr Mater* (2008), vol. 58, no. 10, pp. 894–897. (DOI: 10.1016/j.scriptamat.2008.01.011)

[73] M. Zubair et al., "Laves phases in Mg-Al-Ca alloys and their effect on mechanical properties," *Materials Design* (2023), vol. 225, pp. 111470. (DOI: https://doi.org/10.1016/j.matdes.2022.111470)

[74] B. H. Kim, K. C. Park, Y. H. Park, and I. M. Park, “Microstructure and creep properties of Mg-4Al-2Sn-1(Ca,Sr) alloys,” *Transactions of Nonferrous Metals Society of China (English Edition)* (2010), vol. 20, no. 7, pp. 1184–1191. (DOI: 10.1016/S1003-6326(09)60276-4)

[75] K. Meshinchi Asl, A. Tari, and F. Khomamizadeh, “The effect of different content of Al, RE and Si element on the microstructure, mechanical and creep properties of Mg-Al alloys,” *Materials Science and Engineering A (*2009), vol. 523, no. 1–2, pp. 1–6. (DOI: 10.1016/j.msea.2009.06.048)

[76] S. Spigarelli, M. Regev, E. Evangelista, and A. Rosen, “Review of creep behaviour of AZ91 magnesium alloy produced by different technologies,” 2001, *IOM Communications Ltd.* doi: 10.1179/026708301101510483.

[77] K. Meshinchi Asl, A. Tari, and F. Khomamizadeh, “The effect of different content of Al, RE and Si element on the microstructure, mechanical and creep properties of Mg-Al alloys,”

Materials Science and Engineering: A (2009), vol. 523, no. 1–2, pp. 1–6. (DOI: 10.1016/j.msea.2009.06.048)

[78] A. Viswanath, H. Dieringa, K. K. Ajith Kumar, U. T. S. Pillai, and B. C. Pai, "Investigation on mechanical properties and creep behavior of stir cast AZ91-SiCp composites," *Journal of Magnesium and Alloys* (2015), vol. 3, no. 1, pp. 16–22. (DOI: 10.1016/j.jma.2015.01.001)

[79] A. Kiełbus, "Microstructure and Properties of Casting Magnesium Alloys Designed to Work in Elevated Temperature," in *Magnesium Alloys - Selected Issue*, IntechOpen, 2018. (DOI: 10.5772/intechopen.80291)

[80] A. K. S. Bankoti, A. K. Mondal, C. S. Perugu, B. C. Ray, and S. Kumar, "Correlation of Microstructure and Electrochemical Corrosion Behavior of Squeeze-Cast Ca and Sb Added AZ91 Mg Alloys," *Metall Mater Trans A Phys Metall Mater Sci* (2017), vol. 48, no. 10, pp. 5106–5121. (DOI: 10.1007/s11661-017-4244-1)

[81] W. Blum, P. Zhang, B. Watzinger, B. V Grossmann, and H. G. Haldenwanger, "Comparative study of creep of the die-cast Mg-alloys AZ91, AS21, AS41, AM60 and AE42," *Materials Science and Engineering A* (2001), vol. 319-321, pp. 735–740. (DOI: https://doi.org/10.1016/S0921-5093(00)02016-5)

[82] P. Zhang, "Creep behavior of the die-cast Mg-Al alloy AS21," *Scr Mater* (2005), vol. 52, no. 4, pp. 277–282. (DOI: 10.1016/j.scriptamat.2004.10.017)

[83] K. Wei, L. Y. Wei, and R. Warren, "Creep Behaviour and Microstructure of Magnesium Die Cast Alloys AZ91 and AE42," *Materials Science Forum* (2007), vol. 546–549, pp. 73–76. (DOI: 10.4028/www.scientific.net/msf.546-549.73)

[84] Geranmayeh AR, Mahmudi R, Movahedi-Rad A, et al., "High-temperature mechanical properties of AZ61 and AZ61-0.7Si magnesium alloys," *Kov Mater.* (2012), vol. 50, pp. 393–397.

[85] P. S. Roodposhti, A. Sarkar, K. L. Murty, and R. O. Scattergood, "Dislocation Density Evolution During Creep of AZ31 Mg Alloy: A Study by X-ray Diffraction Line Profile Analysis," *Metallography, Microstructure, and Analysis*, vol. 4, no. 5, pp. 337–343. (DOI: 10.1007/s13632-015-0220-6)

[86] W. Qudong *et al.*, "Effects of Ca addition on the microstructure and mechanical properties of AZ91magnesium alloy," *Journal of Materials Science* (2001), vol. 36, pp. 3035-3040.

[87] A. A. Luo, M. P. Balogh, and B. R. Powell, “Creep and Microstructure of Magnesium-Aluminum-Calcium Based Alloys,” *Metallurgical and Materials Transactions A* (2002), vol. 33, pp. 567-574.

[88] D. Amberger, P. Eisenlohr, and M. Göken, “Microstructural evolution during creep of Ca-containing AZ91,” *Materials Science and Engineering: A* (2009), vol. 510–511, no. C, pp. 398–402. (DOI: 10.1016/j.msea.2008.04.115)

[89] J. Majhi and A. K. Mondal, “Microstructure and impression creep characteristics of squeeze-cast AZ91 magnesium alloy containing Ca and/or Bi,” *Materials Science and Engineering: A* (2019), vol. 744, pp. 691–703. (DOI: 10.1016/j.msea.2018.12.067)

[90] B. Kondori and R. Mahmudi, “Effect of Ca additions on the microstructure and creep properties of a cast Mg–Al–Mn magnesium alloy,” *Materials Science and Engineering: A* (2017), vol. 700, pp. 438–447, Jul. 2017. (DOI: 10.1016/j.msea.2017.06.007)

[91] K. Hirai, I. Takeuchi, Y. Takigawa, T. Uesugi, and K. Higashi, “Optimization of the Mg-Al-Zn-Ca-Sr alloy composition based on the parameter A’ in the constitutive equation for the climb-controlled dislocation creep including the stacking fault energy,” *Materials Science and Engineering: A* (2012), vol. 551, pp. 19–24. (DOI: 10.1016/j.msea.2012.04.06)

[92] Y. Nakaura, A. Watanabe, and K. Ohori, “Effects of Ca,Sr Additions on Properties of Mg-Al Based Alloys,” *Materials Transactions* (2006), vol. 47, no. 4, pp. 1031-1039.

[93] D. Zhang *et al.*, “Effects of minor Sr addition on the microstructure, mechanical properties and creep behavior of high pressure die casting AZ91-0.5RE based alloy,” *Materials Science and Engineering: A* (2017), vol. 693, pp. 51–59. (DOI: 10.1016/j.msea.2017.03.055)

[94] I.P. Moreno et al., "Microstructural Characterization of a Die-cast Magnesium-Rare Earth Alloy," *Scripta Materialia* (2001), vol. 45, pp. 1423-1429.

[95] B. Wang, X. Wang, J. Zhou, G. Zhang, and F. Liu, “Effects of solution heat treatment on microstructure and mechanical properties of Mg-3Al-1Si-0.3Mn-xSr alloy,” *Materials Science and Engineering: A* (2014), vol. 618, pp. 210–218. (DOI: 10.1016/j.msea.2014.09.044)

[96] H. J. Kang, J. Y. Park, Y. S. Choi, and D. H. Cho, “Influence of the solution and artificial aging treatments on the microstructure and mechanical properties of die-cast Al–Si–Mg alloys,” *Metals (Basel)* (2022), vol. 12, no. 1. (DOI: 10.3390/met12010071)

[97] M. B. Yang, C. Y. Qin, and F. S. Pan, “Effects of heat treatment on microstructure and mechanical properties of Mg-3Sn-1Mn magnesium alloy,” *Transactions of Nonferrous Metals Society of China (English Edition)* (2011), vol. 21, no. 10, pp. 2168–2174. (DOI: 10.1016/S1003-6326(11)60990-4)

[98] G. T. Kridli, P. A. Friedman, and J. M. Boileau, “Manufacturing processes for light alloys,” in *Materials, Design and Manufacturing for Lightweight Vehicles*, Elsevier Ltd., (2010), pp. 235–274. (DOI: 10.1533/9781845697822.2.235)

[99] B. R. Powell, P. E. Krajewski, and A. A. Luo, “Magnesium alloys for lightweight powertrains and automotive structures,” in *Materials, Design and Manufacturing for Lightweight Vehicles*, Elsevier (2020), pp. 125–186. (DOI: 10.1016/B978-0-12-818712-8.00004-5)

[100] M. R. Ghomashchi and A. Vikhrov, “Squeeze casting: an overview,” *Journal of Materials Processing Technology* (2000), vol. 101, Issues 1-3, pp. 1-9. (DOI: https://doi.org/10.1016/S0924-0136(99)00291-5)

[101] C. S. Goh, K. S. Soh, P. H. Oon, and B. W. Chua, “Effect of squeeze casting parameters on the mechanical properties of AZ91-Ca Mg alloys,” *Mater Des* (2010), vol. 31, pp. 550-553. (DOI: 10.1016/j.matdes.2009.11.039)

[102] G. A. Chadwick, “Squeeze casting of metal matrix composites using short fibre preforms,” *Materials Science and Engineering A* (1991), vol. 135, 30, pp. 23-28. (DOI: https://doi.org/10.1016/0921-5093(91)90530-Z)

[103] K. B. Nie, X. J. Wang, K. K. Deng, F. J. Xu, K. Wu, M. Y. Zheng,“Microstructure, Mechanical Properties And Deformation Behavior Of Az91-Based Magnesium Alloys,” Journal of Alloys and Compounds (2124), vol. 617, 25, pp. 979-987.

[104] N. Tahreen, D. F. Zhang, F. S. Pan, X. Q. Jiang, D. Y. Li, and D. L. Chen, “Strengthening mechanisms in magnesium alloys containing ternary I, W and LPSO phases,” *J Mater Sci Technol* (2018), vol. 34, no. 7, pp. 1110–1118. (DOI: 10.1016/j.jmst.2017.12.005)

[105] C. S. Kim *et al.*, “Prediction models for the yield strength of particle-reinforced unimodal pure magnesium (Mg) metal matrix nanocomposites (MMNCs),” *J Mater Sci* (2013), vol. 48, no. 12, pp. 4191–4204. (DOI: 10.1007/s10853-013-7232-x)

[106] K. Ma *et al.*, “Mechanical behavior and strengthening mechanisms in ultrafine grain precipitation-strengthened aluminum alloy,” *Acta Mater* (2014), vol. 62, no. 1, pp. 141–155. (DOI: 10.1016/j.actamat.2013.09.042)

[107] K. S. Tun and M. Gupta, “Improving mechanical properties of magnesium using nano-yttria reinforcement and microwave-assisted powder metallurgy method,” *Compos Sci Technol* (2007), vol. 67, no. 13, pp. 2657–2664. (DOI: 10.1016/j.compscitech.2007.03.006)

[108] D. N. Seidman, E. A. Marquis, and D. C. Dunand, “Precipitation strengthening at ambient and elevated temperatures of heat-treatable Al(Sc) alloys,” *Acta Materialia* (2002), vol. 50, issue 16, pp. 4021-4035. (DOI: https://doi.org/10.1016/S1359-6454(02)00201-X)

[109] C. Booth-Morrison, D. C. Dunand, and D. N. Seidman, “Coarsening resistance at 400 °c of precipitation-strengthened Al-Zr-Sc-Er alloys,” *Acta Mater* (2011), vol. 59, no. 18, pp. 7029–7042. (DOI: 10.1016/j.actamat.2011.07.057)

[110] R. Zeng, “PRECIPITATION HARDENING IN AZ91 MAGNESIUM ALLOY,” 2013.

[111] J. F. Nie, “Effects of precipitate shape and orientation on dispersion strengthening in magnesium alloys,” *Scr Mater* (2003), vol. 48, no. 8, pp. 1009–1015. (DOI: 10.1016/S1359-6462(02)00497-9)

[112] Z. Zhang and D. L. Chen, “Contribution of Orowan strengthening effect in particulate-reinforced metal matrix nanocomposites,” *Materials Science and Engineering: A* (2008), vol. 483–484, no. 1-2 C, pp. 148–152. (DOI: 10.1016/j.msea.2006.10.184)

[113] Z. Zhang and D. L. Chen, “Consideration of Orowan strengthening effect in particulate-reinforced metal matrix nanocomposites: A model for predicting their yield strength,” *Scr Mater (2006)*, vol. 54, no. 7, pp. 1321–1326. (DOI: 10.1016/j.scriptamat.2005.12.017)

[114] L. Liu, J. Zhang, and C. Ai, “Nickel-Based Superalloys,” *Encyclopedia of Materials: Metals and Alloys*, Elsevier (2021), pp. 294–304. (DOI: 10.1016/B978-0-12-803581-8.12093-4)

[115] C. H. C. Aceres and D. M. Rovera, “Solid solution strengthening in concentrated Mg±Al alloys.” *Journal of Light Metals* (2001), vol. 1, Issue 3, pp. 151-156. (DOI: https://doi.org/10.1016/S1471-5317(01)00008-6)

[116] A. Akhtars and E. Teghtsoonian, “Solid Solution Strengthening of Magnesium Single Crystals-I Alloying Behaviour In Basal Slip,” *Acta Metallurgica* (1969), vol. 17, Issue 11, pp. 1339-1349. (DOI: https://doi.org/10.1016/0001-6160(69)90151-5)

[117] S. Spigarelli, M. Cabibbo, E. Evangelista, M. Talianker, and V. Ezersky, “Analysis of the creep behaviour of a thixoformed AZ91 magnesium alloy,” *Materials Science and Engineering A (2000)*, vol. 289, Issues 1-2, pp. 172-181. (DOI: https://doi.org/10.1016/S0921-5093(00)00911-4)

[118] T. G. Langdon, “Identifying creep mechanisms at low stresses,” *Materials Science and Engineering A (2000)*, vol. 283, Issues 1-2, pp. 266-273. (DOI: https://doi.org/10.1016/S0921-5093(00)00624-9)

[119] F. Boioli, P. Carrez, P. Cordier, and A. M. Goryaeva, *Multiscale Modeling of the Mantle Rheology: The RheoMan Project*. (2018) (Available: https://www.researchgate.net/publication/327920426)

[120] “Mechanical Behaviour of Materials Chapter 05-2 Dislocation: Mechanics.”

[121] H. K. D. H. Bhadeshia, “Mechanisms and Models for Creep Deformation and Rupture.” (2003). DOI: 10.1016/B0-08-043749-4/05106-5)

[122] T. Mori, M. Koda, R. Monzen, and T. Mura, “Particle Blocking In Grain Boundary Sliding And Associated Internal Friction,” *Acta Metallurgica* (1983), vol. 31, Issue 2, pp. 275-283. (DOI: https://doi.org/10.1016/0001-6160(83)90104-9)

[123] V. Paidar and S. Takeuchi, “Superplastic Deformation Carried By Grain Boundaries,” *Acta Metallurgica et Materialia* (1992), vol. 40. Issue 7, pp. 1773-1782. (DOI: https://doi.org/10.1016/0956-7151(92)90120-4)

[124] H. Yang, S. Gavras, and H. Dieringa, “Creep Characteristics of Metal Matrix Composites,” in *Encyclopedia of Materials: Composites*, vol. 1, Elsevier, (2021), pp. 375–388. (DOI: 10.1016/B978-0-12-803581-8.11822-3)

[125] V. C. Igwemezie, C. C. Ugwuegbu, J. U. Anaele, and P. C. Agu, “Review of physical metallurgy of creep steel for the design of modern steam power plants - fundamental theories and parametric models,” *Journal of Engineering Science and Technology Review* (2015), vol. 8, no. 5, pp. 84–94. (DOI: 10.25103/jestr.085.12)

[126] M. Regev, A. Rosen, and M. Bamberger, “Qualitative Model for Creep of AZ91D Magnesium Alloy,” *Metallurgical and Materials Transactions A* (2001), vol. 32, pp. 1335-1345. (DOI: https://doi.org/10.1007/s11661-001-0224-5)

[127] H. Shastri, A. K. Mondal, K. Dutta, H. Dieringa, and S. Kumar, “Microstructural correlation with tensile and creep properties of AZ91 alloy in three casting techniques,” *J Manuf Process* (2020), vol. 57, pp. 566–573. (DOI: 10.1016/j.jmapro.2020.07.010)

[128] V. Gaffard, J. Besson, and A. F. Gourgues-Lorenzon, “Creep failure model of a tempered martensitic stainless steel integrating multiple deformation and damage mechanisms,” *Int J Fract* (2005), vol. 133, no. 2, pp. 139–166. (DOI: 10.1007/s10704-005-2528-8)

[129] S. Spigarelli, M. Regev, E. Evangelista, and A. Rosen, “Review of creep behaviour of AZ91 magnesium alloy produced by different technologies,” *Materials Science and Technology* (2001), vol. 17, Issue 6, pp. 627-638. (DOI: 10.1179/026708301101510483)

[130] I. Khoubrou, B. Nami, S.M. Miresmaeili, et al., “Influence of punch diameter on impression creep behavior of AZ91 magnesium alloy,” *Materials Science and Technology* (2022), Vol. 38, Issue 7, pp. 425-435. (DOI: https://doi.org/10.1080/02670836.2022.2045550)

[131] J. P. Rouse, F. Cortellino, J. Shingledecker, and others, "Small punch creep testing: Review on modelling and data interpretation," *Mater. Sci. Technol.* (2013), vol. 29, no. 11, pp. 1328-1345, 2013. (DOI: https://doi.org/10.1179/1743284713Y.0000000278)

[132] G. K. Williamson and R. E. Smallman, “III. Dislocation densities in some annealed and cold-worked metals from measurements on the X-ray Debye-Scherrer spectrum,” *Philosophical Magazine* (1956), vol. 1, no. 1, pp. 34–46. (DOI: 10.1080/14786435608238074)

[133] P. S. Roodposhti, A. Sarkar, K. L. Murty, and R. O. Scattergood, “Dislocation Density Evolution During Creep of AZ31 Mg Alloy: A Study by X-ray Diffraction Line Profile Analysis,” *Metallography, Microstructure, and Analysis* (2015), vol. 4, no. 5, pp. 337–343. (DOI: 10.1007/s13632-015-0220-6)

[134] T. Shintani, Y. Murata, Y. Terada, and M. Morinaga, “Evaluation of dislocation density in a Mg-Al-Mn-Ca alloy determined by X-ray diffractometry and transmission electron microscopy,” *Mater Trans* (2010), vol. 51, no. 6, pp. 1067–1071. (DOI: 10.2320/matertrans.M2010021)

[135] G. K. Williamsont and W. H. Hallt, “X-ray Line Broadening From Filed Aluminium And Wolfram,” *Acta Metallurgica* (1953), vol. 1. Issue 1. pp. 22-31. (DOI: https://doi.org/10.1016/0001-6160(53)90006-6)

[136] Y. Li and T. G. Langdon{, “High Strain Rate Superplasticity in Metal Matrix Composites: The Role of Load Transfer,” *Acta Materialia* (1998), vol. 46, Issue 11, pp. 3937-3948. (DOI: https://doi.org/10.1016/S1359-6454(98)00073-1)

[137] J. Cadek, V. Sustek, L. Kloc%, and E. Evangelista, “A Threshold creep behaviour of an Mg-Zn-Ca-Ce-La alloy processed by rapid solidification,” *Materials Science and Engineering: A* (1996), vol. 215, Issues 1-2, pp. 73–83. (DOI: https://doi.org/10.1016/0921-5093(96)10263-X)

[138] B. Kondori and R. Mahmudi, “Effect of Ca additions on the microstructure and creep properties of a cast Mg–Al–Mn magnesium alloy,” *Materials Science and Engineering: A* (2017), vol. 700, pp. 438–447. (DOI: 10.1016/j.msea.2017.06.007)

[139] H. Patil, A. Jain, A. Marodkar, P. Kumar, A. Ghosh, and H. Borkar, “Creep deformation study of squeeze cast AZ91 magnesium alloy,” *Materials Science and Technology (United Kingdom)* (2023), vol. 39, no. 15, pp. 1926–1938. (DOI: 10.1080/02670836.2023.2186055)

[140] Y. B. Unigovski, “Creep-Rupture Behavior of Die-Cast Magnesium Alloys,” *Journal of Metals, Materials and Minerals (*2009), vol. 19, no. 1, pp. 1-7.

[141] F. Naghdi and R. Mahmudi, “The microstructure and creep characteristics of cast Mg-4Zn-0.5Ca and Mg-4Zn-0.5Ca-2RE alloys,” *Materials Science and Engineering: A* (2014), vol. 610, pp. 315–325. (DOI: 10.1016/j.msea.2014.05.043)

[142] F. Naghdi, R. Mahmudi, J. Y. Kang, and H. S. Kim, “Threshold creep behaviour of an aged Mg–Zn–Ca alloy,” *Materials Science and Engineering: A* (2017), vol. 696, pp. 536–543. (DOI: 10.1016/j.msea.2017.04.104)

[143] S. Kashiwase, M. Unekawa, H. Hisazawa, and Y. Terada, “Three-dimensional morphology of C15-Al2Ca precipitates in a Mg-Al-Ca alloy,” *Nippon Kinzoku Gakkaishi/Journal of the Japan Institute of Metals* (2019), vol. 83, no. 6, pp. 193–197. (DOI: 10.2320/jinstmet.J2019009)

[144] J. Song, J. She, D. Chen, and F. Pan, “Latest research advances on magnesium and magnesium alloys worldwide,” Mar. 01, 2020, *National Engg. Reaserch Center for Magnesium Alloys*. (DOI: 10.1016/j.jma.2020.02.003)

[145] T. Chen, S. Hu, S. Li, and Q. Huo, “Uncovering the unexpected changes of creep properties in AZ-series Mg alloys,” *Materials Science and Engineering: A* (2022), vol. 857. (DOI: 10.1016/j.msea.2022.144056)

[146] T. Sato and M. V. Kral, “Microstructural evolution of Mg-Al-Ca-Sr alloy during creep,” *Materials Science and Engineering: A* (2008), vol. 498, no. 1–2, pp. 369–376. (DOI: 10.1016/j.msea.2008.08.006)

[147] M. Zubair *et al.*, “Strengthening of Mg–Al–Ca alloys with C15 and C36 Laves phases,” *J Mater Res* (2023), vol. 38, no. 15, pp. 3613–3627. (DOI: 10.1557/s43578-023-01082-x)

[148] X. Yang, H. Hou, Y. Zhao, L. Yang, and P. Han, “First-principles investigation of the structural, electronic and elastic properties of Al2Ca and Al4Sr phases in Mg-Al-Ca(Sr) alloy,” *Journal Wuhan University of Technology, Materials Science Edition* (2014), vol. 29, no. 5, pp. 1049–1056. (DOI: 10.1007/s11595-014-1042-0)

[149] Xin Zhang, “Applications of kinetic methods in thermal analysis: A Review,” *Engineered Science* (2020), vol. 14, PP. 1-13.

[150] T. Nayeri, M. Yari, and S. Sadreddini, “Effect of Sr on the Microstructure and Properties of Mg-6Al Alloy,” *Protection of Metals and Physical Chemistry of Surfaces* (2016), vol. 52, no. 2, pp. 273–278. (DOI: 10.1134/S2070205116020209)

[151] B. H. Kim, K. C. Park, Y. H. Park, and I. M. Park, “Microstructure and creep properties of Mg-4Al-2Sn-1(Ca,Sr) alloys,” *Transactions of Nonferrous Metals Society of China (English Edition)* (2010), vol. 20, no. 7, pp. 1184–1191. (DOI: 10.1016/S1003-6326(09)60276-4)

[152] K. Hazeli, A. Sadeghi, M. O. Pekguleryuz, and A. Kontsos, “The effect of strontium in plasticity of magnesium alloys,” *Materials Science and Engineering: A* (2013), vol. 578, pp. 383–393. (DOI: 10.1016/j.msea.2013.04.101)

[153] A. Tang, F. Pan, M. Yang, and R. Cheng, “Mechanical properties and microstructure of magnesium-aluminum based alloys containing strontium,” *Mater Trans* (2008), vol. 49, no. 6, pp. 1203–1211. (DOI: 10.2320/matertrans.MOV2007315)

[154] B. Zheng, L. Zhao, X. B. Hu, S. J. Dong, and H. Li, “First-principles studies of Mg17Al12 ,Mg 2 Al 3 ,Mg 2 Sn,MgZn 2 ,Mg 2 Ni and Al 3 Ni phases,” *Physica B Condens Matter* (2019), vol. 560, pp. 255–260. (DOI: 10.1016/j.physb.2018.11.067)

[155] D. W. Zhou, J. S. Liu, S. H. Xu, and P. Peng, “Thermal stability and elastic properties of Mg3Sb2and Mg3Bi2 phases from first-principles calculations,” *Physica B Condens Matter* (2010), vol. 405, no. 13, pp. 2863–2868. (DOI: 10.1016/j.physb.2010.04.013)

[156] J. Dai *et al.*, “Diffusion behavior and reactions between Al and Ca in Mg alloys by diffusion couples,” *J Mater Sci Technol* (2018), vol. 34, no. 2, pp. 291–298. (DOI: 10.1016/j.jmst.2017.10.007)

[157] H. Shastri, A. K. Mondal, K. Dutta, H. Dieringa, and S. Kumar, “Microstructural correlation with tensile and creep properties of AZ91 alloy in three casting techniques,” *J Manuf Process* (2020), vol. 57, pp. 566–573. (DOI: 10.1016/j.jmapro.2020.07.010)

[158] J. Majhi, T. Das, A. Basu, and A. K. Mondal, “An analysis of microstructure and impression creep response of squeeze-cast AZ91–xBi–ySr alloys,” *Materials Science and Technology (United Kingdom)* (2020), vol. 36, no. 6, pp. 731–742. (DOI: 10.1080/02670836.2020.1736763)

[159] R. M. Wang, A. Eliezer, and E. M. Gutman, “An investigation on the microstructure of an AM50 magnesium alloy,” *Materials Science and Engineering: A* (2003), vol. 355, no. 1–2, pp. 201–207. (DOI: 10.1016/S0921-5093(03)00065-0)

[160] Z. Zhao, Q. Chen, Y. Wang, and D. Shu, “Microstructures and mechanical properties of AZ91D alloys with Y addition,” *Materials Science and Engineering: A* (2009), vol. 515, no. 1–2, pp. 152–161. (DOI: 10.1016/j.msea.2009.03.030)

[161] J. Yan, Y. Sun, F. Xue, S. Xue, Y. Xiao, and W. Tao, “Creep behavior of Mg-2 wt.%Nd binary alloy,” *Materials Science and Engineering: A* (2009), vol. 524, no. 1–2, pp. 102–107. (DOI: 10.1016/j.msea.2009.06.008)

[162] Yanlong Ma, Jin Zhang, Mingbo Yang, "Research on microstructure and alloy phases of AM50 magnesium alloy," *Jornal of Alloys and Compounds* (2009), vol. 479, Issues 1-2, no. 11, pp. 515-521. (DOI: https://doi.org/10.1016/j.jallcom.2008.03.047)

[163] C. H. Cáceres, C. J. Davidson, J. R. Griffiths, and C. L. Newton, “Effects of solidification rate and ageing on the microstructure and mechanical properties of AZ91 alloy,” *Materials Science and Engineering: A* (2002), vol. 325, Issues 1-2, pp. 344-355. (DOI: https://doi.org/10.1016/S0921-5093(01)01467-8)

[164] L. Čížek, M. Greger, L. Pawlica, L. A. Dobrzański, and T. Tański, "Study of selected properties of magnesium alloy AZ91 after heat treatment and forming," in *Journal of Materials Processing Technology* (2004), vols. 157-158, pp. 466–471. (DOI: 10.1016/j.jmatprotec.2004.07.149)

[165] Y. Li, Y. Chen, H. Cui, B. Xiong, and J. Zhang, "Microstructure and mechanical properties of spray-formed AZ91 magnesium alloy," *Mater Charact* (2009), vol. 60, no. 3, pp. 240–245. (DOI: 10.1016/j.matchar.2008.09.007)

[166] S. N. Chen, W. Yang, H. Yu, and Y. L. Zhang, "Effects of microstructure modification and pressurized solidification on mechanical property of AZ91 alloy," *J Alloys Compd* (2014), vol. 611, pp. 1–6. (DOI: 10.1016/j.jallcom.2014.05.033)

[167] X. Xia, W. Zhao, X. Feng, H. Feng, and X. Zhang, "Effect of homogenizing heat treatment on the compressive properties of closed-cell Mg alloy foams," *Mater Des* (2013), vol. 49, pp. 19–24. (DOI: 10.1016/j.matdes.2013.01.064)

[168] M. S. Silva, C. Barbosa, O. Acselrad, and L. C. Pereira, "Effect of Chemical Composition Variation on Microstructure and Mechanical Properties of a 6060 Aluminum Alloy," *J Mater Eng Perform* (2004), vol. 13, no. 2, pp. 129–134. (DOI: 10.1361/1059949041830).

[169] Q. Chen *et al.*, "The mechanisms of grain growth of Mg alloys: A review,", *National Engg. Research Center for Magnesium Alloys* (2022), vol. 10, Issue 9, pp.2384-2397. (DOI: 10.1016/j.jma.2022.09.001)

[170] Z. Liu, C. Wang, J. Cheng, and J. Guo, "An Improved Grain Growth Model and Its Application in Gradient Heat Treatment of Aero-Engine Turbine Discs," *Materials* (2023), vol. 16, no. 19, pp.6584. (DOI: 10.3390/ma16196584)

[171] M. Kunst, A. Fischersworring-Bunk, G. L'Esperance, P. Plamondon, and U. Glatzel, "Microstructure and dislocation analysis after creep deformation of die-cast Mg-Al-Sr (AJ) alloy," *Materials Science and Engineering: A* (2009), vol. 510–511, no. C, pp. 387–392. (DOI: 10.1016/j.msea.2008.07.078)

[172] B. Kondori and R. Mahmudi, "Effect of Ca additions on the microstructure, thermal stability and mechanical properties of a cast AM60 magnesium alloy," *Materials Science and Engineering: A* (2010), vol. 527, no. 7–8, pp. 2014–2021. (DOI: 10.1016/j.msea.2009.11.043)

[173] S. M. Liang, R. S. Chen, J. J. Blandin, M. Suery, and E. H. Han, “Thermal analysis and solidification pathways of Mg-Al-Ca system alloys,” *Materials Science and Engineering: A* (2008), vol. 480, no. 1–2, pp. 365–372. (DOI: 10.1016/j.msea.2007.07.025)

[174] A. Afsharnaderi, M. Malekan, M. Emamy, J. Rasizadeh Ghani, and M. Lotfpour, “Microstructure Evolution and Mechanical Properties of the AZ91 Magnesium Alloy with Sr and Ti Additions in the As-Cast and As-Aged Conditions,” *J Mater Eng Perform* (2019), vol. 28, no. 11, pp. 6853–6863. (DOI:10.1007/s11665-019-04396-2)